

JOURNÉES SCIENTIFIQUES, WORKSHOP



JOURNÉES SCIENTIFIQUES D'URSI-FRANCE



LA MÉTROLOGIE AU CŒUR DES TECHNOLOGIES CONTEMPORAINES

FONDAMENTAUX, METHODES ET INSTRUMENTS, DE LA RF JUSQU'A L'OPTIQUE

10-12 JUN 2025, PARIS 6^E, CAMPUS DES CORDELIERS

METROLOGY AT THE HEART OF TODAY'S TECHNOLOGIES

FUNDAMENTALS, METHODS AND INSTRUMENTS, FROM RF TO OPTICS

LES SEPT CONSTANTES FONDAMENTALES DE LA PHYSIQUE
 Les unités hertz (Hz), coulomb (C), lumen (lm) et watt (W) sont reliées aux unités seconde (s), mètre (m), kilogramme (kg), ampère (A), kelvin (K), mole (mol) et candela (cd).

- h** La constante de Planck est fixée et strictement égale à $6,626\ 070\ 15 \times 10^{-34}$ J.s (ou $m^2 \cdot kg/s$ en unités de base)
- c** La vitesse de la lumière dans le vide est fixée et strictement égale à 299 792 458 m/s
- $\Delta\nu_{Cs}$** La fréquence de la transition hyperfine de l'état fondamental de l'atome de césium 133 non perturbé est fixée et strictement égale à 9 192 631 770 Hz
- e** La charge élémentaire est fixée et strictement égale à $1,602\ 176\ 634 \times 10^{-19}$ C (ou A.s en unité de base)
- k** La constante de Boltzman est fixée et strictement égale à $1,380\ 649 \times 10^{-23}$ J/K (ou $m^2 \cdot kg/s^2 \cdot K$ en unités de base)
- N_A** La constante d'Avogadro est fixée et strictement égale à $6,022\ 140\ 76 \times 10^{23}$ mol⁻¹
- K_{cd}** L'efficacité lumineuse d'un rayonnement monochromatique de fréquence 540×10^{12} Hz est fixée et strictement égale à 683 lm/W (ou $lm \cdot s^3/m^2 \cdot kg$ en unités de base)

150 years of the Metre Convention

1570-1870

LE CENTRE

* Constantes dont les valeurs n'étaient pas fixées avant 2017.

Crédit illustration de couverture : Atelier Isatis – Dijon

ACTES

PROCEEDINGS

TABLE DES MATIERES

EDITORIAL.....	6
COMITÉS.....	8
PROGRAMME.....	9
RÉSUMÉS DES KEYNOTES ET EXPOSÉS INVITÉS	12
PRIX DE THÈSE EN RADIOSCIENCES	21
TABLE DES MATIERES DES SESSIONS ET ARTICLES (pagination de 1 à 110)	24
LISTE DES AUTEURS.....	111

EDITORIAL

L'édition 2025 des Journées scientifiques d'URSI-France, sous l'égide de l'Académie des sciences, a pour thème : « La Métrologie au cœur des technologies contemporaines - *Fondamentaux, méthodes et instruments, de la RF jusqu'à l'optique* ».

La métrologie est la science de la mesure. Elle définit les principes et les méthodes permettant de garantir la confiance des mesures. Pour cela, elle développe et veille à maintenir des étalons nationaux de référence, reconnus sur le plan international et qui permettent à l'industrie de raccorder leurs instruments de mesure au Système International d'unités (SI). Il s'agit d'une science transversale qui s'applique dans tous les domaines où des mesures quantitatives sont effectuées, relevant à la fois de problématiques fondamentales et d'objectifs applicatifs. C'est la raison pour laquelle, même en se restreignant à ceux pour lesquels les ondes électromagnétiques jouent un rôle, il est ici question d'une multiplicité de sujets.

Le programme de ces Journées scientifiques illustre l'importance absolue de la métrologie qui est au cœur des technologies contemporaines. Les deux conférences plénières portent sur les 150 ans de la Convention du mètre et le SI au service du développement technologique ainsi que sur l'évolution des unités SI utilisées en radioélectricité. Les cinq conférences invitées portent quant à elles sur l'infrastructure de recherche innovante REFIMEVE permettant la dissémination ultra-précise des références nationales de temps et de fréquence, l'imagerie par caméra planaire micro-ondes pour la détection du cancer du sein, la mesure non perturbatrice de champs électromagnétiques, la nouvelle plateforme de mesure de diffraction MIMOSA en chambre anéchoïque, ainsi qu'un panorama des projets de recherche européens en métrologie électrique.

Les dix-neuf communications orales et les quatre thèses de jeunes scientifiques nominés, présentées sur ces deux jours et demi, ont fait l'objet d'une sélection par le comité scientifique et le jury pour le prix de thèse. Elles abordent des thématiques diverses liées à la métrologie électromagnétique : capteurs électromagnétiques et optiques, dosimétrie électromagnétique et exposimétrie, mesures électromagnétiques des objets biologiques, mesures haute fréquence, localisation électromagnétique et radar, mesure des SER et des signatures. Les exposés et les discussions qui les suivront seront au choix en Français ou en Anglais.

Les Journées scientifiques 2025 se tiennent sur le Campus des Cordeliers, avec le soutien de Sorbonne Université, du Groupement de recherche Ondes, du Bureau des longitudes, du Laboratoire national de métrologie et d'essais et du Bureau international des poids et mesures. Des posters célébrant les 150 ans de la Convention du mètre et des expositions par des industriels sont au programme de ces journées.

Enfin, comme chaque année, les Journées scientifiques accueillent la remise de la médaille du CNFRS/URSI-France, honorant une personnalité qui a contribué de façon remarquable aux progrès dans le domaine des radiosciences et à l'animation de la communauté scientifique. Le « Prix de thèse en radiosciences » sera attribué le 12 juin matin à un(e) jeune scientifique afin de récompenser ses travaux. Enfin, un prix du meilleur article « jeune scientifique » sera remis par le comité scientifique à un doctorant ou post-doctorant, premier auteur de la communication.

Joseph Achkar

Président du Comité scientifique des Journées scientifiques 2025 d'URSI-France

Tahsin Akalin, Djamel Allal, Olivier Meyer, Julien Sarrazin, Yann Le Bihan

Vice-présidents du Comité scientifique des Journées scientifiques 2025 d'URSI-France

EDITORIAL

The 2025 edition of the URSI-France Workshop, under the aegis of the Académie des sciences, has the theme: "Metrology at the heart of contemporary technologies - Fundamentals, methods and instruments, from RF to optics."

Metrology is the science of measurement. It defines the principles and methods for ensuring the confidence of measurements. To this end, it develops and ensures the keeping of national reference standards, recognized internationally, which allow industry to get traceability of their measuring instruments to the International System of Units (SI). It is a transversal science that applies to all fields where quantitative measurements are carried out, relating to both fundamental issues and application objectives. This is why, even if we restrict ourselves to those for which electromagnetic waves play a role, a multiplicity of topics are discussed here.

The program of the workshop illustrates the absolute importance of metrology, which is at the heart of contemporary technologies. The two plenary conferences focus on the 150th anniversary of the Metre Convention and the SI to serve new technology developments, as well as on the evolution of SI units used in radioelectricity. The five invited lectures focus on the innovative REFIMEVE research infrastructure enabling the ultra-precise dissemination of national time and frequency references, microwave planar camera imaging for breast cancer detection, non-disruptive measurement of electromagnetic fields, the new MIMOSA diffraction measurement platform in anechoic chamber, as well as an overview of European research projects in electrical metrology.

The nineteen oral presentations and the four theses by young scientists nominated, presented over these two and a half days, were selected by the scientific committee and the jury for the thesis prize. They address various themes related to electromagnetic metrology: electromagnetic and optical sensors, electromagnetic dosimetry and exposimetry, electromagnetic measurements of biological objects, high-frequency measurements, electromagnetic localization and radar, RCS and signature measurements. Presentations and discussions that follow will be in French or English.

The 2025 Workshop is being held on the Campus des Cordeliers, with the support of Sorbonne Université, the Groupement de recherche Ondes, the Bureau des longitudes, the Laboratoire national de métrologie et d'essais and the Bureau international des poids et mesures. Posters celebrating the 150th anniversary of the Metre Convention and industrial exhibitions are on the program for this workshop.

Finally, as every year, the workshop host the CNFRS/URSI-France medal ceremony, honouring a person who has made an outstanding contribution to progress in the field of radioscience and to the animation of the scientific community. The "Thesis Prize in Radioscience" will be awarded on the morning of 12 June to a young scientist as a reward for their work. Finally, a prize for the best "young scientist" paper will be awarded by the scientific committee to a doctoral or postdoctoral student, first author of the paper.

Joseph Achkar

Chair of the scientific committee of URSI-France 2025 Workshop

Tahsin Akalin, Djamel Allal, Olivier Meyer, Julien Sarrazin, Yann Le Bihan

Vice-Chairs of the scientific committee of URSI-France 2025 Workshop

COMITÉS

Président du Comité Scientifique : Joseph Achkar (LNE-OP, Observatoire de Paris)

Co-présidents : Tahsin Akalin (IEMN, U. Lille), Djamel Allal (LNE), Olivier Meyer (GEEPS, Sorbonne U.), Julien Sarrazin (GEEPS, Sorbonne U.), Yann Le Bihan (GEEPS, U. Paris-Saclay)

Joël Andrieu (XLIM, U. Limoges) Aktham Asfour (G2elab, U. Grenoble Alpes) Stéphan Briaudeau (LNE-CNAM) Alexis Chevalier (Lab-STICC, U. Bretagne Occidentale) Baptiste Chupin (LNE-OP, Observatoire de Paris) Andrea Cozza (GEEPS, CentraleSupélec) Raffaele D'Errico (LETI, CEA) Jean-Marc Decitre (ASNR) Cédric Durand (STMICROELECTRONICS) Omar Elmazria (Institut Jean Lamour, U. Lorraine) Katia Grenier (LAAS, CNRS) Kamel Haddadi (IEMN, U. Lille) Lucien Hammen (INRS) Pierre-Marie Jacquart (Dassault Aviation) Pierre-Etienne LÉVY (DER "Sciences de l'Ingénierie Électrique et Numérique", ENS Paris-Saclay)	Rodolphe Le Targat (LNE-OP, Observatoire de Paris) Laurent le Coq (IETR, U. Rennes) Laurent Pecastaing (SIAME, U. de Pau et des Pays de l'Adour) Odile Picon (ESYCOM, U. Gustave Eiffel) François Piquemal (LNE) Paul-Eric Pottier (LNE-OP, CNRS) Philippe Pouliguen (DGA/AID) Frédéric Pythoud (METAS, Suisse) Christophe Risacher (IRAM) Christophe Roblin (LTCI, Télécom Paris) Enrico Rubiola (FEMTO-ST, U. Bourgogne-Franche-Comté) François Sarrazin (IETR, U. Rennes) Olivier Tantot (XLIM, U. Limoges) Joe Wiart (LTCI, Télécom Paris) Maxim Zhadobov (IETR, CNRS)
--	--

Président du Comité d'Organisation : Alain SIBILLE (URSI-France & LTCI, Télécom Paris)

Joël Hamelin (URSI-France) Lluis M. Mir (CNRS & URSI-France)	Hervé Sizun (URSI-France)
---	---------------------------

PROGRAMME

Mardi 10 juin 2025

08:30 - 09:30	Accueil café, Enregistrement (Cloître)
09:30 - 09:40	Ouverture des JS 2025 (Amphi Pasquier) - Lluis M. Mir, Joseph Achkar, Alain Sibille
09:40 - 10:20	Exposé keynote : La convention du mètre Convention et le SI : 150 années pour servir de nouveaux développements technologiques (Amphi Pasquier) - Marc Himbert (CNAM)
10:20 - 10:50	Pause café (Cloître)
10:50 - 11:50	Session 1 : Capteurs électromagnétiques et optiques (Amphi Pasquier)
10:50 - 11:10	> Capteur résonnant pour détection d'obstacles dans de l'eau douce - Nicolas TROESCH, Institut d'Electronique et des Systèmes, Hydrosiences Montpellier
11:10 - 11:30	> First steps of low cost PCB E-near field radiation metrology with microwave imaging scanner - Nolane DELILLE, Université de Bourgogne - Jerome ROSSIGNOL, Université de Bourgogne - SEBASTIEN LALLECHERE, Safran Tech - BLAISE RAVELO, NUIST
11:30 - 11:50	> Micro-resonators for dynamic investigation of soft matter: From particle sedimentation to product stability - Jordan Gastebois, Institut d'Électronique et des Technologies du numÉrique
11:50 - 12:20	Exposé invité : Imagerie par caméra planaire micro-ondes pour la détection du cancer du sein à l'aide d'apprentissage profond (Amphi Pasquier) - Ambroise Diès, Nadine Joachimowicz et Hélène Roussel (GEEPS, Sorbonne Université)
12:20 - 14:00	Déjeuner (Cloître)
14:00 - 14:30	Exposé invité : Mesure non perturbatrice de champs électromagnétiques avec des antennes RX optiques (Amphi Pasquier) - Lionel Duvillaret (KAPTEOS)
14:30 - 15:30	Session 2 : Dosimétrie électromagnétique et exposimétrie (Amphi Pasquier)
14:30 - 14:50	> Correlation Analysis on UL EMF Exposure in France Metropolitan Areas - QUNFEI SUN, Laboratoire d'Informatique Paris Descartes
14:50 - 15:10	> Hybrid approach of the measurement of actual head EMF exposure - Shanshan Wang, Télécom Paris
15:30 - 15:50	Exposé industriel : Phase Noise Analysis Overview (Amphi Pasquier) - Karim Louertani, Rohde & Schwarz (Amphi Pasquier)
15:50 - 16:20	Pause café (Cloître)
16:20 - 16:50	Exposé invité : Le projet REFIMEVE (Amphi Pasquier) - Paul-Eric Pottie (LNE-OP, CNRS)
16:50 - 17:10	Session 3 : Mesures électromagnétiques des objets biologiques, diagnostics et bio-détection (Amphi Pasquier)
16:50 - 17:10	> Analyse non-invasive du taux de sucre dans les tubercules de pommes de terre par mesures diélectriques micro-ondes - Clément Lenoir, Institut d'Électronique, de Microélectronique et de Nanotechnologie - UMR 8520
17:10 - 17:30	Session 4 : session ouverte (Amphi Pasquier)
17:10 - 17:30	> Negative time experimentation with RC-network based low-pass NGD circuit - Blaise Ravelo, NUIST
17:30 - 17:40	Pause (Amphi Pasquier)
17:40 - 18:00	Remise de la médaille du CNFRS / URSI France par Francis-André Wollman - Chair: Lluis M. Mir (Amphi Pasquier)
18:00 - 18:40	Exposé invité par Joe Wiart, médaillé 2025 (Amphi Pasquier)
19:00 - 21:00	Cocktail dinatoire (Cloître)

09:00 - 09:10	Introduction jour 2
09:10 - 09:50	Exposé keynote : L'évolution des unités SI utilisées en radioélectricité- Luc Erard, François Piquemal (LNE)
09:50 - 10:50	Session 5 (1^{re} partie) : Mesures haute fréquence, outils et méthodes de calibrage (Amphi Pasquier)
09:50 - 10:10	> Millimeter-wave radioastronomy measurement challenges - Christophe Risacher, Institut de RadioAstronomie Millimétrique
10:10 - 10:30	> Novel Thermopile Design for Waveguides and Coaxial Microcalorimeters in the Frequency range from DC – 40 GHz - Doudou BA, Laboratoire National de Métrologie et d'Essais [Trappes]
10:30 - 10:50	> Calibrated measurements of dopant concentration on vertical nanowires by scanning microwave microscopy - José A. Morán-Meza, Laboratoire National de Métrologie et d'Essais [Trappes]
10:50 - 11:20	Pause café (Cloître)
11:20 - 12:20	Session 5 (2^e partie) : Mesures haute fréquence, outils et méthodes de calibrage (Amphi Pasquier)
11:20 - 11:40	> Station de Mesure on-Wafer Nano-Robotisée Assistée par IA : Automatisation, Précision et Évaluation des Performances - Clément Lenoir, Institut d'Électronique, de Microélectronique et de Nanotechnologie - UMR 8520, Institut de Recherche sur les Composants logiciels et matériels pour l'Information et la Communication Avancé - USR 3380 - Kamel Haddadi, Institut d'Électronique, de Microélectronique et de Nanotechnologie - UMR 8520, Institut de Recherche sur les Composants logiciels et matériels pour l'Information et la Communication Avancé - USR 3380
11:40 - 12:00	> On-Wafer Calibration for Nanodevice Characterization up to 110 GHz - Daouda Seck, Institut d'Électronique, de Microélectronique et de Nanotechnologie - UMR 8520, Laboratoire National de Métrologie et d'Essais [Trappes]
12:00 - 12:20	> Densités de Probabilité du Lag-1 dans les Séries Temporelles Linéaires et Circulaires Modélisant les Processus de Brassage - Rabah Florian Monsef, GeePS
12:20 - 14:00	Déjeuner (Cloître)
14:00 - 14:30	Exposé invité : - La nouvelle plateforme de mesure de diffraction MIMOSA - Jean-Michel Geffrin (Institut Fresnel, Aix Marseille Université)
14:30 - 15:30	Session 6 : Localisation électromagnétique et radar, mesure des SER et des signatures (Amphi Pasquier)
14:30 - 14:50	> Localization of metallic lost tools using UHF RFID system - Nawres Hamrouni, Institut de Recherche en Systèmes Electroniques Embarqués
14:50 - 15:10	> Metasurface for direction of arrival estimation - Nawel Meftah, LEME, Univ Paris Nanterre - Shah Nawaz Burokur, LEME, Univ Paris Nanterre
15:10 - 15:30	> Surveillance de foule à l'aide d'une antenne à ondes de fuite dans une communication et détection intégrées - Mathis Melki, Laboratoire Génie électrique et électronique de Paris
15:30 - 16:00	Pause café (Cloître)
16:00 - 16:40	Session 7 : Session ouverte (Amphi Pasquier)
16:00 - 16:20	> Stacked Multi-Via Mushroom-Type EBG Structures with Glide Symmetry - Ashray Ugle, Laboratoire de Génie Électrique et Électronique de Paris, Université Paris-Saclay, CentraleSupélec, CNRS, 1Sorbonne Université
16:20 - 16:40	> Dispersive Analysis of Waveguides for Leaky-Wave Antennas - Yuhuan Tong, Laboratoire Génie électrique et électronique de Paris, Laboratoire de Génie Electrique et Electronique de Paris
16:40 - 18:00	Assemblée générale d'URSI-France 2025

Jeudi 12 juin 2025

09:00 - 09:05	Introduction jour 3 (Amphi Pasquier)
09:05 - 09:35	Exposé invité : Projets de recherche européens en métrologie électrique - Djamel Allal (LNE)
09:35 - 09:45	Remise du prix de thèse en radiosciences 2025 (Amphi Pasquier) - Lluís M. Mir, Alain Sibille, Karl-Ludwig Klein
09:45 - 10:15	Exposé invité : Electro(magnetic) fields interactions with cells: mechanistic insights and potential new therapeutic applications - Leslie Vallet
10:15 - 10:45	Pause café (Cloître)
10:45 - 10:50	Introduction à la session ouverte "prix de thèse" (Amphi Pasquier) - Lluís M. Mir, Alain Sibille, Karl-Ludwig Klein
10:50 - 11:10	> Contrôle électrique de l'injection de spin dans les diodes électroluminescentes avec un injecteur à couple spin-orbite (Amphi Pasquier) - Pambiang-Abel Dainone
11:10 - 11:30	> Shipborne Global Navigation Satellite Systems for Offshore Atmospheric Water Vapor Monitoring (Amphi Pasquier) - Aurélie Panetier
11:30 - 11:40	Remise du prix "jeune scientifique" (Amphi Pasquier)
11:40 - 12:00	Clôture des JS 2025 et présentation des JS 2026 d'URSI-France (Amphi Pasquier) - Joseph Achkar, Lluís M. Mir, Alain Sibille, Joe Wiat

RÉSUMÉS DES KEYNOTES ET EXPOSÉS INVITÉS

KEYNOTE : Marc HIMBERT (CNAM)

The Metre Convention and the SI: 150 years to serve new technology developments

L'origine du système métrique remonte à la Révolution française à la fin du XVIIIe siècle. Avant cette période, la France, comme de nombreux autres pays, utilisait une multitude d'unités de mesure locales et régionales. La Révolution a ainsi mis en avant la nécessité d'un système uniforme, facilement compréhensible et appliqué dans tout le pays, dans un souci de rationalisation. En 1790, l'Assemblée nationale française a constitué une commission pour définir une unité de mesure universelle et a adopté le système métrique fondé sur un système décimal d'unités. Ce groupe de travail, dirigé par le scientifique Jean-Charles de Borda et comprenant d'autres figures notables comme Lavoisier et Laplace, a proposé une nouvelle unité fondamentale : le mètre. Cette unité était fondée sur la circonférence de la Terre, en particulier la dix-millionième partie de l'arc de méridien terrestre entre le pôle Nord et l'équateur. Cette définition fut officialisée en 1799 avec la fabrication d'un prototype en platine. A la même époque, le système métrique, MKS, incluait également l'unité de masse, le kilogramme, et de temps, la seconde. Le 20 mai 1875, la Convention du Mètre est signée par 17 pays à Paris, établissant le Bureau international des poids et mesures (BIPM) pour assurer la cohérence des mesures. Sous son égide, le mètre a ensuite connu plusieurs redéfinitions : en 1960, il fut lié à la longueur d'onde d'une radiation du krypton-86, puis en 1983, il fut défini comme la distance parcourue par la lumière dans le vide en $1/299\,792\,458$ de seconde, garantissant une précision extrême. L'ensemble des unités initiales ont fait également l'objet de nombreux travaux de recherche afin d'en améliorer leur définition au fil des 150 ans d'existence de la convention du mètre. En parallèle et avec le développement des mesures pour l'industrie, le commerce, la santé, les transactions commerciales, quatre unités (ampère, kelvin, candela et mole) ont été ajoutées aux trois unités initiales. Cet ensemble de 7 unités a été officialisé en 1960 par la création du SI (Système international d'unités), ce choix conventionnel de sept grandeurs et unités permet de construire des unités pour toutes les grandeurs des domaines couverts.

L'évolution des unités SI utilisées en radioélectricité

Unités électriques

Historiquement, les unités électriques du SI, telles que l'ampère, le volt et l'ohm, ont d'abord été définies expérimentalement à la fin du XIXe siècle à partir d'effets électromagnétiques.

L'ampère a été initialement défini comme le courant qui dépose une masse d'argent de 0,001118 gramme par seconde sur la cathode d'un électrolyseur de nitrate d'argent, puis en 1948, comme l'intensité d'un courant produisant une force donnée entre deux fils parallèles. Pour la réalisation de l'ohm, l'affaire était plus délicate car utilisant une colonne de mercure (d'une section de 1 mm² et d'une longueur de 106,3 cm). Cet ohm mercuriel a été remplacé par des étalons à base de fils résistifs bobinés de valeurs de résistance très stables et plus faciles d'emploi.

A partir du 1er janvier 1990, la représentation de l'ohm devenait quantique en la reposant sur la constante de von Klitzing ($R_K = 25\,812,807\ \Omega$) accessible à partir de l'effet Hall quantique.

Le volt, unité de tension électrique, était autrefois réalisé à partir d'une pile étalon saturée en cadmium inventée par Weston. Près d'un siècle plus tard cette représentation du volt a été améliorée avec l'utilisation des références électroniques à diodes Zener. A partir de 1990 également, ces étalons matériels ont été remplacés par des étalons quantiques à base de jonctions Josephson pour représenter le volt en fonction de la constante de Josephson ($K_J = 483\,597,9\ \text{GHz/V}$).

En 2019, une réforme majeure du SI a conduit à la redéfinition des unités de base de sorte qu'elles soient toutes définies à partir de constantes de la physique. L'ampère est désormais défini en fonction de la charge élémentaire de l'électron ($e = 1,602\,176\,634 \times 10^{-19}\ \text{C}$), garantissant une meilleure précision et stabilité et les constantes de von Klitzing et Josephson sont directement définies en fonction de la charge élémentaire et de la constante de Planck. L'ensemble des grandeurs et unités électriques ont été redéfinies en conséquence, sans changement majeur, sauf éventuellement dans les laboratoires mettant en œuvre les expériences liées à la réalisation du volt et de l'ohm.

Les grandeurs radiofréquences de base telles que la puissance, l'affaiblissement, le facteur de réflexion, champ électromagnétique, facteur d'antennes... ont conservé leurs réalisations et traçabilité aux SI par le biais des grandeurs définies en courant continu puis basse fréquence. En revanche, la bande de fréquence couverte s'est notamment élargie jusqu'au terahertz.

Unité de temps

Le temps à longtermes été défini par des phénomènes astronomiques, comme la durée d'un jour solaire moyen. En 1967, la seconde a été redéfinie comme la durée de 9 192 631 770 périodes de la radiation émise par la transition entre deux niveaux de l'atome de césium-133. Avec l'avènement des horloges atomiques, cette définition permet une précision temporelle inégalée. Des recherches sont en cours pour la remplacer par une définition encore plus précise fondée sur des horloges optiques fonctionnant avec des atomes comme l'ytterbium ou le strontium.

Electrical units

Historically, SI electrical units, such as the ampere, the volt, and the ohm, were first defined experimentally in the late 19th century based on electromagnetic effects.

The ampere was initially defined as the current that deposits a mass of silver weighing 0.001118 grams per second on the cathode of a silver nitrate electrolyzer, and then, in 1948, as the intensity of a current producing a given force between two parallel wires. Deriving the ohm was more complicated because it required a mercury column (with a cross-section of 1 mm² and a length of 106.3 cm). This mercury ohm was later replaced by standards based on wound resistive wires with very stable and easier-to-use resistance values. As of January 1, 1990, the representation of the ohm became quantum, based on the von Klitzing constant ($R_K = 25,812.807\ \Omega$), accessible from the quantum Hall effect.

The volt, a unit of electrical voltage, was formerly produced from a saturated cadmium standard cell invented by Weston. Nearly a century later, this representation of the volt was improved with the use of Zener diode electronic references. Also starting in 1990, these material standards were replaced by quantum standards based on Josephson junctions to represent the volt as a function of the Josephson constant ($K_J = 483,597.9 \text{ GHz/V}$).

In 2019, a major reform of the SI led to the redefinition of the base units so that they are all defined based on physical constants. The ampere is now defined based on the elementary charge of the electron ($e = 1.602 176 634 \times 10^{-19} \text{ C}$), ensuring greater accuracy and stability, and the von Klitzing and Josephson constants are directly defined based on the elementary charge and Planck's constant. All electrical quantities and units were redefined accordingly, without major changes, except possibly in laboratories conducting experiments related to the realization of the volt and the ohm.

Basic radiofrequency quantities such as power, attenuation, reflection factor, electromagnetic field, antenna factor, etc., have retained their realizations and traceability to the SI through quantities defined in direct current and then low frequency. On the other hand, the frequency band covered has notably expanded to terahertz.

Unit of Time

Time has long been defined by astronomical phenomena, such as the length of a mean solar day. In 1967, the second was redefined as the duration of 9,192,631,770 periods of the radiation emitted by the transition between two levels of the cesium-133 atom. With the advent of atomic clocks, this definition allows for unparalleled temporal precision. Research is underway to replace it with an even more precise definition based on optical clocks powered by atoms such as ytterbium or strontium.

Imagerie par caméra planaire micro-ondes pour la détection du cancer du sein à l'aide d'apprentissage profond

Cette étude porte sur l'imagerie mammaire. Une approche spectrale basée sur le théorème de diffraction de Fourier est combinée à une paire d'U-NET pour réaliser l'imagerie quantitative en temps réel du sein. La paire d'U-NET est entraînée sur la base des spectres des courants induits afin d'obtenir en sortie les spectres de contrastes diélectrique associés. La base de données spectrales est construite en utilisant des combinaisons de cavités anthropomorphiques permettant de modéliser différents type de seins (avec ou sans tumeur). La fonction de coût WMAPE est associée à l'optimiseur Adam pour effectuer l'optimisation. Des résultats numériques sont présentés pour valider le concept proposé et démontrer la transformation apportée par les U-NETs.

This study focuses on breast imaging. A spectral approach based on the Fourier diffraction theorem is combined with a pair of U-NETs to perform real-time quantitative human breast imaging. The U-NET pair is trained based on the input of an induced current spectrum and the output of a contrast dielectric spectrum. A spectral database is constructed using combinations of anthropomorphic cavities. The weighted mean absolute percentage error (WMAPE) loss is associated with the Adam optimizer to perform optimization. Numerical results are presented to validate the proposed concept to demonstrate the transformation brought about by the U-NETs.

EXPOSÉ INVITÉ : Lionel DUVILLARET & Gwenaël GABORIT (Kapteos SAS)

Mesure non perturbatrice de champs électromagnétiques avec des antennes RX optiques

La mesure de champs électromagnétiques revêt une importance capitale dans de nombreux domaines allant du médical (vérification de l'innocuité des implants médicaux en IRM) jusqu'à la physique fondamentale (mesure d'impulsions électromagnétiques géantes créées par interaction laser-matière) en passant par les secteurs des télécoms, de la défense ou de l'aérospatial. Chaque fois qu'un champ électromagnétique doit être mesuré de manière qualitative et/ou quantitative s'offrent à l'expérimentateur les solutions usuelles que sont :

- les antennes classiques à bande passante généralement limitée à moins d'une décade et au facteur d'antenne proportionnel au logarithme de la fréquence,
- les capteurs dérivatifs (D-dots et B-dots) qui présentent des restrictions d'usage et des bandes passantes généralement limitées à quelques GHz.

Outre les limitations évoquées supra, ces capteurs métalliques ne permettent de réaliser des mesures non perturbatrices qu'en champ lointain ou au mieux en zone de Fresnel avec des restrictions.

Nous présenterons l'alternative que constituent les antennes optiques avec leurs avantages et leurs limitations. Comparativement aux antennes classiques, elles présentent :

- une bande passante extrêmement élevée,
- une taille millimétrique indépendante de la fréquence,
- une quasi absence de perturbation induite y compris en zone de champ proche réactif,
- une adaptation à tout milieu (gaz, liquides, plasmas froids),
- un seuil de dommage supérieur au champ de claquage dans l'air,
- une sélectivité nettement supérieure,
- un facteur d'antenne constant jusqu'à quelques GHz puis décroissant au-delà,

Cet ensemble d'avantages se paye par une sensibilité en net retrait pour les fréquences inférieures à 10 GHz, limitant de fait leur utilisation aux champs forts et aux mesures en champ proche pour lesquelles elles sont justement adaptées.

Des exemples de mesure illustreront ce comparatif entre antennes RX classiques d'une part, et RX optiques d'autre part.

The measurement of electromagnetic fields is of vital importance in many fields, from medicine (checking the safety of medical implants in MRI) to fundamental physics (measuring giant electromagnetic pulses created by laser-matter interaction), not forgetting the telecom, defense and aerospace sectors. Whenever an electromagnetic field needs to be measured qualitatively and/or quantitatively, the experimenter is offered the usual solutions:

- *conventional antennas with a bandwidth generally limited to less than a decade, and an antenna factor proportional to the logarithm of the frequency,*
- *derivative sensors (D-dots and B-dots), which have restrictions on use and bandwidths generally limited to a few GHz.*

In addition to the limitations mentioned above, these metallic sensors can only be used for non-interfering measurements in the far field, or at best in the Fresnel zone, with some restrictions.

We present the alternative of optical antennas, with their advantages and limitations. Compared with conventional antennas, they offer:

- *an extremely high bandwidth*
- *a millimetric size, independent of frequency,*
- *virtually no induced interference, even in near-reactive fields,*
- *adaptation to any medium (gases, liquids, cold plasmas),*
- *a higher damage threshold than the breakdown field in air,*
- *a significantly higher selectivity,*

- *a constant antenna factor up to a few GHz, decreasing thereafter,*

This set of advantages comes at the price of a much lower sensitivity at frequencies below 10 GHz, limiting their use to strong fields and near-field measurements, for which they are ideally suited.

Measurement examples will illustrate this comparison between conventional RX antennas on the one hand, and optical RX on the other.

EXPOSÉ INVITÉ : Paul-Eric POTTIE (LNE-OP, CNRS)

La métrologie au cœur des réseaux : l'aventure REFIMEVE

Dans un monde où les technologies avancées dépendent de plus en plus d'un temps et d'une fréquence parfaitement maîtrisés, la métrologie joue un rôle central et souvent invisible. REFIMEVE incarne cette révolution : une infrastructure de recherche innovante permettant la dissémination ultra-précise des références nationales de temps et de fréquence, élaborées au Laboratoire Temps-Espace LNE-OP, vers plus de 30 laboratoires via le réseau optique RENATER. Fondée sur une avancée majeure dans le contrôle des fréquences optiques, cette infrastructure repose sur la stabilisation active des retards de propagation sur plusieurs milliers de kilomètres de fibre. Je présenterai les principes, les technologies employées – aujourd'hui transférées à un consortium industriel – et les performances obtenues sur plus de 9 000 km de réseau. Enfin, j'aborderai une perspective fascinante : l'usage de REFIMEVE comme capteur sismologique géant, exploitant les fluctuations de délai comme traceur du mouvement du sol sur des échelles inédites.

In a world where advanced technologies increasingly rely on ultra-precise control of time and frequency, metrology plays a central—yet often invisible—role. REFIMEVE is a pioneering research infrastructure that distributes France's national time and frequency references, developed at the Laboratoire Temps-Espace - LNE-OP, to over 30 laboratories via the RENATER optical network. Built upon a major breakthrough in optical frequency control, the system stabilizes propagation delays over thousands of kilometers of fiber. This talk will introduce the key concepts, the enabling technologies—now transferred to an industrial consortium—and the performance achieved over more than 9,000 km of network. Finally, I will explore a novel perspective: using REFIMEVE as a giant seismic sensor by interpreting delay fluctuations as signatures of ground motion, enabling a new kind of geophysical observatory on a scale larger than seismic wavelengths.

La nouvelle plateforme de mesure de diffraction MIMOSA

La plateforme MIMOSA (pour Multi Incidences Multi Orientations Scattering and diffraction Analyzer) est un nouveau dispositif qui permet de caractériser la diffraction des ondes électromagnétiques divers objets dans presque toutes les directions. Cet équipement original et installé dans l'ancienne chambre anéchoïque du CCRM à Marseille. Il est constitué de deux bras portiques qui permettent de déplacer indépendamment deux antennes sur une sphère de 1,5 m de rayon, au centre de laquelle est placée l'objet étudié. Nous mettons à profit le principe d'analogie microonde pour mettre à l'échelle des gigahertz des problèmes utilisant des ondes allant des fréquence radio à l'optique. Nous présenterons deux études utilisant cette analogie et réalisées avec MIMOSA : la diffusion des particules circumstellaires, et la caractérisation de la structure interne des astéroïdes.

The MIMOSA (Multi Incidences Multi Orientations Scattering and diffraction Analyzer) platform is a new setup for characterizing the diffraction by objects of electromagnetic waves in almost any direction. This original equipment is installed in the former anechoic chamber of the CCRM in Marseille. It consists of two gantry arms which independently

move two antennas on a sphere of 1.5 m radius, at the center of which the object under study is placed. We take advantage of the microwave analogy principle to scale problems involving waves ranging from radio frequencies to optics to the gigahertz band. We will present two studies using this analogy and carried out with MIMOSA: the scattering of circumstellar particles, and the characterization of the internal structure of asteroids.

EXPOSÉ INVITÉ : Djamel ALLAL (LNE)

Projets de recherche européens en métrologie électrique

Cette présentation décrit l'évolution et l'impact des principaux programmes de recherche d'EURAMET dans le domaine de la métrologie. Nous commencerons par souligner les réalisations du Programme européen de recherche en métrologie (EMRP, 2009-2016) et du Programme européen de métrologie pour l'innovation et la recherche (EMPIR, 2014-2020), qui ont tous deux contribué à encourager la collaboration européenne dans le domaine de la métrologie.

L'accent sera ensuite mis sur l'actuel partenariat pour la métrologie (2021-2027), cofinancé dans le cadre d'Horizon Europe. Cette initiative ambitieuse vise à fournir des solutions métrologiques de pointe.

Une partie importante de cette session sera consacrée aux projets en cours et à venir dans le cadre du partenariat de métrologie, en particulier dans le domaine de l'électricité. Nous explorerons les recherches innovantes menées pour faire progresser les capacités de mesure dans ce secteur, en soulignant son importance pour diverses applications et les avancées technologiques futures.

This presentation describes the evolution and impact of EURAMET's main research programmes in the field of metrology. We will start by highlighting the achievements of the European Metrology Research Programme (EMRP, 2009-2016) and the European Metrology Programme for Innovation and Research (EMPIR, 2014-2020), both of which have helped foster European collaboration in the field of metrology.

The focus will then shift to the current Partnership for Metrology (2021-2027), co-funded under Horizon Europe. This ambitious initiative aims to provide cutting-edge metrology solutions.

A significant part of this session will be devoted to current and future projects under the Metrology Partnership, particularly in the field of electricity. We will explore the innovative research being carried out to advance measurement capabilities in this sector, highlighting its importance for various applications and future technological advances.

PRIX DE THÈSE EN RADIOSCIENCES

Le prix de thèse en radiosciences 2025, sous l'égide d'URSI-France, a été remis à la lauréate le jeudi 12 juin 2025. Ce prix, d'une valeur de 1500 €, sponsorisé par [l'Agence nationale des fréquences \(ANFR\)](#), est destiné à récompenser annuellement des travaux de doctorat d'excellente qualité s'inscrivant dans un ou plusieurs des domaines scientifiques de l'URSI. Les critères de sélection, les conditions d'éligibilité et de recevabilité, ainsi que la procédure de candidature sont consultables sur le site d'URSI-France : <https://www.ursi-france.org/ursi-france/prix-de-these-en-radiosciences>

The 2025 radio science PhD award, under the aegis of URSI and URSI-France, has been presented to the laureate on Thursday, June 12. This award, worth 1,500 €, sponsored by « Agence Nationale des Fréquences » (ANFR), is intended to reward annually high-quality doctoral work in one or more of the scientific fields of URSI. The selection criteria, the conditions of eligibility and admissibility, as well as the application procedure, can be consulted on the URSI-France web site: <https://www.ursi-france.org/ursi-france/prix-de-these-en-radiosciences>

Electro(magnetic) fields interactions with cells: mechanistic insights and potential new therapeutic applications

Leslie Vallet, lauréate du prix de thèse en radiosciences 2025

Thèse réalisée à l'Institut Gustave Roussy, Université ParisSaclay

Many biological processes in living organisms are controlled by endogenous electro(magnetic) fields (EMFs). Modulating biological functions by applying exogenous EMFs is of great interest. The development of current and future applications relies on a deep understanding of the interactions between EMFs and living organisms. Pulsed electric fields (PEFs), i.e. short high voltage electric pulses, can permeabilize the cell membrane. This phenomenon (electroporation) is commonly used (even in the clinics) to vectorize agents into cells. Currently, PEF delivery requires electrodes to be brought into contact with the tissue to be treated, meaning invasiveness for deep tissues treatment. Subnanosecond duration PEFs (subnsPEFs) could pave the way for contactless PEF delivery. In this work, subnsPEFs were found to generate efficient cell permeabilization through molecular mechanisms different from those operating with PEFs of longer durations. Calcium (Ca²⁺) oscillations were also examined in mesenchymal stem cells (MSCs) under proliferation and differentiation conditions. Natural Ca²⁺ oscillations patterns could then be hacked using microsecond duration PEFs, which could subsequently influence cell fate. This is of particular interest for regenerative therapies. Finally, using dielectrophoresis, important changes in the (di)electrical properties of MSCs in the differentiation early stages could be evidenced, opening perspectives of non-damaging cell separation techniques which could also benefit research and clinical applications.

Controlling the helicity of light by electrical magnetization switching

Pambiang Abel Dainone, nominé pour le prix de thèse en radiosciences 2025

Thèse réalisée à l'Institut Jean Lamour, Université de Lorraine

Spin light-emitting diodes (spin-LEDs) are promising devices for bridging spintronics and photonics by enabling the generation of circularly polarized light from spin-polarized carriers. However, most spin-LEDs still require external magnetic fields to control light helicity, limiting their integration and practical use. In this work, we report a spin-LED operating at room temperature that overcomes this limitation by employing spin-orbit torque (SOT) to electrically reverse the magnetization of a spin injector with perpendicular magnetic anisotropy. This allows non-volatile and fully electrical control of the circular polarization (P_c) of the emitted light. Our standard spin-LED achieves a world-record P_c of 40% at zero field. Furthermore, the SOT spin-LED demonstrates reversible helicity switching between +30% and -30%, with stable modulation over 60 cycles without degradation.

These results pave the way for CMOS-compatible, ultrafast, and polarization-encoded optical communication including space-light data transfer.

Shipborne Global Navigation Satellite Systems for Offshore Atmospheric Water Vapor Monitoring

Aurélie Panetier, nominée pour le prix de thèse en radiosciences 2025

Thèse réalisée à l'ENSTA Bretagne, Brest

Global Navigation Satellite Systems (GNSS) have been developed for localization since the 1990s. Nowadays, precise positioning involves atmospheric propagation delay estimation, enabling the retrieval of precipitable water vapor (PWV) valuable for atmospheric studies. GNSS PWV is currently integrated into weather forecast models and supplements climate datasets over land. More recently, GNSS PWV has expanded to shipborne antennas, providing crucial atmospheric information over oceans.

This work proposes and validates shipborne GNSS precise positioning methods to deliver suitable PWV for offshore climate studies. Tests on real and simulated datasets identified the best processing configuration, which was applied to GNSS data from five vessels from the French Oceanographic Fleet (FOF) from 2015 to 2022. Comparisons with external datasets showed encouraging results, validating previous research on a larger scale. For the first time, intrinsic accuracy was estimated by comparing PWV from crossing vessels, yielding a difference of $-0.01 \pm 0.63 \text{ kg/m}^2$, suitable for climate studies.

As 70% of the Earth's surface is covered by water, these results emphasize the potential of shipborne GNSS for global climate.

Table des matières

Actes_entete.pdf	1
Capteurs électromagnétiques et optiques	1
Micro-resonators for dynamic investigation of soft matter: From particle sedimentation to product stability, Gastebois Jordan [et al.]	1
First steps of low cost PCB E-near field radiation metrology with microwave imaging scanner, Delille Nolane [et al.]	7
Capteur résonnant pour détection d'obstacles dans de l'eau douce, Troesch Nicolas [et al.]	15
Mesures haute fréquence, outils et méthodes de calibrage	22
Calibrated measurements of dopant concentration on vertical nanowires by scanning microwave microscopy, Morán-Meza José A.	22
Novel Thermopile Design for Waveguides and Coaxial Microcalorimeters in the Frequency range from DC – 40 GHz, Ba Doudou	25
On-Wafer Calibration for Nanodevice Characterization up to 110 GHz, Seck Daouda [et al.]	33
Millimeter-wave radioastronomy measurement challenges, Risacher Christophe . .	41
Station de Mesure on-Wafer Nano-Robotisée Assistée par IA : Automatisation, Précision et Évaluation des Performances, Lenoir Clément [et al.]	47
Densités de Probabilité du Lag-1 dans les Séries Temporelles Linéaires et Circulaires Modélisant les Processus de Brassage, Monsef Rabah Florian	55

Dosimétrie électromagnétique et exposimétrie	59
Hybrid approach of the measurement of actual head EMF exposure, Wang Shan-shan [et al.]	59
Correlation Analysis on UL EMF Exposure in France Metropolitan Areas, Sun Qunfei [et al.]	65
Localisation électromagnétique et radar, mesure des SER et des signatures	70
Metasurface for direction of arrival estimation, Meftah Nawel [et al.]	70
Localization of metallic lost tools using UHF RFID system, Hamrouni Nawres [et al.]	76
Surveillance de foule à l'aide d'une antenne à ondes de fuite dans une communication et détection intégrées, Melki Mathis [et al.]	82
Mesures électromagnétiques des objets biologiques, diagnostics et bio-détection	86
Analyse non-invasive du taux de sucre dans les tubercules de pommes de terre par mesures diélectriques micro-ondes, Sebbache Mohamed [et al.]	86
Session ouverte	95
Negative time experimentation with RC-network based low-pass NGD circuit, Rav-elo Blaise [et al.]	95
Dispersive Analysis of Waveguides for Leaky-Wave Antennas, Tong Yuhuan [et al.]	104
Stacked Multi-Via Mushroom-Type EBG Structures with Glide Symmetry, Ugle Ashray [et al.]	107
Liste des auteurs	111
Sponsors.pdf	111
URSI_France_CNFRS_.pdf	112

Capteurs électromagnétiques et optiques

Micro-résonateurs pour l'étude dynamique de la matière molle : De la sédimentation des particules à la stabilité des produits

Micro-resonators for dynamic investigation of soft matter: From particle sedimentation to product stability

J. Gastebois ¹, A. Szymczyk ², G. Paboeuf ³, V. Vié ^{3,4}, A. Saint-Jalmes ³, H. Lhermite ¹, H. Cormerais ^{1,5},
F. Gauffre ² and B. Bêche ¹

¹Université de Rennes, CNRS, Institut d'Électronique et des Technologies du numéRique - IETR UMR 6164, F-35000 Rennes, France.

²Université de Rennes, CNRS, Institut des Sciences Chimiques de Rennes - ISCR UMR 6226, F-35000 Rennes, France.

³Université de Rennes, CNRS, Institut de Physique de Rennes - IPR UMR 6251, F-35000 Rennes, France

⁴Université de Rennes, UAR 2025 ScanMAT, F-35000, Rennes, France.

⁵Centrale/Supélec, Campus de Rennes, F-35510 Cesson-Sévigné, France.

E-mail: jordan.gastebois@univ-rennes.fr

bruno.beche@univ-rennes.fr ; <https://www.ietr.fr/bruno-beche>

Mots clés : Micro-résonateurs, Dispersion colloïdales, Sédimentation, Stabilité et potentiel zêta.

Keywords: Micro-resonators, Colloidal dispersion, Sedimentation, Stability and zeta potential.

Résumé/Abstract

Ce travail vise à présenter les avancées récentes dans l'analyse de la matière molle à l'aide de la photonique intégrée et de techniques résonantes quasi-surfaciques. Il met en lumière la polyvalence de la structure résonante conçue, composée de micro-résonateurs, en démontrant son application en tant que « Mesureur de vitesse de Sédimentation », « Viscosimètre Optique » et « Zétamètre Optique Résonant » pour l'analyse de solutions transparentes, sombres ou opaques. Ces dispositifs sont développés pour répondre à la problématique de la stabilité de dispersions colloïdales lors d'un stockage à long terme. Des micro-résonateurs organiques UV210, fabriqués par photolithographie en UV profond, sont intégrés dans une plateforme optique permettant un suivi dynamique du processus étudié. Des expériences menées avec des nanoparticules de silice dispersées dans l'eau révèlent une corrélation nette entre l'évolution du signal résonant et la sédimentation de ces nanoparticules. En revanche, l'étude de poudres de noir de carbone dispersées dans de l'eau contenant un tensioactif montre l'absence de sédimentation, ce qui confirme la capacité des structures résonantes à détecter des systèmes colloïdaux stables, même dans des milieux sombres. Ces résultats sont validés et corroborés avec des mesures rhéologiques et de potentiel zêta.

This work aims to thoroughly present recent advancements in soft matter analysis using integrated photonics and quasi-surfacic resonant techniques. Specifically, it highlights the versatility of the designed resonant structure, made of organic micro-resonators, demonstrating their application as a "Sedimentation Rate Meter," "Optical Viscometer," and "Resonant Optical Zetameter" for analyzing transparent, dark, and opaque solutions. These devices are designed to address the challenge of monitoring the long-term stability of colloidal dispersions. Organic UV210 micro-resonators, fabricated via deep UV photolithography, are integrated into an optical test-platform for real-time monitoring and data processing. Experiments on silica nanoparticles into water shows a correlation between resonant signal evolution and sedimentation. The study of black carbon into water with a surfactant shows conversely the absence of sedimentation and then the capability of the structures of detecting stable product even in dark substances. These results are validated through complementary rheological and zeta potential measurements.

1 Introduction

The industrial interest of this research is significant in assessing the dynamic behavior of colloidal dispersions prior to large-scale product production. Stable colloidal dispersions rely on equilibrium between electrostatic forces between dispersed particles, maintaining a stable particle cloud. Perturbation in this equilibrium, arising from changes in particle charge or environmental conditions, can lead to aggregation, sedimentation, and phase changes that compromise product longevity. Identifying stable versus unstable products is critical in pre-industrial applications, such as latex rubber, paints or agro alimentary products [1-3].

This study introduces an integrated photonic platform based on quasi-surfacic resonant micro-resonators to monitor colloidal dispersion behavior in real time. Fabricated from UV210 polymer via deep UV photolithography, these racetrack resonators interact with the surrounding medium through evanescent fields, enabling high-sensitivity detection over hundreds of micrometers [4-6]. Excited by a superluminescent diode, the resonant signal, tracked via Free Spectral Range (FSR) variations, provides insight into dispersion dynamics, including in highly absorbing or opaque solutions. Conventional commercial devices often struggle to analyze dark or opaque substances because their measurement principle is about volumetric light propagation, which is hindered by strong absorption. In contrast, the light circulating within micro-resonators in our approach probes the environment over hundreds of micrometers, even in optically challenging substances.

To this end, the second part of this paper focuses on the principle of resonant measurement. The fabrication process of the micro-resonators is briefly presented, along with the integration of the photonic chip into the optical experimental setup. The third part is dedicated to the behavior of colloidal dispersions with silica nanoparticle suspensions into water and into water plus glycerol and with black carbon dispersions into water and into water plus an anionic surfactant. Initial experiments reveal a correlation between the evolution of the resonant signal and the sedimentation process. Modifying the host medium by adding glycerol introduces the concept of an optical resonant viscometer by changing the sedimentation rate visible by the FSR slope variation. Subsequently, the study of carbon black nanopowder dispersions in aqueous media demonstrates the ability to distinguish between stable and unstable systems through the addition of an anionic surfactant. A clear correlation between the slope of the FSR variation and dispersion stability is thoroughly analyzed. These findings are supported by complementary rheological and zeta potential measurements. Finally, the last section concludes the study.

2 Resonant principle measurement and experimental set-up

A basic configuration, where the fabrication processes and the geometry is depicted in Figure 1, consists of unidirectional coupling between a racetrack micro-resonator (MR) and a bus waveguide. Resonance occurs when the round-trip phase condition equals $2m\pi$ (where m is an integer), resulting in resonant wavelengths given by [7]:

$$\lambda_{res,m} = n_{eff} \frac{P}{m} \quad (2.1)$$

Here, n_{eff} is the effective refractive index of the propagating mode, P the resonator's geometric parameter, and m the mode number. Changes in the upper cladding environment, such as migration, sedimentation, or densification, affect n_{eff} , providing insights into soft matter behavior.

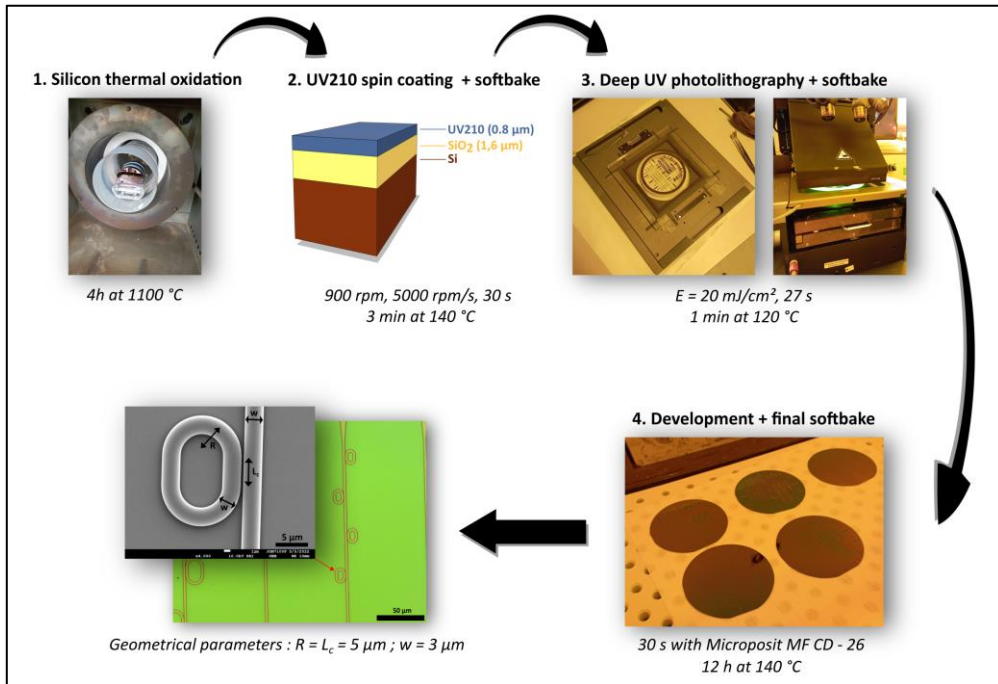


Figure 1: Fabrication process of the resonant structure, along with an SEM image of an MR coupled to an access waveguide, with the geometrical parameters highlighted.

The spectral difference between two successive resonant wavelengths, known as the Free Spectral Range (FSR), is monitored through an optical test platform and is defined by:

$$FSR = \frac{\lambda_0^2}{P \cdot n_{eff}^{gpe}} \quad (2.2)$$

Where λ_0 is the excited wavelength, and n_{eff}^{gpe} the group refractive index of the structure incorporating modal dispersion. The resonant structures are fabricated from organic resin (UV210) via deep-UV photolithography on oxidized silicon, feature micrometer-scale patterns with 400-nanometer gaps between the access waveguide and MRs. A Superlum diode emitting at 795 nm excites the resonances, with a broad emission spectrum (40 nm) generating multiple resonant peaks. These peaks enable dynamic observation of soft matter processes. Data acquisition is performed with an Ocean Optics spectrometer, controlled via MATLAB, which also performs real-time Fast Fourier Treatment (FFT) to calculate dynamically the FSR evolution. This integrated platform enables dynamic soft matter investigations, specifically colloid dispersion migration and stability assessment, using compact and cost-effective devices.

3 Results

3.1 Toward sedimentation and viscosity measurements

Initial studies were conducted on transparent silica nanoparticles (NPs) migration into water. A tank filled with 168 μ L of water was placed in direct contact with the photonic chip, creating a three-layer waveguide structure with the core (UV210) sandwiched between the lower cladding (SiO_2) and the upper cladding (water). Introducing 5 μ L with a microliter pipette of a solution containing silica NPs, at a concentration of 2 mg/mL, altered the upper cladding's refractive index, impacting the global effective refractive index of the structure. The mode's evanescent tail acted as a probe, detecting sedimentation and migration processes. An increase in FSR is a specific signature of the sedimentation process [8,9]. The moment the FSR reaches its peak value marks the end of sedimentation, enabling precise comparison of the experimentally measured sedimentation rate with the theoretical value predicted by the classical Stokes model. During this phase of sedimentation, the nanoparticles (NPs) form a compact layer above the waveguide core, where their density and concentration increase, resulting in a decrease in guiding capacity, mathematically corresponding to a decreased n_{eff}^{gpe} (increased FSR with equation 2.2). In Figure 2.b, the sedimentation process appears to conclude around 145 minutes. After this point, a second phase of rearrangement among the NPs occurs before the FSR stabilizes. This second phase is attributed to a pinning effect caused by the finite dimensions of the tank placed above the chip, leading to curvature at the water/air interface. Evaporation is more pronounced at the center of the tank than at the edges, further increasing the curvature. This increased curvature "sweeps" the NPs across the chip surface, causing their rearrangement and leading to a stabilized FSR appearing at 200 minutes.

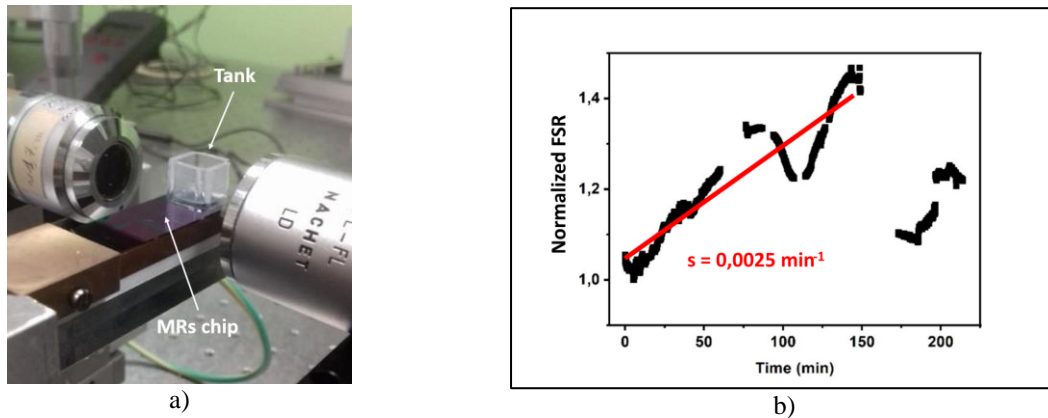


Figure 2: a) Tank filled with the colloidal dispersion, composed of silica NPs into water, in direct contact with the photonic chip. b) Plot of the normalized FSR evolution over time for silica NPs into water. The first phase of sedimentation associated to a FSR slope end at 145 minutes followed by a rearrangement phase with a final stabilized FSR at 225 minutes.

Additional experiments were conducted by adding glycerol to the initial solution in the tank. Silica NPs solutions were also added, and the FSR evolution was recorded. The slope associated with the FSR evolution during the first phase, corresponding to sedimentation, was plotted as a function of the glycerol concentration (Figure 3a). In parallel, viscosity measurements were performed using a mechanical rheometer on four solutions with glycerol

concentrations of 0%, 10%, 20%, and 30% (Figure 3.b). From these data, a mathematical relationship between the viscosity and the slope of FSR(t) could be established. Thus, by monitoring the resonant signal of a mixture during the sedimentation process, the viscosity of the mixture can be determined.

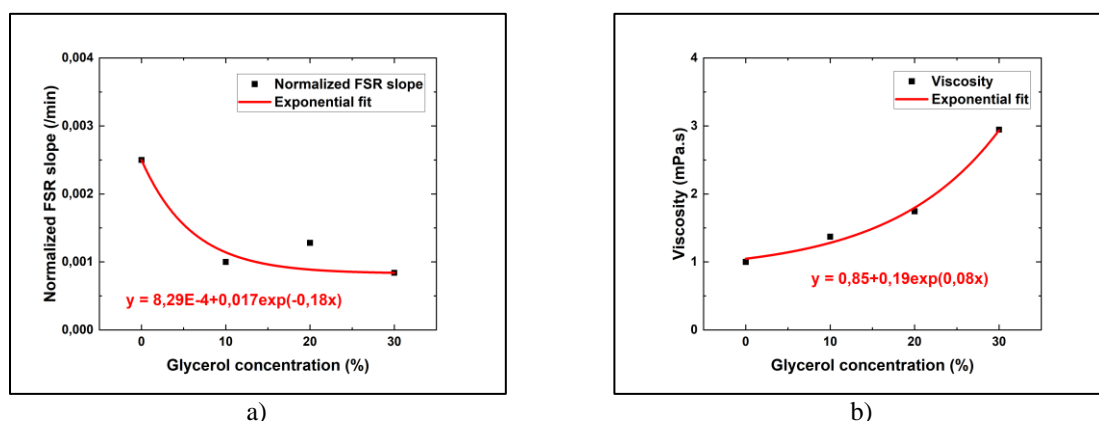


Figure 3: a) Normalized FSR slope as a function of the glycerol concentration. b) Average viscosity of each sample as a function of the glycerol concentration where the non-linearity clearly appears.

3.2 Toward product stability

This study was extended to dark solutions by replacing silica NPs with carbon black nanopowder. Sedimentation was clearly observed for various concentrations (ranging from 0.1 to 0.5 mg/mL), demonstrating the platform's capability to analyze dark substances. It is noteworthy that the sedimentation process may not begin immediately at the start of the experiment (Figure 4). Indeed, the solution can remain relatively stable for several minutes or even up to an hour before the particles start to aggregate and subsequently begin to sediment irreversibly. Therefore, it is important to conduct measurements over several hours (typically 3 to 4 hours) before concluding whether sedimentation occurs. Replacing the water with an anionic surfactant solution, the sodium dodecyl sulfate (SDS), stabilized the colloid through equilibrium between repulsive and attractive forces, maintaining a constant FSR (Fig. 3). This confirmed the capability to discriminate between stable and unstable colloids dynamically and those results are corroborated by zeta potential measurements (Figure 4). The water and SDS solution successfully surpasses the stability threshold of $|\geq 30 \text{ mV}|$, a characteristic indicator of colloidal dispersion stability [10-12]. These results demonstrate its suitability for testing industrial pre-products.

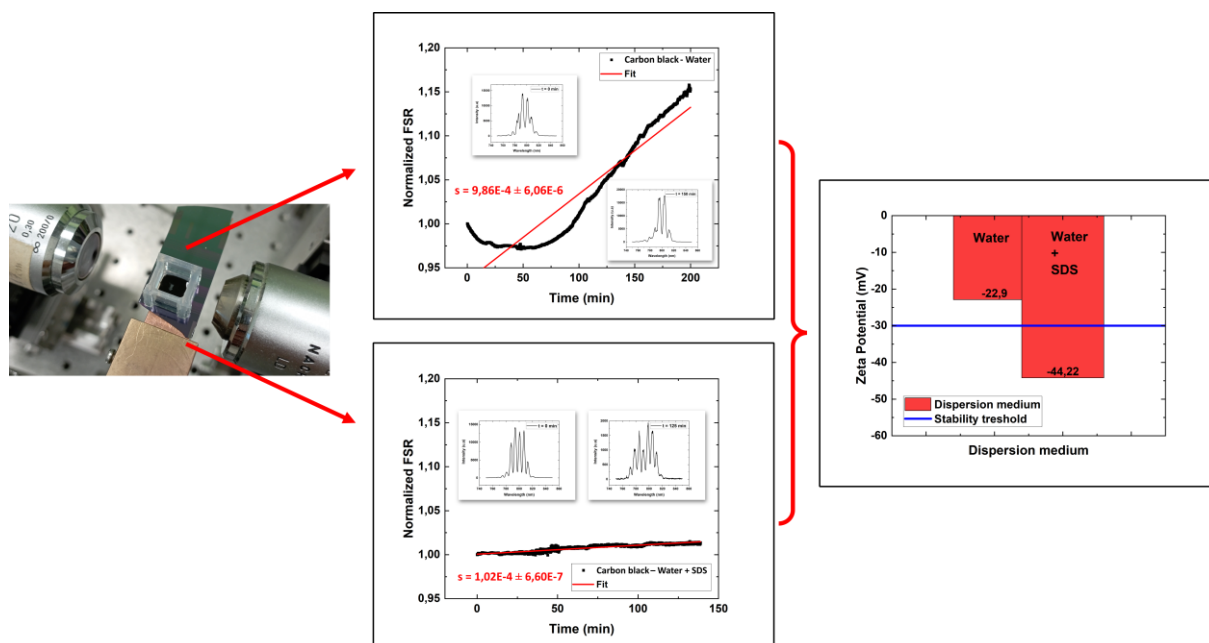


Figure 4: On the left, a tank filled with a carbon black suspension in contact with the photonic chip. In the center, a plot of the normalized FSR over time for carbon black dispersed in water and in water with added SDS. The absence of sedimentation (no FSR slope) observed for the dispersion with SDS is corroborated by zeta potential measurements (shown on the right), where the solution exceeds the stability threshold for colloidal dispersions.

4 Conclusion

Such optronic device developed in cleaning room and incorporated into an optical test platform enable investigation of pre-product stability from industrial. It principle based on a quasi-surfacic resonant signal allow to detect sedimentation and migration in colloidal dispersions. Its ability to probe dark and opaque substances and its capacity for real-time FSR monitoring highlight its potential for cost-effective and efficient stability analyses in various industries.

Aknowledgments

The authors would like to thank the “Fondation d’Entreprise Grand Ouest” plus the “Fondation Rennes 1” for the financial support. This publication is also supported by the European Union through European Regional Development Fund (ERDF), Ministry of Higher Education and Research, CNRS, Brittany region, Conseils Départementaux d’Ille et-Vilaine and Côtes d’Armor, Rennes Métropole, and Lannion Trégor Communauté, through the CPER Project CyMoCod. The authors also thank the NanoRennes platform for the DUV process.

References

- [1] Grotenhuis, E.; Tuinier, R.; de Kruif, C. G. Phase Stability of Concentrated Dairy Products. *Journal of Dairy Science* **2003**, *86* (3), 764–769. [https://doi.org/10.3168/jds.S0022-0302\(03\)73657-1](https://doi.org/10.3168/jds.S0022-0302(03)73657-1).
- [2] Bellich, B.; Franzin, M.; Curci, D.; Cirino, M.; Maestro, A.; Bennati, G.; Stocco, G.; Adami, G.; Maximova, N.; Grasso, D. L.; Barbi, E.; Zanon, D. Long-Term Stability of Glycopyrrolate Oral Solution Galenic Compound at Different Storage Conditions. *Pharmaceutics* **2024**, *16* (8), 1018. <https://doi.org/10.3390/pharmaceutics16081018>.
- [3] Jacob, J.; Grelier, S.; Grau, M.; Chorein, B. Effect of Dispersing Agents on the Stability of Recycled Paints. *Coatings* **2022**, *12* (11), 1722. <https://doi.org/10.3390/coatings12111722>.
- [4] Li, Q.; Vié, V.; Lhermite, H.; Gaviot, E.; Bourlieu, C.; Moréac, A.; Morineau, D.; Dupont, D.; Beaufils, S.; Bêche, B. Polymer Resonators Sensors for Detection of Sphingolipid Gel/Fluid Phase Transition and Melting Temperature Measurement. *Sensors and Actuators A: Physical* **2017**, *263*, 707–717. <https://doi.org/10.1016/j.sna.2017.07.037>.
- [5] Malmir, K.; Habibiyan, H.; Ghafoorifard, H. An Ultrasensitive Optical Label-Free Polymeric Biosensor Based on Concentric Triple Microring Resonators with a Central Microdisk Resonator. *Optics Communications* **2016**, *365*, 150–156. <https://doi.org/10.1016/j.optcom.2015.12.007>.
- [6] Castro-Beltrán, R.; Garnier, L.; Saint-Jalmes, A.; Lhermite, H.; Cormerais, H.; Fameau, A.-L.; Gicquel, E.; Bêche, B. Microphotonics for Monitoring the Supramolecular Thermoresponsive Behavior of Fatty Acid Surfactant Solutions. *Optics Communications* **2020**, *468*, 125773. <https://doi.org/10.1016/j.optcom.2020.125773>.
- [7] Rabus, D. G., *Integrated ring resonators*, Springer, **2007**.
- [8] Bêche, B.; Lhermite, H.; Vié, V.; Garnier, L. Method for determining a sedimentation or creaming rate, CNRS/Université Rennes, international extension *PCT n° PCT/EP2019/051103*, + *United States, Patent n° : U.S. Application Number n° 16/966,416*, **2020**.
- [9] Garnier, L.; Gastebois, J.; Lhermite, H.; Vié, V.; St Jalmes, A.; Cormerais, H.; Gaviot, E.; Bêche, B. On the detection of nanoparticle cloud migration by a resonant photonic surface signal towards sedimentation velocity measurements. *Results In Optics*, **2023**, *12*, 100430.1-13. <https://doi.org/10.1016/j.rio.2023.100430>
- [10] Gastebois J.; Szymczyk, A.; Paboeuf, G.; Scholkopf, F.; Vié, V.; St Jalmes, A.; Lhermite, H.; Cormerais, H.; Gauffre, F.; Bêche, B. Exploring colloidal stability and migration dynamics through integrated photonic into aqueous black carbon dispersion. *SPIE Edition - The international Society for Optical Engineering, Sensors + Imaging : Remote Sensing for Agriculture, Ecosystems, and Hydrology*, **2024**, 13191-64, 1-10. <https://doi.org/10.1117/12.3030910>
- [11] Ramaye, Y.; Dabrio, M.; Roebben, G.; Kestens, V. Development and Validation of Optical Methods for Zeta Potential Determination of Silica and Polystyrene Particles in Aqueous Suspensions. *Materials* **2021**, *14* (2), 290. <https://doi.org/10.3390/ma14020290>.
- [12] Lunardi, C. N.; Gomes, A. J.; Rocha, F. S.; De Tommaso, J.; Patience, G. S. Experimental Methods in Chemical Engineering: Zeta Potential. *The Canadian Journal of Chemical Engineering* **2021**, *99* (3), 627–639. <https://doi.org/10.1002/cjce.23914>.

Proposition de méthodologie de mesure champ proche électrique à faible coût avec un imageur à micro-ondes

First steps of low-cost PCB E-near field radiation metrology with microwave imaging scanner

N. Delille¹, J. Rossignol¹, S. Lalléchère², B. Ravelo³

¹Univ. Bourgogne Europe, Dijon, France, {jerome.rossignol@ube.fr, nolane_delille@etu.u-bourgogne.fr}

²Safran Tech, Paris-Saclay, France, sebastien.lallechere@safrangroup.com

³NUIST, Nanjing 210044, Jiangsu, China, blaise.ravelo@yahoo.fr

Mots clés : champ électrique champ proche (E-NF), compatibilité électromagnétique (CEM), instrumentation, technique d'imagerie micro-ondes

Keywords: Electric near-field (E-NF), PCB emission, radiated electromagnetic compatibility (EMC), microwave imaging technique

Résumé/Abstract

Ce travail porte sur le développement d'un dispositif d'imagerie micro-ondes à bas coût (< 800 €) destiné à la cartographie des champs proches électrique et magnétique émis par des circuits imprimés (PCB). Il s'inscrit dans une démarche de recherche ouverte avec une forte vocation pédagogique. L'imageur repose sur une sonde monopole planaire pour la détection du champ électrique à 5,36 GHz, ainsi qu'une sonde magnétique dédiée. L'ensemble du système s'appuie sur des solutions à bas coût, incluant la fabrication de circuits micro-rubans et un banc de mesure automatisé combinant une imprimante 3D et une radio logicielle (SDR). Une attention particulière est portée à la versatilité du dispositif intégrant l'interface CNC, programmé en Python, et conçu pour être facilement adaptable à divers contextes de mesure grâce aux avancées récentes en impression 3D. Cette modularité avec CNC ouvre la voie à la réalisation d'une série de systèmes reproductibles, en vue de constituer une base de données expérimentale de grande ampleur. Celle-ci pourra être exploitée pour l'entraînement de modèles d'apprentissage profond, avec pour objectif une caractérisation automatique et prédictive des comportements électromagnétiques des circuits.

This work presents the development of a low-cost microwave imaging system (< €800) for mapping electric near-field (E-NF) and magnetic near-field (H-NF) radiated by printed circuit boards (PCBs). The project includes in the frame of an open research initiative with strong educational objectives. The imaging platform is based on a planar monopole probe for electric field detection at 5.36 GHz combined with a dedicated magnetic field probe. The setup relies on cost-effective solutions, including manufactured microstrip circuits and an automated measurement bench integrating a 3D printer operating with computer numerical control (CNC) and a software-defined radio (SDR). Special attention is paid to the versatility of the CNC system, which is fully programmable in Python and designed to be easily reconfigurable for various measurement scenarios, leveraging recent advances in 3D printing technologies. This modular approach enables the development of a series of reproducible systems aimed at building a large-scale experimental database. Such a dataset can be used to train deep learning models, paving the way for automated and predictive electromagnetic compatibility (EMC) characterization of electronic circuits.

1 Introduction

Nowadays, despite the spectacular technological development progress towards the 6G communication system, the electromagnetic compatibility (EMC) constraint remains an open challenge due to the tremendous increase of electronic printed circuit board (PCB) design density [1-2]. To deal with EMC issues, the electromagnetic (EM) radiation measurement of whether electric or magnetic in the near-field (NF) region is a well-established technique for monitoring defects in electronic circuits. When the PCB operates in a confined space, the NF emission becomes a breakthrough for EMC engineers [3]. The EM NF scanning technique is particularly useful to solve electrical and electronic system problems as the EMC source localization [4-5]. The NF emission scanners must follow EM emission measurement technique standard as IEC-61967 [6]. For example, the radiated emission illustrated by the synoptic diagram shown in Figure 1 must be validated with the 50-Ω microstrip line PCB as device under test (DUT) [7].

One of metrological challenges expected in radiated EMC engineering, the NF measurement performance depends on the probe characteristics [8]. Several ambitious developments of EMC radiated NF test benches were designed and tested in the literature [3-5, 7, 9-10].

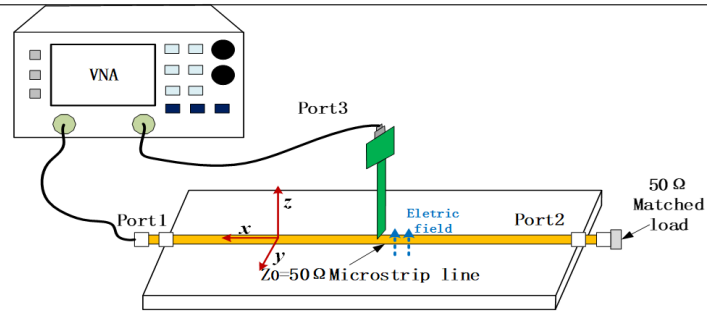


Figure 1: E-NF probe test synoptic diagram [7]

Some NF probes were alongside commercially available imaging systems [11]. These design solutions rely typically on high-precision positioning systems, ultra-sensitive electric (E)-field probes, and laboratory-grade high-frequency spectrum analyzers. Most PCB EM radiation scanning techniques are based on the magnetic (H)-field probe [12-13]. Such systems, designed for research or industrial qualification, come with development or acquisition costs which may reach tens of thousands of euros per complete setup [11]. While they offer high-resolution and highly accurate field mapping, their operation requires advanced expertise, involves complex calibration procedures, and renders them impractical for educational use both in terms of cost and usability. However, the emergence of 5G communications has ushered in an era of more affordable high-frequency measurement tools, particularly using software-defined radios (SDRs). This trend opens the way to the democratization of NF measurements at microwave frequencies by addressing the economic accessibility criteria necessary to equip students with enough imagers for hands-on lab sessions. To meet this need, a target unit cost of €800 per imager is considered acceptable for widespread deployment, assuming a relative positioning accuracy (depending on the positioning model used). The electromagnetic interference (EMI) imaging system must be intuitive and easy to use for undergraduate students [14], while being robust and reliable enough to withstand intensive use and occasional mishandling during laboratory activities. Finally, in the context of a long-term project aimed at integrating artificial intelligence (AI) models into EMC applications, the number of available imaging units becomes a critical factor. The AI-based approaches require large datasets for training, making it essential to maximize the number of imagers in operation to collect sufficient measurement data. The approach presented in this article fully aligns with the goal of democratizing low-cost EMC measurement tools. The result of a long-standing collaboration between the authors, this work provides a detailed overview of the developed samples and probes fabricated with computer numerical control (CNC) milling, as well as the experimental setup used for measurements. The E-NF test bench validation results will also be discussed, offering insights into the system's performance for the intended applications.

2 Design and fabrication of radiating PCB DUT and NF probes



Figure 2: CNC milling used, spatial resolution, electric and magnetic probes

The design and implementation of PCB DUT and NF probes under study belongs in the frame of pedagogical unit in the electronics and electrical engineering major in the University of Bourgogne Europe. All E- and H-NF probes including the test samples are manufactured by CNC milling (Figure 2-①: here using a Technodrill 3D CIF). Figure 2 depicts the apparatus, the minimum spatial resolution (Figure 2-②) achievable on the circuit, and the probes obtained. The E-NF probe is based on a coplanar design (Figure 2-③) with an ungrounded tip; its length was chosen to meet narrow-band measurement requirements at 5.3 GHz. The tip width is limited by the mechanical resolution of the CNC and is typically on the order of tens of micrometers. In first approximation, the E-probe orientation can be associated to the NF field tangential component.

The E-NF probe represented by a microstrip monopole antenna printed on Rogers substrate with 0.3 mm thickness and relative permittivity $\epsilon_r=8$ photographed in Figure 3 was designed, fabricated and tested for the imager test bench. This probe has a challenging performance in terms of operation frequency f_0 and the cylindrical antenna diameter of about 0.05 mm. The probe arm length enables it to adapt to the targeted scanning frequency. Table 1 indicates the E-NF probe specifications as f_0 , quality factor Q , reflection coefficient $S_{11}(f_0)$ and -10 dB cut-off frequencies, lower f_{low} and upper f_{up} ones.

Table 1: Designed E-NF probe specifications

Designation	f_0	$S_{11}(f_0)$	Q	f_{low}	f_{up}
Value	5.36 GHz	-24.79 dB	44.6	5.3 GHz	5.42 GHz

The second type is a H-field probe (Figure 2-④), inspired by the design presented in [15]. It consists of a grounded coplanar line followed by a circular loop, where the final third of the loop devoid of ground plane is the actual active sensing region. This simple design for both probes could be used on a basis for a lab on double layer PCB manufacturing using the tools available at the lab like the Technodrill. The microstrip samples layout are also presented (Figures 3), incorporating common defects such as cut (open) lines, faulty segments, 90° bends, and rounded or chamfered corners.

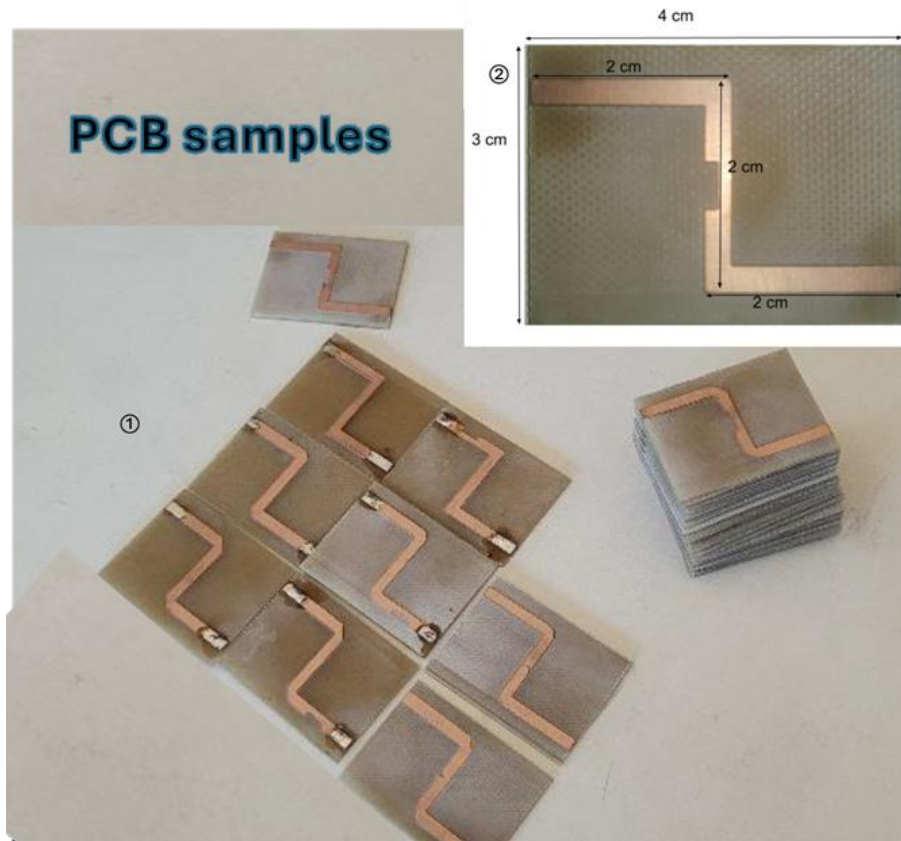


Figure 3: Serie of PCB sample and dimensions

The DUT sample is a PCB measuring 40 mm \times 30 mm, on which a 3 mm-wide microstrip line was made using a Technodrill 3 CNC milling machine (see Figure 3-②). An SMA connector is mounted at each end of the microstrip, the RF generator is connected to one side, while the opposite end is terminated with a short-circuit plug.

3 E-NF test bench operation principle

Figure 4 illustrates the synoptic of the operation principle of the considered E-NF imager test bench. The XY-planar scanner test bench is constituted by a vector signal generator ① which generates the input excitation

defined by the amplitude and the operation frequency of the input signal injected to the DUT represented by PCB ③ and the automatic test bench ② controlling the NF probe ④ scanning motion.

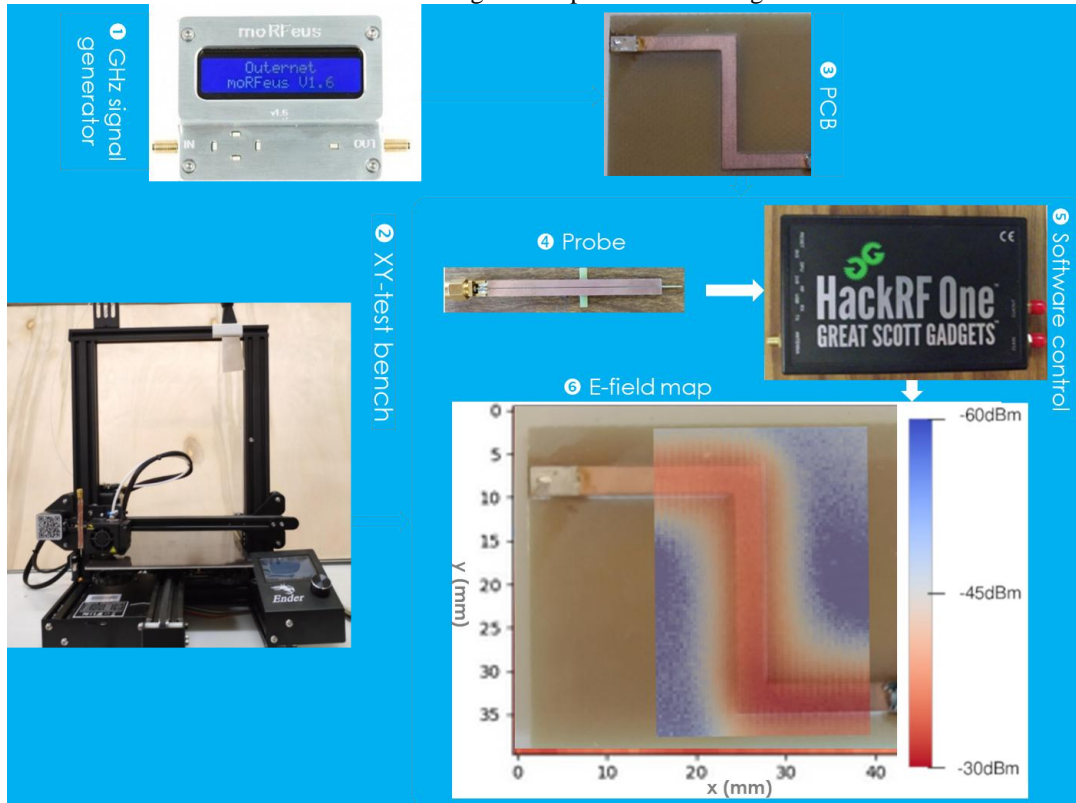


Figure 4: Illustrative diagram of E-NF imager test bench and Sample test with defaults

The measured data are visualized and stored via the software embedding module referenced HackRF One ⑤ to generate the E-NF map ⑥ in the XY-plan. The core of the system is based on a modified Ender 3 Pro 3D printer. This printer was selected for its ability to perform precise movements (<0.1 mm [10]) while remaining highly affordable (approximately €200). Due to its mechanical design, the printer requires positional referencing before each operation. This homing procedure relies on three micro-switches, one for each axis, to define the origin (zero) position. The second main component of the imaging system is a software-defined radio (SDR), specifically the HackRF One. The SDRs offer substantial advantages over traditional spectrum analyzers, not only because of their significantly lower cost (see [16], e.g., price comparison with Rohde & Schwarz spectrum analyzers), but also due to their ease of use and flexibility in a wide range of RF measurement scenarios [17]. The HackRF One operates from 1 MHz to 6 GHz and connects to a computer via USB, making it a convenient and compact solution for spectral analysis [18]. The third subsystem is a signal generator based on the MoRFFeus device. This USB-controlled frequency generator operates across a wide range, from 85 MHz to 5.4

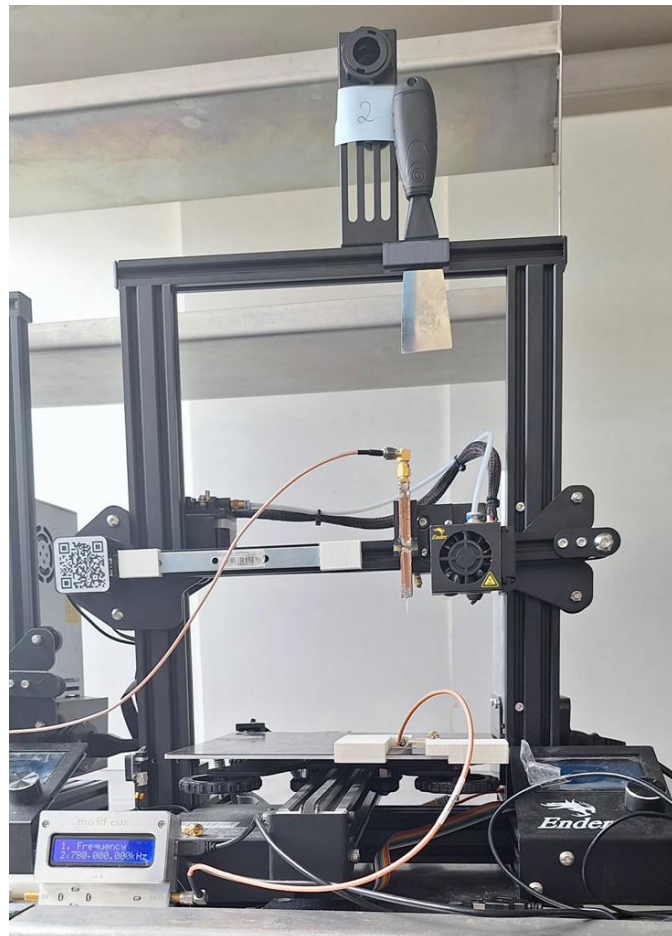


Figure 5: Full Set-up of microwave imager

It is essential for injecting EM signals into the PCB under test, enabling controlled excitation during the imaging process. The whole system is represented in Figure 5. All components of the imaging system are controlled via a central computer. A dedicated software application was developed specifically for this purpose. This software interfaces with three main elements, such as the 3D printer, the MoRFeus RF signal generator, and the HackRF spectrum analyzer. The 3D printer is operated through a serial interface using a USB-to-serial converter. The control is performed via standard G-code commands, which are widely used across CNC systems [20]. The Python script sends these commands to precisely control probe movement along the two-imaging axes (X and Y). The RF generator is controlled over USB using the Python library provided by the MoRFeus project [21], which allows the user to set frequency and output power programmatically. Finally, the HackRF spectrum analyzer is controlled using the `hack RF_sweep` command-line utility, which enables signal acquisition by sweeping across a specified frequency range. The sweeping range is centered on the defined frequency and is 2MHz wide. The graphical user interface (GUI) was developed using the Qt framework. It provides an intuitive and centralized control panel that enables the user to operate up to six imaging units simultaneously. Through the interface, the user can configure measurement parameters, including setting the operating frequency for each of the RF signal generators (currently supporting up to four independent sources). In addition to live system control, the GUI also includes features for browsing and displaying previously acquired images stored in the database, enabling quick access to past measurements for comparison or analysis. The control interface representative screenshot is shown in Figure 6.

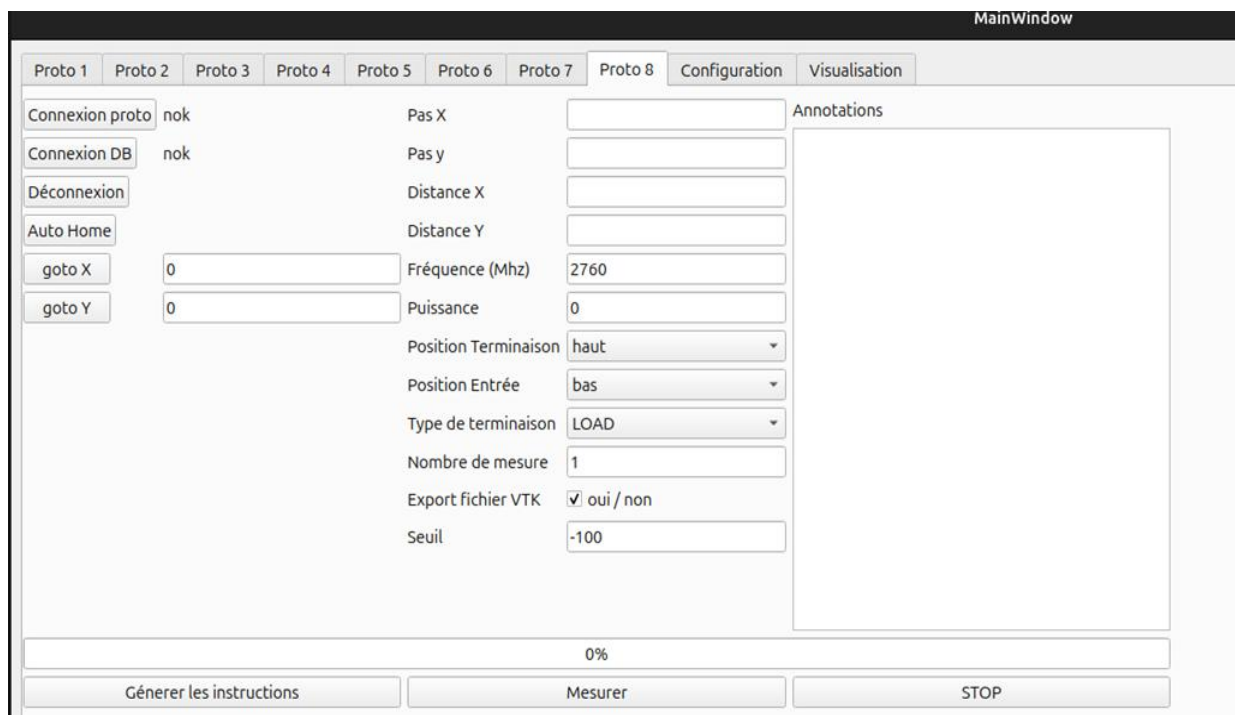


Figure 6: Image of the GUI of the program

Once the user initiates a measurement, a dedicated thread is launched to manage the entire acquisition process. For each measurement point predefined in a separate command file generated in advance, the probe is moved to the corresponding position using G-code instructions. At each point, data is acquired from the HackRF device via the `HackRF_sweep` command-line utility. The spectral data collected at each position is saved to an individual file. These files are then processed collectively at the end of the scan to reconstruct the final field distribution image. Upon completion of the measurement sequence, all individual data files are read, and the final image is generated and stored in a MongoDB database. This database not only allows for efficient storage and retrieval of measurement results but also supports the visualization and comparison of previous measurements. Additionally, if required, the data can be exported in VTK (Visualization Toolkit) format, enabling further post-processing or visualization with external tools such as ParaView or similar platforms. Additional development was carried out on the software to support its use in a teaching laboratory context. In particular, the application was adapted to run reliably under Windows, and its stability was improved to ensure

consistent operation across multiple imagers working at the same time. For the purposes of practical lab sessions, the configuration of the imager components will be fixed and predefined, significantly reducing the configuration work needed by students. This allows students to focus on the core objectives of the laboratory, namely EM field imaging without being burdened by low-level system configuration tasks.

4 Measuring EM fields: E-NF test result with the developed imager test bench

4.1 Measurement Process and parameters

The scanning procedure is used to acquire the NF image of this PCB. After configuring the imager, the auto-homing sequence is initiated from the graphical user interface. The key parameters include the initial probe position and the distance to the final position, which together define the scanning area as a rectangular region. Additional parameters such as the spatial step size (in both X and Y directions) were set according to the desired resolution. Finally, the RF generator output power is configured to its maximum value (0 dBm) for all subsequent measurements. To validate the performance of the developed imaging system, several EM E-NF measurements were conducted on the previously described PCB sample. These tests aimed to evaluate the system's ability to capture and represent both electric and magnetic field distributions with sufficient spatial resolution and stability. Those tests were also aimed at finding the best measurement height. In the remainder of this document, we will restrict our focus solely to measurements associated with the electrical probe. All the following images are achieved with an open circuit terminating the line.

4.2 Influence of space resolution

The first experiment focused on high-resolution E-NF measurements or mapping over the microstrip structure. Figures 7 present the resulting image acquired using the E-NF probe with a spatial step size of 0.1 mm.

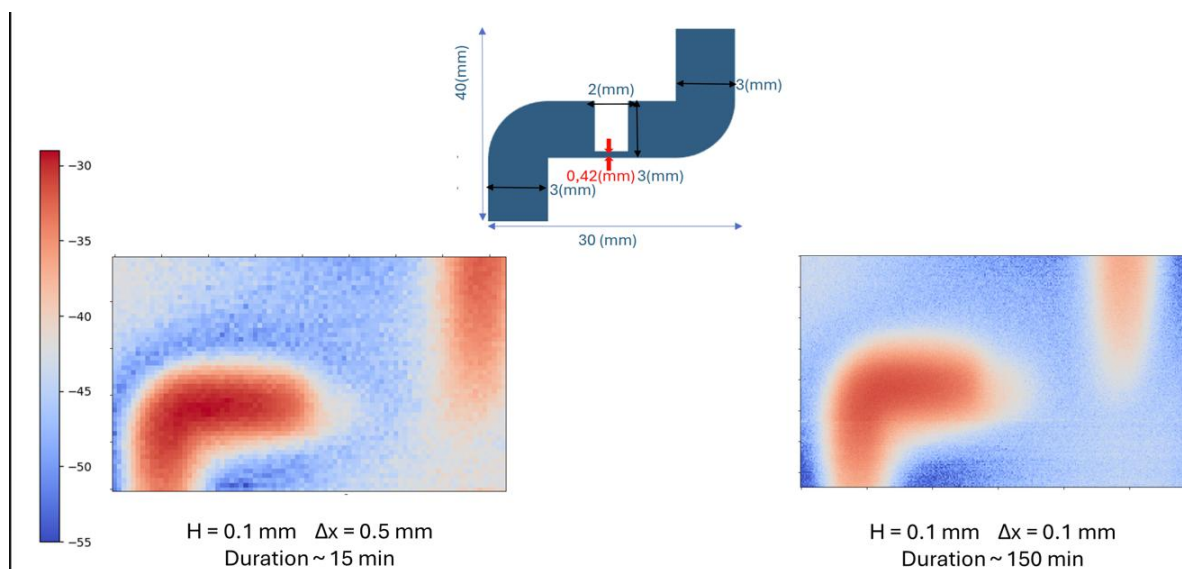


Figure 7: Impact of space resolution of E-NF image and the tested PCB

The measurement was performed at a frequency of 2780 MHz, corresponding to the excitation signal provided by the RF generator. This frequency is right at the peak of the probe resonance curve in the 2 GHz range. We can clearly see on this image the microstrip line with this hole. It is to be noted that the thin copper line running across the hole cannot be seen. The sample selection proposed in Figure 7 is intended to demonstrate the system's measurement capabilities. Specifically, the chosen sample deliberately presents a case of severe line reduction, a feature that remains challenging to detect due to the spatial resolution constraints of current 3-D printing technologies. Overcoming this limitation represents a key objective for the development of next-generation printers.

4.3 Influence of the gap between the DUT PCB sample and probe

The third experiment aimed to assess the impact of the electric field probe's height on image quality. A series of measurements were performed with the probe positioned at varying distances from the microstrip surface, ranging from 0.1 mm to 4.1 mm in 0.5 mm increments. Figure 8 shows the set of resulting images acquired at a frequency of 2780 MHz with a spatial step size of 0.5 mm. These images illustrate how increasing probe height affects both the amplitude and the clarity of the measured electric field distribution. From this experiment, it is

evident that the optimal probe height for such measurements is as close to the surface as possible. The minimal height maximizes sensitivity to the NF variations and minimizes background noise, which otherwise becomes more prominent at greater distances due to reduced field intensity and increased susceptibility to environmental interference.

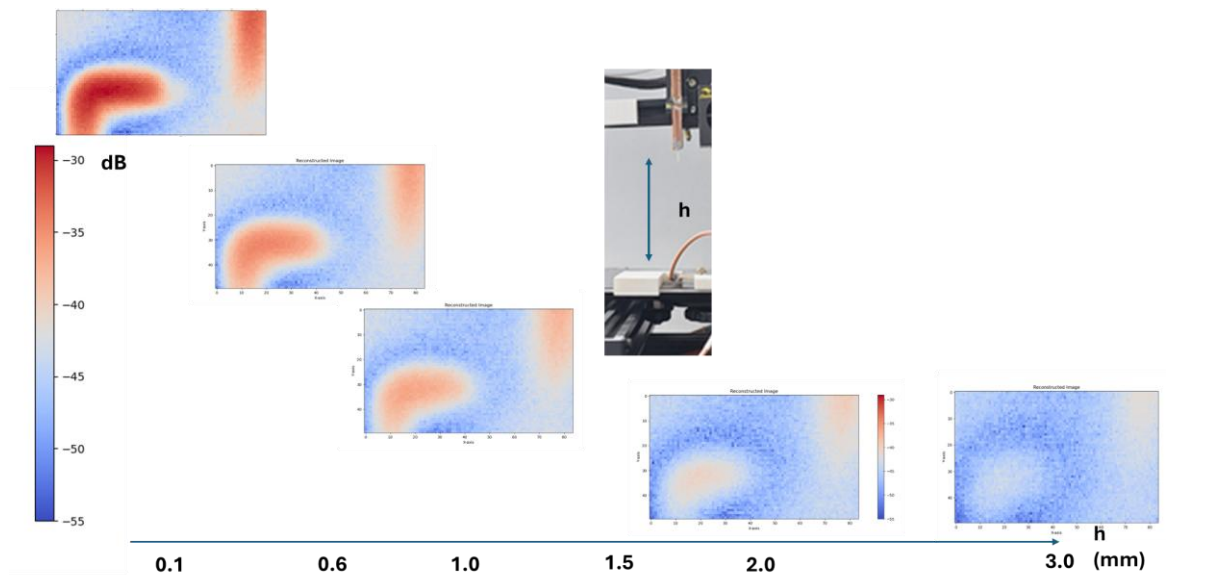


Figure 8 : Influence of the distance E-NF probe to PCB DUT sample

4.4 Influence of the considered test frequency

The performed experiment aimed to assess the impact of the chosen frequency for imaging on the measured E-NF and the subsequent image quality. A series of measurements were performed with the probe positioned at 0.5 mm from the surface and the imaging frequency was increased from 2760 to 2800 MHz with 10 MHz step. The images shown in Figures 9 represent the evolution of the E-NF versus the used frequency close to the resonance. The E-NF mapping is essentially based on the imaging frequency of the used probe resonance range.

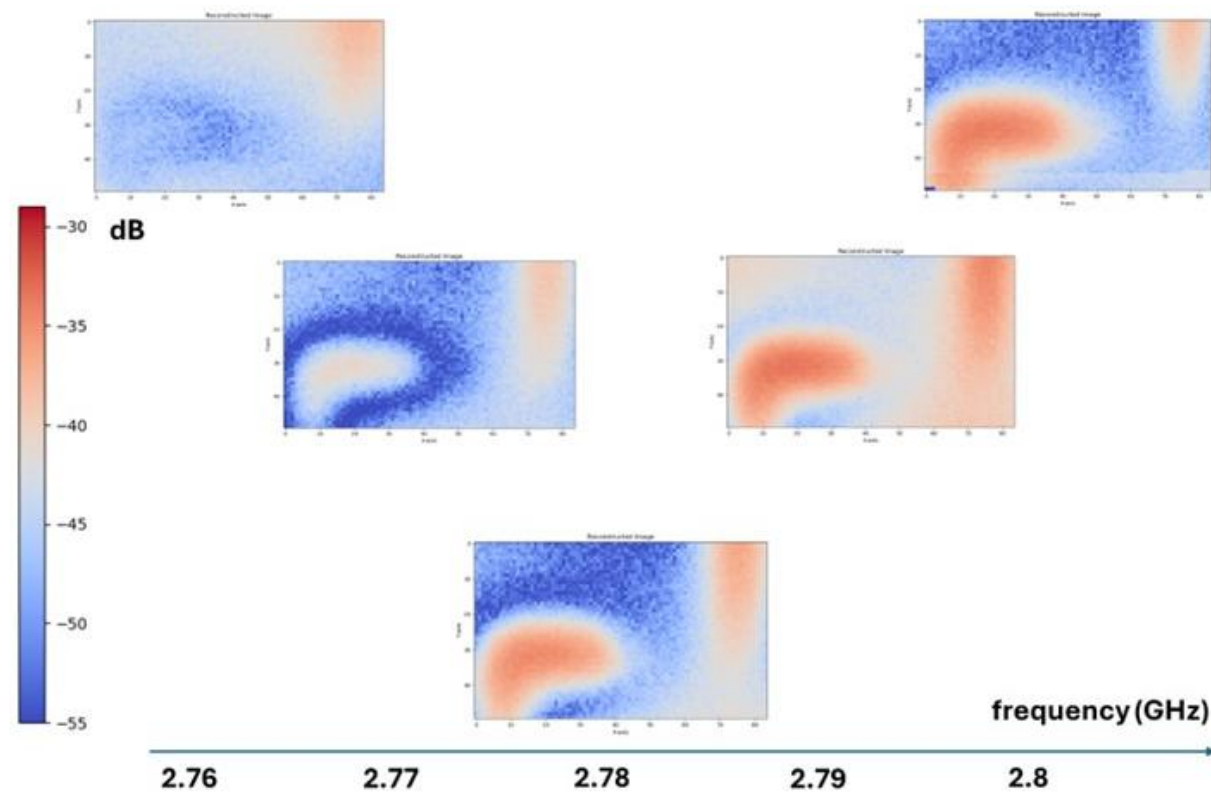


Figure 9 : Evolution of the E-NF image versus the used frequency close to the resonance

5 Conclusion

In this study, we have introduced a low-cost EM field imaging system designed both as a metrological tool and as an educational resource. The device, developed for serial production, is currently deployed in teaching programs at the University of Bourgogne Europe. While the system is subject to the inherent limitations of its class namely, a restricted operational frequency band, limited scanning speed, and the spatial resolution constraints dictated by 3D printing technologies, the methodology adopted is inherently scalable and adaptable. This flexibility opens pathways not only for NF EM measurements but also for susceptibility assessments. In addition, the system's versatility enables the systematic generation of datasets, thus supporting the development and training of deep learning models for future advanced applications.

Références bibliographiques

- [1] K. Wiklundh, and P. Stenumgaard, "EMC challenges with 6G," in Proc. 2022 Int. Symp. EMC – EMC Europe, Gothenburg, Sweden, 2022, pp. 19-24.
- [2] P. Stenumgaard, "How will 6G affect EMC?," *Electronic Environment*, <https://www.electronic.se/2020/02/25/how-will-6g-affect-emc/>
- [3] J. Rossignol, D. Stuerger, G. Bailly, A. Harrabi, S. Girard, and S. Lalléchère, "Microwave microscopy applied to EMC problem: Visualisation of electromagnetic field in the vicinity of electronic circuit and effect of nanomaterial coating," *Advanced Electromagnetics*, vol. 6, no. 2, pp. 33–39, 2017.
- [4] P. Maheshwari, V. Khilkevich, D. Pommerenke, H. Kajbaf and J. Min, "Application of emission source microscopy technique to EMI source localization above 5 GHz," 2014 IEEE International Symposium on Electromagnetic Compatibility (EMC), Raleigh, NC, USA, 2014, pp. 7-11.
- [5] P. Maheshwari, H. Kajbaf, V. V. Khilkevich and D. Pommerenke, "Emission Source Microscopy Technique for EMI Source Localization," *IEEE Trans. EMC*, vol. 58, no. 3, pp. 729-737, June 2016.
- [6] IEC, "Integrated circuits - Measurement of electromagnetic emissions - Part 1: General conditions and definitions," IEC 61967-1:2018, <https://webstore.iec.ch/publication/59799>
- [7] H. Jia, F. Wan, X. Cheng, V. Mordachev, N. M. Murad and B. Ravelo, "Electric near-field scanning for electronic PCB electromagnetic radiation measurement", *Measurement*, Vol. 228, No. 114355, Feb. 2024, pp. 1-8.
- [8] M. Kanda, "Standard probes for electromagnetic field measurements," *IEEE Trans. AP*, vol. 41, no. 10, 1993, pp. 1349-1364.
- [9] X. Peng, et al., "Simulation-based electromagnetic radiation anti-interference measures and verification," *Journal of Microwaves*, vol. 30, no. S2, 2014, pp. 58-60.
- [10] N. Mai-Khanh, et al, "An Integrated High-Precision Probe System in 0.18- μm CMOS for Near-Field Magnetic Measurements on Cryptographic LSIs," *IEEE Sensors*, vol. 13, no. 7, 2013, pp. 2675-2682.
- [11] <https://yictechnologies.com/emc-desktop-scanner/>, Accessed Apr. 20, 2025.
- [12] Y. Liu, et al., "Time-Domain Magnetic Dipole Model of PCB Near-Field Emission," *IEEE Trans. EMC*, vol. 58, no. 5, Oct. 2016, pp. 1561-1569.
- [13] Y. Liu and B. Ravelo, "Fully time-domain scanning of EM near-field radiated by RF circuits," *PIER B*, vol. 57, 2014, pp. 21-46.
- [14] A. Roy, "Imagerie Microondes : Reflet de CEM en 5G (In French)", Master Thesis, University of Bourgogne Europe, 2024.
- [15] <https://www.changpuak.ch/electronics/MagneticFieldProbe.php>, Accessed Apr. 20, 2025.
- [16] <https://theemcshop.com/manufacturers/rohde-schwarz-rf-test-equipment/rohde-schwarz-spectrum-analyzers/?srsltid=AfmBOoroYFc78QoVrd0LrYhj40zdz8oIT6U2EDFrwrjI4ahU9yb0t1FX>, Accessed Apr. 20, 2025.
- [17] <https://www.scielo.br/j/jmoea/a/TCg4wdgNMmHZVK9TGZKZS8C/?lang=en>, Accessed Apr. 20, 2025.
- [18] https://hackrf.readthedocs.io/en/latest/hackrf_one.html, Accessed Apr. 20, 2025.
- [19] <https://www.crowdsupply.com/othersnet/morfeus>, Accessed Apr. 20, 2025.
- [20] https://www.science.smith.edu/resources/cdf/pdf_files/Techno_GCODE%20Commands.pdf, Accessed Apr. 20, 2025.
- [21] <https://pypi.org/project/morfeus/>, Accessed Apr. 20, 2025.

Capteur résonnant pour détection d'obstacles dans de l'eau douce *Resonant sensor for obstacle detection in fresh water*

Nicolas Troesch*¹, Arnaud Vena¹, Séverin Pistre², Philippe Combette¹

¹IES Montpellier, Université de Montpellier, nicolas.troesch@umontpellier.fr

²HSM HydroSciences Montpellier, Université de Montpellier,

Karst, Capteur, Résonnant, Eau douce // Karst, Sensor, Resonant, Fresh water

Résumé/Abstract

Cet article présente un nouveau dispositif de détection d'environnement sous-marin et d'obstacles utilisant un capteur résonnant fonctionnant dans une plage de fréquences allant de 50 à 180 MHz. La conception du capteur ne nécessite pas un processus de fabrication complexe. L'électronique du capteur est relativement simple et à faible consommation d'énergie. Les résultats de simulation et les mesures pratiques en environnement contrôlé valident les travaux supplémentaires sur cet outil novateur, qui est un capteur basse consommation basé sur une antenne résonante, capable de détecter des parois rocheuses et des poches d'air avec une portée de détection de 200 mm.

This paper presents a new underwater environment and obstacle detection device using a resonant sensor operating in the frequency range from 50 to 180MHz. The sensor design does not require a complex manufacturing process. The sensor electronic is fairly simple and low power. Simulation results and practical measurement in a controlled environment validate the additional work on this novel tool, which is a low-power sensor based on a resonant antenna that is able to detect rock walls and air pockets with a detection range of 300-400 mm.

1 Introduction

Afin de faire face aux pressions climatiques et anthropiques à venir sur les hydrosystèmes et les ressources en eau, il est indispensable de proposer des outils d'ingénierie permettant la reconnaissance et la gestion des réservoirs karstiques. En effet, les réservoirs karstiques alimentent 25% de la population mondiale en eau potable [1]. Ils représentent donc une ressource en eau souterraine importante, mais qui pourrait dans de nombreux cas être davantage exploitée notamment sur les rives de la Méditerranée. Depuis 50 ans, la compréhension des processus qui contrôlent leur fonctionnement hydrodynamique a très largement progressé. Cette progression a permis d'améliorer leur modélisation mais des obstacles majeurs demeurent ; Ils sont liés à la caractérisation de leur structure interne et à l'organisation des écoulements.

Même si les réservoirs karstiques sont particulièrement anisotropes et hétérogènes, un réseau organisé et hiérarchisé de conduits concentre et contrôle les écoulements vers un ou plusieurs exutoires. Or, la reconnaissance de ces conduits se limite actuellement à l'utilisation de traceurs artificiels donnant une vitesse "à vol d'oiseau" entre une entrée d'eau et un exutoire, ou à l'exploration en plongée qui ne peut concerner qu'une infime partie des conduits. Face à ces difficultés, l'imagerie géophysique et les simulateurs stochastiques font partie des pistes actuelles mais ces méthodes manquent de précision pour générer une cartographie fiable des conduits. Ainsi, l'absence d'informations plus précises sur la géométrie des conduits, sur les conditions d'écoulement à travers ceux-ci ou sur l'évolution de la qualité de l'eau le long des drains constitue un réel verrou pour développer des modèles de gestion des aquifères karstiques. L'objectif principal de cet article est de développer un capteur faible consommation à intégrer dans une capsule étanche autonome emportée par l'eau. Celle-ci devra être capable de détecter une paroi à l'intérieur d'un karst dans le but de reconstruire son parcours dans les conduits. Aujourd'hui, il existe un nombre conséquent de moyens de détecter un objet ou une paroi à l'aide de différentes technologies. Mais dans le domaine du karst, les technologies les plus fréquemment utilisées sont les capteurs à ultra-sons [2] et les capteurs laser [3]. Ces deux solutions donnent d'excellents résultats lorsqu'il s'agit de véhicules autonomes sous-marins, mais dans notre cas, nous recherchons une solution intégrable dans une capsule et à faible consommation d'énergie. Notre conception s'inspire des capacités d'électrolocalisation des anguilles et d'autres espèces de poissons [4], [5], qui ont été précédemment étudiées par G. Baffet et al [6], [7], [8]. Le capteur sera placé à l'intérieur d'une capsule autonome transportée par l'eau. Cette recherche vise à créer un capteur à faible consommation capable de détecter les parois ou les poches d'air au sein d'un karst et de reconstruire le tracé du conduit. Dans cet article, nous visons à augmenter la portée de détection en concevant des capteurs fonctionnant

autour de leur fréquence de résonance. Nous aborderons tout d'abord la géométrie du capteur proche d'un dipôle, puis les résultats des simulations, ensuite nous présenterons des mesures en conditions réelles afin de valider nos simulations, ensuite nous présenterons un design intégrable pour une structure simple, puis nous présenterons une solution d'amélioration de la résolution spatiale du capteur. Pour finir nous exposerons ensuite des perspectives suite à cette étude et enfin nous concluons.

2 Théorie / Modèle / Simulation

Les environnements karstiques sont principalement composés de roches solubles, comme des roches carbonatées et calcaires. L'eau a une permittivité relative d'environ 80. En revanche, il est difficile de donner une valeur précise pour la permittivité des roches calcaires, celle-ci dépend de différents facteurs chimiques. La mesure effectuée par le capteur se réalise entre deux éléments principaux (Ea et Eb) qui constituent un résonateur basé sur un dipôle terminé par des pads capacitifs (cf. Figure 1). La présence d'un obstacle affecte le champ électrique par une modification de la permittivité relative autour du résonateur. L'étude consiste à mesurer l'impédance du dipôle composé des deux électrodes Ea et Eb . Dans notre cas, nous allons nous intéresser à la différence de permittivité relative entre l'eau, les roches et l'air au-dessus de la surface de l'eau. Lorsque le résonateur se trouve à proximité d'une roche, on observe un décalage de la fréquence de résonance. Cela est dû au fait que la constante diélectrique des roches est généralement plus faible que celle de l'eau, ce qui entraîne une diminution de la permittivité effective autour du dipôle, et les lignes de champs sont plus dispersées (cf. Figure 1), entraînant une variation de son impédance. Cette étude se concentre sur la mesure de la fréquence de résonance du dipôle. En analysant le paramètre S_{11} , l'impédance Z_{11} peut être extraite afin de déterminer la fréquence de résonance. Les branches Ea et Eb sont constituées de deux plans de cuivre de rayon r reliés à deux fils de cuivre de longueur L .

Pour affiner le modèle de nos simulations, nous avons décidé de mener une campagne de caractérisation de roches provenant de différentes strates. La permittivité relative des roches prélevées aux alentours de Montpellier a été mesurée à travers différentes couches à l'aide d'un kit d'évaluation diélectrique pour couches minces (*DAK-TL2*) connecté à un analyseur de réseau vectoriel *ZNH26*. La plage de fréquences utilisée s'étend de 4 MHz à 20 GHz, comme indiqué à la Figure 2. Les échantillons de roche ont été découpés et polis afin d'obtenir une surface lisse et plane avec une épaisseur de $3,5 \text{ mm} \pm 0,5 \text{ mm}$. Ces échantillons proviennent de strates caractérisées par leur âge géologique. L'eau présente une permittivité relative de $\epsilon_{r_{eau}} = 78$ et une conductivité de $200 \text{ } \mu\text{S/cm}$. La Figure 2 met en évidence un léger contraste dans la permittivité relative mesurée, allant de $\epsilon_r = 5$ pour le Valanginien à près de $\epsilon_r = 8$ pour le Berriasien.

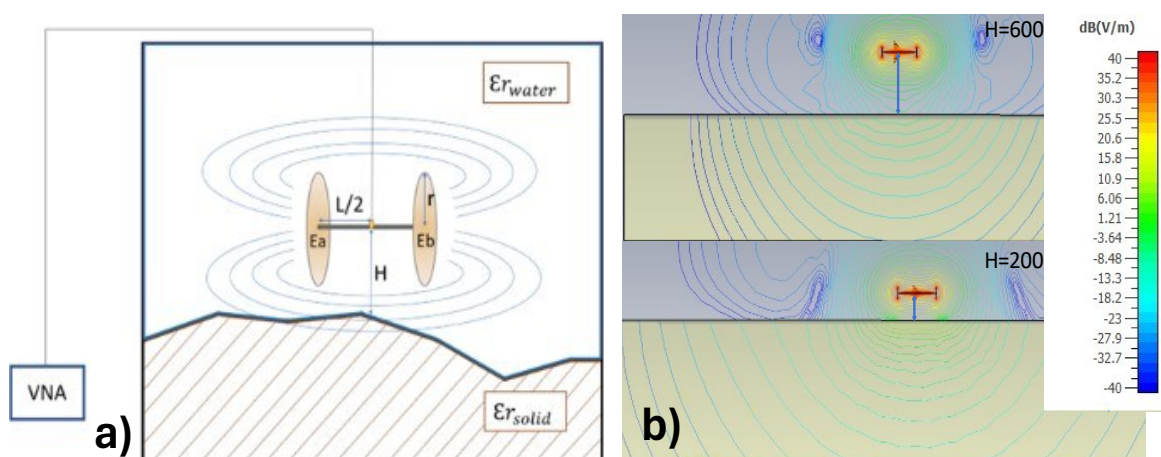


Figure 1: a) Principe de détection d'obstacle par mesure d'impédance d'un résonateur ; b) Exemple de deux simulation pour un set de paramètres $r=50\text{mm}$, $L=200 \text{ mm}$ avec $H=[600 ;200]\text{mm}$

Pour ces simulations, nous avons utilisé CST Microwave Studio et effectué des simulations avec le solveur fréquentiel. L'environnement de simulation est composé de notre dipôle, une grande structure d'un matériau caractérisé par la permittivité mesurée et l'environnement caractérisé par de l'eau douce avec une permittivité relative de $\epsilon_{reau} = 78$ et une conductivité de $200 \mu\text{S/cm}$.

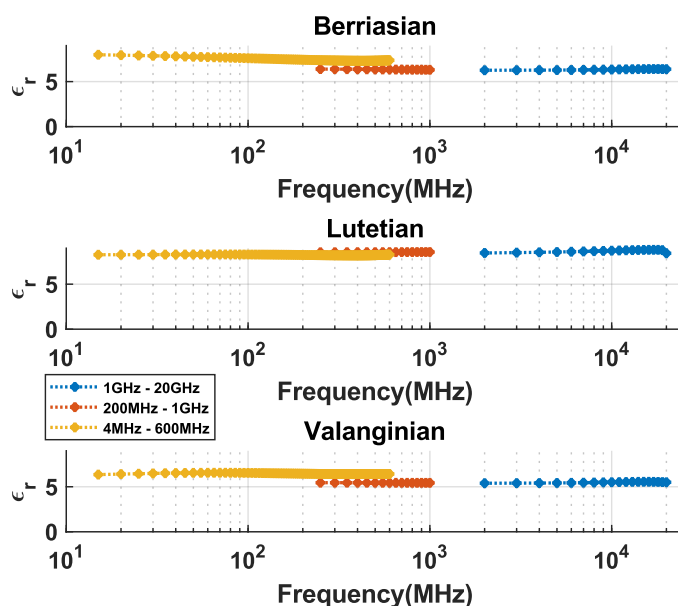


Figure 2: Permittivité relative d'échantillon de roches provenant de différentes strates, pour une gamme de fréquence de 4MHz à 20GHz

La structure karstique simulée est volontairement grande afin d'avoir un volume de roche beaucoup plus grand par rapport à la taille du capteur et donc de limiter les effets de bord. Pour caractériser le dipôle, deux simulations paramétriques ont été réalisées. L'une sur le rayon r et l'autre sur la longueur L (cf. Figure 3) La longueur L et le rayon r du dipôle agissent directement sur la portée de détection. En effet, plus ces paramètres sont élevés, plus nous augmentons sa portée. D'après les résultats de simulation, ces paramètres permet d'obtenir une portée de détection proche de 700 mm pour $L=500$ mm et d'environ 400 mm pour $L=200$ mm dans l'eau douce. Pour l'application visée dans le contexte d'un environnement karstique, nous devons minimiser la taille du dipôle afin qu'il puisse être intégré dans des capsules autonomes. Pour conclure, un bon compromis entre la taille et la distance de détection consiste à choisir $L = 200$ mm et r entre 10 mm et 50 mm.

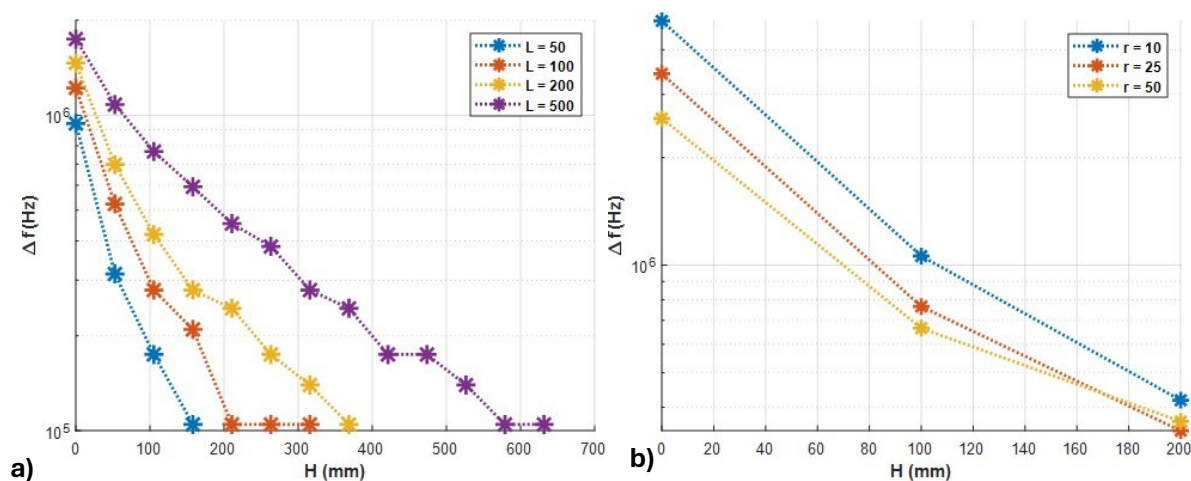


Figure 3: a) Variation de la fréquence de résonance en fonction de la hauteur du capteur (H), pour différentes longueur (L) ; b) Variation de la fréquence de résonance en fonction de la hauteur du capteur (H), pour différents rayon (r)

3 Validation

Des mesures ont été effectuées à la source de Lauret située à environ 30 km au nord de Montpellier. La source de Lauret, qui n'est plus exploitée, provient de l'aquifère karstique de l'Hortus (Valanginien supérieur), isolé des autres aquifères de la région. Notamment la source du Lez qui est plus profonde dans les strates jurassiques alimentant plus de 400.000 habitants. Au moment de nos mesures, le débit d'eau était constant mais pas aussi fort qu'en période d'inondation, c'est pourquoi nous n'avions qu'une profondeur d'eau de 1,10 m pour effectuer nos mesures. Sur place, un analyseur de réseau vectoriel, ZNH26, a été connecté à un câble SMA de 6 m de long directement à notre dipôle (cf. Figure 4.b).

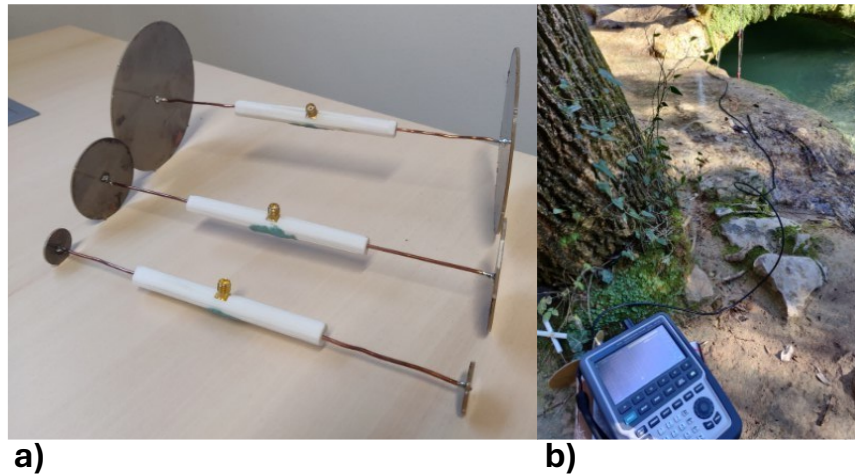


Figure 4: a) Dipôles ($r=10,25,50$ mm ; $L=200$ mm) (L) ; b) Environnement de mesure

Nous avons mesuré le paramètre S_{11} de 1 à 100 MHz et avons ensuite calculé la matrice Z_{11} . (Nous avons ensuite localisé la fréquence de résonance de chaque matrice pour calculer la figure 7. Les dipôles ont été réalisés à l'aide de deux cercles découpés dans une plaque de cuivre simple face d'une épaisseur de $35\mu\text{m}$ de cuivre. Ces deux plaques ont été soudées à deux fils de cuivre (100mm de long avec un diamètre de 0.025mm) soudés à un connecteur SMA. Afin de rigidifier les dipôles, un manchon imprimé en 3D entoure les deux fils de cuivre (cf. figure 4.a).

Il convient de noter qu'une fine couche isolante a été déposée sur les parties en cuivre. Les résultats sont en accord avec les simulations, ce qui confirme que nous pouvons détecter la proximité de roches. En effet, il y a le même comportement dans le déplacement de la fréquence de résonance de la structure en simulation et en pratique. (Figure 5 & Figure 3.a). Grâce à la symétrie du dipôle, nous sommes capables de détecter la présence d'air. Effectivement, l'eau et l'air ont une permittivité différente, ce qui nous donne la possibilité de différencier les deux matériaux dans nos mesures. Les mesures ont été effectuées avec une incertitude sur la hauteur H de $\Delta = \pm 50$ mm, et garantissent pour un résonateur de longueur $L=200$ mm une distance de détection comprise entre 300 et 400 mm en fonction du rayon r des électrodes.

4 Intégration électronique

Cette section vise à proposer une électronique simple nous permettant d'intégrer la mesure de la fréquence de résonance en se passant d'un analyseur de réseau vectoriel utilisé précédemment. Les mesures ont été effectuées dans un aquarium rempli de 300 mm d'eau douce. Une méthode électronique simple a été utilisée pour enregistrer le déplacement de la fréquence de résonance. Un générateur a été utilisé pour envoyer un signal à la fréquence de résonance du capteur ($f = 80,9$ MHz) vers un détecteur de puissance RF CPDETLS-4000. La tension aux bornes du composant a ensuite été mesurée à l'aide d'un oscilloscope (voir Figure 6). Pour appliquer ce principe dans un

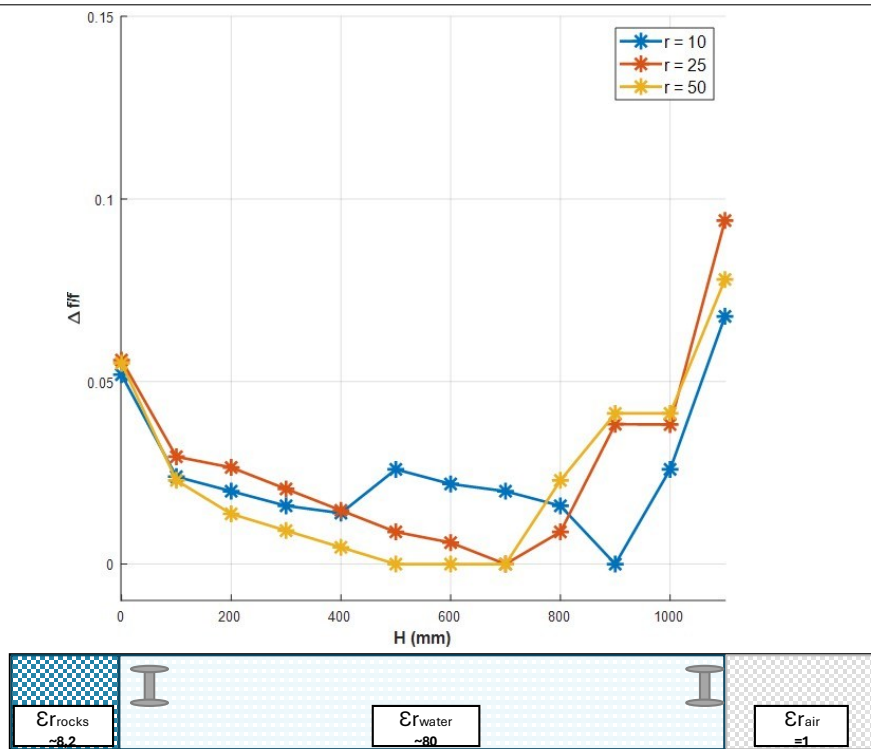


Figure 5: Mesures de la fréquence de résonance en fonction de la hauteur du capteur (H) pour une longueur $L = 200$ mm et pour différentes valeurs de rayon (r)

système embarqué, nous pourrions connecter un VCO et un ADC à un microcontrôleur afin de réaliser les mêmes mesures. Dans cette expérience, nous avons mesuré la tension moyenne pour différentes hauteurs allant de $H = 0$ mm à $H = 180$ mm. Les résultats de simulation indiquent que la fréquence de résonance de la structure est modifiée par la présence d'un matériau présentant un contraste élevé de permittivité relative par rapport à l'eau. En générant un signal à la fréquence de résonance de la structure et en le plaçant à proximité d'un matériau, la permittivité relative de ce matériau peut être déterminée en observant le changement de fréquence de résonance de la structure et l'augmentation de tension qui en résulte. La Figure 6 montre que nous avons pu détecter la présence d'une paroi, ainsi que la table, le fond de l'aquarium et l'air.

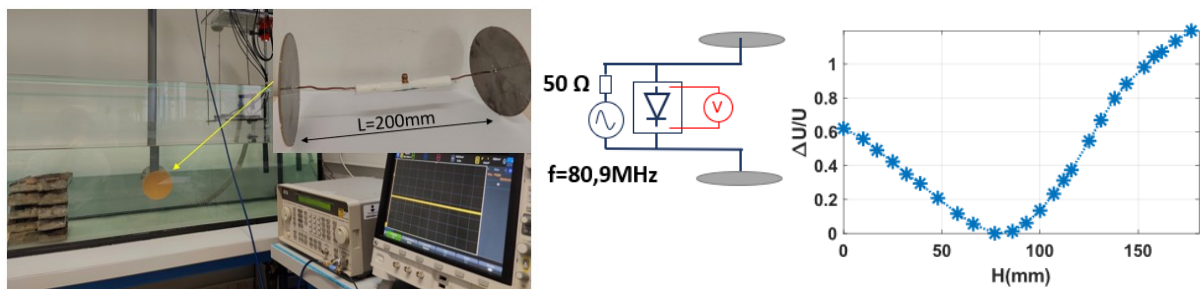


Figure 6: Variation relative de la tension (U) aux bornes du capteur en fonction de la hauteur (H) ; Electronique simple dans un environnement contrôlé

5 Détection d'obstacles en 2D / 3D

Les parties précédentes ont démontré la possibilité d'utiliser un résonateur pour la détection d'obstacle en champ proche. Dans cette partie nous allons essayer d'améliorer la résolution spatiale du capteur. Le premier design proposé est composé de trois branches, nommées (Ea , Eb , Ec), connectées par des ports ($S1$, $S2$, $S3$). Nous avons réalisé des simulations pour ce design en utilisant *CST Microwave Studio* et le solveur fréquentiel, allant de 120 MHz à 170 MHz. La structure rocheuse a été modifiée pour ajouter sur $\frac{1}{4}$ de sa surface, une marche de la

moitié de l'épaisseur du bloc de roche (cf. figure 7). Il est à noter que la fréquence de résonance de la structure va dépendre du design utilisé.

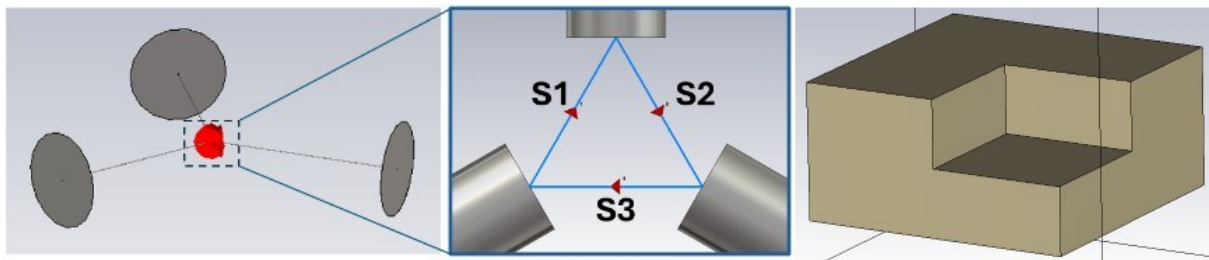


Figure 7: Capteur trois fils & structure rocheuse en simulation

La figure 8 montre le champ électrique généré par chaque capteur et leurs « points chauds » sur les matériaux rocheux. Pour les capteurs S1 et S3, l'une des branches se trouve au-dessus de la marche. Par conséquent, la fréquence de résonance des structures est moins influencée par la roche car le contraste de permittivité relative autour de S1 et S3 à cet endroit est plus important qu'autour de S2. En mesurant la fréquence de résonance de chaque capteur successivement, on peut extraire les courbes sur la figure 8 démontrant ainsi la détection d'une irrégularité dans une structure rocheuse.

Le second design proposé est composé de six branches, nommées (Ea, Eb, \dots, Ef), connectées par des ports ($S1, S2, \dots, S6$) (cf. Figure 9). Nous avons réalisé des simulations pour ce design en utilisant *CST Microwave Studio* et le solveur fréquentiel, allant de 120 MHz à 170 MHz. Ce design nous permettrait de coupler une détection d'irrégularité surfacique ainsi qu'une détection de proximité. La figure 10 démontre le fonctionnement de ce capteur en simulation.

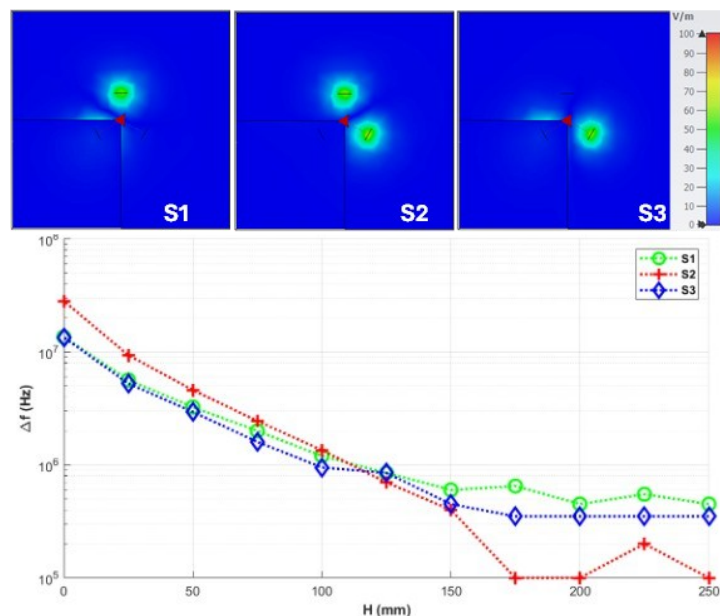


Figure 8: Capteur trois fils et visualisation du champ électrique ; Variation de la fréquence de résonance pour les trois ports en fonction de la hauteur (H)

6 Conclusion

Ce travail démontre la capacité à détecter des cavités et des variations dans les structures rocheuses à l'aide d'un capteur placé dans de l'eau douce. L'ajout de branches réalisé par rapport aux structures précédentes ont permis d'améliorer la résolution spatiale de notre capteur. Cependant il est à noter que la version actuelle n'est

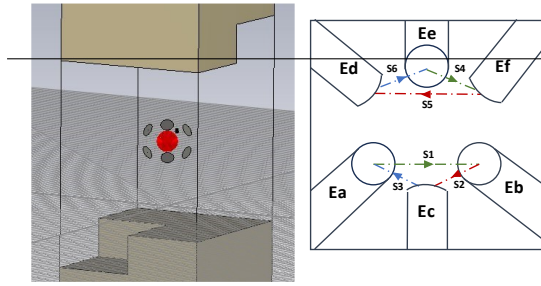


Figure 9: Environnement de simulation & vue schématique

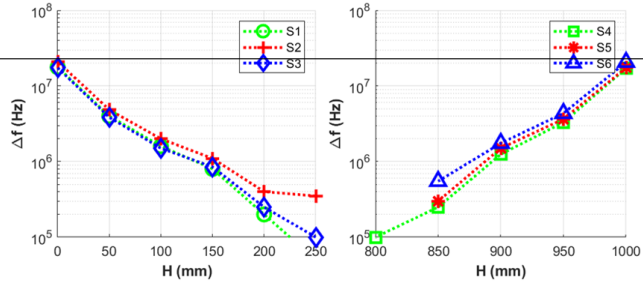


Figure 10: Variation de la fréquence de résonance en fonction de la hauteur (H) du capteur à 6 ports

pas intégrable pour faute de son encombrement, de plus l'ajout de branches impacte directement la distance de détection, passant d'une distance de détection de 400mm à une distance de 200mm pour le design à six branches. Une amélioration serait de trouver un design souple permettant aux branches d'évoluer sans contraindre la capsule dans l'environnement. Nous avons également démontré une méthode permettant d'intégrer nos mesures sans recourir à un analyseur de réseau vectoriel, ce qui réduit ainsi la consommation d'énergie de notre capteur et rend l'électronique intégrable. De plus, cette étude fournit des mesures fiables de la permittivité relative de différentes couches rocheuses dans la plage de 4 MHz à 20 GHz, données encore non mesurée dans le domaine. Nos travaux futurs se concentreront sur la miniaturisation du capteur, l'installation de l'électronique de conditionnement pour le capteur à six branches, et l'exploration du potentiel de catégorisation des objets présentant des permittivités variables le long du trajet de la capsule dans l'eau.

Références

- [1] N. Goldscheider *et al.*, 'Global distribution of carbonate rocks and karst water resources', *Hydrogeology Journal*, vol. 28, pp. 1–17, Apr. 2020, doi: 10.1007/s10040-020-02139-5.
- [2] M. Alarab, 'An acoustic shield for karstic exploration with underwater robot', phdthesis, Université Montpellier, 2021. Accessed: Feb. 08, 2023. [Online]. Available: <https://theses.hal.science/tel-03442894>
- [3] D. Modarress, P. Svitek, K. Modarress, and D. W. Wilson, 'Micro-Optical Sensors for Underwater Velocity Measurement', in *2007 Symposium on Underwater Technology and Workshop on Scientific Use of Submarine Cables and Related Technologies*, Apr. 2007, pp. 235–239. doi: 10.1109/UT.2007.370801.
- [4] K. Wang, L. Cui, and K. D. Do, 'An underwater electrosensory membrane bio-inspired by weakly electric fish', in *2016 IEEE/RSJ International Conference on Intelligent Robots and Systems (IROS)*, Daejeon, South Korea: IEEE, Oct. 2016, pp. 4951–4956. doi: 10.1109/IROS.2016.7759727.
- [5] J. R. Solberg, K. M. Lynch, and M. A. MacIver, 'Robotic Electrolocation: Active Underwater Target Localization with Electric Fields', in *Proceedings 2007 IEEE International Conference on Robotics and Automation*, Apr. 2007, pp. 4879–4886. doi: 10.1109/ROBOT.2007.364231.
- [6] G. Baffet, F. Boyer, and P. B. Gossiaux, 'Biomimetic localization using the electrolocation sense of the electric fish', in *2008 IEEE International Conference on Robotics and Biomimetics*, Bangkok: IEEE, Feb. 2009, pp. 659–664. doi: 10.1109/ROBIO.2009.4913079.
- [7] V. Lebastard, C. Chevallereau, A. Girin, F. Boyer, and P. B. Gossiaux, 'Localization of small objects with electric sense based on kalman filter', in *2012 IEEE International Conference on Robotics and Automation*, May 2012, pp. 1137–1142. doi: 10.1109/ICRA.2012.6224824.
- [8] Y. Morel, V. Lebastard, and F. Boyer, 'Neural-based underwater surface localization through electrolocation', in *2016 IEEE International Conference on Robotics and Automation (ICRA)*, May 2016, pp. 2596–2603. doi: 10.1109/ICRA.2016.7487417.

Mesures haute fréquence, outils et méthodes de calibrage

Calibrated measurements of dopant concentration on vertical nanowires by scanning microwave microscopy

José Morán-Meza¹, José Penuelas², Nicolas Chauvin², Philippe Régreny², François Piquemal¹

¹Laboratoire national de métrologie et d'essais (LNE), 29 Avenue Roger Hennequin, FR-78197, Trappes, France

²Ecole Centrale de Lyon, CNRS, INSA Lyon, Université Claude Bernard Lyon 1, CPE Lyon, INL, UMR5270, Ecully 69130, France

Keywords : Dopant profiling, nanowire, calibration method, scanning microwave microscopy.

Abstract

Arrays of vertically aligned semiconducting GaAs nanowires (NWs) with radial and axial p-n junctions constitute the core element for novel photovoltaic cells for enhanced efficiency [1]. Nevertheless, the accurate characterization of their junctions' dopant concentrations (N_a) is crucial for screening defective NWs and analyze their effects on solar cell performance. To this end, high-resolution measurements are performed using electrical scanning probe microscopy techniques with reference N_a values for traceable measurements on NWs.

Scanning microwave microscopy (SMM) is a powerful technique for measuring impedances at the nanoscale with sub-50-nm spatial resolution. A conductive tip is in contact with the sample surface and connected to a RF source in the GHz range. Measuring the impedance of doped semiconductor with a native oxide layer enables the determination of its dopants concentration levels [2]. To perform quantitative N_a measurements, SMM was calibrated using a reference sample based on p-doped GaAs multilayers with different doping levels N_a ranging from $6 \cdot 10^{16}/\text{cm}^3$ to $1 \cdot 10^{19}/\text{cm}^3$, measured by secondary-ion mass spectrometry.

The SMM calibration on doped GaAs multilayer samples show a good agreement for N_a values with a combined uncertainty of 10%. We have also found a deviation of 20% for N_a values on another similar GaAs multilayer sample, which corresponds to two standard deviations. The SMM calibration allowed us to extract the doping levels of p-doped GaAs NWs, with preliminary N_a values of $(5.0 \pm 1.2) \cdot 10^{18}/\text{cm}^3$ and $(4.6 \pm 1.1) \cdot 10^{18}/\text{cm}^3$, which are in the same order of magnitude as the estimated values of about $3.3 \cdot 10^{18}/\text{cm}^3$ and $1.8 \cdot 10^{18}/\text{cm}^3$, respectively.

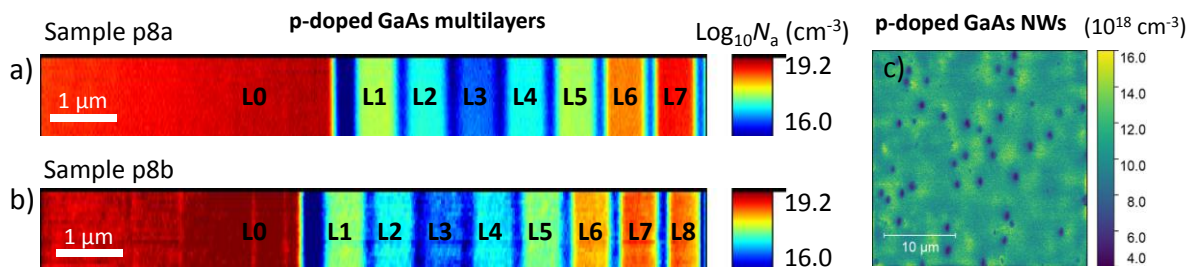


Figure 1. Dopant concentration map on similar p-doped GaAs multilayers (a,b) and p-doped GaAs NWs (c).

References:

[1] Y. Zhang and H. Liu, *Crystals*, 9, 87 (2019)

[2] A. Buchter *et al*, *Review of Scientific Instruments* 89, 023704 (2018)

Acknowledgement:

This research project is supported by the European Union and is funded within the scope of the European Metrology Programme for Innovation and Research (EMPIR) project 19ENG05 NanoWires entitled 'High throughput metrology for nanowire energy harvesting devices'.

Novel Thermopile Design for Waveguides and Coaxial Microcalorimeters in the Frequency range from DC – 40 GHz

Doudou BA¹, Alexis LITWIN¹

¹Laboratoire National de Métrologie et d'Essais, {doudou.ba@lne.fr}

Keywords: Thermopile, Microcalorimeter, microwave power, primary standard

Mots clés: Thermopile, Microcalorimètre, Puissance HF, Etalon primaire

Abstract

This work introduces a novel thermopile design for microcalorimeters used in high-frequency microwave power measurements. The thermopile, composed of Copper-Constantan thin-film junctions on an FR4 substrate, enhances sensitivity and accuracy in detecting heat generated when microwave power is applied to a reference power sensor. The new design significantly improves output voltage, leading to better measurement precision. The study focuses on three microcalorimeter setups developed at the Laboratoire National de Métrologie et d'Essais (LNE): a 7 mm coaxial system (APC-7 connector, 10 MHz – 18 GHz) and two waveguide-based systems for K-band (18 – 26.5 GHz) and Ka-band (26.5 – 40 GHz). Experimental results demonstrate that the redesigned thermopile increases voltage output, thereby enhancing sensitivity in microwave power measurements. The Performance comparisons between the new thermopile and the previous design indicate a marked improvement in microcalorimeter efficiency and reliability.

Résumé

Ce travail présente une nouvelle conception de thermopile pour les microcalorimètres utilisés dans la mesure de puissance micro-ondes haute fréquence. La thermopile, constituée de jonctions en film mince Cuivre-Constantan sur un substrat FR4, améliore la sensibilité et la précision dans la détection de la chaleur générée lorsqu'une puissance micro-onde est appliquée à un capteur de puissance de référence. Le nouveau design améliore considérablement la tension de sortie, conduisant à une meilleure précision des mesures. L'étude porte sur trois configurations de microcalorimètres développées au Laboratoire National de Métrologie et d'Essais (LNE) : un système coaxial de 7 mm (connecteur APC-7, 10 MHz – 18 GHz) et deux systèmes à guide d'ondes pour la bande K (18 – 26,5 GHz) et la bande Ka (26,5 – 40 GHz). Les résultats expérimentaux montrent que la thermopile revisitée augmente la tension de sortie, renforçant ainsi la sensibilité des mesures de puissance micro-ondes. Les comparaisons de performances entre la nouvelle thermopile et la précédente indiquent une nette amélioration de l'efficacité et de la fiabilité des microcalorimètres.

1 Introduction

In microwave and millimeter wave applications, there are increasing demands for power measurements [1] – [2]. It is essential for processes, which consist to test the conformity of telecommunication equipment and their proper deployment and use as well. The traceability of microwave power has been obtained using microcalorimeter systems. Since their introduction in 1950s, it is an essential measurement technique for microwave power metrology and continues to be fundamental for most of the National Metrology Institutes (NMIs) as the primary calibration capabilities system for the realization of the primary power standard in microwave frequency [3] – [5]. The traceability of the microwave power is achieved through the measurement of the effective efficiency (η_{eff}) of the reference power standard by the microcalorimeter. The microcalorimeter makes these reference power standard traceable to the direct current (DC) standard, which is SI quantity. The calibrate reference power sensor, which are generally bolometric type sensor in most of NMIs, are then used in direct comparison technique to calibrate microwave power sensor or some microwave power meter. To understand or introduce the role of the thermopile in microcalorimeter measurements systems, it should be useful to give briefly a summary of the microcalorimeter principle in first place.

For the calibration of the reference microwave power sensors, Figure 1 shows the microcalorimeter schematic design that are widespread use as primary microwave power standard. It include the feeding path line that connect the microwave source and DC source to the reference microwave power sensor, a dummy path line that is connected to the dummy microwave power sensor, the thermal insulation line, thermostatic water bath, thermopile and so on. The feeding path line is used for the injection of microwave power, DC or lower frequency signal. The

dummy path is used for temperature reference, no signal is injected. The thermal insulation line helped to reduce the thermal transfer on the feeding line of the calorimeter. The thermostatic water bath maintain the thermal stability of the temperature from outside thermal fluctuation. The effective efficiency of the microwave reference power sensor is determine by using a substitution method which consist of measuring the temperature rise in the calorimeter when it is alternatively supplied with RF power and a reference power (DC or at lower frequency signal 1 KHz for instance). It measure the degree of power transference to the power sensor under calibration when HF frequency power is applied or not. It is define as shown in equation below:

$$\eta_{eff} = \frac{P_{DC\ sub}}{P_{RF\ abs}} \quad (1)$$

Where $P_{DC\ sub}$ is the substituted DC power (or bolometric power) and $P_{RF\ abs}$ is the totale microwave power in the power sensor.

For more details regarding the microcalorimeter, principle is beyond the scope of this study. Therefore, for more specifics, on can refers to these references [6] – [8].

The thermopile primary function in a calorimeter is to detect and measure the heat generated by the microwave power sensor. When microwave power is applied in the power sensor, a parasite thermal loss appear in the microcalorimeter. These losses can be sometimes very low, at the μW level. Therefore, it is crucial to have a very highly sensitive thermopile device to detect them. The purpose of this paper is to replace the thermopile used for microcalorimeter in the frequency range from 10 MHz to 40 GHz that are very bulky with limited number of thermocouple junctions with new thermopile in thin-film to enhance the sensitivity. For the validation of the new thermopile being introduced in the microcalorimeter by comparing the performance data of microcalorimeter with the case of suing the old design of thermopile and the declared CMCs by LNE.

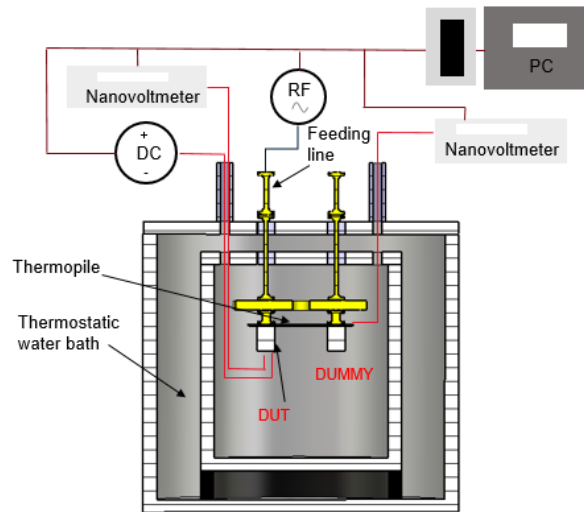


Figure 1: Microcalorimeter set up

2 Microcalorimeter systems description

For this study, three set of microcalorimeters have been used and constructed by Laboratoire National de Metrologie et d'Essais (LNE). One set is a 7 mm coaxial microcalorimeters covering frequency range of 10 MHz – 18 GHz and having and APC-7 connector. Two sets are K Band IEC-R220 (18 – 26.5 GHz) and Ka Band IEC-R320 (26.5 – 40 GHz) waveguide microcalorimeters. The calorimeters are identified as of Joule twin type. The microcalorimeters systems set-up are specifically design for measurement of the effective efficiency of the bolometer mounts type of power sensor. The components of the microcalorimeters are shown in figure 1 and describe schematically in figure 2.

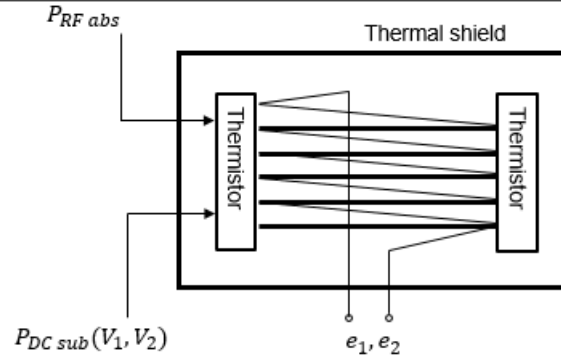


Figure 2: Schematic description of the microcalorimeter

As previously noted, in figure 1 and figure 2, the microwave power standard are two bolometer mount assembled into two symmetrical feeding path. The power measurement of the bolometer mount by microcalorimeter method consist of the measurement of the amount of RF power being transfer to the bolometer element (thermistor). This is done through the measurement of the total heat absorbed by the thermistor when RF power is applied or when it is not applied. The resistance of the thermistor in the feeding path line is keep at a constant value by a self-balancing dc bridge during the measurement process. When the RF power is off and the thermistor is dc-biased by self-balancing dc bridge as shown in figure 2, the dc power dissipation is given by formula below:

$$\frac{V_1^2}{R} = \frac{e_1}{k_1} \quad (2)$$

Where V_1 is self-balancing bridge voltage when RF power is off, R is the operating resistance (in ohms) of the thermistor, e_1 is the output voltage of the thermopile corresponding to V_1 and k_1 (in $V \cdot W^{-1}$) is the sensitivity of the thermopile to power dissipation at the thermistor.

When RF power is applied, the self-balancing bridge reduce the dc power by an amount equivalent to the RF power applied to keep the thermistor operating resistance unchanged and equal to R . the total power dissipated (P_{tot}) in the thermistor is given by equation below :

$$P_{tot} = gP_{RF\ abs} + \frac{V_2^2}{R} = \frac{e_2}{k_2} \quad (3)$$

Where g is a frequency dependent correction factor for microcalorimeter and bolometer mount combination, when we integrated the RF power loss in the bolometer mount and microcalorimeter feeding transmission line. V_2 is self-balancing bridge voltage when RF power is applied. e_2 is the output voltage of the thermopile corresponding to V_2 . k_2 (in $V \cdot W^{-1}$) is the sensitivity of the thermopile to power dissipation when bolometer mount is dc-bias and RF energized at the same time. For this study, we assume the thermopile response for all three microcalorimeter are linear, therefore, factors k_1 and k_2 are equal ($k_1 \approx k_2$).

As shown in equation (1) for the calculation of the effective efficiency, the substituted dc power $P_{DC\ sub}$ can be expressed by equation below:

$$P_{DC\ sub} = \frac{V_1^2 - V_2^2}{R} \quad (4)$$

The substituted dc power by equivalence, correspond to the net RF power absorbed in the thermistor. It is always less than the RF power applied in the bolometer mount.

By combining equations (1) to (4) above, the effective efficiency of the power sensor can be expressed as function of bias voltage and the output thermopile voltage:

$$\eta_{eff} = g \frac{1}{1 + \frac{e_2 - e_1}{e_1} \frac{v_1^2}{v_1^2 - v_2^2}} \quad (5)$$

The accurate measurement of the effective efficiency depends on the determination of g . As noted previously, the totality of RF power applied is not absorbed by the thermistor since we have RF loss in the thermal isolation section waveguide in front of the bolometer mount. Therefore, the RF power dissipated in the thermistor is less than the RF power applied in the microcalorimeter ($P_{RF\ abs}$) and the determination of g correct this source of measurement errors. The detail calculation and the expression of the correction factor g is given by [9] :

$$g = 1 + 0.115 A_{dB} \quad (6)$$

Where A_{dB} is measured insertion loss of the thermal isolation section waveguide in front of the bolometer mount. Therefore, the determination of g is done by using a vector network analyzer (VNA) to estimate the power dissipation in the thermal isolation section waveguide of the microcalorimeter.

3 Thermopile design and use as a power detector

The thermopile is an essential component in the microcalorimeter set up for measuring the RF power dissipated in the system. To achieve accurate RF power measurements with high sensitivity and stability, the thermopile design must meet these requirements by detecting small changes in temperature differences between the active thermistor and the reference thermistor in the system when RF power and DC power are applied. For 7 mm coaxial microcalorimeter in APC-7 connector, the thermopile design has 70 pairs of Copper-Constantan thermocouples connected in series, which were realized on 400 μm RF4 substrate. For waveguide microcalorimeter in K Band and Ka Band, thermopile design have respectively 38 and 26 pairs of Copper-Constantan thermocouples connected in series and realized on top 400 μm RF4 substrate as well. In each set of microcalorimeter, the number of thermocouple was maximized by realizing a two layers type of thermopile with Copper in one side of the FR4 substrate and Constantan in the other side. Both side of the FR4 substrate are connect with vias as junctions, when compare to the former thermopile design where all the thermocouples are realized on top of the substrate. Another advantage of the two layers design is to bring the thermocouples junction much more closer to the RF path of the active thermistor as shown in figure 3.

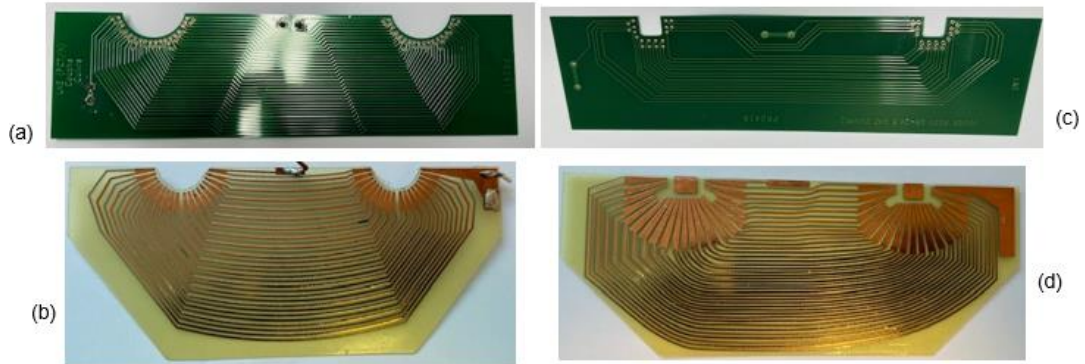


Figure 3: Pictures of the thermopiles. (a) 7 mm coaxial microcalorimeter new design. (b) 7 mm coaxial microcalorimeter former design. (c) Waveguide microcalorimeter K Band new design. (D) Waveguide microcalorimeter K Band former design.

Detail assembly of thermopile assembly in microcalorimeter is shown in figure 4. Two dielectric support are used on top and at the bottom of the thermopile to allow and to keep thermal contact with the active thermistor and thermistor used a reference. This is crucial for the measurement of the temperature rise that occur on the active thermistor when RF or DC power is applied with respect to the temperature of thermistor reference.

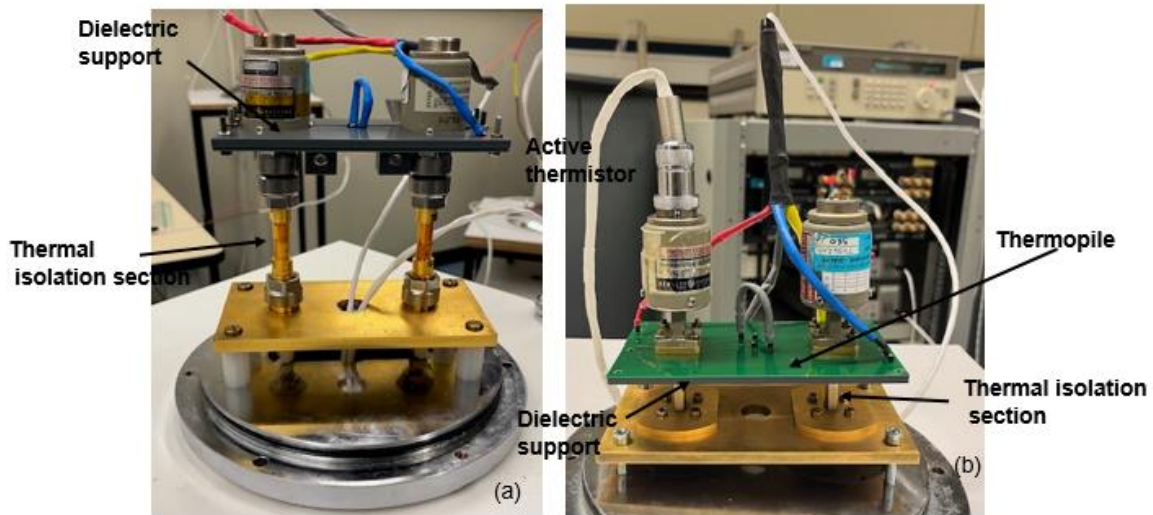


Figure 4: Pictures of the microcalorimeter head. (a) 7 mm coaxial microcalorimeter. (b) Waveguide microcalorimeter K Band.

Figure 5 and Figure 6 shows the thermopile output voltage of each microcalorimeter for three frequencies point and for 10 mW power substitution in DC. For the 7 mm coaxial microcalorimeter, the output voltage for the new thermopile is between 1.151 mV to 1.169 mV, which is more than three time higher than the former thermopile output voltage (0.3330 mV to 0.340 mV). Moreover, for the same substituted power, the results achieve regarding the thermopile output voltage () are higher than those reported by Kwon and all [10] (0.665 mV to 0.680 mV) and by Clague [11] (0.109 mV to 0.112 mV). K Band IEC-R220 (18 – 26.5 GHz) waveguide microcalorimeter, the output voltage vs time measured is between 0.267 mV to 0.272 mV for the new thermopile design and between 0.133 mV to 0.135 mV for the old version. Regarding the Ka Band IEC-R320 (26.5 – 40 GHz) waveguide microcalorimeters, the results show an output voltage between 0.226 to 0.233 mV, which is two time higher than those measured with former thermopile version (0.165 mV to 0.171 mV). Therefore, the new thermopile design response largely increase measurement sensitivity when compare to the former thermopile design.

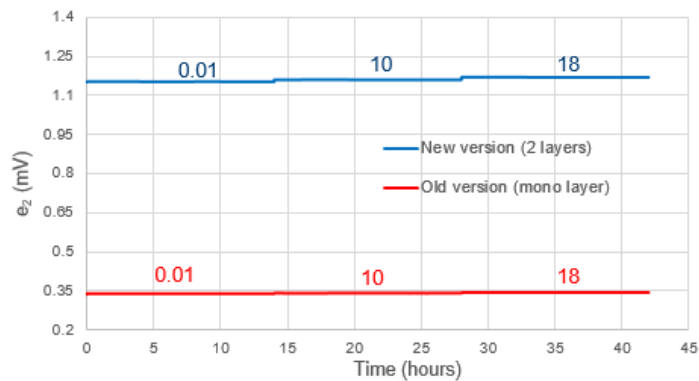


Figure 5: Thermopile output voltage versus time acquisitions for three frequencies (GHz). 7 mm coaxial microcalorimeter in APC7 connector.

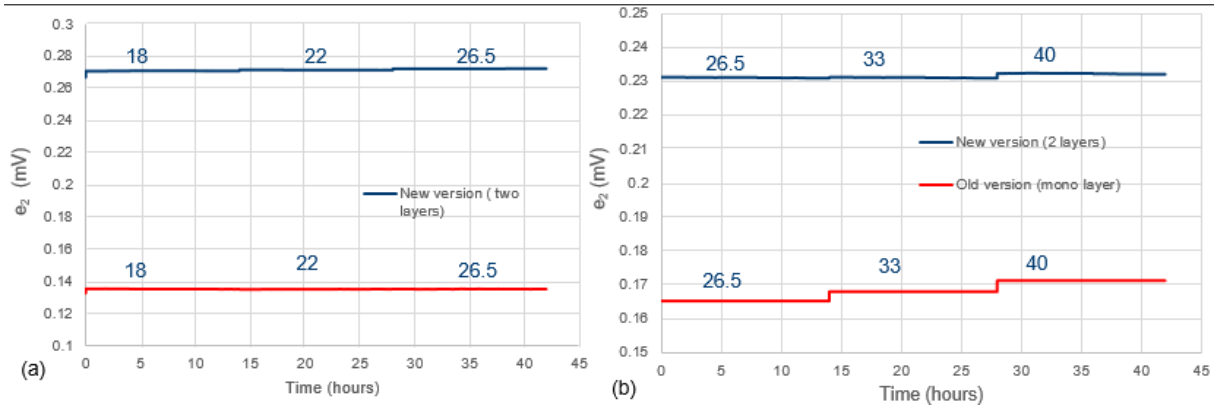


Figure 6: Thermopile output voltage versus time acquisitions for three frequencies (GHz). (a) Waveguide microcalorimeter k Band. (b) Waveguide microcalorimeter Ka Band.

When designing the thermopile, a key critical parameter one should consider is the internal electrical resistance. In the microcalorimeter systems, thermopile can be describe as voltage signal generator and the electrical noise depends mainly to the Johnson noise, which is given by formula below:

$$V_{noise} = \sqrt{4 k_B T_e B R_{th}} \quad (7)$$

Where k_B is the Boltzmann constant, T_e is the external temperature at which the thermopile operates, B is the noise bandwidth of the instrument that read the thermopile output voltage and R_{th} is the thermopile internal electrical resistance.

Typically, for the 7 mm coaxial microcalorimeter in APC7, R_{th} value of the new thermopile and the former one are respectively 546.5Ω and 98Ω . Therefore the Signal-To-Noise Ratio (SNR) are 1.48×10^{10} and 7.22×10^9 for the new thermopile and the former respectively. That led to a gain of around 6 dB. Regarding the waveguide microcalorimeter in K Band, R_{th} are 150Ω and 320Ω for the former thermopile and the new version respectively. This provide a gain of about 5 dB when comparing the signal output voltage. In the case of the waveguide microcalorimeter Ka Band, the resulting gain result between the two thermopiles design can be expressed approximatively 1.3 dB.

4 Effective efficiency results and comparison

For the validation and comparison, we characterized in the microcalorimeter thermistor mounts that were used as transfer standard. The results are shown in Table 1.

For the 7 mm coaxial, K band waveguide and the Ka band waveguide thermistor mounts, the results show good agreements within the assigned uncertainties ($\Delta\eta_e$) when compared with the declared CMCs values. Regarding the comparison with the two thermopiles, the improvement of the thermopile responsivity slightly improve the microcalorimeter performances as show in figure 7.

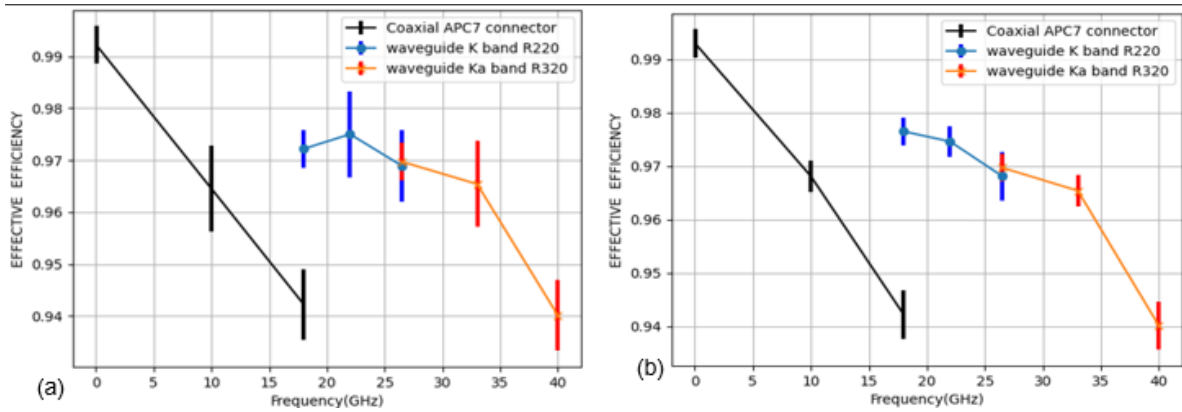


Figure 7: Effective efficiency measurement results. (a) Microcalorimeter with old thermopile design. (b) Microcalorimeter with new thermopile design.

Transfer Standard	Frequency (GHz)	Old thermopile design		New thermopile design		LNE Expanded Uncertainty CMC
		η_e	$\Delta\eta_e$	η_e	$\Delta\eta_e$	
HP 8478B APC-7	0.01	0.9922	0.0036	0.9930	0.0026	0.0026
	10	0.9645	0.0083	0.9681	0.0029	
	18	0.9422	0.0064	0.9422	0.0045	
HP K486A	18	0.9722	0.0064	0.9765	0.005	0.0046
	22	0.9750	0.0061	0.9746	0.0051	
	26.5	0.9689	0.0056	0.9681	0.0048	
HP R486A	26.5	0.9697	0.0087	0.9697	0.008	0.008
	33	0.9654	0.0117	0.9654	0.008	
	40	0.9401	0.0101	0.9401	0.008	

Table 1: Results of the effective efficiency measurement

5 Conclusion

For primary RF power measurement, new design of thermopiles have been developed and evaluated in the coaxial (using APC-7 connector) and waveguide (K band and Ka band) microcalorimeters. The result clearly show a gain in the voltage measurement and responsivity of the thermopile. As a result of this work, the set of thermopile improve our microcalorimeter performances regarding the effective efficiency measurement within the assigned uncertainties level.

Références

- [1] A. S. Brush, "Measurement of microwave power – A review of techniques used for measurement of high- frequency," RF. IEEE Instrum. Meas. Mag. 2007, 38, 1473-1476.
- [2] C. Dehos, J. L. Gonzales, A. De Domenico, D. Ktésas and L. Dussopt, "Millimeter-wave access backhauling : The solution of the exponential data traffic increase in 5G mobile communications systems," IEEE Commun. Mag., vol.52, no, 9, pp 88-95, Sep. 2014.
- [3] A. C. Macpherson, "A microwave microcalorimeter," Rev. Sci. Instrum. , vol. 26, no. 1, pp. 27 – 66. Jan. 1959.
- [4] L. Brunetti and E. T. Vremera, "A New Microcalorimeter for the measurements in 3.5-mm Coaxial Line," IEEE Trans. Instrum. Meas., vol. 52, no. 2, Apr. 2003.
- [5] N. S. Chung, J. Sin, H. Bayer, and R. Honigbaum, "Coaxial and waveguide microcalorimeters for RF and microwave power standards," IEEE Trans. Instrum. Meas., vol. 38, no. 2, pp. 460 – 464, Apr. 1989.
- [6] "Diversification et Amélioration des Moyens de Mesure de Puissance ($f < 40$ GHz)," Bureau National de Métrologie, rapport LCIE no 1204, Etude no 691 80 022, 1992.

-
- [7] P. J. Skilton, "Developments in United kingdom waveguide Power Standards," DTIC, report no 80006, Apr. 1980.
- [8] M. E. Harvey, "WR15 microwave calorimeter and bolometer unit," Nat. Bur. Stand. , Tech. Note 618, may 1972.
- [9] " Mesures de Puissance a des Fréquences Supérieures à 40 GHz," Bureau National de Métrologie, rapport LCIE no 1344, Etude no 695 80 232, Avr. 1996.
- [10] J. Y. Kwon, T. W. Kang, and N. W. Kang, "development of a Type-N Coaxial Microcalorimeter for RF and Microwave Power Standards at KRISS," IEEE Trans. Instrum. Meas., vol. 64, no. 6, pp. 1520 – 1526, Jun. 2015.
- [11] F. R. Clague, "Microcalorimeter for 7 mm Coaxial Transmission Line," NIST Tech. Note 1358, Aug. 1993.

On-Wafer Calibration for Nanodevice Characterization up to 110 GHz

Daouda Seck^{1,2}, José Morán-Meza¹, Florent Marlec², Clément Lenoir², Mohamed Sebbache², Djamel Allal¹, Kamel Haddadi²

¹Laboratoire National de Métrologie et d'Essais, Paris, France, {daouda.seck}@lne.fr

¹Laboratoire National de Métrologie et d'Essais, Paris, France, {djamel.allal}@lne.fr

²Univ. Lille, CNRS, Univ. Polytechnique Hauts-de-France, UMR 8520 - IEMN - Institut d'Electronique de Microélectronique et de Nanotechnologie, France, {kamel.haddadi}@univ-lille.fr

Keywords: On-wafer, S-parameters, Calibration algorithms, Ground Signal Ground (GSG) configuration, Coplanar Waveguide (CPW), RF Nano characterization.

Abstract/Résumé

Miniaturized on-wafer calibration structures for accurate nanodevice characterization up to 110 GHz are proposed. The proposed design integrates microscale and nanoscale sections connected by a tapered transition, ensuring impedance matching while maintaining geometric consistency. The propagation characteristics (propagation constant, permittivity and characteristic impedance) of nano and micro coplanar waveguide (CPW) structures are evaluated analytically and experimentally, using TRL (Thru-Reflect-Line) and multilines-TRL calibration algorithms. The results show the validity, but also the limitations of the approach. These results contribute to the establishment of traceable S-parameter standards, enhancing the reliability of nanoscale on-wafer characterization.

Des structures d'étalonnage miniaturisées sur wafer pour une caractérisation précise des nanodispositifs jusqu'à 110 GHz sont proposées. La conception proposée intègre des sections à l'échelle micrométrique et nanométrique reliées par une transition conique, assurant une adaptation d'impédance tout en maintenant une cohérence géométrique. Les caractéristiques de propagation (constante de propagation, permittivité et impédance caractéristique) des structures coplanaires (CPW) nano et micro sont évaluées de manière analytique et expérimentale, en utilisant les algorithmes d'étalonnage : TRL (Thru-Reflect-Line) et Multilines-TRL. Les résultats montrent la validité, mais aussi les limites de l'approche. Ces résultats contribuent à l'établissement des étalons de paramètres S traçables, améliorant la fiabilité de la caractérisation sur wafer à l'échelle nanométrique.

1 Introduction

The miniaturization of electronic devices has enhanced energy efficiency while maintaining the performance/cost ratio in various applications. However, size reduction alters circuit impedance, deviating from the 50Ω reference of RF and microwave measurement instruments like VNAs, leading to measurement inaccuracies [1], [2]. To improve on-wafer nanodevice characterization, it is crucial to develop calibration structures at the nanoscale dimension [3]. The traceability of on-wafer devices S-parameter measurements is a challenge to ensure the reliability of measurement results. Standards are in place for traceability of electrical measurements to nationally and internationally certified units such as the SI ohm, the watt and the meter [4]. Addressing this traceability for on-wafer measurements requires perfect knowledge of the electrical propagation characteristics of the CPW line, in particular its propagation constant, permittivity and characteristic impedance [5], [6].

2 Design and Fabrication

The basic structure comprises two sections (Fig. 1): a microscale coplanar waveguide (CPW) transmission line (TL) compatible with GSG probes (pitch $> 50 \mu\text{m}$) and matched to 50Ω impedance, and a nanoscale section. These segments are connected via a tapered transition, ensuring impedance matching while preserving the geometric aspect ratio.

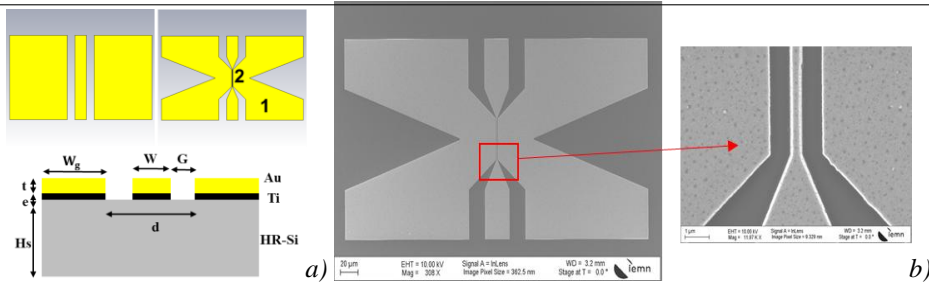


Fig. 1. a) CPW structure configuration b) Scanning electron microscopy (SEM) image of the CPW TL.

Conventional microscale structures are also considered to provide additional insights into propagation characteristics. The substrate is high-resistivity Silicon ($\epsilon_r = 11.9$ and $\sigma = 0.00025$ S/m) with gold conductors. A titanium layer (23-25 nm thick) ensures adhesion to the substrate while serving as a resistive element ($48.9 \Omega/\square$). The DC conductivity of thin-film gold is extracted in two ways: DC measurement via a bias tee using the same GSG probes ($\sigma = 3.24 \times 10^7$ S/m) and measurement using a 4-probe technique ($\sigma = 3.7 \times 10^7$ S/m) (Fig. 2). This last measurement configuration consists of simultaneously injecting a 1 mA current via two DC probes and capturing the voltage via two other DC probes. The relationship between these two quantities allows extracting DC resistance and then deriving the DC conductivity. The dimensional and geometric parameters are detailed in Table 1.

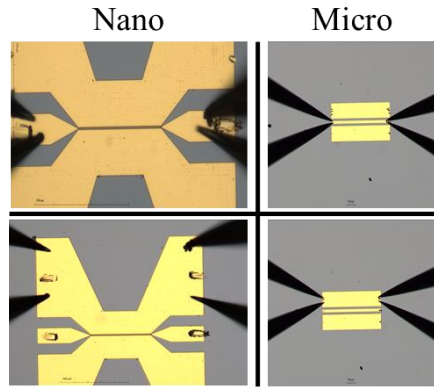


Fig. 2: Measurement configuration of the 4 probes technique.

Table 1: Dimensional parameters (see Fig. 1)

Parts	Terms	Dimensions
Trace width 1	W1	27 μm
Trace width 2	W2	500 nm
Gap 1	G1	18.2 μm
Gap 2	G2	850 nm
Ground width 1	Wg1	137 μm
Ground width 2	Wg2	40 μm
Gold thickness	t	350 nm
Titanium thickness	e	23 nm
Substrate height	Hs	350 μm

3 Measurement principle

Understanding the transmission characteristics of a transmission line—such as its characteristic impedance Z_c , propagation constant γ , and effective relative permittivity ϵ_{reff} —is essential in RF and microwave engineering. The parameters γ and ϵ_{reff} can be directly extracted from measured S-parameters of two transmission lines of different lengths using a Vector Network Analyzer (VNA), through a TRL-based (Thru-Reflect-Line) calibration and extraction method, as detailed in [7]. In particular, the effective permittivity and the propagation constant are related by:

$$\epsilon_{\text{reff}} = -\left(\frac{c}{2\pi f \gamma}\right)^2. \quad (1)$$

The characteristic impedance is obtained using the method proposed by Mark and Williams, which is based on the propagation constant [8] and capacitance measurements [9]. The entire on-wafer measurement procedure relies on a two-port measurement model (Fig. 3), typically described by Equation (2). This equation establishes the relationship between the measured data and the intrinsic properties of the Device Under Test (DUT). Specifically, M denotes the measured scattering matrix of the DUT, referenced to the system's measurement planes. The matrices X and Y account for systematic errors introduced upstream and downstream of the DUT, respectively, due to imperfections in the measurement setup—such as connectors, adapters, or cables. The term T_{DUT} represents the true response of the DUT, corrected for these systematic errors.

$$M = X \cdot T_{DUT} \cdot Y \quad (2)$$

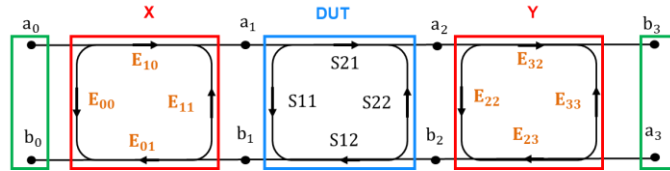


Fig. 3: Two-port measurement model.

4 Experimental Results

The measurements are carried out using an on-wafer probe station connected to a Rohde & Schwarz ZVA67 Vector Network Analyzer (VNA) equipped with millimeter-wave extenders (Fig. 4), operating over the frequency range of 250 MHz to 110 GHz. The VNA output power and the intermediate frequency (IF) bandwidth are set to -15 dBm and 50 Hz, respectively. Ground-signal-ground (GSG) Infinity IXT110 probes from FormFactor are used. The ambient temperature is maintained and actively controlled at approximately 23 °C throughout the measurements.

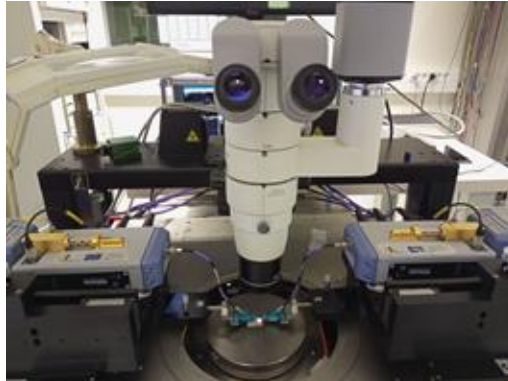


Fig. 4: Experimental measurement setup.

Uncalibrated measurements were performed on both CPW structures with conventional and nanoscale dimensions. The raw S-parameter data were subsequently processed using both standard TRL and multiline TRL calibration techniques [10]. The multiline TRL approach employed nine transmission lines with lengths ranging from 200 μm (serving as the thru standard) to 2250 μm , along with a short-circuit reflect standard positioned at the center of the thru.

In metrological applications, it is essential to identify and evaluate fluctuations in measurement results. Accordingly, the influence of different sets of transmission lines on the determination of the propagation constant and derived parameters was analyzed in order to ensure measurement accuracy and robustness.

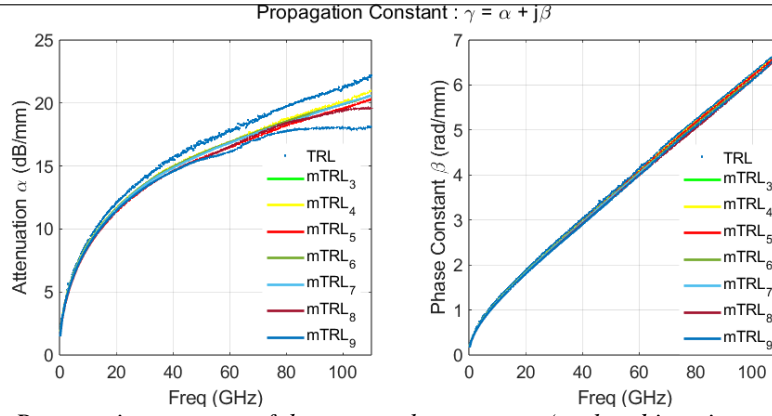


Fig. 5: Propagation constant of the nanoscale structures (real and imaginary parts).

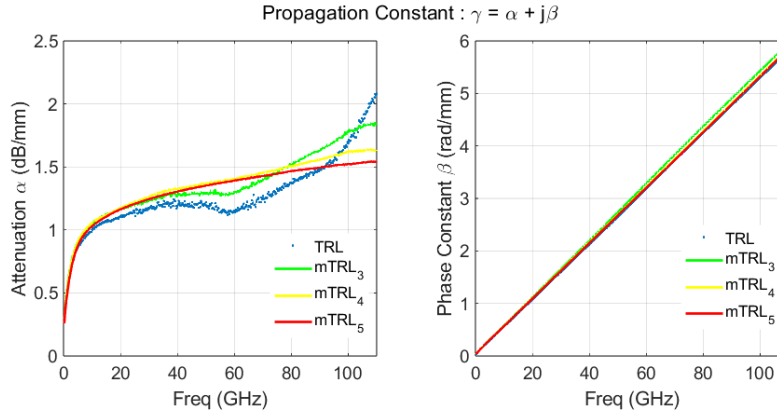


Fig. 6: Propagation constant of the microscale structures (real and imaginary parts).

Figures 5 and 6 present the propagation constants of the nanoscale and microscale CPW structures, respectively. In both cases, the multiline TRL (mTRL) method demonstrates superior precision, particularly when a sufficient number of transmission lines is used. From low frequencies up to approximately 20 GHz, the attenuation constant α obtained using both TRL and mTRL methods is nearly identical; however, notable discrepancies emerge at higher frequencies. These deviations in attenuation are primarily attributed to the increasing influence of measurement noise and dispersion phenomena. In contrast, the phase constant remains practically unaffected, showing excellent agreement across methods. This consistency is also reflected in the effective permittivity, derived from Equation (1), which is used to identify the minimum and maximum values for further analysis.

In addition to experimental characterization, electromagnetic simulations are performed using both Keysight Advanced Design System (ADS) and an analytical approach. The latter is based on the Heinrich model, which analytically describes coplanar waveguides (CPWs) by incorporating cross-sectional dimensions—such as the signal line width (W), gap (G), ground width (W_g), and metal thickness (t)—along with material properties like conductor conductivity (σ) and substrate permittivity (ϵ_r). This enables the calculation of the distributed transmission line parameters: per-unit-length resistance (R), inductance (L), capacitance (C), and conductance (G) [11]. Recent developments have extended the Heinrich model by including additional physical effects such as surface roughness, radiation losses, and frequency-dependent dispersion to improve agreement with experimental data [12], [13], [14].

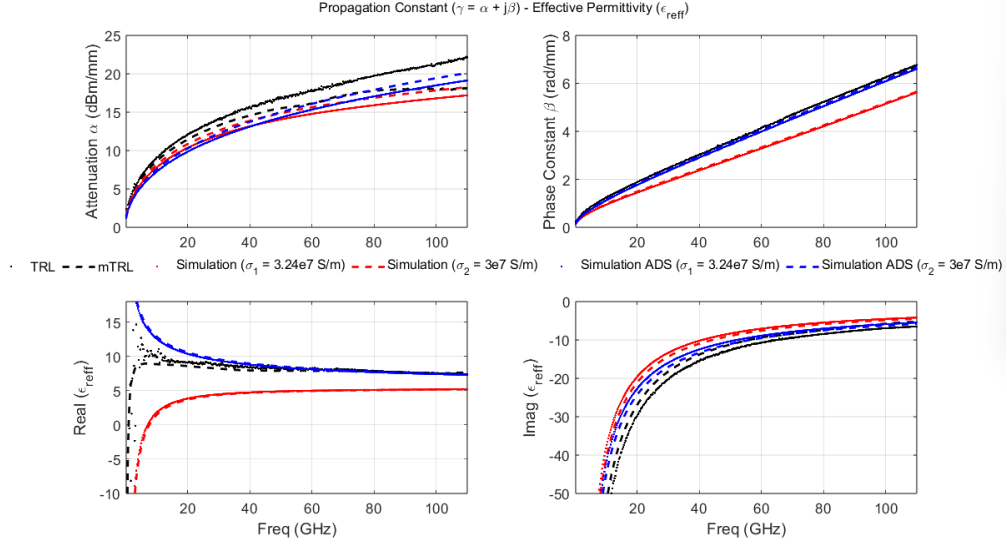


Fig. 7: Propagation constant and effective permittivity of the microscale structures (real and imaginary parts).

The measured DC conductivity ($\sigma=3.24\times 10^7$ S/m) and the theoretical value ($\sigma=3\times 10^7$ S/m) were incorporated into the simulations. The propagation constant and effective permittivity, experimentally extracted using TRL and multilayer TRL methods, were compared with those obtained from both ADS and analytical simulations (Fig. 7). The comparison reveals notable discrepancies, particularly in the attenuation constant, despite the use of an advanced CPW model that accounts for radiation and dispersion effects. These deviations highlight the limitations of existing models and the sensitivity of attenuation to complex frequency-dependent phenomena.

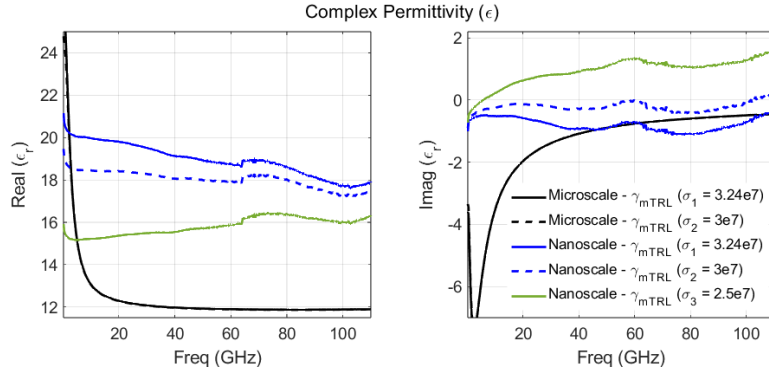


Fig. 8: Extracted complex permittivity of the micro and nanoscale structures.

The quasi-TEM analytical model proposed in [11] enables the determination of the distributed parameters—resistance (R), inductance (L), capacitance (C), and conductance (G)—of a CPW TL, based on the cross-sectional geometry, metal conductivity (σ), relative permittivity (ϵ_r), and loss tangent ($\tan\delta$) of the substrate. By combining the analytically derived values of R and L with the experimentally measured propagation constant γ , it is possible to extract the per-unit-length capacitance C_m and conductance G_m , as described in Equation (3) and discussed in [15], [16].

$$G_m + i\omega C_m = \gamma^2 / (R + j\omega L) \quad (3)$$

With the values of C_m and G_m determined, it becomes possible to calculate the relative permittivity ϵ_r and the loss tangent $\tan\delta$, using Equations (4) and (5). These expressions incorporate the factors F_{low} and F_{up} , which are derived from the analytical model introduced in [11].

$$\epsilon_r = \frac{C_m}{2\epsilon_0 F_{low}} - \frac{F_{up}}{F_{low}} \quad (4)$$

$$\tan\delta = \frac{G_m}{2\omega\epsilon_0\epsilon_r F_{low}} \quad (5)$$

Following this procedure, the complex permittivity of the substrate was evaluated for both micro- and nanometric scale structures. Three conductivity values were considered in the analysis: the first, $\sigma_1=3.24\times 10^7$ S/m, was obtained from direct current (DC) measurements performed on the nanostructures, while the other two— $\sigma_2=3.00\times 10^7$ and $\sigma_3=2.50\times 10^7$ S/m— correspond to theoretical assumptions.

Figure 8 presents the extracted complex permittivity ϵ_r . The complex permittivity of the silicon substrate is determined following the methodology described in [15], [16], with the real part estimated at approximately 11.89. However, when this same approach is applied to nanometric structures, the extracted permittivity deviates from the expected value. Specifically, a real part ranging between 15.17 and 16.34 is observed (see Fig. 8). This discrepancy may be attributed, on the one hand, to differences in cross-sectional aspect ratios between micro- and nanometric structures, as outlined in Heinrich’s analytical model [11]. On the other hand, deviations may also result from fabrication-induced variations that affect the electrical characteristics of the transmission line. The characteristic impedance is determined from the propagation constant γ , linear capacitance C_m and linear conductance G_m .

$$Z_c = \frac{\gamma}{(G_m + j\omega C_m)} \quad (6)$$

In addition, the model described in [17], combined with 3D electromagnetic simulations performed using CST Microwave Studio, allows for the calculation of theoretical per-unit-length capacitance and conductance values for both micro- and nanometric CPW transmission lines. Based on [17], capacitance values of 164.208 pF/m and 125.698 pF/m are obtained for the micro- and nanometric structures, respectively. The corresponding CST simulation results yield capacitances of 168 pF/m for the micrometric line and 142 pF/m for the nanometric line. It is worth noting that the linear conductance term can be neglected in both cases, as $G \ll \omega C$.

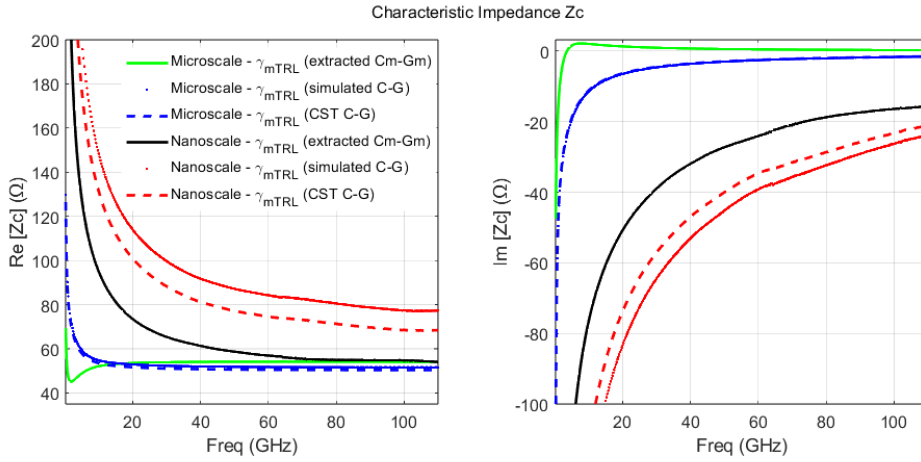


Fig. 9: Characteristic impedance of the micro and nanoscale structures.

The measured propagation constants are associated to the values of capacitance obtained from [15], [16], [17] and CST simulations to derive the characteristic impedance. For micro CPW TL, the impedance at 110 GHz is 54 Ω against 51.6 and 50.37Ω of CST and analytical capacitance. It is coherent with respect to relation (6) because in reality there are phenomena such as dispersion and radiation that can influence the distributed elements ($RLCG$) of the line. Similarly, there is a significant difference in the impedance of the nano CPW line, 54.04 Ω against 77.36 and 68.48Ω at 110 GHz. This disparity is due to the lack of perfect control of linear capacity. At least this approach makes it possible to determine impedance.

The mTRL approach enables the correction of raw measurement data for various DUTs, including reflective structures and selected TLs. As illustrated in Fig. 10, it becomes evident that using long transmission lines at the nanoscale is not advantageous due to significant losses and attenuation. Specifically, the transmission coefficient

S_{21} decreases substantially with increasing line length, highlighting the impact of conductor and dielectric losses at these scales.

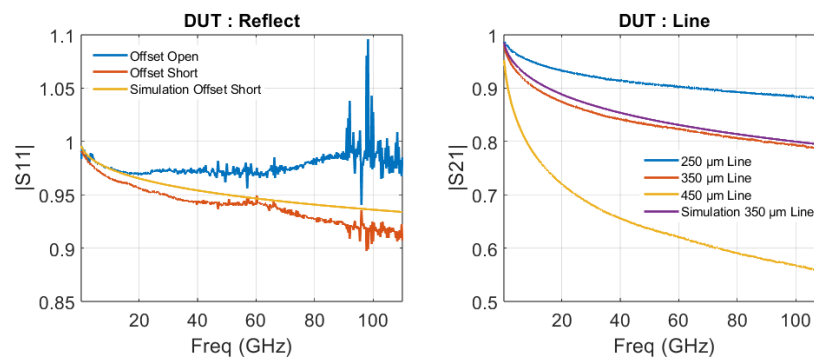


Fig. 10 Corrected S -parameters of Reflects and Lines at nanoscale.

As shown, the reflection responses (S_{11}) of the open and short circuits are more susceptible to fluctuations. These two reflect standards are defined at a distance of $15\ \mu\text{m}$ from the thru standard and are particularly sensitive to probe positioning and movement. For this reason, they are considered uncertainty-prone structures. Consequently, their behavior is of particular interest when assessing the overall uncertainty budget of the measurement process.

5 Conclusion

The propagation characteristics—including the propagation constant, effective and complex permittivity, and characteristic impedance—were evaluated for two coplanar waveguide structures with distinct dimensions: one at the nanometric scale and the other at the micrometric scale. This study reveals notable differences between the two configurations, particularly a significant increase in dielectric losses and more pronounced attenuation in the nanometric lines. It demonstrates the feasibility of establishing a correlation between theoretical models and experimental results for the characterization of coplanar transmission lines. However, the findings also emphasize the limitations of classical analytical models, which fail to fully capture the physical phenomena emerging at nanometric scales. This work thus provides a meaningful contribution toward the development of new calibration standards adapted for high-frequency characterization of nanoscale devices.

Acknowledgement

This project (BELC157) has received funding from the Réseau National de la Métrologie Française (RNMF) and from the Association Nationale de la Recherche et de la Technologie ANRT under grant 2022/0073. This work was supported in part by the Frech Renatech network.

References

- [1] S. H. Happy, K. Haddadi, D. Theron, T. Lasri and G. Dambrine, "Measurement Techniques for RF Nanoelectronic Devices: New Equipment to Overcome the Problems of Impedance and Scale Mismatch," in *IEEE Microwave Magazine*, vol. 15, no. 1, pp. 30-39, Jan.-Feb. 2014.
- [2] C. Mokhtari *et al.*, "Nanorobotics and Automatic On-Wafer Probe Station with Nanometer Positioning Accuracy," *2023 IEEE MTT-S International Conference on Numerical Electromagnetic and Multiphysics Modeling and Optimization (NEMO)*, Winnipeg, MB, Canada, 2023, pp. 22-24.
- [3] Seck, Daouda, Djamel Allal, and Kamel Haddadi. "On-Wafer TRL Calibration Design for Microwave Nanoscale and High Impedance Measurement." *2024 IEEE Symposium on Wireless Technology & Applications (ISWTA)*. IEEE, 2024.
- [4] D. J. Bannister and D. I. Smith, "Traceability for on-wafer CPW S -parameter measurements," *IEE Colloquium on Analysis, Design and Applications of Coplanar Waveguides*, London, UK, 1993, pp. 7/1-7/6.
- [5] Arz, Uwe. "Traceability for On-Wafer S -Parameter Measurements." *Workshop Determining Accuracy of Measurements at High Frequencies—from Error to Uncertainty, 37th European Microwave Conference*. 2007.

- [6] Arz, Uwe, et al. "Traceable coplanar waveguide calibrations on fused silica substrates up to 110 GHz." *IEEE Transactions on Microwave Theory and Techniques* 67.6 (2019): 2423-2432.
- [7] Engen, G. F., & Hoer, C. A. (1979). Thru-reflect-line: An improved technique for calibrating the dual six-port automatic network analyzer. *IEEE transactions on microwave theory and techniques*, 27(12), 987-993.
- [8] Marks, R. B., & Williams, D. F. (1991). Characteristic impedance determination using propagation constant measurement. *IEEE Microwave and guided wave Letters*, 1(6), 141-143.
- [9] Williams, D. F., & Marks, R. B. (1991). Transmission line capacitance measurement. *IEEE Microwave and guided wave letters*, 1(9), 243-245.
- [10] Hatab, Ziad, Michael Gadringer, and Wolfgang Bösch. "Improving the reliability of the multiline tml calibration algorithm." *2022 98th ARFTG Microwave Measurement Conference (ARFTG)*. IEEE, 2022.
- [11] Heinrich, W. (1993). Quasi-TEM description of MMIC coplanar lines including conductor-loss effects. *IEEE transactions on microwave theory and techniques*, 41(1), 45-52.
- [12] Gold, Gerald, et al. "High-frequency modeling of coplanar waveguides including surface roughness." *Advances in Radio Science* 17 (2019): 51-57.
- [13] Schnieder, Frank, Thorsten Tischler, and Wolfgang Heinrich. "Modeling dispersion and radiation characteristics of conductor-backed CPW with finite ground width." *IEEE Transactions on Microwave Theory and Techniques* 51.1 (2003): 137-143.
- [14] Phung, G. N., et al. "Improved modeling of radiation effects in coplanar waveguides with finite ground width." *2020 50th European Microwave Conference (EuMC)*. IEEE, 2021.
- [15] U. Arz and J. Leinhos, "Broadband Permittivity Extraction from On-Wafer Scattering-Parameter Measurements," 2008 12th IEEE Workshop on Signal Propagation on Interconnects, Avignon, France, 2008, pp. 1-4, doi: 10.1109/SPI.2008.4558382.
- [16] U. Arz and D. F. Williams, "Uncertainties in complex permittivity extraction from coplanar waveguide scattering-parameter data," 81st ARFTG Microwave Measurement Conference, Seattle, WA, USA, 2013, pp. 1-6, doi: 10.1109/ARFTG.2013.6579047.
- [17] <https://wcalc.sourceforge.net/cgi-wcalc.html>

Mesurer les ondes millimétriques pour la radioastronomie *Millimeter-wave radioastronomy measurement challenges*

*Christophe Risacher*¹

¹IRAM, risacher@iram.fr

Radioastronomie, THz, millimeter waves, calibration

Résumé/Abstract

La radioastronomie dans les longueurs d'onde millimétriques est un domaine qui a vu le jour il y a plus de 50 ans. Les techniques ont évolué avec le temps pour atteindre des sensibilités sans précédent. Pour obtenir une résolution spectrale extrêmement élevée, la spectroscopie est réalisée à l'aide de techniques hétérodynes. Les composants cryogéniques critiques utilisent des mélangeurs supraconducteurs et des amplificateurs très faible bruits. Un aperçu de l'état de l'art dans ce domaine sera fourni, ainsi que les perspectives pour la future génération d'instruments. Une discussion sur les techniques de mesure et d'étalonnage sera également fournie, montrant les nombreux défis auxquels il faut faire face lors de la mesure de signaux extrêmement faibles dans le régime millimétrique.

Radioastronomy in the millimeter wavelengths is a field that started more than 50 years ago. Techniques have evolved with time to reach unprecedented sensitivities. To achieve extremely high spectral resolution, spectroscopy is achieved using heterodyne techniques. The critical cryogenic components are using superconducting mixers and amplifiers. An overview of the state of the art in this field will be provided together with the perspective for future generation of instruments. A discussion on the measurement techniques and calibration will also be provided, showing the many challenges that are faced when measuring extremely weak signals in the millimeter regime.

1 Introduction

Millimeter radioastronomy usually refers to observations performed between 1 mm to 4 mm wavelengths, or equivalently between 70 GHz and 300 GHz. This area of astronomy is crucial to understand better the life-cycle of stars, where this wavelength allows better probing the cold universe.

Within this field, there exists different instrumentation families. The first allows to measure large RF bandwidths with low to moderate spectral resolution. Such instruments are called continuum instruments, using technologies such as Ge:Ga photoconductors, NTD Ge bolometers, superconducting transition edge sensors (TES) or more recently superconducting microwave kinetic inductors (MKID). This technology has reached a level of maturity where thousands of pixels can populate large arrays, performing efficient mapping.

The second type of instruments using coherent detectors allow achieving extremely high resolution, in particular this permits to extract kinematics information of the atomic or molecular emission/absorption lines. In this work, we will restrict ourselves to this field, using heterodyning techniques to allow very high-resolution spectral measurements. More information on both type of instrumentation can be found in [1].

2 Heterodyne receivers for millimeter astronomy

To be able to measure frequencies between 70-300 GHz, historically observatories have used Schottky mixers, cryogenically cooled to improve the sensitivities. Figure 1 shows a schematic of a representative receiver for millimeter waves, using a mixer as first active component in the system. A local oscillator reference signal is needed to allow mixing the RF input down to intermediate frequencies (IF), in the microwave range where commercial components allow further processing.

In the 1980s, development of superconductor-insulator-superconductor junctions (SIS) allowed to improve drastically the performance [2]. Indeed, compared to the best Schottky mixers available at the time, sensitivities were improved by an order or magnitude. Figure 2 shows typical layout of a SIS junction and how it is incorporated onto a quartz chip, with RF tuning circuit and antenna to couple the RF signal from the waveguide to the SIS junction. It is interesting also to note the progress done at IRAM. Some of the first SIS mixers used movable backshorts in the 1990s to allow single band operation (Figure 3 - left). Now, SIS mixers use much more complex architecture, performing sideband separation without movable backshorts, using several junctions, with input RF hybrid and output IF hybrids, all integrated into a single mixer block (Figure 3 - right).

Very recently, in 2020 [3], high electron mobility transistors (HEMTs) have equaled the SIS mixers in term of noise performance up to 115 GHz and work is ongoing to push further in frequency their performance [Manchester?].

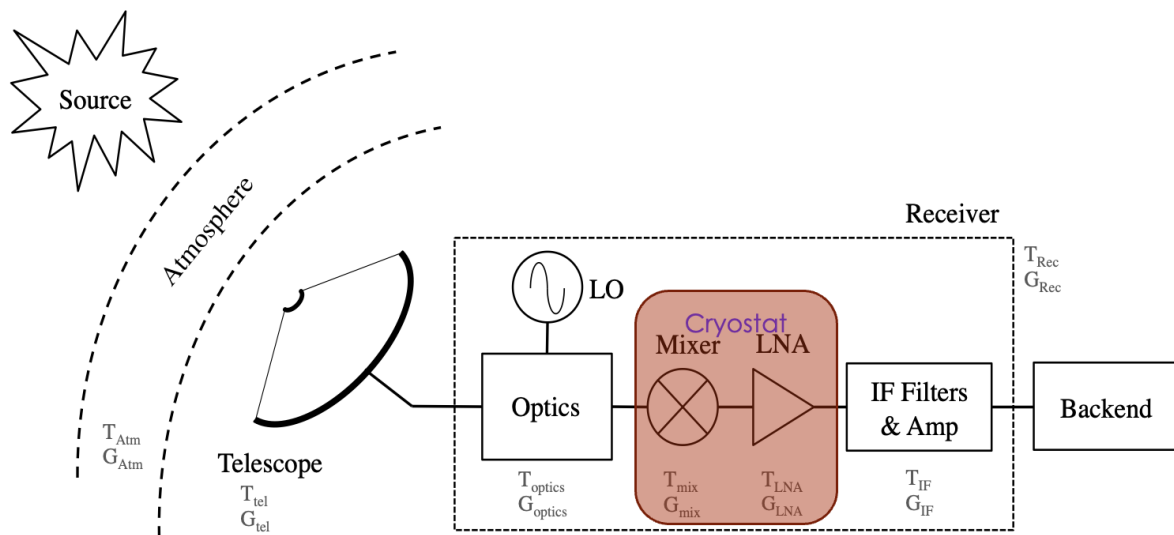


Figure 1: Schematic of a heterodyne receiver. Usually, a cryostat is used to cool down the critical components, the mixer and the low noise amplifier.

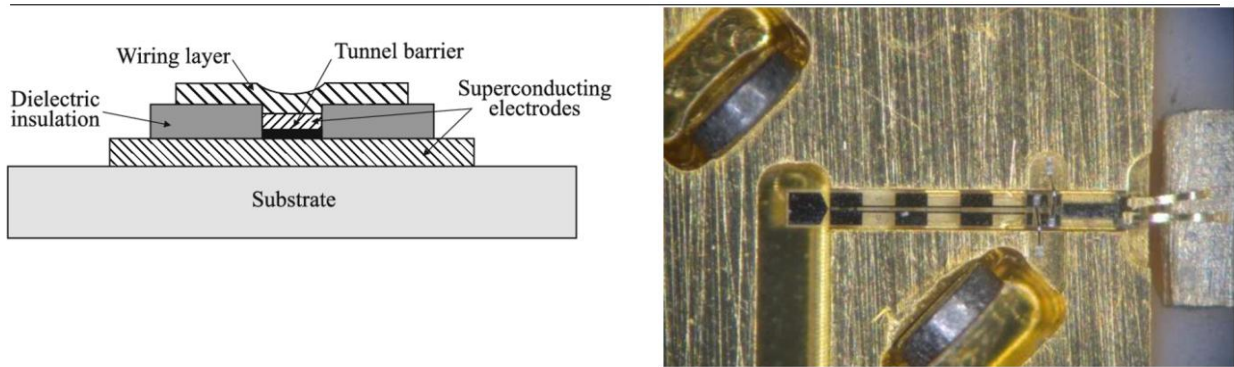


Figure 2: Left: SIS mixer cross section view. Right: SIS mixer on a quartz substrate integrated into a mechanical block.

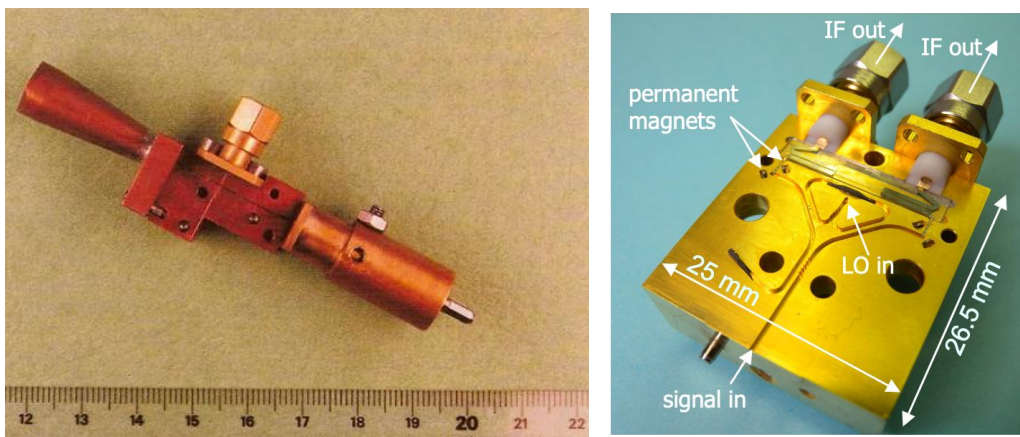


Figure 3: Left: View of a single sideband SIS mixer at used at IRAM in the 1990s. Right: current generation of sideband separating SIS mixer, integrating all components in one mechanical block with no movable parts

3 Measurement techniques for millimeter astronomy

To characterize the millimeter wave receivers, several steps are usually performed.

Component level

All components are usually characterized individually before their integration into the full system. For the optical elements, mirrors, RF windows/filters, dichroics and corrugated horns, they are characterized using beam measurement setups of varying complexity. Typically, beam direction and characteristics are measured in those setups using a motorized X-Y stage. The emitter is usually an RF signal in the millimeter range of interest, using Gunn oscillators or harmonic mixers driven by low frequency synthesizers. The measurement setups allow to recover both the phase and amplitude of the signal.

For some individual components, S-parameters measurements can be performed using commercial and customized vector network analyzers. IRAM has built in the early 2000s several frequency extenders for a PNA-X VNA, exactly adapted for our frequency bands of interest (see for example Figure 4). For example, the band 70-116 GHz that we use on our observatories is not coinciding perfectly with the commercial W-band, where extenders cover only 75-110 GHz.

Losses estimation for some components can be achieved with more accuracy than using the VNAs, by using a test SIS receiver. We perform noise temperature measurement of the test receiver with and without the device under test (DUT) placed at the receiver input. Difference of the receiver noise temperature between measurements will allow estimating a more precise loss value for the DUT. Typically, better than 0.5% accuracy can be achieved as opposed to about 3-5% with VNA S-parameter S₂₁ measurements.



Figure 4: Measurement in reflection of an IRAM dichroic, using custom made frequency extenders connected to a PNA-X vector network analyzer.

Full system characterization:

With the full instrument assembled, before its installation on a telescope, the final characterization is performed in the laboratory (see Figure 5) and then a technical commissioning on site is typically performed (Figure 6).

- Laboratory characterization:
 - Noise temperature determination of the full system – can be limited to the receiver with input optics but can also include the full representative backend and corresponding IF pre-processing, if available. The receiver operation when looking at the cold sky at various weather conditions should always be linear. Therefore, the calibration procedure consists of:
 - Cold load measurement – historically done at 77K using an absorber dipped into liquid Nitrogen
 - Hot load measurement – historically done at 290K using an absorber at room temperature
 - Having two independent measurements at distinct temperatures allow then to calibrate the sky observations using these two sets of data. The assumption is that the receiver behaves linearly between those two measurements, which is usually the case. Nowadays, the cold/hot temperatures can be quite different than what was mentioned earlier. Several observatories, for simplicity, use a hot and hotter load (for example 290K and ~380K – heated load). In those cases, linearity issues are more likely and must be considered.
 - Optics verification: with the beam measurement setups, final adjustment of the beam alignment and verification of the beam quality of the full system are performed.
 - Tuning table preparation: During this measurement session, usually many tuning points are prepared to fully optimize the receiver performance. The SIS mixer bias setting, DC voltage and pumping levels are determined. At IRAM, we usually provide tuning tables every 0.5 GHz step. Major difficulty is to avoid spurs or spurious signal within our intermediate frequency band (IF). Therefore, this tuning step ensures that we will have clean bandpass.
 - Receiver stability and standing waves: The final verification and tuning optimization also ensures that the receivers is stable enough for deep integrations and that the receiver bandpass is exempted from large standing waves, which would also hinder observation of weak lines.



Figure 5: In the Grenoble laboratories, the full receiver is installed in the same support frame which will then be connected to the telescope receiver cabin interface ring. Full characterizations are performed in this configuration. Detail of the receiver design can be found in [4]

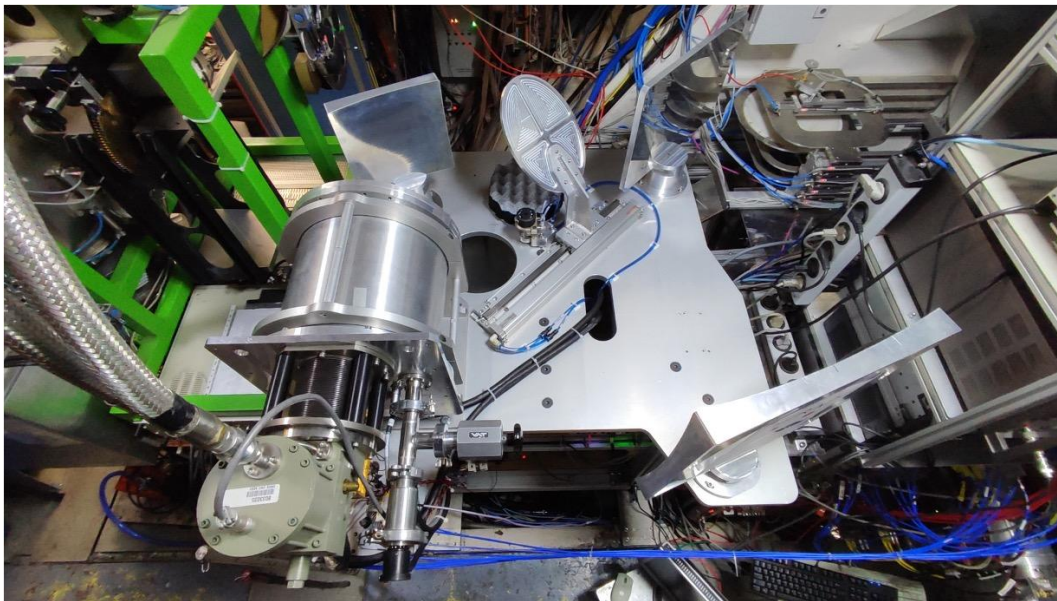


Figure 6: Example of installation of a receiver on a telescope. In this case, a 1x3 W-band HEMT receiver is installed at the 30m IRAM telescope in southern Spain for a test campaign.

- On-site technical commissioning:
 - One the receiver system is installed on site, before releasing it to the scientific community, final verifications and characterizations are needed. This will verify the laboratory measurements, but more importantly will verify that in its final configuration and environment, no surprises are present, such as RFI or standing waves from the telescope optics.
 - Optical alignment is crucial. Verification on site will allow to verify that the RF beam is well centered on the telescope optical axis. If not, this will translate into efficiency losses, pointing offsets which can also produce beam aberrations.
 - The cold/hot calibration ate usually performed every 20 minutes, allowing to measure the receiver noise temperature and those measurement allow the sky observations to be calibrated. For the proper signal calibration, a SKY measurement will be needed (not looking at the scientific source, but close-by). This will allow determining the atmospheric contributions, atmospheric features, opacity, allowing to derive the precipitable water vapour (PWV).
 - Before the observations, the telescope should also be well focused and pointed, to allow achieving the best signal to noise and accurate observations.

4 Perspectives

We have provided a short overview of the state-of-the-art instrumentation used for very high-resolution spectroscopy in millimeter waves and some of the measurement techniques. For the instrumentation evolution in the near future:

- HEMT cryogenic amplifiers highest frequencies of operation have finally reached the ~100 GHz range where they can achieve comparable performance as SIS mixers. Work is undergoing to push this frequency limit to 200 or 300 GHz range.
- Other components are being studied for the past 20 years, such as superconducting traveling wave amplifiers (KID or Josephson mixer based), with the promise of event lower sensitivities.
- As current components are almost quantum noise limited, efforts can also be placed into more complex architectures, for example balanced sideband separation mixers.
- Integration of multi-pixel arrays is progressing, though still at a low pace. Compared with continuum instrumentation which already use thousands of pixels, heterodyne receivers only successfully demonstrated tenths of pixels.

For the measurement techniques, historically millimetre wave astronomical instrumentation needed to develop its own method and tools to characterize the components. With the commercial advent of millimetre waves (and THz in general), commercial products are spreading very quickly and will therefore allow easier and cheaper measurement for our field. Only drawback is that the commercial W-band (75-110GHz), D-band (110-170 GHz) and H-band (220-330 GHz) do not overlap so well with our receiver frequency bands (70-116 GHz, 125-180 GHz, 200-280GHz).

References

- [1] T. Wilson, et al. “Tools of Radio Astronomy”, 2013 DOI 10.1007/978-3-642-39950-3.
- [2] J. Tucker, M. Feldman “Quantum detection at millimeter wavelengths”. In: *Reviews of Modern Physics* 57.4, pp. 1055–1113, Oct. 1985. doi: [10.1103/RevModPhys.57.1055](https://doi.org/10.1103/RevModPhys.57.1055).
- [3] P. Yagoubov, et. al. “Wideband 67-116 GHz receiver development for ALMA Band 2”, *A&A*, 634:A46, Feb. 2020. doi: 10.1051/0004-6361/201936777.
- [4] J.-Y. Chenu, et al. “The Front-End of the NOEMA Interferometer”, *IEEE Transactions on Terahertz Science and Technology*, Year: 2016, Volume: 6, Issue: 2

Station de Mesure on-Wafer Nano-Robotisée Assistée par IA : Automatisation, Précision et Évaluation des Performances

AI-Enhanced Nano-Robotic Wafer Measurement Station: Automation, Precision, and Performance Evaluation

Clément Lenoir¹, Mohamed Sebbache¹, Daouda Seck^{1,2}, Djamel Allal², Kamel Haddadi¹

¹Univ. Lille, CNRS, Centrale Lille, Univ. Polytechnique Hauts-de-France, UMR 8520 - IEMN - Institut d'Électronique de Microélectronique et de Nanotechnologie, IRCICA USR-3380, F-59000 Lille, France
[\[kamel.haddadi@univ-lille.fr\]](mailto:kamel.haddadi@univ-lille.fr)

²Laboratoire National de Métrologie et d'Essais, Paris, France.

Mots clés: Mesures sous pointes hyperfréquences, Calibration, Nano-robotique, Intelligence artificielle
Index Terms: Microwave on-wafer measurements, Calibration, Nano-robotics, Artificial intelligence

Résumé/Abstract

This work presents a nano-robotic on-wafer probe station integrating an AI-assisted vision system to optimize probe alignment and enhance measurement precision. Machine vision algorithms optimize probe positioning, reduce measurement errors, and enhance reproducibility. Real-time image data processing and pattern matching enable adaptive calibration for robust performance under varying conditions. Preliminary results show significant improvements in speed and accuracy over conventional RF methods. This approach offers a next-generation solution for precise on-wafer RF measurement.

Ce travail présente une station de mesure sous-pointes nano-robotisée intégrant un système de vision assistée par IA, permettant des mesures entièrement automatisées et de haute précision. Des algorithmes de vision par ordinateur optimisent le positionnement des sondes, réduisent les erreurs de mesure et améliorent la répétabilité. Le traitement en temps réel des images et la reconnaissance de motifs permettent une calibration adaptative pour une performance robuste dans des conditions variables. Les résultats préliminaires montrent des améliorations significatives en termes de rapidité et de précision par rapport aux méthodes conventionnelles. Cette approche constitue une solution de nouvelle génération pour la mesure RF de précision sous-pointes.

1 Introduction

High-frequency characterization of micro- and nano-electronic devices relies on on-wafer RF probe stations. Traditionally, these stations are manually operated or semi-automated, making measurements prone to alignment errors, operator-dependent accuracy, and difficult-to-control variability. These limitations become critical as device complexity increases, operating frequencies rise, and industrial demands grow for precision, repeatability, and automation.

Over the last two decades, the semiconductor industry has witnessed a continuous trend toward device miniaturization, in accordance with Moore's Law and beyond. Today's integrated circuits routinely incorporate components with sub-10 nm features and operate at millimeter-wave and even terahertz frequencies. This scaling down has pushed the performance envelope but also magnified the sensitivity of RF measurements to even the slightest misalignment or probing error. As a result, traditional probe stations—designed for larger, less sensitive structures—struggle to meet the precision and repeatability required at these scales. Simultaneously, the demand for high-throughput and highly reproducible characterization has grown with the advent of 5G, 6G, advanced radar systems, quantum computing, and heterogeneous integration platforms. These technologies impose strict constraints on RF measurement uncertainty, especially in scenarios where impedance mismatches or parasitic effects can significantly distort results. Manual or semi-automated stations are increasingly becoming bottlenecks in terms of speed, accuracy, and operational consistency.

Manual probe positioning leads to variability in alignment, increased measurement errors, and limited reproducibility [1], [2]. The process is time-consuming, requiring skilled technicians to ensure proper calibration and probing accuracy. Furthermore, such setups lack adaptability for the delicate probing of advanced high-

frequency devices, where fine RF quantities need to be reliably extracted [3], [4]. These shortcomings highlight the urgent need for a fully automated, high-precision solution.

In this context, the integration of advanced technologies such as nano-robotics, computer vision systems, and artificial intelligence offers a promising alternative. These technologies not only automate repetitive and delicate tasks but also significantly improve alignment precision and result reliability. Through real-time image recognition and pattern analysis, probe positioning can be dynamically optimized, reducing human errors and operator-induced variability.

To address these challenges, we present a fully automated on-wafer probe station that integrates nano-positioners and an AI-assisted machine vision system. The system enables automatic calibration based on advanced image recognition algorithms and precise detection of probe-to-substrate contact. This paper describes the mechanical and software architecture of the station, the operation of the vision system, the positioning algorithms, and preliminary experimental results using an ISS 101-190-C impedance standard.

2 Architecture of the Measurement Station

2.1 Overview of the Architecture

The proposed measurement station is a fully automated platform designed for high-precision RF probing, with a particular focus on Ground-Signal-Ground (GSG) alignment. This system is built from scratch. The station integrates various components, each serving a distinct function but all contributing to the seamless operation of the measurement process. These components include two independently controlled probe arms, a nano-robotized wafer chuck, piezoelectric nanorobotic positioners, and an advanced optical and mechanical setup [5][6] [7] [8].

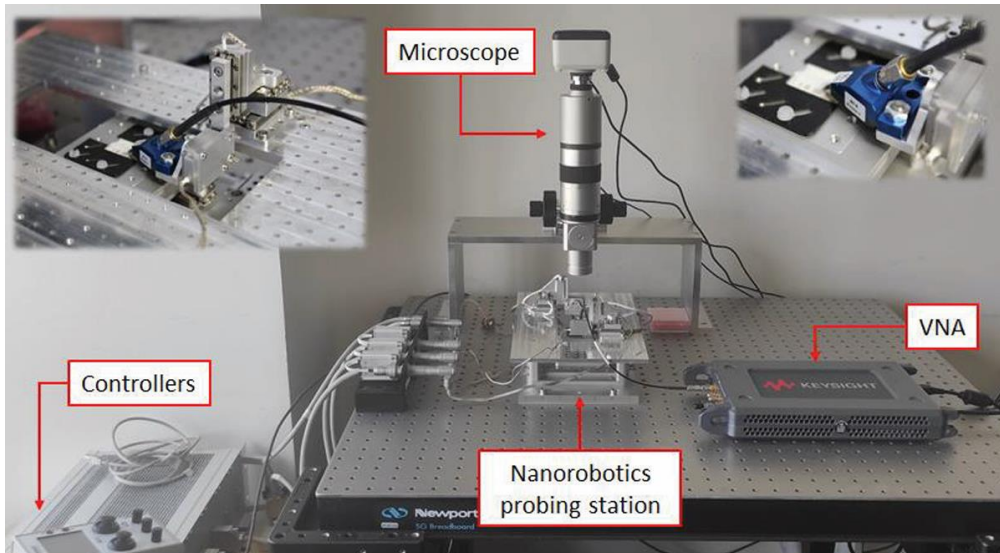


Figure 1. Nano-robotic on-wafer RF probe station.

The mechanical base of the station is a Newport® M-VIS3036-SG2-325A optical table, with volume $750 \times 900 \times 59 \text{ mm}^3$, equipped with pneumatic isolators that offer horizontal and vertical isolation at 5 Hz and 10 Hz, respectively, ensuring 90% and 98% vibration isolation. This feature is crucial in mitigating building vibrations and enhancing the overall stability of the measurement process.

At the heart of the measurement process, a Keysight® 5008A Streamline Series USB Vector Network Analyzer (VNA) is used to measure S-parameters across a frequency range from 100 kHz to 53 GHz. The compact design of the Streamline VNA facilitates its integration directly onto the optical table, minimizing cable lengths and reducing associated measurement uncertainties. The system leverages LabVIEW® for full automation, providing seamless control over the measurement process. Flexible MegaPhase® UltraPhase cables, with a 30 cm length and an operating frequency of up to 67 GHz, are used to connect the VNA to the probes. These cables are chosen for their light weight, flexibility, and minimal signal attenuation, ensuring that no excessive tension is applied to the positioners.

To assist with precise probe-to-pad alignment, a Moticam® CAM-1080P HDMI camera, with 2 MP resolution and 60 frames per second at 1080p, is mounted above the probing area. This camera, coupled with a Moticam dedicated software, enables real-time image acquisition and facilitates calibration for dimensional measurements. Additionally, a Moticam OP-Z10 Zoom Microscope, offering optical magnification from 0.85x to 8.5x, provides detailed visual feedback for probe positioning, with a resolution down to 2.5 μm . A SmarAct® MCS2 controller coordinates the positioning system, with closed-loop control providing high precision. The system includes a total of 11 stages for controlling the probe arms and chuck, enabling fine-tuned adjustments in both translation and rotation. Furthermore, custom attachment pieces, designed using SolidWorks®, ensure secure mounting of FormFactor® Infinity GSG probes onto the positioners, addressing the mechanical challenges posed by the probes' geometry.

2.2 Nano-robotic Actuation System

The measurement station employs SmarAct® piezoelectric nano-positioners, specifically selected for their resolution, repeatability, and compact design. These nano-positioners, crucial for high-precision RF probing, are employed in the control of both the probe arms and the chuck. Each probe holder is mounted on a stack of SmarAct stages, enabling precise control along the X, Y, Z, and θ axes. Meanwhile, the chuck is positioned using three stages—two linear and one rotational—providing three degrees of freedom (DoF) in X, Y, and ϕ axes. The probes themselves are mounted on four stages—three linear and one rotational—allowing four degrees of freedom (DoF) in X, Y, Z, and θ axes.

The SmarAct stages used in the system are part of the SLC and SR series, specifically designed for closed-loop operation with integrated capacitive sensors, ensuring sub-nanometer resolution. The linear stages, such as the SLC-17 and SLC-24 models, provide exceptional rigidity and straightness, with travel ranges of 16–21 mm and resolution down to 1 nm. For rotational motion, the SR series stages provide continuous, unrestricted rotation, with resolutions of 25 μ° for the probe stages and 15 μ° for the chuck.

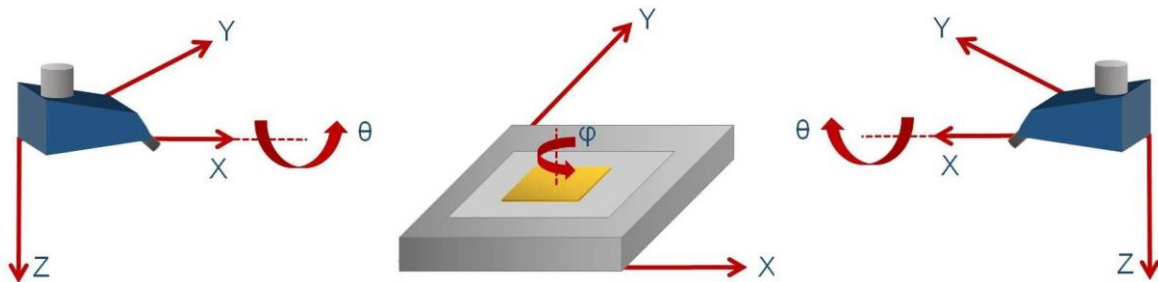


Figure 2. Visualization of the 11 nano-positioners DOFs.

This setup ensures that the system achieves high precision in positioning, essential for repeatable and accurate RF measurements. With closed-loop control, the nano-positioners can maintain stable positioning over extended periods, even when subject to external factors such as cable tension or mechanical vibrations.

2.3 Description of the ISS 101-190-C Standard

The ISS 101-190-C calibration substrate, developed by FormFactor®, is widely recognized in the RF metrology community for its precision and reliability. It is designed to facilitate Short-Open-Load-Thru (SOLT) calibrations in coplanar waveguide (CPW) configurations, offering well-defined reference structures, clearly marked alignment targets, and consistent geometries that are essential for automated vision-based detection and alignment.

In our station, the automation for alignment and calibration is currently limited to the use of the ISS 101-190-C substrate. This approach was chosen for simplicity and reproducibility, enabling smooth integration with the existing positioning and control systems. The ISS 101-190-C provides a standardized and well-documented interface, making it easier to automate the calibration process.

2.4 Software Control and Automation

LabVIEW™ serves as the central hub for the automation process, managing the entire sequence of operations from image recognition to positioner movements and VNA control. The automated system operates as follows:

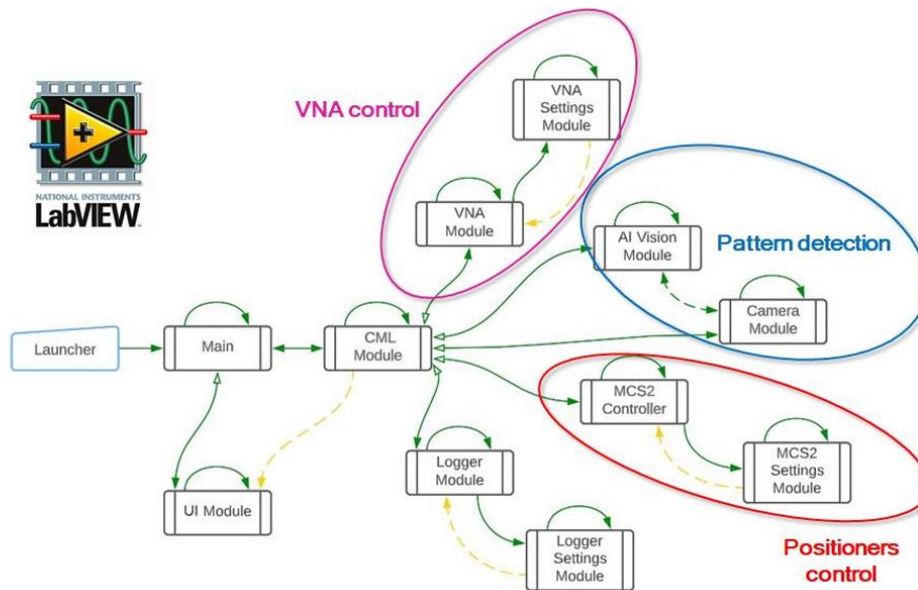


Figure 3. LabVIEW algorithm modules tree.

Image Recognition and Positioning: The first step in the process is pattern detection, which is achieved using a combination of the camera module and the AI Vision module. The camera module links the camera to LabVIEW™, managing the camera's settings and parameters. The AI Vision module is a dedicated LabVIEW component that handles image recognition, including template matching and alignment. These modules work together to detect the position of the ISS 101-190-C calibration substrate and the corresponding pads for the probes.

Positioner Control: Once the correct position has been identified through image recognition, the system uses the MCS2 Settings module to configure the SmarAct® positioners. This module defines the settings for each of the stages (probe and chuck positioners), and the MCS2 controller executes the movement commands, adjusting the positioners in X, Y, Z, and θ/ϕ directions. The positioners are precisely controlled to ensure alignment with the DUT (Device Under Test) as per the predefined parameters.

VNA Integration and Data Acquisition: The VNA control module includes the VNA Settings module, which manages the configuration of the Keysight® 5008A Streamline Series VNA. This module sends commands to trigger measurements and acquire data once the positioners are correctly aligned. The VNA module in LabVIEW™ executes these commands and saves the measurement results for further analysis.

3 Computer Vision and Artificial Intelligence for Probe Alignment

3.1 Pattern Recognition Algorithms

The vision system relies exclusively on NI Vision Assistant for pattern matching to identify the positions of the probes and calibration elements on the ISS 101-190-C calibration substrate. The process begins with the capture of high-resolution images of the calibration substrate and the probes, followed by real-time image processing using template-based pattern matching techniques.

In this context, template matching is used to locate key features, such as the tips of the probes and the various calibration standards (open, short, load, and thru) on the substrate. The system compares predefined templates of these features against the captured images. By calculating the similarity between the template and regions within the image, it accurately identifies the positions of the probes and calibration structures.

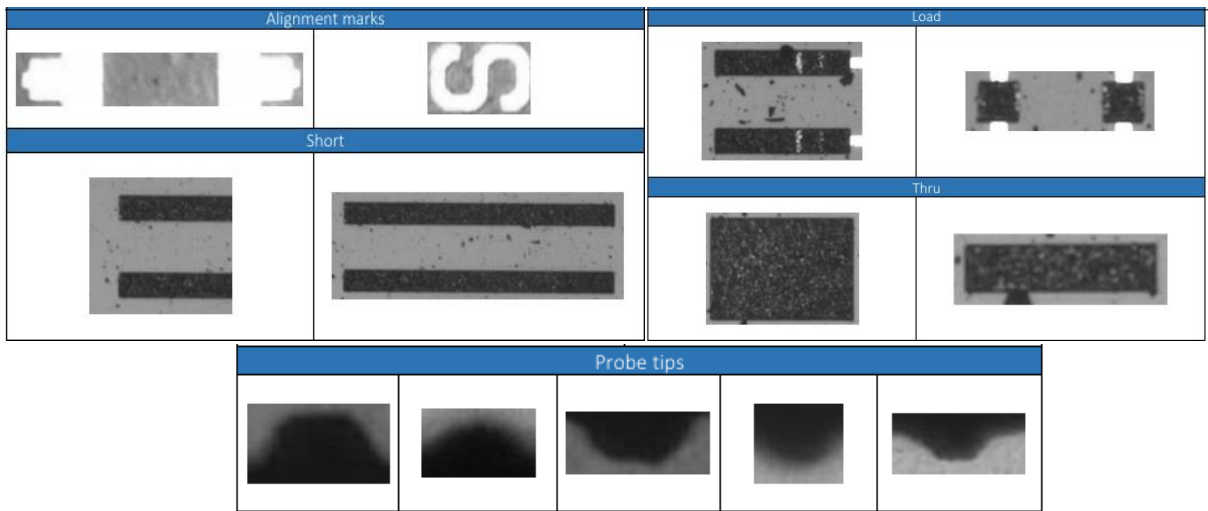


Figure 4. Sample pictures used as template for the machine vision module.

NI Vision Assistant provides an intuitive environment for configuring these pattern matching routines. The templates for each probe and calibration element are created manually, ensuring that the system can recognize these features in different image frames. The matching algorithm then identifies the best match based on pattern similarity, giving precise locations of the probe tips and calibration structures. Once the positions of these features are determined, the system can calculate alignment corrections in the X, Y, and θ axes. These corrections are then transmitted to the SmarAct® controllers, which adjust the positioning of the probes accordingly, ensuring precise alignment with the calibration standards.

3.2 Positioning Logic

The positioning of the probes and chuck is guided by a set of precise calculations and algorithms that utilize the results from the machine vision system. The key objective is to achieve accurate alignment of the probes with the calibration structures on the ISS 101-190-C substrate, ensuring repeatable and reliable measurements.

To achieve this, the system divides each calibration standard and probe structure into three key sections. This segmentation allows for the creation of reference lines, which are essential for determining the relative alignment of the probes. For the calibration standards, the system identifies a central line that runs through the standard, and similarly, for the probes, it identifies the three distinct points (or "teeth") of the probe tips. These three points are used to construct a reference line for each probe.

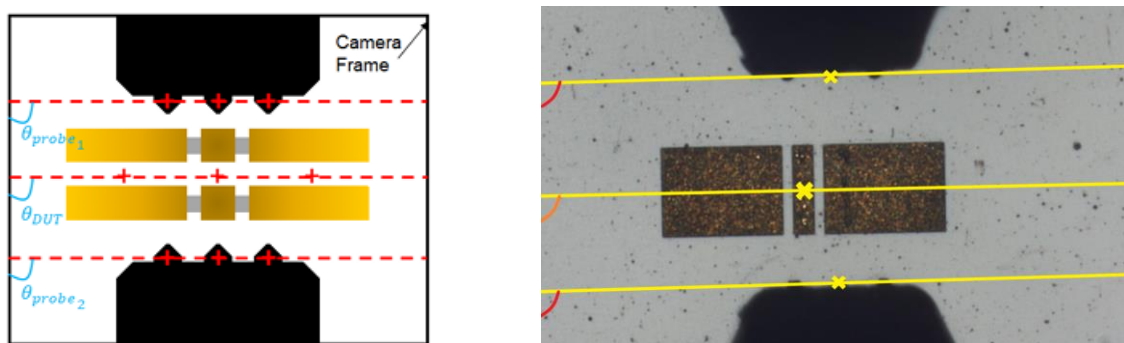


Figure 4. Automatic probe positioning and angular corrections.

Once the reference lines for both the standards and probes are established, the system calculates the angular difference between the probe lines (both upper and lower probes) and the corresponding lines of the standards. This angular deviation serves as the basis for further adjustments. The positioning algorithm then calculates the necessary adjustments required to bring the probes into precise alignment with the standards. This process involves a combination of P control loops and other fine-tuning algorithms to ensure smooth and accurate movements of

the positioning stages. The P controller helps to minimize the error between the current position of the probes and the target positions by adjusting the speed and acceleration of the stages in real-time. Additionally, a set of safety protocols is implemented to prevent any potential damage to the equipment. These safety mechanisms monitor the motion of the stages and ensure that they do not exceed defined limits, avoiding issues such as collisions or overtravel. If any irregularities are detected, the system halts movement immediately, ensuring the safety of both the DUT and the probing equipment.

This combination of precise calculation, real-time control, and safety measures ensures that the system operates with both high precision and reliability, minimizing errors and preventing mechanical issues during the alignment process.

3.3 Contact Detection via Image Feedback

Beyond static alignment, the vision system also plays a crucial role in detecting physical contact between the probe tips and the DUT. Contact is primarily identified by monitoring changes in the optical signature of the probe tip, such as deformation or change in reflectivity, and by analyzing motion discontinuities in the Z-axis. Overtravel refers to the continued downward movement of the probe tip after initial contact with the DUT, while skating describes the lateral movement of the probe tip on the wafer surface as a result of overtravel. In our system, these phenomena are differentiated by analyzing the movement patterns of the probe. If a downward motion in the Z-axis (indicating probe approach) is accompanied by a simultaneous movement of the probe in the X-axis, this indicates lateral motion (skating) of the probe tip along the surface.

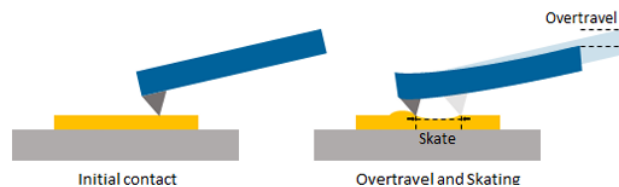


Figure 5. Overtravel and skating principle

This image-based contact detection is supplemented with real-time feedback from the SmarAct positioning stages, which allows precise monitoring of probe movement in all axes. By correlating Z-axis motion with X-axis visual displacement, the system can accurately identify when skating occurs, thus confirming probe contact. The combination of optical feedback and positional data provides a robust, real-time approach to avoid overtravel and minimize the risks of probe damage or inaccurate measurements. This technique has proven highly repeatable in identifying probe contact moments, ensuring precise and reliable RF probing through multiple contact cycles, even in the presence of skating and overtravel.

3.4 Calibration Routine and Contact Procedure

The procedure for executing a 2-port calibration on the 101-190 C Impedance Standard Substrate (ISS) in relation to the positioner behavior follows a systematic sequence:

Phase 1: In this phase, the system leverages the feedback from the camera and the AI Vision Module to identify the alignment marks on the ISS. Specifically, the center of each alignment mark is located, and the angle between the structure and the camera frame is determined. In addition, the tips of the two probes are detected, with the system calculating their centers and the angle between the line connecting the probe tips and the camera frame's parallel.

Phase 2: Once the alignment marks and probe tips are identified, the probes are aligned based on the coordinates gathered in Phase 1. Using the positioners for the probes and the chuck, the system ensures that the probes' tips are perfectly centered over the structure, with the angle between the probes and the structure set to zero. Following alignment, the probes are lowered until they make good contact with the ISS. The positions of the probes along the X and Y axes are then saved and locked to prevent any further movement.

Phase 3: At this stage, the operator selects one of the four calibration standards. The AI Vision Module will recognize the chosen standard, locating its center and angle in a manner similar to the process in Phase 1.

Phase 4: The standard is then centered in relation to the probes using only the chuck positioners. After the alignment is completed, the probes are lowered, and the measurement is initiated (once the probes touch the surface, an additional overtravel is applied to ensure the probe tips are perfectly aligned with the alignment structure. As recommended by the ISS manufacturer, this overtravel is set to 20 μm . The system automatically detects the initial contact when the probes start to "skate" on the surface, with this value being pre-set manually and incorporated into the program). Following the measurement, the probes are raised, and the chuck is reset. Phases 3 and 4 are repeated for each of the calibration standards.

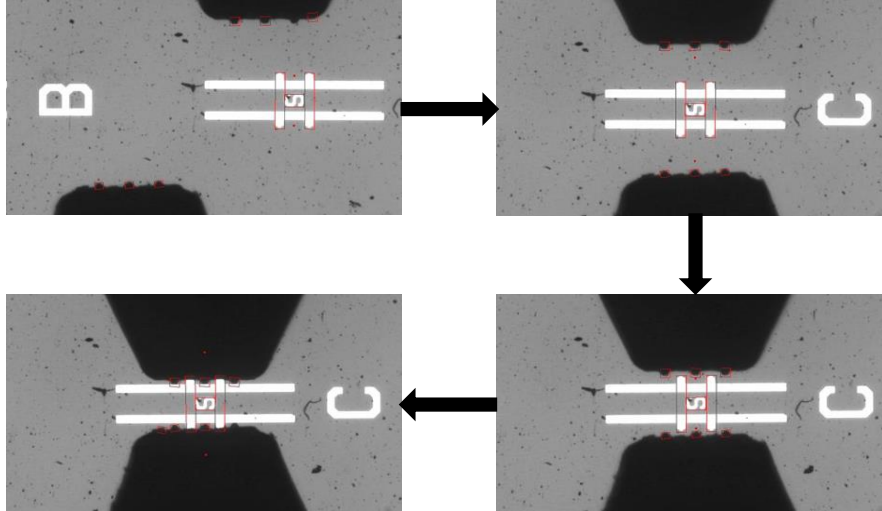


Figure 6. Execution of phase 1 & 2 on an alignment pad.

4 Experimental Results and Performance Evaluation

4.1 Automated SOL Calibration and probe-positioning Protocol

To validate our nano-robotic positioning system, all calibrations were driven by the same control program. We performed ten consecutive SOL calibrations on each of the three standards (open, short, load), under three distinct conditions:

Automated with probe retraction/repositioning, after each calibration cycle the probes were fully retracted and then automatically repositioned on the same target point. Automated in-contact, the probes remained in continuous contact with the standard between cycles (no movement). Manual, the same operator performed ten approach-retract calibration cycles by hand, using a conventional manual probe station.

All ten repetitions for each method were carried out under identical environmental and VNA settings.

4.2 Statistical analysis of calibration residuals

From each calibration trial, we extracted the three VNA error-term residuals, directivity (δ), reflection-tracking (τ), and source-match (μ) and computed their 3σ standard deviations over the 1–50 GHz frequency range. The table below presents a summary of these residual values specifically at 10 GHz for comparison across the three measurement methods.

Residual error	10 GHz		
	3σ		
	Manual	In contact Automated	In movement Automated
δ_1	7.4267×10^{-4}	1.1703×10^{-4}	1.4900×10^{-4}
τ_1	2.3201×10^{-3}	4.4022×10^{-4}	5.2248×10^{-4}
μ_1	4.0472×10^{-3}	3.1665×10^{-4}	2.6407×10^{-4}

Figure 7. Residual calibration errors (3σ) at 10 GHz for manual, in-contact & in-movement automated probing methods

Comparable reductions, by roughly one to two orders of magnitude, were seen for τ and μ . Overall, fully automated probe handling (both in-contact and retract-reposition modes) cuts calibration residuals by up to 90% versus manual probing, yielding up to a 40% decrease in total measurement uncertainty.

4.3 Automation Benefits and Performance Metrics

The transition from manual to fully automated probe handling delivers clear operational and safety advantages. By orchestrating every approach–retract and standard-exchange step through a unified control program, the system eliminates most of the subtle misalignments and contact-force fluctuations that inevitably arise when an operator manually adjusts the probes. Automation therefore not only boosts consistency between successive calibrations, but also greatly reduces the risk of occasional probe crashes or substrate scratching. Software safety interlocks continuously monitor tip loading and travel limits; any deviation beyond predefined thresholds triggers an immediate motion halt, preserving both delicate probe tips and valuable wafer samples. Moreover, once a calibration sequence is initiated, the station can proceed through multiple SOL routines without human intervention—freeing human resources from repetitive tasks and allowing them to focus on higher-level analysis rather than manual alignment. These combined improvements in reliability, reproducibility, and hardware protection make the AI-augmented probe station particularly well suited for environments where operator access is limited or where sample throughput and equipment longevity are critical.

5 Conclusion

We have demonstrated an AI-powered, nano-robotic on-wafer probe station that consistently outperforms manual methods in terms of calibration repeatability and hardware safety. Our experiments show dramatic reductions in VNA error-term residuals—directivity, reflection tracking, and source match—when the entire SOL procedure is driven by automated scripts. Safety features and collision-avoidance routines virtually eliminate probe damage and substrate mishandling, while the hands-off operation streamlines workflow and minimizes user-dependent variability. Future work will deepen this validation by extending the range of calibration standards (e.g., thru, line) and measurement frequencies, refining the AI algorithms to adaptively compensate for probe wear, and compiling a larger statistical dataset across multiple device types. These results demonstrate the system’s ability to meet the stringent demands of both research laboratories and high-volume RF test facilities.

Acknowledgement

This work was supported, in part by the EPM project 23IND10 OnMicro, in part by the French Renatech network, and in part by the CPER Hauts de France project IMITECH.

References

- [1] F. Mubarak *et al.*, "An Interlaboratory Comparison of On-Wafer S-Parameter Measurements up to 1.1 THz," in *IEEE Transactions on Terahertz Science and Technology*.
- [2] H. Happy *et al.*, "Measurement Techniques for RF Nanoelectronic Devices: New Equipment to Overcome the Problems of Impedance and Scale Mismatch," in *IEEE Microwave Magazine*, vol. 15, no. 1, pp. 30-39, Feb. 2014.
- [3] K. Daffe *et al.*, "On-Wafer Broadband Microwave Measurement of High Impedance Devices-CPW Test Structures with Integrated Metallic Nano-Resistances," *2018 48th European Microwave Conference (EuMC)*, Madrid, Spain, 2018, pp. 25-28.
- [4] M. Horibe, "Improvement of Measurement Uncertainty of THz Waveguide Vector Network Analyzers," *2021 96th ARFTG Microwave Measurement Conference (ARFTG)*, San Diego, CA, USA, 2021, pp. 1-4.
- [5] C. Mokhtari *et al.*, "Impact of GSG Probe to Pads Contact Repeatability for On-Wafer RF Measurements," *2021 IEEE 7th International Conference on Smart Instrumentation, Measurement and Applications (ICSIMA)*, Bandung, Indonesia, 2021, pp. 241-246
- [6] C. Mokhtari *et al.*, "New Generation of On-Wafer Microwave Probe Station for Precision GSG Probing," *2022 24th International Microwave and Radar Conference (MIKON)*, Gdansk, Poland, 2022, pp. 1-4.
- [7] C. Mokhtari, *et al.*, "Automated and Robotic On-Wafer Probing Station," *2023 IEEE Symposium on Wireless Technology & Applications (ISWTA)*, Kuala Lumpur, Malaysia, 2023, pp. 99-102
- [8] C. Mokhtari *et al.*, "Exploring Nanorobotics Integration with Microwave and Millimeter-Wave Techniques for Advanced On-wafer Measurement," *2024 5th International Conference in Electronic Engineering, Information Technology & Education (EEITE)*, Chania, Greece, 2024, pp. 1-6.

Densités de Probabilité du Lag-1 dans les Séries Temporelles Linéaires et Circulaires Modélisant les Processus de Brassage

Probability Densities of Lag-1 in Linear and Circular Time Series Modeling Stirring Processes

Rabah Monsef^{1,2}

¹Université Paris-Saclay, CentraleSupélec, CNRS, Laboratoire de Génie Electrique et Electronique de Paris (GeePS), 91192 Gif-sur-Yvette, France, rabah.monsef@centralesupelec.fr

²Sorbonne Université, CNRS, Laboratoire de Génie Electrique et Electronique de Paris, 75252 Paris, France

Mots clés : *Chambres Réverbérantes, Autocorrélation, Brassage, Électromagnétisme Statistique*

Keywords : *Reverberation Chambers, Autocorrelation, Stirring Processes, Statistical Electromagnetism*

Résumé/Abstract

Dans les études de chambres réverbérantes, les séries temporelles linéaires (STL) sont traditionnellement utilisées pour modéliser les processus de brassage au sein d'une chambre réverbérante, y compris pour les brasseurs rotatifs. Un travail récent [1] a introduit les séries temporelles circulaires (CTS) comme modèle plus adapté. Cet article complète ce modèle en dérivant la fonction de densité de probabilité (PDF) associée et propose une expression révisée de la PDF mieux adaptée aux brasseurs linéaires. Les expressions proposées améliorent l'accord avec les résultats numériques par rapport aux modèles existants, tout en fournissant un accord satisfaisant pour les modèles circulaires appliqués aux brasseurs rotatifs.

In reverberation chamber studies, linear time series (LTS) have traditionally been used to model stirring processes within a reverberation chamber, including for rotating stirrers. Recent work [1] introduced circular time series (CTS) as a more suitable model. This paper extends the CTS model by deriving the associated probability density function (PDF) and proposes a revised PDF expression better suited for linear stirrers. The proposed expressions improve the agreement with numerical results compared to the expression commonly adopted in the community, while also delivering satisfactory results for circular models applied to rotating stirrers.

1 Introduction

In reverberation chambers (RCs), mechanical stirring ensures field uniformity and isotropy. Field values at each stirrer position are typically modeled using linear time series (LTS), which works well for sliding stirrers but is less suitable for rotating stirrers due to inherent correlations between the first and last positions. Despite this, LTS models remain widely used in the RC community [2-4].

To address this limitation, recent work [1] introduced Circular Time Series (CTS), as a better model for rotating stirrers, though its statistical properties, particularly the PDF of the lag-1 correlation coefficient as a function of stirrer positions referred to as N , remain underexplored in the community. This paper addresses this question by deriving the lag-1 PDF for CTS, enabling a rigorous comparison with [5] and studying the influence of N on models' accuracy.

2 Linear and Circular Correlation Models

In the following, we present and recall correlation models when linear and circular time series are considered. Time series apply to a given cartesian components of the electric field in an RC where overmoded conditions are assumed. Real and imaginary parts of the field can be regarded as Gaussian accordingly. For a sake of brevity, we will use variable x to refer to the real or imaginary part of the electric field and subscripts L and C will be used to refer to LTS and CTS models, respectively. Variables x_L and x_C are standardized such that they follow a $N(0, 1)$ law, which is centered and has unit variance.

Regarding autocorrelation models, we use an AR-1 model to describe the relationships between consecutive samples such that,

$$\begin{cases} x_{L_1} = \varepsilon_1 \\ x_{L_2} = \rho x_{L_1} + \alpha_L \varepsilon_2 \\ \vdots \\ x_{L_N} = \rho x_{L_{N-1}} + \alpha_L \varepsilon_N \end{cases}, \quad (1)$$

where $\alpha_L = \sqrt{1 - \rho^2}$ and,

$$\begin{cases} x_{C_1} = \rho x_{C_N} + \alpha_c \varepsilon_1 \\ x_{C_2} = \rho x_{C_1} + \alpha_c \varepsilon_2 \\ \vdots \\ x_{C_N} = \rho x_{C_{N-1}} + \alpha_c \varepsilon_N \end{cases}, \quad (2)$$

where $\alpha_c = \alpha_L \sqrt{1 - \rho^N / (1 + \rho^N)}$. We can conveniently express (1) and (2) using matrices [1], referred to as $\underline{\mathbf{A}}_{LN}$ and $\underline{\mathbf{A}}_{CN}$ such that,

$$\underline{\mathbf{A}}_{LN} = \begin{bmatrix} 1 & 0 & 0 & \dots & \dots & 0 \\ \rho & \alpha_L & 0 & \dots & \dots & 0 \\ \rho^2 & \rho \alpha_L & \alpha_L & \dots & \dots & 0 \\ \vdots & \vdots & \vdots & \ddots & \ddots & \vdots \\ \rho^{N-1} & \rho^{N-2} \alpha_L & \rho^{N-3} \alpha_L & \dots & \dots & \alpha_L \end{bmatrix}, \quad \underline{\mathbf{A}}_{CN} = \frac{\alpha_c}{1 - \rho^N} \begin{bmatrix} 1 & \rho^{N-1} & \rho^{N-2} & \dots & \rho \\ \rho & 1 & \rho^{N-1} & \dots & \rho^2 \\ \rho^2 & \rho & 1 & \dots & \rho^3 \\ \vdots & \vdots & \vdots & \ddots & \vdots \\ \rho^{N-1} & \rho^{N-2} & \rho^{N-3} & \dots & 1 \end{bmatrix}. \quad (3)$$

These operators allow generating samples based on linear and circular time series such that,

$$\begin{cases} \mathbf{x}_L = \underline{\mathbf{A}}_{LN} \underline{\varepsilon} \\ \mathbf{x}_C = \underline{\mathbf{A}}_{CN} \underline{\varepsilon} \end{cases}, \quad (4)$$

where $\underline{\varepsilon}$ is a vector of standardized random gaussian variables.

3 Lag-1 Probability Density Distribution

In this section we present three different PDFs expressions for lag-1 correlation coefficient. Explicit expressions of each of them are based on assumptions that urged us computing Monte-Carlo (MC) simulations to evaluate to what extent these expressions hold.

It turns out that the most frequently used PDF in the community is given by [5] such that,

$$\Psi_K(r) = \frac{N-2}{\sqrt{2\pi}} \cdot \frac{\Gamma(N-1)}{\Gamma(N-\frac{1}{2})} \frac{(1-\rho^2)^{\frac{(N-1)}{2}} (1-r^2)^{\frac{N-4}{2}}}{(1-\rho r)^{N-\frac{3}{2}}} \left[1 + \frac{1+\rho r}{4(2N-1)} + \dots \right], \quad (5)$$

The reference written in German was not accessible – subsequently we are not aware of the assumptions behind this expression. The derivation of another PDF expression for lag-1 coefficient for LTS can be found in Eq (6-7) of Ref. [6]. In order to have an explicit expression the author has to exclude cases for which ρ is close to ± 1 , leading to,

$$\Psi_{L,D} \sim \frac{N}{2\sqrt{\pi}} \frac{\Gamma(\frac{1}{2}N-1)}{\Gamma(\frac{1}{2}N-\frac{1}{2})} \frac{\sqrt{1-\rho^2} (1-r^2)^{\frac{N}{2}-1}}{(1-\rho r)(1-2\rho r+\rho^2)^{\frac{1}{2}N-1}} (1+O(N^{-1})), \quad (6)$$

Derivation of the PDF for CTS can also be found in [6] although previously derived in [7]. It leads to the following expression given by Eq (3-7) of Ref. [6], such that,

$$\Psi_C(r) \sim \frac{1}{\sqrt{\pi}} \frac{\Gamma(\frac{N}{2}+1)}{\Gamma(\frac{N}{2}+\frac{1}{2})} \frac{(1-r^2)^{\frac{(N-1)}{2}}}{(1-2\rho r+\rho^2)^{\frac{N}{2}}}, \quad (7)$$

where the subscript C refers to the circular nature and where the validity domain exclude cases for which ρ is close to ± 1 .

4 Monte-Carlo Simulations

Running Monte-Carlo simulations, 25000 realizations were considered using N samples in time series. Fig. 1 shows the numerical PDFs for CTS (squares) and LTS (circles), overlaid with the analytical models given by (5) (solid line), (6) (dotted line) and (7) (dashed line). For low correlation level, i.e., for $\rho < 0.5$, it is interesting to see that none of the models really match MC simulations for a poor number of stirrer positions such as 10. These expressions can be considered as sound for a number of stirrer positions greater than 50 for a 0 to 0.5 range correlation level. Beyond a 0.5-correlation level we can observe that (5) gives the worst match even for the largest number of 200 of stirrer positions considered herein. For the other expressions, two things can be observed. First, they behave (quite surprisingly) the same way, and, second, they match numerical results for N greater than 100. This computations allow pointing out conditions under which these expressions hold.

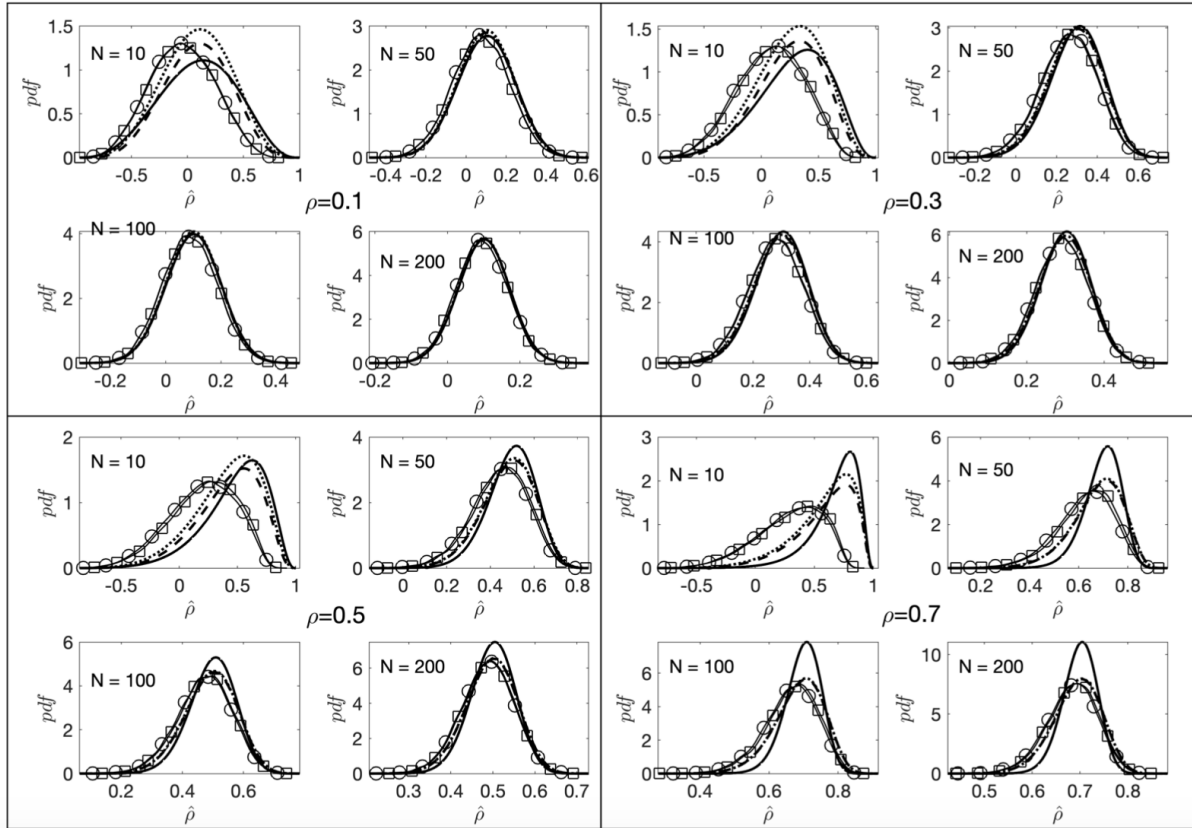


Figure 1: Numerical PDF for CTS (squares) and LTS (circles) with analytical models overlaid ((5)(solid line), (6) (dashed line) and (7) (dotted line)). Four correlation levels have been considered and the number of stirring states is reported in the inset of each case.

Additionally, it is worth remembering that the lags considered here are at the field level, as explained in [9]. When comparing with thresholds provided by standards [8], the mean values of ρ considered here should be squared, meaning that 70% correlation corresponds to less than 50% correlation at the power level.

5 Conclusion

In this work, we derived and compared PDFs for the lag-1 correlation coefficient in both linear and circular time series models. The proposed expressions for LTS and CTS show good agreement with numerical results as long as the number of stirrer states is greater than 50 for correlation level lower than 0.5, whereas 100 stirrer states must be considered for a sound use of them for correlation level larger than 0.5. However, both expressions outperform the commonly used model in the community. These findings provide a more accurate framework for estimating confidence intervals for stirring processes in reverberation chambers, for rotating and linear stirrers.

References

- [1] R. F. Monsef, "Rotating-stirring process and circular time series," *IEEE Transactions on Electromagnetic Compatibility*, vol. 66, no. 5, pp. 1679–1682, 2024.
- [2] C. Lemoine, P. Besnier, and M. Drissi, "Estimating the effective sample size to select independent measurements in a reverberation chamber," *IEEE Transactions on Electromagnetic Compatibility*, vol. 50, no. 2, pp. 227–236, 2008.
- [3] C. Lemoine, P. Besnier, *et al.*, "Using autoregressive models to estimate the number of independent samples available with stirrer rotation in reverberation chamber," in *Electromagnetic Compatibility, 2007. EMC Zurich 2007. 18th International Zurich Symposium on*, IEEE, 2007, pp. 469–472.
- [4] A. Reis, F. Sarrazin, E. Richalot, S. Meric, J. Sol, P. Pouliguen, and P. Besnier, "Radar cross-section pattern measurements in a mode-stirred reverberation chamber: Theory and experiments," *IEEE Transactions on Antennas and Propagation*, 2021.
- [5] H. G. Krauthauser, T. Winzerling, and J. Nitsch, "Statistical interpretation of autocorrelation coefficients for fields in mode-stirred chambers," in *Electromagnetic Compatibility, 2005. EMC 2005. 2005 International Symposium on*, IEEE, vol. 2, 2005, pp. 550–555.
- [6] H. Daniels, "The approximate distribution of serial correlation coefficients," *Biometrika*, vol. 43, no. 1/2, pp. 169–185, 1956.
- [7] R. Leipnik, "Distribution of the serial correlation coefficient in a circularly correlated universe," *The Annals of Mathematical Statistics*, vol. 18, no. 1, pp. 80–87, 1947. [Online]. Available: <https://www.jstor.org/stable/2236104>.
- [8] *Reverberation Chamber Test Methods*, International Electrotechnical Commission (IEC), Std. 61 000-4-21, 2011.
- [9] F. Monsef, A. Cozza, and R. Serra, "Linking lag-1 correlation coefficients between field-related quantities in a reverberation chamber," *IEEE Transactions on Electromagnetic Compatibility*, 2019. DOI: 10.1109/TEM.2019.2928177.

Dosimétrie électromagnétique et exposimétrie

Hybrid approach of the measurement of actual head EMF exposure

Shanshan Wang¹, Jiang Liu¹, Yaru Zhang¹, Joe Wiart¹

¹Chair C2M, LTCl, Telecom Paris, France, {firstname.surname}@telecom-paris.fr

Keywords: Head exposure, Uplink transmit power, Mobile phone

Abstract

With the widespread deployment of communication infrastructures, concerns about human exposure to electromagnetic fields (EMF) have grown significantly. One major component of this exposure is uplink emissions, which refer to the radiofrequency (RF) signals transmitted from a mobile phone to a base station. Here in this work, we adopt the indirect measurement method, by leveraging the information provided by the phone chipset. The measurement campaign is designed and conducted to cover different network technologies, services, by using the equipment called Nemo from Keysight. Afterwards, the transmit power, as well as the other relevant parameters, are extracted and analyzed. The head exposure is calculated by synthesizing the measured data and developed transfer function.

Résumé

Avec le déploiement généralisé des infrastructures de communication, les préoccupations concernant l'exposition humaine aux champs électromagnétiques (CEM) ont considérablement augmenté. Une composante majeure de cette exposition est constituée par les émissions montantes, qui correspondent aux signaux radiofréquences (RF) transmis d'un téléphone mobile à une station de base. Dans ce travail, nous adoptons la méthode de mesure indirecte, en exploitant les informations fournies par la puce du téléphone. La campagne de mesures est conçue et réalisée pour couvrir différentes technologies et services réseau, à l'aide de l'équipement Nemo de Keysight. La puissance d'émission, ainsi que les autres paramètres pertinents, sont ensuite extraits et analysés. L'exposition de la tête est calculée en synthétisant les données mesurées et en développant une fonction de transfert.

1 Introduction

Usually the assessments of radio frequency (RF) electromagnetic field (EMF) exposure is categorized into downlink and uplink. Unlike downlink exposure, which originates from base station antennas and affects a broader area, uplink exposure, which are the emissions from phones, can't be directly measured in situ, as body interactions (reflection, absorption) alter the fields. Their high spatial variability also makes localized measurements unreliable for estimating tissue absorption.

Furthermore, the complexity in modern mobile phones, diverse user scenarios and duration, make the assessment of uplink exposure more difficult. The uplink transmit power varies with factors like network architecture, wireless technology, and application type. To tackle it, a probe placed next to the phone can be used to evaluate the power emitted [1]. However distributed antennas in the mobile phone makes it more challenging to measure the phone's radiated power accurately. In this work, we use the network-based tool, Nemo from Keysight, to measure the transmit power from phone's chipset.

To address the challenges of direct EMF measurement, the EXPLORA project aims to characterize EMF exposure from mobile phones on French networks during voice calls and data use via an indirect method. Phones were tested in various positions to reflect typical usage, across 300 locations in the greater Paris area, ranging from rural to dense urban settings, to ensure diverse environmental representation. A balanced selection of the four main French operators was included for comprehensive and unbiased results. Measurements were taken in different scenarios: near the ear for calls and 30 cm from the body for data use.

Subsequently, the measured phone's transmitted (TX) power are used to evaluate organ-level exposure across various environments, networks, and postures with the help of SAR. SAR is calculated via numerical electromagnetic methods like the Finite-Difference Time-Domain (FDTD) technique. Here in this paper, digital models of the phone and human body were used for simulation. SAR estimation was performed using Sim4Life software and the Duke model from the Virtual Family, with phone placement mimicking real-world usage (at the ear for calls, in front of the user for data).

2 Measurement description

2.1 Measurement device

NEMO, a system by Keysight, enables indirect measurement of mobile phone TX power by accessing data from the telecom processor, including emitted power, frequencies, and data rates. Drive test equipment modifies the phone's OS to log these parameters, e.g., every 500 ms on Qualcomm chipsets. NEMO Handy, an Android app, captures wireless diagnostics per 3GPP standards. This method is adopted in this paper for independent assessments of real TX power across varied environments and mobility scenarios.

A phantom is utilized in the measurement as shown in Figure 1. The phantom consists of a head model and a right hand model, both filled with standardized equivalent liquid in compliance with IEC standards. The experimental protocol, similar as used in [2], includes two configurations: the first is designed for voice calls with the cell phone positioned adjacent to the phantom head, while the second, with the phone placed in front of the head, is intended for data transmission. During the measurement, 4G and 5G bands are locked respectively to compare the difference between two. Applications including VoCS, VoIP, Video call, FTP file uploading are used in the measurement protocol.



Figure 1: Phantom placement and measurement protocol

2.2 Measurement protocol

A dedicated measurement protocol was implemented (see Table 1). Voice call attempts lasted 15 seconds, with a maximum call duration of 150 seconds. The protocol involved band-locking GSM (900 MHz) for a 30-second VoCS call, then UMTS (900 or 2100 MHz) for 30-second VoCS and VoIP (WhatsApp) calls, followed by LTE (700–2600 MHz) for similar calls, with bands selected based on local base station services. To simulate speech transmission—important for technologies with discontinuous transmission—a standard text was read into a nearby microphone. For data, each attempt lasted up to 60 seconds, transmitting a 70 MB file via SFTP over UMTS and LTE, with frequency bands locked accordingly.

Nemo Commands	User Posture	Time	Attempt Timeout
Bandlock GSM	Ear-Holding		
Default Voice Call		30s	15s
Bandlock UMTS			
Default Voice Call		30s	15s
WhatsApp Voice Call		30s	15s
Bandlock LTE			
Default Voice Call		30s	15s
WhatsApp Voice Call		30s	15s
Change Posture			
Bandlock UMTS	Face-Viewing		

FTP Data Upload 70 MB		<150s	60s
Bandlock LTE			
FTP Data Upload 70 MB		<150s	60s

Table 1: Measurement protocol

3 Transfer Function

Using the numerical human model Duke and the numerical phone model, the SAR in organs and part of the body have been calculated. We first determine the power applied to the antenna that induces 1 W/kg, then estimate the SAR in any organ based on the SAR induced by the numerical phone operating at maximum output. Using Nemo, we record the maximum power emitted throughout the entire call and compare the actual emitted power to this maximum. The Table 2 provide the transfer function of a power emitted to the SAR in brain and whole body. As described previously the power emitted by the phone is considered as the maximum and is inducing a SAR over 10g equal to 1w/kg.

Voice Position				
	Brain Grey-matter	Brain white-matter	Head	Whole body
900 MHz	0.99	1.57	9.81	2.33
1.8 GHz	1.31	0.62	3.64	0.61
2.1 GHz	0.81	0.33	4.34	0.74
2.6 GHz	0.22	0.09	2.11	0.47
3.5 GHz	0.13	0.04	1.32	0.38
In Front of eyes				
	Brain Grey-matter	Brain white-matter	Head	Whole body
900 MHz	0.38	0.24	0.37	2.32
1.8 GHz	0.01	0.01	0.026	0.55
2.1 GHz	0.008	0.004	0.031	0.61
2.6 GHz	0.004	0.002	0.016	0.48
3.5 GHz	0.002	0.00093	0.017	0.26

Table 2: Transfer function for two positions

4 Results and Discussion

4.1 Tx power analysis

The total call durations for VoIP and VoLTE were 20.4 min at 700 MHz, 18.2 min at 800 MHz, 27.3 min at 1800 MHz, 13.1 min at 2100 MHz, and 25.7 min at 2600 MHz. In case of VoLTE the total call durations were 20.3 min at 700 MHz, 17.7 min at 800 MHz, 33.7 min at 1800 MHz, 13.6 min at 2100 MHz, and 22.7 min at 2600 MHz. These call durations were obtained from 40, 35, 61, 27, and 45 calls conducted over VoIP and VoLTE on 700 MHz, 800 MHz, 1800 MHz, 2100 MHz, and 2600 MHz bands, respectively. As a result, the calls on the 2100 MHz band are less representative compared to those on the 1800 MHz and 2600 MHz bands.

Figure 2 presents the average TX power of VoLTE and VoIP across the 700 MHz, 800 MHz, 1800 MHz, 2100 MHz, and 2600 MHz frequency bands. As shown in Figure 2, at 700 MHz, the average TX power for VoIP and VoLTE were 13.4 mW and 14.5 mW, respectively. At 800 MHz, the TX power for VoIP and VoLTE were 15.7 mW and 15.8 mW, respectively. In the 1800 MHz band, where large number of measurements were taken, the average TX power for VoIP and VoLTE were 4.9 mW and 9.3 mW, respectively. At 2100 MHz, the TX power for VoIP and VoLTE were 4.9 mW and 6.5 mW, respectively. Finally, at 2600 MHz, the TX power for VoIP and VoLTE were 18 mW and 20.6 mW, respectively. The average TX power values vary significantly across different frequency bands, with VoLTE generally exhibiting higher power levels than VoIP.

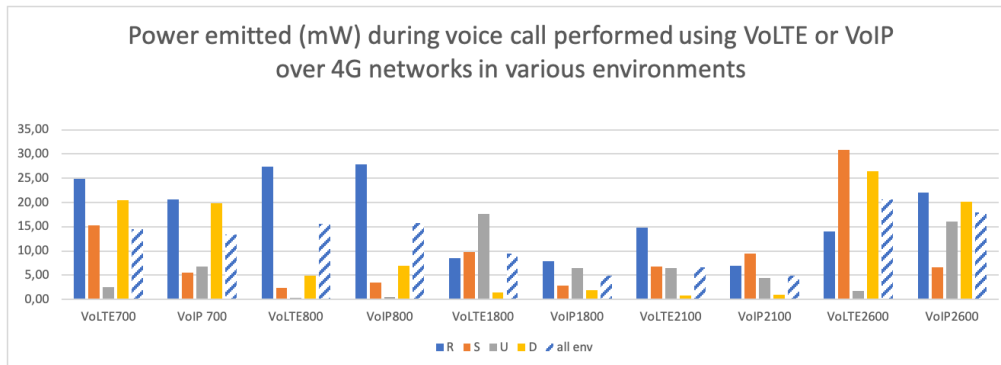


Figure 2. TX power (mW) of VoLTE and VoIP over LTE networks. R, S, U, D represent Rural, Suburban, Urban, and Dense Urban environments.

To assess the TX power during data transmission, we employed the SFTP protocol to transfer a 70 MB file. As illustrated in Figure 3, the average TX power measured on the 700 MHz, 800 MHz, 1800 MHz, 2100 MHz, and 2600 MHz bands was 89 mW, 171 mW, 107 mW, 114 mW, and 95 mW, respectively. The duration of the transmission varied depending on the throughput at the specific time and location of the measurements. For the conducted measurements, the average transmission durations corresponding to the aforementioned frequency bands were 1.63 minutes, 1.51 minutes, 1.18 minutes, 1.25 minutes, and 1.33 minutes, respectively.

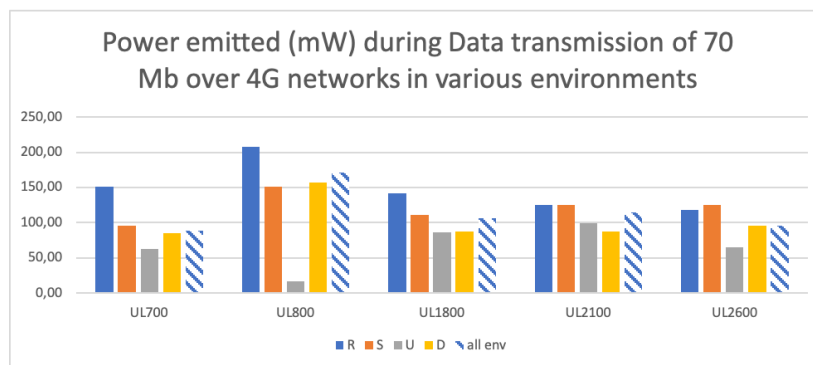


Figure 3. Emitted power(mW) during DATA transmission of 70 MB over 4G networks in various environments. R, S, U, D represent Rural, Suburban, Urban, and Dense Urban environments.

5 Conclusion

In conclusion, this paper provides a robust and realistic assessment of EMF exposure from mobile phones in France by combining extensive field measurements with advanced numerical simulations. By measure uplink TX power in different usage scenarios across diverse environments and network types, and estimating SAR using validated human and device models, the study offers valuable insights into real-world exposure levels. This indirect approach effectively overcomes the limitations of direct in-situ measurements, enabling a comprehensive evaluation of organ-level exposure and supporting informed risk assessment in mobile phone usage.

6 Acknowledgement

This work was supported in part by EU Project SEAWAVE through the Horizon Europe Research and Innovation Program under Grant 101057622, and ANSES project EXPLORA.

References

- [1] Mazloun, T., Bories, S., Dassonville, D., & Wiart, J. (2023, August). Impact of Sampling Frequency on the Performance of DEVIN: A personal EM UL Exposimeter. In 2023 XXXVth General Assembly and Scientific Symposium of the International Union of Radio Science (URSI GASS) (pp. 1-4). IEEE.
- [2] Liu, J., Zhang, Y., Chikha, W. B., Wang, S., Samaras, T., Jawad, O., ... & Wiart, J. (2024). Assessment of EMF Exposure Induced by Wireless Cellular Phones in Various Usage Scenarios in France. IEEE Access.

Correlation Analysis of UL EMF Exposure in Urban Environments

Qunfei SUN¹, Shanshan WANG², Jiang LIU³, Yarui ZHANG⁴, Joe WIART⁵, Farid NAIT-ABDESSELAM⁶

¹Laboratoire d'Informatique Paris Descartes, {qunfei.sun}@etu.u-paris.fr

²Télécom Paris, {shanshan.wang}@telecom-paris.fr

³Télécom Paris, {liu.jiang32009}@163.com

⁴Télécom Paris, {yarzhang}@telecom-paris.fr

⁵Télécom Paris, {joe.wiart}@telecom-paris.fr

⁶Laboratoire d'Informatique Paris Descartes, {farid.nait-abdesselam}@u-paris.fr

Keywords: EMF Exposure, LTE, UL, 5G NR, EMF Exposure measurements, Base station antenna

Abstract/Résumé

Uplink (UL) electromagnetic field (EMF) exposure remains relatively underexplored, as most research has primarily focused on downlink (DL) exposure. Accurately assessing UL exposure is challenging due to adaptive power control mechanisms and the complexity of real-world propagation environments. This study investigates the correlation between user equipment (UE) transmission power and the distance to the nearest serving base station (BS). Field measurements were conducted across both indoor and outdoor environments in the Paris metropolitan area, covering four communication scenarios: traditional voice calls, WhatsApp voice calls, WhatsApp video calls, and FTP data transfers. By identifying the key influencing factors, this work supports the development of machine learning models for predicting UL EMF exposure levels more accurately.

L'exposition aux champs électromagnétiques (CEM) en liaison montante (UL) reste relativement peu explorée, la plupart des recherches se concentrant sur l'exposition en liaison descendante (DL). L'évaluation précise de l'exposition UL est difficile en raison des mécanismes adaptatifs de contrôle de puissance et de la complexité des environnements de propagation réels. Cette étude explore la corrélation entre la puissance d'émission de l'équipement utilisateur (UE) et la distance à la station de base (BS) la plus proche. Des mesures de terrain ont été effectuées en intérieur et en extérieur dans la région métropolitaine de Paris. Quatre scénarios de communication ont été couverts : appels vocaux traditionnels, appels vocaux WhatsApp, appels vidéo WhatsApp et transferts de données FTP. En identifiant les facteurs clés influents, ce travail soutient le développement de modèles d'apprentissage automatique. Ces modèles visent à prédire plus précisément les niveaux d'exposition UL aux CEM.

1 Introduction

Radio frequency (RF) electromagnetic field (EMF) exposure has become an increasingly important topic in today's technology landscape, with regulatory bodies such as the International Commission on Non-Ionizing Radiation Protection (ICNIRP) [1] establishing strict exposure limits. Although extensive research has been carried out on Downlink (DL) exposure from base stations (BS) [2,3], Uplink (UL) exposure from user equipment (UE) has received considerably less attention despite the device's proximity to the user. The dynamic nature of indoor and outdoor environments—compounded by advanced power control mechanisms in modern networks (e.g., 4G LTE and 5G NR, including features like beamforming and massive MIMO)—further complicates the assessment of UL exposure.

This paper uses measurement data from the European SEAWave project to analyze the correlation between UE transmission power, UE received power, and the distance to the nearest matched base BS. The measurements were performed by researchers from Télécom Paris using NEMO, a chipset-level monitoring tool developed by Keysight. Four communication services, e.g., voice calls, WhatsApp voice calls, WhatsApp video calls, and FTP data transfer, were evaluated in both indoor and outdoor environments. In this work we analyzed 380 measurements collected in the Ile-de-France area, computing Pearson correlations between UL transit power Tx, reference signal received power (RSRP) and distance to matched BS. We then examine how the correlation varies across indoor outdoor scenarios and across 4 different applications. By identifying key influencing factors through correlation studies, this work contributes to improving UL EMF exposure assessment and lays the groundwork for future work on machine learning-based prediction models.

2 Measurement protocols

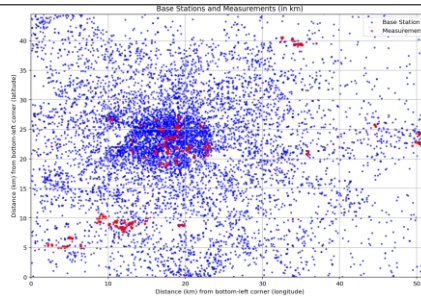


Figure 1: Base stations and measurement locations at Ile-de-France area

Measurements were conducted across 160 locations in the Île-de-France area, covering 89 indoor locations (e.g., metro platforms, residential buildings) and 69 outdoor locations (e.g., streets, parks). The broad range of locations and scenarios greatly enhances the robustness and generalizability of the correlation findings. Figure 1 illustrates the spatial distribution of base stations and measurement locations throughout the Ile-de-France region. The measurement protocol aims to compare differences between 4 services FTP, VOIP, Video, VOIP, and difference between 5G enabled and disabled. These services were chosen because they employ distinct combinations of resource allocations, power-control mechanisms, and frequency bands, ensuring our measurements capture the full spectrum of UL behaviors across diverse network scenarios. For instance, FTP and video services predominantly utilized LTE bands (1800 MHz, 2100 MHz, 2600 MHz), while voice calls relied on lower-frequency bands. Measurements were repeated under 5G-enabled and 5G-disabled conditions to assess the impact of EN-DC (E-UTRA-NR Dual Connectivity) and 5G NR bands (e.g., 3500 MHz).

3 Correlation studies

3.1 Methodology

Physical uplink shared channel (PUSCH) is the main channel serving UE data transfer. If the UE only transmits user data at a given subframe/slot/subslot i , equation (1) from [5] governs LTE UL power control of PUSCH incorporating with higher layer configured parameters such as $P_{MAX,c}$, and $\alpha_c \cdot PL_c$.

$$P_{PUSCH,c}(i) = \min \left\{ \begin{array}{l} P_{MAX,c}(i), \\ 10 \log_{10} \left(M_{PUSCH,c}(i) \right) + P_{OPUSCH,c}(j) + \alpha_c(j) \cdot PL_c + \Delta_{TF,c}(i) + f_c(i) \end{array} \right\} \quad [\text{dBm}] \quad (1)$$

Where, i = subframe/slot/subslot i

j = higher layer configured factor

$P_{MAX,c}$ = maximum allowed UE transmit power for cell c

$M_{PUSCH,c}$ = number of assigned resource blocks

$P_{OPUSCH,c}$ = nominal transmit power

α_c = path loss compensation factor

PL_c = estimated path loss

$\Delta_{TF,c}$ = power offset

$f_c(i)$ = closed-loop correction adjustment

The estimated pathloss PL_c strongly depends on the environmental factors such as distance to the BS and indoor/outdoor and buildings and was estimated using the equation below:

$$PL_c = \text{reference signal power} - \text{higher layer filtered RSRP} \quad (2)$$

The NEMO tool provided chipset-level monitoring of UE Tx, RSRP and communication related information including band, resource blocks and application types. BS and base station antenna (BSA) metadata were sourced from Cartoradio, the French regulatory authority's official database. By integrating NEMO-derived UE data with Cartoradio's BS/BSA records, the nearest matched BSA for each measurement point was identified, enabling precise calculation of the UE-to-BS distance. This distance metric was subsequently analyzed to quantify its influence on key variables of interest, such as Tx power and RSRP.

3.2 Pearson correlation between RSRP and distance to BS

RSRP (Reference Signal Received Power) is the linear average of received power across the allocated bandwidth, serving as an indicator of signal quality and coverage. In power control of LTE [5], RSRP is also used by the UE to evaluate path loss to the BS. Consequently, studying the correlation between RSRP and distance provides insight into how path loss behaves over varying conditions and for different applications.

As expected, Figure 2 illustrates that RSRP declines with increasing distance, particularly outdoors ($r = -0.54$ for voice calls), which is consistent with the theoretical increase in path loss. Indoor RSRP showed minimal correlation ($r = -0.01$ for FTP), further highlighting the complexity of indoor propagation.

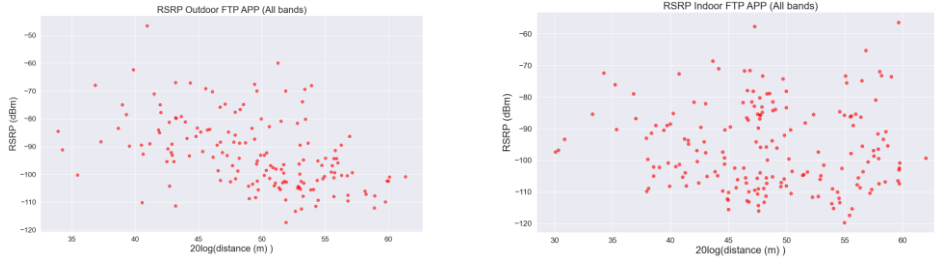


Figure 2: averaged RSRP at a specific measurement point and linked BS distance in FTP service

3.3 Pearson correlation between RSRP and Tx

As outlined by the power control mechanism (Equation (1)), Tx is adjusted based on an estimated path loss, which depends on the difference between the reference signal power and the higher layer filtered RSRP. Hence, the correlation between RSRP and Tx also reflects the interplay between DL and UL dynamics.

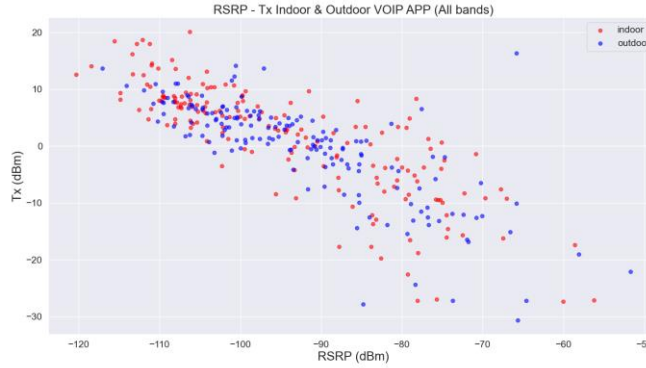


Figure 3: RSRP – Tx indoor & outdoor scenarios

A negative linear relationship was observed (Figure 3), confirming that UEs increase Tx power to compensate for higher path loss (lower RSRP). This aligns with Equation (1), where Tx power is adjusted based on estimated PL_c .

3.4 Pearson correlation between Tx and distance to BS

The objective of this study was to identify key factors influencing Tx in relation to the distance from the UE to the BS. Outdoor measurements demonstrate a clear increase in Tx as the distance increases, as seen in the left side of Figure 4. In contrast, indoor results indicate a weaker correlation between the distance to the BS and the corresponding Tx power level—an effect likely attributable to the presence of indoor-distributed antennas and the higher attenuation due to building materials. The strong outdoor correlation suggests distance is a critical factor

for UL exposure prediction in open environments, whereas indoor models may require additional information of indoor antennas. Similar trends are found in the other type of services.

According to the link budget equation, path loss (expressed in dB) and transmit and receive powers (both expressed in dBm) relate in a manner that suggests a linear relationship between Tx power and $\alpha 10\log(r)$, where r is the distance to the matched BS.

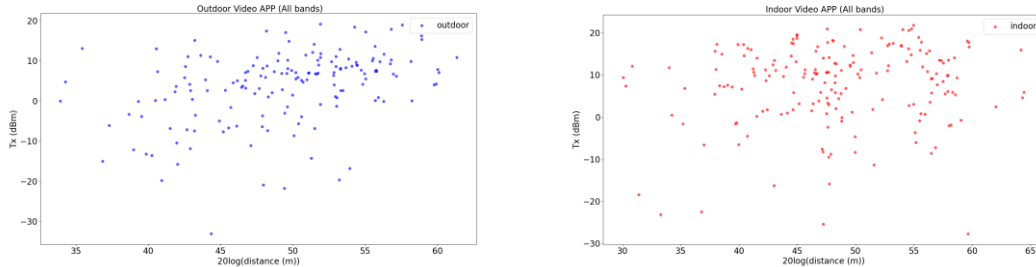


Figure 4 : averaged Tx power at a specific measurement point and linked BS distance in Video application

3.5 Correlations in different scenarios

The following table summarizes the Pearson correlation coefficients for both outdoor and indoor scenarios:

	Outdoor Scenario				Indoor Scenario			
	1st BS		2nd BS		1st BS		2nd BS	
	Tx	RSRP	Tx	RSRP	Tx	RSRP	Tx	RSRP
FTP	0.33	-0.46	0.31	-0.36	-0.16	-0.05	-0.24	-0.01
Video	0.38	-0.44	0.25	-0.34	-0.05	-0.01	-0.07	0.05
VOIP	0.4	-0.43	0.29	-0.33	-0.05	-0.01	-0.09	0.05
Voice	0.56	-0.54	0.53	-0.55	0.19	-0.22	0.16	-0.14

Table 1: Tx and $20\log(\text{distance})$ correlation

The outdoor scenario results in Table 1 clearly show higher positive correlation values, supporting the theoretical expectation that distance significantly influences Tx in open environments. Correlation results in Table 1 also clearly indicate that for outdoor scenarios, the decay in RSRP with increasing distance is more pronounced, validating the expected path loss behavior over larger distances. Indoor results on the other hand indicate a weak or inverse correlation. Voice call applications showed the highest outdoor correlations, likely due to unique power control requirements and shows the impacts of applications.

The variability observed among the different applications suggests that the type of service has a measurable impact on both downlink and uplink dynamics. This finding is important when considering the development of ANN-based prediction models.

3.6 Discussion

The results from our correlation studies underscore the essential role that both propagation environment and service type play in governing UL performance. Outdoor scenarios tend to adhere more closely to the theoretical models of path loss, while indoor environments introduce variability likely due to signal attenuation by physical structures. The detailed statistical analysis provided by Pearson correlation coefficients validates the expected trends.

The distinct differences observed across the various communication services (e.g., voice calls, video streaming) highlight the need for deeper exploration into uplink (UL) transmission behaviors. This insight is particularly valuable for the future development of machine learning models aimed at predicting UL EMF exposure, as it

suggests that traditional methods—which often generalize across services—may fail to address the unique transmission patterns and environmental factors inherent to real-world applications.

4 Conclusion

In summary, this study provides valuable insights into the correlation between UL transmission power and distance to the nearest matched BS, evaluated across multiple services and environments. These results provide foundational insights for developing machine learning models to predict UL EMF exposure. Future work should integrate additional variables and investigating UE behaviors in different applications.

References

- [1] ICNIRP et al., “Guidelines for limiting exposure to electromagnetic fields (100 kHz to 300 GHz),” *Health Physics*, vol. 118, pp. 483–524, 2020.
- [2] S. Wang and J. Wiart, “Sensor-aided EMF exposure assessments in an urban environment using artificial neural networks,” *International Journal of Environmental Research and Public Health*, vol. 17, p. 3052, Sep. 2020.
- [3] S. Wang, T. Mazloun, and J. Wiart, “Prediction of RF-EMF exposure by outdoor drive test measurements,” in *Proc. Telecom 3*, 2022, pp. 396–406.
- [4] J. Liu, Y. Zhang, W. B. Chikha, et al., “Assessment of EMF exposure induced by wireless cellular phones in various usage scenarios in France,” *IEEE Access*, 2024.
- [5] 3GPP, “Evolved Universal Terrestrial Radio Access (E-UTRA); Physical layer procedures,” 3GPP TS 36.213, 2021.

Localisation électromagnétique et radar, mesure des SER et des signatures

Metasurface for direction of arrival estimation *Métasurface pour l'estimation de la direction d'arrivée*

N. Meftah¹, B. Ratni¹, M. N. El Korso², S. N. Burokur¹

¹ LEME, Univ Paris Nanterre, F92410 Ville d'Avray, France, sburokur@parisnanterre.fr

² Université Paris-Saclay, CNRS, CentraleSupélec, Laboratoire des signaux et systèmes, 91190 Gif-sur-Yvette, France

Keywords: metasurface, reconfigurability, direction of arrival.

Mots clés : métasurface, reconfigurabilité, direction d'arrivée.

Abstract/ Résumé

A metasurface solution for the estimation of direction of arrival of electromagnetic waves is presented. The metasurface, which is programmable, is used as a reflector with an adjustable pointing direction to scan the azimuth plane for sensing and reflecting incoming waves to a power detector placed at a focal point, thereby estimating the incident direction. Furthermore, in order to achieve rapid and precise direction of arrival (DOA) estimation, a processing layer based on a pre-trained multilayer neural network is exploited to interpret variation in recorded power levels.

Une solution à base de métasurface est présentée pour estimer la direction d'arrivée des ondes électromagnétiques. La métasurface, qui est programmable, est utilisée comme un réflecteur où la direction de pointage est ajustable pour scanner l'azimut afin de capter et réfléchir les ondes incidentes vers un détecteur de puissance placé à un point focal, et ainsi estimer la direction d'arrivée. De plus, afin d'obtenir une estimation rapide et précise de la direction d'arrivée (DOA), une couche de traitement basée sur un réseau neuronal multicouche pré-entraîné est exploitée pour interpréter la variation des niveaux de puissance enregistrés.

1 Introduction

Direction of arrival (DOA) estimation, which consists in finding the direction of incoming waves, holds a major role in communications [1], localization [2] and tracking [3]. Due to its importance, various calculation methods and hardware structures have been developed in this field. In a general manner, DOA is estimated through the use of phased array antennas and various calculation methods [4], ranging from beamforming with Fast Fourier Transform (FFT) technique to algorithms such as MUSIC and ESPRIT [5]. Despite their remarkable resolution and accuracy, these algorithms present limitations in terms of computational and storage resources and their performance is significantly degraded for non-ideal conditions and imperfect antenna arrays.

Metasurfaces, which are composed of subwavelength unit cells, present the ability to manipulate electromagnetic waves at a subwavelength scale [6]-[8]. Hence, metasurfaces enable to design specific phase distributions that allow to manipulate scattering patterns [9]. As such, a programmable metasurface combined to a single receiver enables to extract direction information from variations in received power levels [10]-[12]. Deep learning algorithms have recently been proposed as interesting methods to treat complex problems while requiring moderate computational resources [13]-[14]. Hence, artificial intelligence appears to be a complementary method with respect to traditional algorithms for direction finding from simple and low-cost systems. A metasurface, assisted by artificial intelligence, has also been applied for efficient and accurate DOA estimation [15]. However, large amounts of data are still required, and computations remain time-consuming.

Here, we present a programmable flat metasurface reflector where the pointing direction can be adjusted by varying its voltage-controlled phase profile to scan the azimuth plane for DOA estimation. By continuously varying the pointing direction of the metasurface reflector, a series of power levels received by the detector is measured and recorded. When the received power level reaches a maximum, the corresponding pointing angle enables estimating the DOA. Then, a processing layer based on a pre-trained multilayer neural network is exploited to interpret the subtle variations in recorded power levels, enabling both fast and accurate DOA estimation without refining the scanning step of the metasurface reflector. Hence, the proposed system is able to estimate the DOA with an accuracy of 1° for a coarse angular scanning of the azimuth plane with step of 5° .

2 Platform architecture for DOA estimation

The schematic of the platform architecture exploited in this study to estimate the DOA is illustrated in Fig. 1. A programmable metasurface operating around 10 GHz, as designed in [16]. The metasurface is composed of 30×30 unit cells with periodicity $p = 6$ mm. Each cell consists of two copper strips having a width $w = 0.5$ mm and separated by a gap $g = 1.9$ mm incorporating a voltage-controlled varactor diode, all printed on a 1.52 mm thick dielectric substrate with relative permittivity $\epsilon_r = 4.5$. The metasurface is used as an electronically scannable reflector to redirect incoming signals toward a radiofrequency power detector at a focal point to record the power level for each electronic scanning. The phase profiles are electronically adjusted by a voltage control system biasing the varactor diodes incorporated in the metasurface. Cyllindro-parabolic phase profiles are applied to the metasurface as

$$\phi(x) = \frac{2\pi}{\lambda} \left(\frac{(x-x_0)^2}{4F} \right) + \phi_0 \quad (1)$$

where λ is the free space operating wavelength, $F (= 30$ mm) is the focal distance, and ϕ_0 denotes the reflection phase at location x_0 . The orientation of the virtual parabola is controlled by shifting x_0 from its original position for a specific reception direction in the azimuth plane.

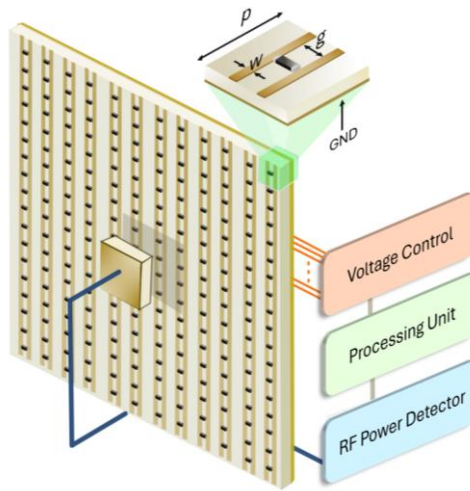


Figure 1: Architecture of the direction of arrival estimation system based on a programmable metasurface used as a parabolic reflector and a receiving antenna positioned at the focal distance. The geometric dimensions of the unit cell composing the metasurface are: $p = 6$ mm, $w = 0.5$ mm and $g = 1.9$ mm.

The first step consists in having a library of phase profiles versus pointing directions of the metasurface reflector. Hence, a patch antenna is placed at the focal point to illuminate the metasurface reflector, and the two are mounted and fixed on a rotating plate. A receiving horn antenna is fixed at a distance of 3 m to measure the wave reflected by the metasurface when the plate is rotated from -90° to $+90^\circ$. The two antennas (patch and horn) are both connected to a network analyzer and far-field measurements are performed for different parabolic phase profiles corresponding to specific x_0 offsets. 17 phase profiles, corresponding to 17 pointing angles from -40° to $+40^\circ$ by step of 5° , are selected to establish the library (Table I).

x_0 (mm)	-38	-34	-28	-24	-18	-14	-10	-6	0	+6	+10	+14	+18	+24	+28	+34	+38
θ ($^\circ$)	-40	-35	-30	-25	-20	-15	-10	-5	0	5	10	15	20	25	30	35	40

Table 1: Cyllindro-parabolic phase profiles applied for DOA estimation: corresponding scanning angles for x_0 shifts.

3 Deep learning algorithm and model training

For the DOA estimation, the patch antenna is connected to a spectrum analyzer, which acts as a radiofrequency (RF) power detector. A horn antenna is used at the transmitter end in the far-field region and is positioned on a semi-circular rail to launch electromagnetic waves within an azimuth angular range of -40° to $+40^\circ$ with a step as fine as 1° (81 different directions of arrival) toward the metasurface at the receiving end, as presented in Fig. 2a.

The 17 cylindro-parabolic phase distributions are sequentially applied to the metasurface reflector at the receiver end to scan the azimuth plane from -40° to $+40^\circ$ with 5° step. Hence, for each tested angle of arrival, the acquisition system records 17 power levels. The power levels collected at the end of the angular scanning process are then utilized during the estimation phase by a pre-trained Multilayer Perceptron (MLP) model to accurately estimate the DOA with a step resolution of 1° .

The 17 power levels correspond to the features of a sample associated with a given arrival angle. This procedure is repeated two more times for each arrival angle, resulting in a dataset of 243 samples distributed over 81 different targets. It should be noted that training models require a large amount of data to ensure proper generalization and prevent overfitting. To increase the size of our dataset without requiring additional experimentally measured data, a data augmentation technique is used to generate additional data instances. As such, Gaussian noise mimicking natural variations and experimental disturbances observed on the original samples, is introduced. Hence, for each sample in the initial dataset, five new samples are generated to achieve an augmented dataset of 1215 samples. This augmentation approach ensures the integrity of the data by avoiding to introduce bias or transformations that could alter the physical nature of the original data.

Before training, the data is subjected to a structured preprocessing pipeline comprising three steps to standardize the features and maximize the model's performance [17]. First, data normalization is performed by dividing each instance by its maximum, corresponding to bringing the measured floor to zero. Second, a logarithmic transformation is performed to amplify subtle variations in power levels, improving the distinction between features associated with closely spaced incoming angles and enhancing prediction accuracy. Finally, the data is standardized to have a zero mean and unity variance to ensure comparable training conditions across models. For each of the 17 features, the mean and the standard deviation over all samples related to the j^{th} feature are calculated and then applied in the following transformation:

$$x_{ij}^{std} = \frac{x_{ij}^{norm} - \mu_j}{\sigma_j} \quad (2)$$

where x_{ij} is the value of the feature j for the sample i , and $norm$ denotes the normalized data. The dataset is then decomposed into training and test sets, with 80% of the data intended for training and 20% reserved for efficiently testing the performance of the trained model on unseen data.

The MLP training model composed of several fully connected layers of neurons is considered. For evaluating the performances, we use the mean square error (MSE), which is given by:

$$MSE(\mathbf{y}, \hat{\mathbf{y}}) = \frac{1}{n} \sum_{i=1}^n (y_i - \hat{y}_i)^2 \quad (3)$$

where $\mathbf{y} = [y_1, \dots, y_n]$ and $\hat{\mathbf{y}} = [\hat{y}_1, \dots, \hat{y}_n]$, in which y_i is the real DOA value for the i^{th} sample and \hat{y}_i is the value predicted by the model. The MSE is minimized by the iterative learning of weights w and biases b , which is done by backpropagation and gradient descent. Adjustments are therefore made as:

$$w_{mn}^{(l)} = w_{mn}^{(l)} - \alpha \frac{\partial MSE}{\partial w_{mn}^{(l)}} \quad (4)$$

$$b_m^{(l)} = b_m^{(l)} - \alpha \frac{\partial MSE}{\partial b_m^{(l)}} \quad (5)$$

where α is the learning rate, controlling the size of the steps made in the opposite direction of the gradient to reach a local minimum. $w_{mn}^{(l)}$ is the weight between the n^{th} neuron in the $(l-1)^{\text{th}}$ layer and the m^{th} neuron in the l^{th} layer and $b_m^{(l)}$ is the bias associated with the m^{th} neuron in the l^{th} layer.

Bayesian optimization and cross-validation are combined to determine the optimal hyperparameters θ , including the number of layers, neurons, activation function type and learning rate. The optimization process starts by defining a search space for each hyperparameter. Then, cross-validation decomposes the training dataset into k folds, using a different fold each time as the validation set and the remaining $k-1$ for training. Until a convergence where the best performance is reached, the hyperparameters space is systematically explored by Bayesian optimization to identify those minimizing MSE through cross-validation:

$$\theta^* = \arg \min_{\theta} CV_{MSE} \left(MLP(\theta; X_{train}^{std}, Y_{train}) \right) \quad (6)$$

$CV_{MSE} \left(MLP(\theta; X_{train}^{std}, Y_{train}) \right) = \frac{1}{k} \sum_{i=1}^k MSE(y_i, \hat{y}_i)$ is the average of the mean squared errors calculated across the different folds of cross-validation, X_{train}^{std} is the standardized training set and Y_{train} are the corresponding target values. The iterative process gradually refines the choice of hyperparameters, promoting the generalization beyond training data in an effective manner.

4 Experimental validation of DOA estimation

The training performance of the MLP model is validated by the learning curve depicted in Fig. 2b, which demonstrates the absence of overfitting and underfitting, as evidenced by the convergence of the training and cross-validation scores with the increasing size of the training set. Evaluation of the performance of the MLP model on the test set reveals high accuracy in estimating DOA with a mean square error (MSE) of 0.3°^2 . The results show that the MLP training model is robust against noisy data, an essential feature given the fixed objective that the model focuses on learning the trends in power distribution while disregarding noise and fluctuations between different samples. Fig. 2c presents the tight correlation between predicted and actual DOA values, where the linearity of the scattered points confirms the effectiveness of the model. Moreover, a detailed analysis of the prediction errors reveals that 94% of the predictions show less than 1° error, demonstrating the exceptional accuracy of the model.

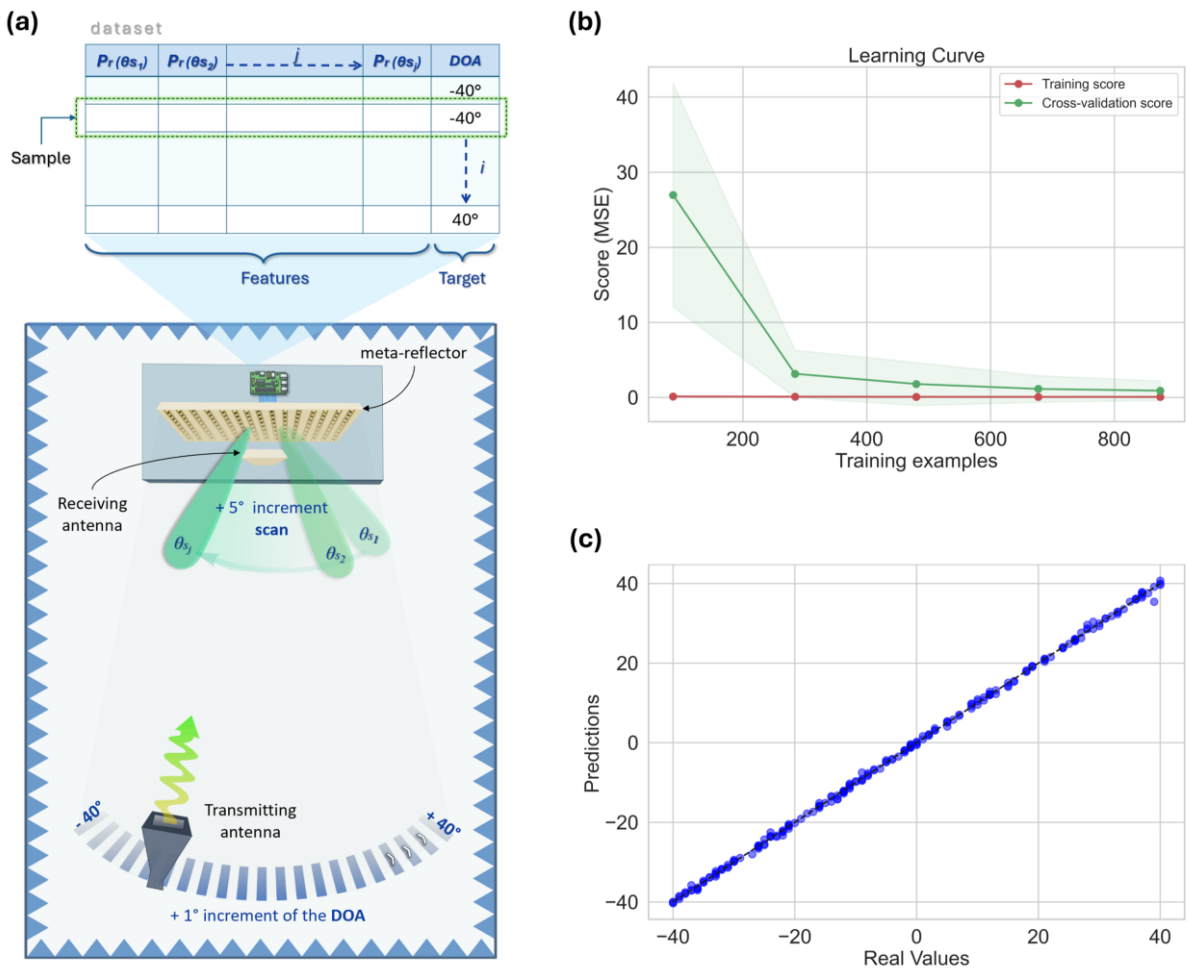


Figure 2: (a) Schematic principle of the metasurface-based platform for DOA estimation. (b) Learning curve of the MLP model for the DOA estimation. (c) Comparison of predicted vs. real DOA values.

5 Conclusions

In this work, a fast and accurate method for estimating DOA has been presented. The platform consists of a programmable metasurface reflector, assisted by deep learning. Our approach takes advantage of the flexibility and speed of reconfiguration of programmable metasurfaces to apply a series of parabolic phase profiles scanning the horizon in search of the direction of arrival of the incoming signal. As such, with a coarse angular scanning of the azimuth plane with step of 5° , the proposed system is able to estimate the DOA with an accuracy of 1° .

References

- [1] S. Roger, M. Cobos, C. Botella-Mascarell, and G. Fodor, "Fast channel estimation in the transformed spatial domain for analog millimeter wave systems," *IEEE Trans. Wireless Commun.*, vol. 20, no. 9, pp. 5926–5941, 2021.
- [2] G. Pau, F. Arena, Y. E. Gebremariam, and I. You, "Bluetooth 5.1: an analysis of direction finding capability for high-precision location services," *Sensors*, vol. 21, no. 11, p. 3589, 2021.
- [3] Y. Tian, S. Liu, W. Liu, H. Chen, and Z. Dong, "Vehicle positioning with deep-learning-based direction-of-arrival estimation of incoherently distributed sources," *IEEE Internet Things J.*, vol. 9, no. 20, pp. 20083–20095, 2022.
- [4] M. Haardt, M. Pesavento, F. Roemer, and M. N. El Korso, "Subspace methods and exploitation of special array structures," in *Acad. Press Libr. Signal Process.: vol. 3* (Eds.: A. M. Zoubir, M. Viberg, R. Chellappa, S. Theodoridis), Elsevier, pp. 651-717, 2014.
- [5] P. K. Eranti and B. D. Barkana, "An overview of direction-of-arrival estimation methods using adaptive directional time-frequency distributions," *Electronics*, vol. 11, no. 9, p. 1321, 2022.
- [6] V. Popov, B. Ratni, S. N. Burokur, and F. Boust, "Non-local reconfigurable sparse metasurface: efficient near-field and far-field wavefront manipulations," *Adv. Opt. Mater.*, vol. 9, no. 4, p. 2001316, 2021.
- [7] R. Feng, B. Ratni, J. Yi, H. Zhang, A. de Lustrac, and S. N. Burokur, "Versatile metasurface platform for electromagnetic wave tailoring," *Photon. Res.*, vol. 9, no. 9, pp. 1650–1659, 2021.
- [8] L. Li, H. Zhao, C. Liu, L. Long, and T. J. Cui, "Intelligent metasurfaces: control, communication and computing," *eLight*, vol. 2, p. 7, 2022.
- [9] B. Ratni, Z. Wang, K. Zhang, X. Ding, A. de Lustrac, G.-P. Piau, and S. N. Burokur, "Dynamically controlling spatial energy distribution with a holographic metamirror for adaptive focusing," *Phys. Rev. Appl.*, vol. 13, no. 3, p. 034006, 2020.
- [10] T. V. Hoang, V. Fusco, M. A. B. Abbasi, and O. Yurduseven, "Single-pixel polarimetric direction of arrival estimation using programmable coding metasurface aperture," *Sci Rep*, vol. 11, no. 1, Art. no. 1, 2021.
- [11] J. W. Wang, Z. A. Huang, Q. Xiao, W. H. Li, B. Y. Li, X. Wan, and T. J. Cui, "High-precision direction-of-arrival estimations using digital programmable metasurface," *Adv. Intell. Syst.*, vol. 4, no. 4, p. 2100164, 2022.
- [12] N. Meftah, B. Ratni, M. N. El Korso, and S. N. Burokur, "Programmable meta-reflector for multiple tasks in intelligent connected environments," *Adv. Mater. Technol.*, vol. 9, no. 12, p. 2400006, 2024.
- [13] H.-Y. Li, H.-T. Zhao, M.-L. Wei, H.-X. Ruan, Y. Shuang, T. J. Cui, P. del Hougne, and L. Li, "Intelligent electromagnetic sensing with learnable data acquisition and processing," *Patterns*, vol. 1, no. 1, p. 100006, 2020.
- [14] C. Qian, B. Zheng, Y. Shen, L. Jing, L. Erping, L. Shen, and H. Chen, "Deep-learning-enabled self-adaptive microwave cloak without human intervention," *Nat. Photon.*, vol. 14, pp. 383–390, 2020.
- [15] M. Huang, B. Zheng, T. Cai, X. Li, J. Liu, C. Qian, and H. Chen, "Machine-learning-enabled metasurface for direction of arrival estimation," *Nanophotonics*, vol. 11, no. 9, pp. 2001-2010, 2022.
- [16] B. Ratni, A. de Lustrac, G.-P. Piau, and S. N. Burokur, "Reconfigurable meta-mirror for wavefronts control: applications to microwave antennas," *Opt. Exp.*, vol. 26, no. 3, pp. 2613–2624, Feb. 2018.
- [17] N. Meftah, B. Ratni, M. N. El Korso, and S. N. Burokur, "Enhanced-resolution learning-based direction of arrival estimation by programmable metasurface," *Adv. Electron. Mater.*, vol. 11, no. 3, p. 2400476, 2025.

Localization of Metallic Lost Tools Using UHF RFID System

Hamrouni Nawres 1, Baccar Sahbi 1, Khalifeh Rania 1, Madjid Haddad 2

¹ *UNIROUEN, ESIGELEC, IRSEEM: Electronics and Systems Department, Saint-Etienne-du-Rouvray, France*
nawresatidel.hamrouni@gmail.com, Sahbi.Baccar@esigelec.fr, Rania.khalifeh@esigelec.fr

² *SEGULA Technologies: R&I, SEGULA Engineering, Rueil Malmaison, France, madjid.haddad@segula.fr*

Keywords: RFID localization, mettalic object tracking, multipath propagation

Abstract/Résumé

This paper presents an enhanced approach for localizing metallic objects in complex industrial environments using UHF RFID technology. We present an improved algorithm based on the Three-Ray Ground Reflection Model that addresses the limitations of traditional RSSI-based methods. Our solution demonstrates significant improvements in accuracy and reliability compared to conventional approaches, particularly in environments with multiple interference sources and reflection paths.

Cet article présente une approche améliorée de la localisation d'objet métalliques dans des environnements industriels complexes basée sur la technologie RFID UHF. Nous présentons un algorithme amélioré basé sur le modèle de réflexion à trois rayons qui compense les limitations des méthodes traditionnelles basées sur le RSSI. Notre solution offre une précision et une fiabilité accrues par rapport aux approches conventionnelles, en particulier, dans les environnements avec source multiple d'interférences et chemins de réflexions.

1 Introduction

Lost or misplaced metallic objects can lead to extended downtimes, significant financial losses, and operational disruptions. Therefore, accurate and reliable localization methods have become a critical area of research and development. While UHF RFID technology has been widely explored as a promising solution for object tracking due to its low cost, scalability, and non-line-of-sight capabilities, traditional methods often suffer from significant limitations. Specifically, they are vulnerable to signal interference, multipath effects, and reflections from metallic surfaces, all of which contribute to reduced localization accuracy and system reliability. Several previous studies have addressed these challenges through different approaches. IoT-based smart warehouse systems have been proposed, integrating RFID with wireless sensor networks to enhance localization and environmental monitoring [1]. Deyle et al. [2] optimized the received signal strength for object detection in domestic environments using directional antennas and sparse sampling strategies, while DiGiampaolo and Martinelli [3] developed a two-stage probabilistic framework based on phase measurements for tracking RFID-tagged objects on warehouse shelves. Despite these, existing methods still face serious challenges when deployed in complex industrial environments with numerous metallic surfaces. Our research aims to improve localization accuracy in advanced industrial facilities. In particular, we propose an enhanced localization algorithm based on the Three-Ray Ground Reflection Model, which more accurately captures the key signal propagation phenomena: direct transmission, ground reflection, and object reflection that dominate in metallic environments. By leveraging phase measurements instead of relying on RSSI, and by integrating the complex multipath behavior into the model, our approach significantly enhances localization precision and robustness.

The rest of this paper is organized as follows: Section 2 describes the proposed localization algorithms and details the Three-Ray Ground Reflection Model. Section 3 presents the implementation flow, simulation setup, and key experimental results. Section 4 concludes the paper with a summary of contributions and future perspectives for industrial deployment.

2 State of Art

The problem of RFID-based localization, particularly in environments with metallic interference, has been actively studied in recent years. Early methods based solely on RSSI measurements were shown to be highly sensitive to multipath effects and environmental noise, leading to limited accuracy in industrial contexts. To address these challenges, models based on phase information and electromagnetic propagation characteristics have been proposed. The work by DiGiampaolo and Martinelli [3] introduced a mobile robot localization technique based on the phase of passive UHF RFID tags. Their system collects phase measurements along a

planned trajectory and matches them to an electromagnetic model to estimate the tag position. Specifically, they proposed a two-stage localization strategy:

- First, the robot moves along a path parallel to a shelf to estimate the horizontal coordinate of the tag, exploiting the symmetry of the phase pattern.
- Second, a movement perpendicular to the shelf allows estimation of the vertical coordinate, refining the tag position.

The phase model used in their approach relates the measured phase ϕ_i at a robot position $s_i=(x_i, y_i, z_R)$ to the tag position (x_T, z_T) through equation 1.

$$\phi_i = \text{mod}\left(-2K\sqrt{(x_i - x_T)^2 + y_i^2 + (z_R - z_T)^2} + \phi_d + \theta_n, \pi\right) \quad (1)$$

Where :

$K = \frac{2\pi}{\lambda}$: The wavenumber,

ϕ_d : Represents a constant phase offset,

θ_n : The measurement noise,

and the modulus operation accounts for phase wrapping due to limited unambiguous range.

This model exploits the fact that phase variations exhibit a local maximum when the robot passes directly in front of the tag, corresponding to the point of minimal distance. While this approach proves highly effective in semi-structured environments like warehouses, it relies on relatively simple propagation assumptions and primarily considers direct-path transmission. In contrast, real-world industrial environments often involve significant signal degradation caused by ground reflections, object-induced multipath effects, and metallic clutter. These conditions severely impact phase consistency and localization precision.

In parallel with this theoretical analysis, we developed and tested an initial localization method, referred to as Algorithm A. This approach uses a grid-based Breadth-First Search (BFS) strategy combined with Received Signal Strength Indicator (RSSI) measurements. The user or robot starts at a known entry point (typically at coordinates (0,0)) and explores adjacent positions in the grid. At each step, RSSI values are measured and compared across directions (e.g., positions (1,0) and (0,1)). The system then moves toward the direction with the stronger RSSI signal, gradually converging toward the tag location. The logical flow of this method is illustrated in Figure 1.

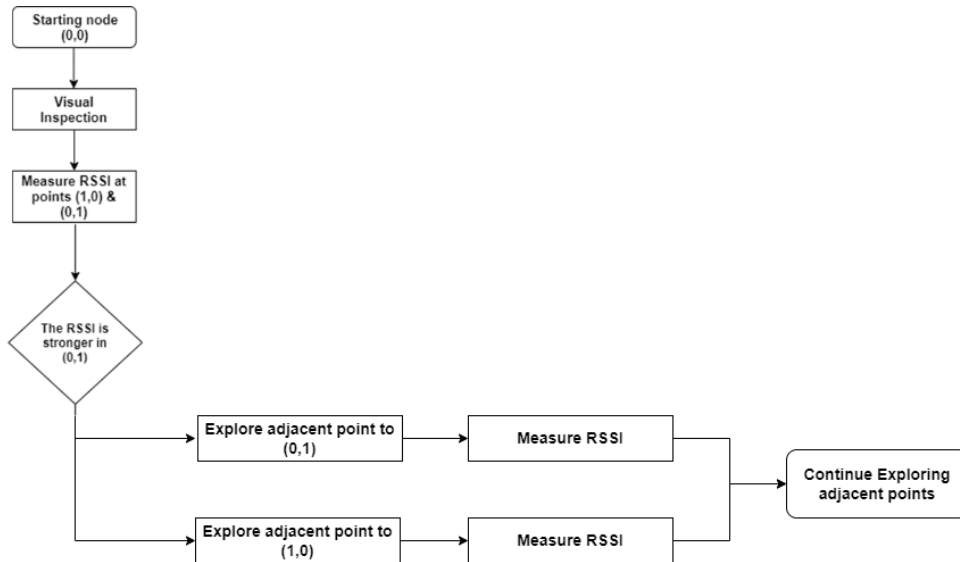


Figure 1: Algorithm A : Step by Step Execution Flow

Although Algorithm A offers a simple and low-cost solution, it suffers from severe limitations in metallic environments. Strong reflections and multipath interference often cause unpredictable fluctuations in RSSI, which can mislead the system and lead to false convergence. Building on this foundation, our work introduces an enhanced phase-based localization approach, incorporating a more advanced signal propagation model :The

Three-Ray Ground Reflection Model. This approach represents the main multipath components encountered in metallic industrial settings and enables accurate tag localization even under complex environmental conditions.

3 Proposed Method: The Three Ray Ground Reflection Model

To overcome the limitations observed with traditional RSSI-based methods and basic grid exploration strategies (Algorithm A), we developed a new localization approach tailored for metallic environments, referred to as Algorithm B. This method leverages a refined electromagnetic propagation model based on the Three-Ray Ground Reflection Model to improve localization accuracy and robustness.

Unlike traditional models that consider only the direct path between the reader and the RFID tag, the Three-Ray Ground Reflection Model incorporates three distinct signal components that influence the received signal:

- Direct Path (d_1): The straight-line signal traveling directly from the transmitter T_x to the tag R_x .
- Ground-Reflected Path (d_2): The signal that reflects off the ground surface before reaching the tag.
- Object-Reflected Path (d_3): The signal that reflects off the surface of the metallic object itself before being received.

These three propagation paths contribute to the final signal phase and amplitude detected at the reader. The model illustrated in Figure 2 provides a more accurate and realistic representation of signal behavior in environments where metallic surfaces introduce significant multipath interference. In this context, x_r represents the horizontal distance between the transmitter and the receiver. This distance directly affects the calculation of the path lengths d_1 , d_2 , and d_3 , which in turn influence both the signal phase and strength at the receiver.

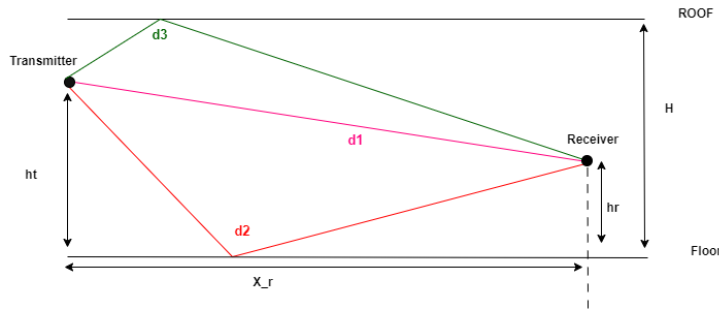


Figure 2:: Visualization of the Three-Ray Ground Reflection Model

By considering these three contributions, the model better captures the complex multipath behavior typical of industrial environments, where reflections and interference are prevalent. Each path introduces different phase shifts and signal strengths, and their combination affects the measured phase at the reader.

To analyse the effect of these paths on the signal phase, it is necessary to quantify the phase shifts introduced by each path relative to the direct path. In the context of multipath propagation, it is critical to evaluate the phase difference introduced by each reflected signal path relative to the direct path. These differences directly influence the total measured phase at the receiver due to constructive or destructive interference. Specifically, the phase differences between the direct path and the reflected paths, equation 2 define the ground-reflected path and the object-reflected path :

$$\Delta\phi_g = \frac{2\pi}{\lambda}(d_2 - d_1) ; \Delta\phi_o = \frac{2\pi}{\lambda}(d_3 - d_1) \quad (2)$$

Where d_1 is the length of the direct path, d_2 is the length of the ground-reflected path, and d_3 is the length of the object-reflected path visualize in figure 2. To model the phase behavior of the signals with high accuracy, we developed a new phase equation based on trigonometric identities, specifically the Law of Cosines (also known as Al-Kashi's theorem). Equation 3 describes the geometric relationships between the RFID reader, the RFID tag, and the reflection points, allowing the determination of phase differences between different signal paths.

The key angles involved in this model such as the angles of incidence and reflection are critical for linking the heights of the transmitter and receiver with the horizontal distances separating them. To accurately describe the propagation paths, we applied fundamental trigonometric principles to these geometric relationships. By leveraging triangle similarity and applying the Law of Cosines, we established precise mathematical expressions that relate the horizontal distance, the heights of the reader and tag, and the signal propagation angles. These relationships allow us to calculate exact path lengths, which are essential for determining the phase differences

between the direct and reflected signals. In the subsequent calculations, we derive the phase difference by define in equation 3 directly using these geometric formulas.

$$\Delta\phi = \frac{2\pi}{\lambda} \left(\frac{((H-h_t)+(H-h_r))\sqrt{d^2-4(H-h_t)(H-h_r)}}{\sqrt{(H-h_t)^2+(H-h_r)^2}-2(H-h_t)(H-h_r)} - \sqrt{(h_r-h_t)^2+d^2} \right) \quad (3)$$

This detailed modeling enables more accurate estimation of phase differences caused by geometry and environmental features. It forms the core of the Three-Ray Ground Reflection Model and is fundamental to our phase-based localization strategy. Unlike simpler models, this approach adapts to realistic configurations and provides enhanced resolution in complex industrial environments.

To account for multiple signal paths, the total received signal $r_{tot}(t)$ is defined in the equation 4 as the coherent sum of all individual signal components $r_i(t)$ arriving at the receiver from different propagation paths, including the direct path and reflected paths.

$$r_{tot}(t) = \sum_{i=1}^N r_i(t) \quad (4)$$

Each $r_i(t)$ represents a signal that travels along a specific path of length d_i , with its own strength and phase shift.

The received power P_r is computed as the time-averaged squared magnitude of the total received signal, as defined in equation (5) for the Three-Ray model. This formulation offers a more precise characterization of signal behavior in complex industrial environments, where multipath effects and reflections significantly impact signal strength and phase.

$$P_r = \langle |r_{tot}(t)|^2 \rangle = P_r = P_{los}(1 + r_1^2 + r_2^2 + 2r_1 \cos(\Delta\phi_1) + 2r_2 \cos(\Delta\phi_2) + 2r_1 r_2 \cos(\Delta\phi_1 - \Delta\phi_2)) \quad (5)$$

Where :

$$P_{los} = \frac{G\lambda^2}{(4\pi d)^2}$$

$$r_1 = \frac{d}{x_1 + x'_1} : \text{The ratio for the ground-reflected path,}$$

$$r_2 = \frac{d}{x + x'} : \text{The ratio for the object-reflected path,}$$

$\Delta\phi_1$ and $\Delta\phi_2$: The phase differences between the direct path and each reflected path, respectively

3.1 Simulation and Evaluation

To evaluate the proposed phase-based localization approach, we implemented Algorithm B based on the Three-Ray Ground Reflection Model. The algorithm operates by comparing measured phase values with theoretical phase patterns generated from the model, identifying the location that minimizes the phase error.

The logic of the algorithm is illustrated in Figure 3, which outlines the two-step estimation process: first along the x-axis (parallel movement) and then along the y-axis (orthogonal refinement). At each step, the reader collects phase data, which are then matched to predicted phase curves.

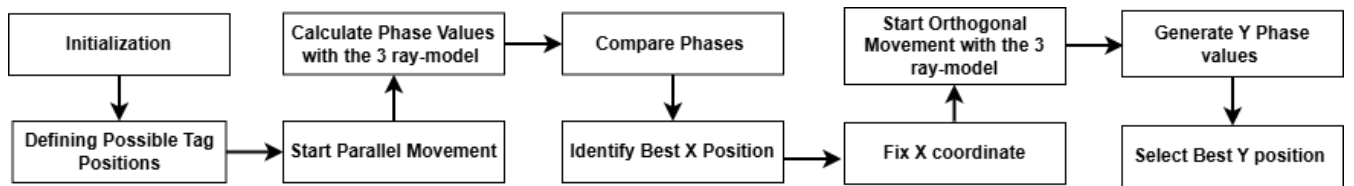


Figure 3 : Flowchart of the simulation based localization algorithm

For each tag position, the simulation computed predicted phase values using the multi-ray model and compared them to measured phases along discrete X-axis positions. The position with the lowest Mean Squared Error (MSE) was selected as the best estimate. As shown in Figure 4, the peak in measured phase indicates the estimated X-coordinate of the tag, allowing the algorithm to localize the tag accurately along the X-axis.

Once the X-coordinate was determined, the algorithm proceeded with a similar process along the Y-axis, using orthogonal movement to refine the tag's vertical position. The simulation estimated the tag's position with high accuracy, yielding an X-coordinate of approximately 4.49 (close to the actual 4.5) and a Y-coordinate of 0.0, matching the true location. Figure 5 illustrates this precision, showing the close alignment between estimated and actual positions along both axes. These results validate the effectiveness of the proposed multi-ray localization algorithm in accurately identifying tag positions, even in multipath environments.

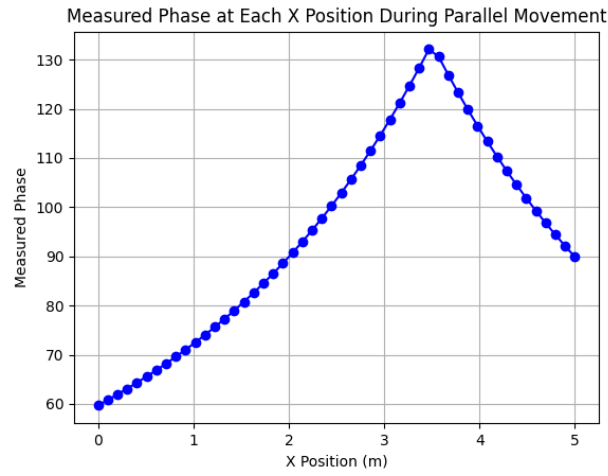


Figure 4 : Measured Phase at Each X Position During Parallel Movement

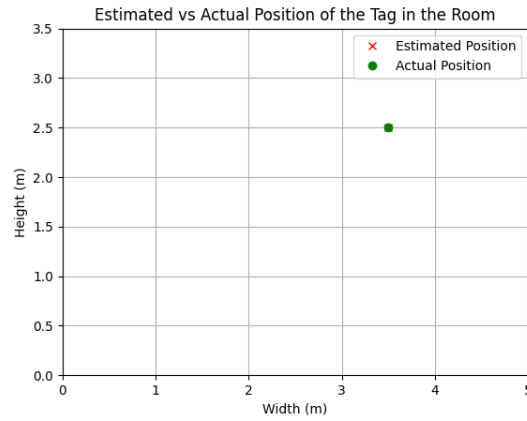
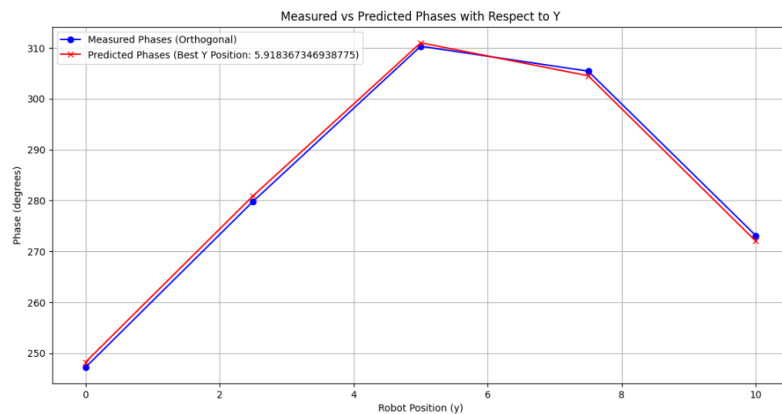


Figure 5 : Comparison of Estimated and Actual Tag Position with Phase Prediction Analysis

Furthermore , figure 6 compares measured and predicted phase values during both stages of the localization process: parallel (X-axis) and orthogonal (Y-axis) movements. In the parallel phase, the close alignment between the measured and predicted curves confirms the accuracy of the estimated X-coordinate . Similarly, in the orthogonal phase, the estimated Y-coordinate closely matches the predicted values, further validating the algorithm’s effectiveness in refining tag localization through two-axis phase analysis.



4 Conclusion

This work addressed the challenge of localizing metallic objects using UHF RFID in complex industrial environments. Two algorithms were developed and evaluated: Algorithm A, based on RSSI and grid movement, performed adequately in simple settings but struggled with multipath interference. To overcome these limitations, Algorithm B was introduced, using a Three-Ray Ground Reflection Model and later extended to a Five-Ray and generalized N-Ray model. This advanced approach incorporates phase calculations and multiple reflection paths, offering significantly improved accuracy in metallic environments. The results confirm the potential of multi-ray RFID models for reliable object localization and highlight promising directions for future research and industrial application.

References

- [1] M. N. Borenovic and A. M. Neskovic, "Comparative analysis of rssi, snr and noise level parameters applicability for wlan positioning purposes," in *IEEE EUROCON 2009*, IEEE, 2009, pp. 1895–1900.
- [2] T. Deyle, M. S. Reynolds, and C. C. Kemp, "Finding and navigating to household objects with UHF RFID tags by optimizing RF signal strength," in *2014 IEEE/RSJ International Conference on Intelligent Robots and Systems*, IEEE, 2014, pp. 2579-2586.
- [3] E. DiGiampaolo and F. Martinelli, "A robotic system for localization of passive UHF RFID tagged objects on shelves," *IEEE Sensors Journal*, vol. 18, no. 20, pp. 8558-8568, 2018.

**Surveillance de foule à l'aide d'une antenne à ondes de fuite dans une
communication et détection intégrées**
*Leaky-wave antenna-based crowd monitoring in Integrate Sensing and
Communications*

Philippe De Doncker¹, Julien Sarrazin², Mathis Melki³

¹*OPERA - Wireless Communications Group, Ecole Polytechnique de Bruxelles (EPB), Université Libre de Bruxelles (ULB), {philippe.dedoncker}@ulb.be*

²*Sorbonne Université, CNRS, Laboratoire de Génie Électrique et Électronique de Paris, 75252, Paris, France
Université Paris-Saclay, CentraleSupélec, CNRS, Laboratoire de Génie Électrique et Électronique de Paris,
91192, Gif-sur-Yvette, {julien.sarrazin}@sorbonne-universite.fr*

³*École Polytechnique de Bruxelles (EPB), Université libre de Bruxelles (ULB), {mathis.melki}@ulb.be*

Keywords: Leaky-Wave Antenna, Monostatic radar processing, Crowd monitoring.

Mots clés : Antenne à ondes de fuite, Traitement radar monostatique, Détection de foule.

Résumé/Abstract

Radar systems utilize electromagnetic signals to detect and track multiple human targets. This study focuses on multi-target tracking using range, Doppler, and Angle-of-Arrival (AoA) measurements from a monostatic radar system. Human crowds are modeled as dielectric cylindrical shells interacting with an incident electromagnetic field. The scattered field generated by the targets is processed to extract channel transfer function coefficients, enabling the derivation of range and Doppler profiles. A key novelty of this work is the use of a leaky-wave antenna at the receiver, which enables AoA estimation with a single-port antenna, therefore reducing system complexity, cost and eliminating the potential phase shift discrepancies inherent to multi-receiver configurations.

Les systèmes radar utilisent des signaux électromagnétiques pour détecter et suivre plusieurs cibles humaines. Cette étude se concentre sur le suivi de cibles multiples par une estimation de distance, d'effet Doppler et d'angle d'arrivée provenant d'un système radar monostatique. Une foule humaine est modélisée par des cylindres diélectriques interagissant avec un champ électromagnétique incident. Le champ diffusé généré par les cibles est traité pour extraire les coefficients de la fonction de transfert du canal, ce qui permet d'obtenir la distance et l'effet Doppler. La principale nouveauté de ce travail est l'utilisation d'une antenne à ondes de fuite comme récepteur, qui permet d'estimer l'angle d'arrivée avec une antenne à port unique, réduisant ainsi la complexité et le coût du système et éliminant les divergences potentielles de déphasage inhérentes aux configurations multirécepteurs.

1 Introduction

The rapid deployment of wireless communication networks has created new opportunities for Integrated Sensing and Communication (ISAC), where the same infrastructure can be leveraged for both data transmission and environmental sensing. By repurposing existing communication signals for radar-like applications, ISAC enables sensing without requiring dedicated transmitters. This approach is particularly promising in the context of 5G and beyond, as the increased bandwidth availability and the flexible numerology of modern communication waveforms such as Orthogonal Frequency-Division Multiplexing (OFDM) facilitate advanced sensing capabilities, including fine-grained motion tracking and environmental awareness [1]. Traditional radar setups exploit these ambient communication signals to track movement but typically require multiple receivers for Angle-of-Arrival (AoA) estimation, while range and Doppler measurements can be obtained with a single receiver. These configurations introduce hardware complexity and potential issues due to phase shift discrepancies between receiver channels.

This study proposes an alternative approach using a single leaky-wave antenna (LWA) as the receiver, operating at 27 GHz with a 400 MHz bandwidth, to achieve comparable performance in range and Doppler estimation while eliminating the phase shift issues inherent in multi-receiver setups. We use OFDM signals based on 5G standards for radar sensing, leveraging their wide bandwidth flexible numerology. The unique frequency-dependent radiation properties of the LWA enable AoA estimation using the MUSIC (Multiple Signal Classification) algorithm without requiring multiple antennas, significantly simplifying hardware requirements. This novel approach takes advantage of ISAC to reduce system complexity while maintaining high-resolution human sensing capabilities, with potential applications in indoor monitoring, crowd behavior analysis, and smart environment interaction.

2 Crowd Monitoring Scenario Description

Crowd monitoring is a crucial aspect of public safety and event management. Tragic incidents, such as the Hillsborough disaster (UK, 1989) and the Astroworld festival tragedy (USA, 2021), highlight the need for real-time

crowd tracking to prevent dangerous levels of congestion [2]. A key factor in crowd management is crowd counting, which allows security personnel to assess density levels and take proactive measures before critical thresholds are exceeded. Additionally, sensing applications gain increasing attention for indoor people tracking and object detection, with use cases including movement classification, intruder detection, and security monitoring in public spaces. However, crowd monitoring must also respect privacy concerns, making non-intrusive solutions that do not rely on cameras particularly desirable. Radar-based sensing offers a viable alternative, enabling real-time tracking while preserving anonymity and mitigating ethical concerns related to visual surveillance.

We explore the feasibility of a radar system for crowd monitoring using a monostatic radar channel, where the transmitter (TX) and receiver (RX) are collocated. The physical medium is free space. TX is modeled as a y -directed lossless $\lambda/2$ dipole, while RX is a leaky-wave antenna receiving signals in the XZ plane. This configuration has been chosen to simplify calculations while remaining consistent with LWA equations, the scan is performed along θ , the elevation angle, within the XZ plane, with $\varphi = 0^\circ$. This 2D plane can be rotated accordingly to match the desired orientation. The system operates using OFDM waveforms inspired by 5G standards like Sounding Reference Signals (SRS) generally used for channel estimation. This waveform choice supports precise range and Doppler estimation, making it particularly suited for tracking human movement in crowded environments.

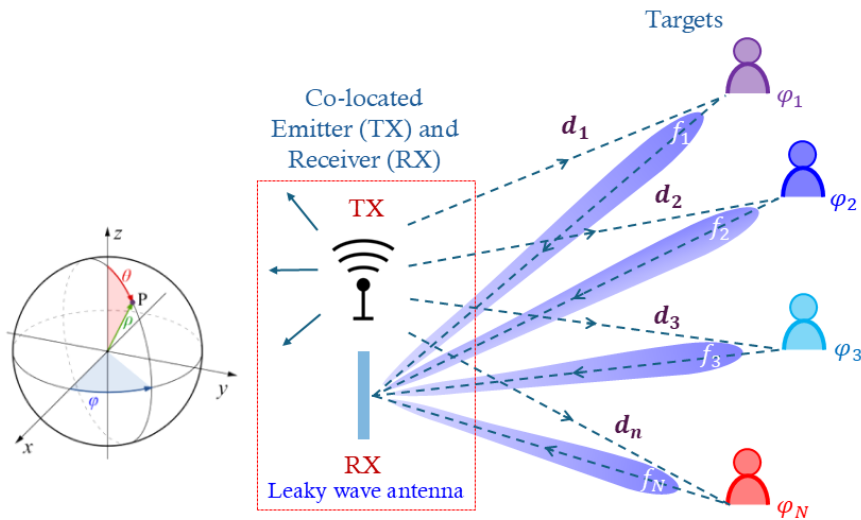


Figure 1: Scenario Description

3 Leaky-Wave Antenna

LWA unique property is its frequency-dependent radiation pattern. Unlike conventional antennas, LWA exploits a dispersive leaky-wave propagation mode, leading to an angle-dependent frequency relationship given by:

$$\cos \theta = \frac{\beta_z}{k_0}$$

Where θ is the receive beam orientation, β_z is the phase constant along the antenna and $k_0 = \frac{2\pi}{\lambda}$ is the free-space wavenumber. This property enables the LWA to act as a natural spatial filter, where different frequency components of the received signal correspond to different angles of arrival. Humans are represented by an infinite cylinder, serving as a target positioned at a random distance d from TX/RX. This simplification is useful to determine the radar cross section of a human and derive the scattered electric field on a target.

To derive the LWA radiation pattern, an air-filled rectangular waveguide with a longitudinal slot is considered. From the equivalence principle and image theory [3][4], the radiation from this structure in region $x > 0$ is approximately due to a z -directed magnetic line current flowing along the z -axis. To simplify, the radiation pattern is assimilated to the Array Factor (AF) of the LWA. The term "Array Factor" in the context of LWAs does not represent an array factor in the traditional sense used for antenna arrays. Instead, it is a mathematical construction used to quantify the contribution of the leaky-wave structure to the overall radiation pattern. Specifically, it describes the factor by which the electric field of an infinitesimal element along the waveguide is multiplied to account for the radiative properties of the LWA. Fig.2 illustrates frequencies responses for different AoAs.

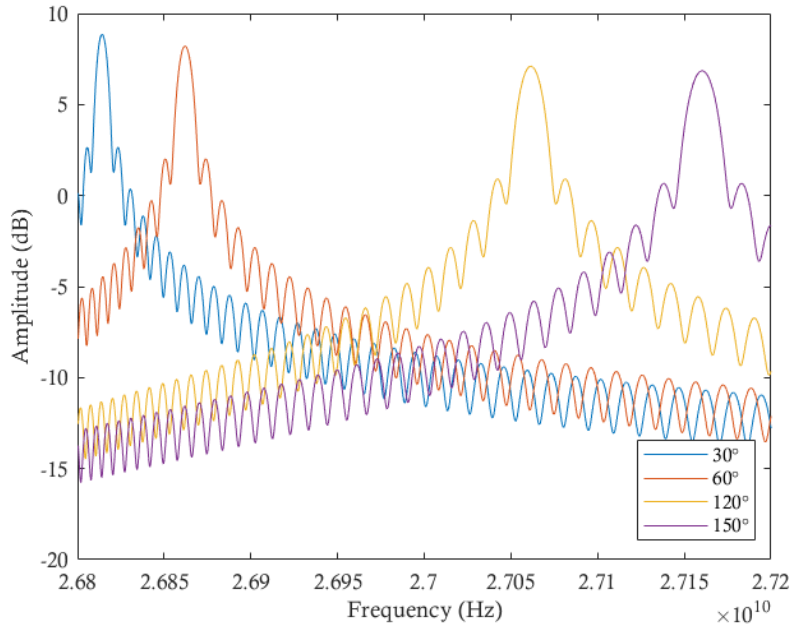


Figure 2: LWA Radiation Pattern

4 Aim of the study

The outlined scenario is well-suited for the Geometry-Based Single Bounce Model (GBSBM), which is commonly employed in radar applications. This model considers only the direct path between the transmitter (TX) and receiver (RX), as well as the first-order reflections from the target, which contribute significantly to the received signal. In the case of a monostatic radar configuration, where the TX and RX are collocated, there is no direct line-of-sight (LOS) path between them. Instead, the primary propagation path is defined by the first-order reflection from the target, which forms a TX-Target-RX path. In this context, the system operates similarly to a classical monostatic radar setup, where the primary goal is to derive the Channel Transfer Function (CTF). The CTF captures the key characteristics of the radar channel, including propagation delays and Doppler shifts that are induced by the motion of the target. These parameters are critical for accurately estimating the range and speed of the target.

This study evaluates the performance of a leaky-wave antenna (LWA) as a receiver compared to classic monostatic radar systems. The LWA radiation pattern might be seen as a windowing effect in the CTF, leading to a spread in the Channel Impulse Response (CIR). Finally, the Doppler-FFT is applied to the CIR to obtain the Range-Doppler Map (RDM). The results demonstrate that the LWA maintains accuracy in target localization while reducing hardware complexity. An example is shown in Fig. 2 for a single target located at 10m with a speed of 4m/s moving away from TX/RX with $\theta = 30^\circ$ and a SNR of 10 dB.

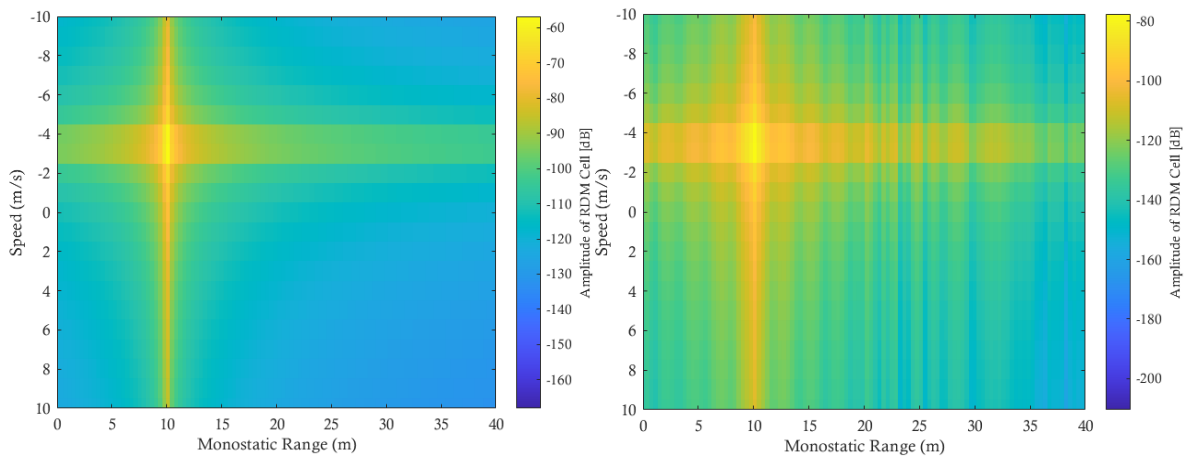


Figure 2: Range Doppler Map with a classic monostatic radar system (left) and with the LWA (right)

While the range and speed are accurately estimated in both cases, the use of the LWA introduces a spread and attenuation effect on the Range-Doppler Map (RDM). This effect arises because the LWA acts as a spatial filter, selectively receiving different frequency components at different angles. Consequently, unlike a conventional omnidirectional receiver that captures the full bandwidth uniformly, the LWA inherently modifies the received signal spectrum based on the angular distribution, leading to a spread and attenuation in the RDM representation. Nevertheless, the LWA provides the significant advantage of providing AoA estimation shown in Fig. 3, which is not possible with a traditional monostatic radar setup.

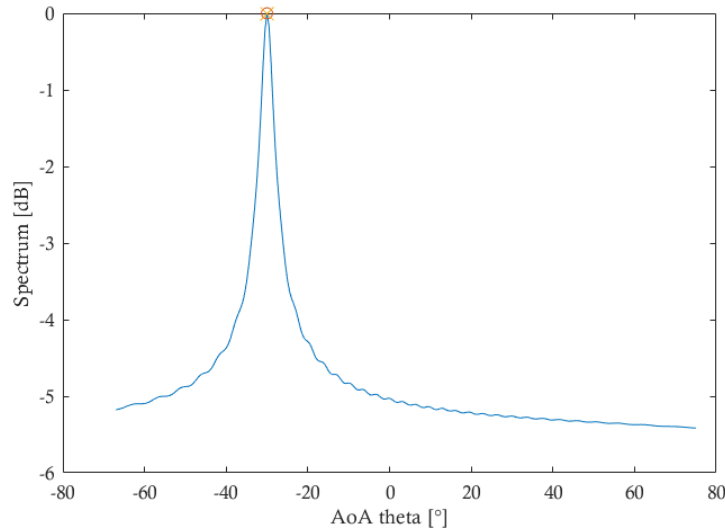


Figure 3: MUSIC Pseudospectrum

Future work will explore multi-receiver configurations to enable triangulation, enhancing real-time tracking capabilities in dynamic environments with minimal receiver infrastructure. This will simplify the radar system and make it more efficient, while still providing accurate localization and tracking of multiple targets, even in complex environments with limited receiver hardware.

5 References

- [1] Z. Wei and F. Liu and C. Masouros and N. Su and A. P. Petropulu, Toward Multi-Functional 6G Wireless Networks: Integrating Sensing, Communication, and Security, *IEEE Communications Magazine*, 4, p. 65-71, 2022
- [2] G. K. Still, *Introduction to crowd science*. CRC Press, 2014
- [3] C. A. Balanis. *Antenna Theory: Analysis and Design*. 3rd. Hoboken, NJ: John Wiley & Sons, 2005.
- [4] R. F. Harrington. *Time Harmonic Electromagnetic Fields*. Piscataway, NJ: Wiley/IEEE Press, 2001

6 Acknowledgements

This work was supported by the ANR BeSensiCom project, grant ANR-22-CE25-0002 of the French Agence Nationale de la Recherche and carried out in the framework of COST Action CA20120 INTERACT.

Mesures électromagnétiques des objets biologiques, diagnostics et bio-détection

Analyse non-invasive du taux de sucre dans les tubercules de pommes de terre par mesures diélectriques micro-ondes

Non-invasive Analysis of Sugar Content in Potato Tubers Using Microwave Dielectric Measurements

Mohamed Sebbache¹, Océane George², Christophe d'Hulst², Clément Lenoir¹, Kamel Haddadi¹

¹Univ. Lille, CNRS, Centrale Lille, Univ. Polytechnique Hauts-de-France, UMR 8520 - IEMN - Institut d'Électronique de Microélectronique et de Nanotechnologie, USR 3380 – IRCICA, F-59000 Lille, France {kamel.haddadi@univ-lille.fr}

²Univ. Lille, CNRS, UMR 8576 - UGSF - Unité de Glycobiologie Structurale et Fonctionnelle, Lille, France {christophe.d-hulst@univ-lille.fr}

Mots clés: Mesures diélectriques, sonde coaxiale ouverte, pommes de terre, taux de sucre, contrôle non destructif (CND)

Index Terms: Dielectric measurements, open-ended coaxial probe, potato tubers, sugar content, non-destructive testing (NDT)

Résumé/Abstract

This study explores a non-invasive and non-destructive approach to analyzing sugar content in potato tubers using dielectric probes. By employing a dielectric measurement kit and a vector network analyzer, we characterized three potato varieties based on their complex permittivity and reflection coefficient. The results show a correlation between dielectric properties and sugar content, paving the way for an *in situ* monitoring method.

Cette étude explore une approche non invasive et non destructive pour l'analyse du taux de sucre dans les tubercules de pommes de terre à l'aide de sondes diélectriques. En utilisant un kit de mesures diélectriques et un analyseur de réseau vectoriel, nous avons caractérisé trois variétés de pommes de terre en fonction de leur permittivité complexe et de leur coefficient de réflexion. Les résultats montrent une corrélation entre les propriétés diélectriques et la teneur en sucre, ouvrant la voie à une méthode de contrôle *in situ*.

1 Introduction

The analysis of sugar content in potato tubers is a key challenge in the agri-food industry, particularly for optimizing storage and subsequent processing [1][2]. This is notably true since the interdiction of the use of anti-germinative molecules in the EU in 2020. To bypass this restriction, potato tubers are stored at lower temperature which in turn triggers the cold-induced sweetening of the tuber increasing the sugar content in that organ. Traditional measurement methods often require tissue-destructive and time-consuming laboratory analyses.

This study explores an alternative approach based on microwave nondestructive testing (MNMT). MNMT methods are attractive for biological, food and chemical applications thanks to their high sensitivity to water [3][4]. In particular, the open-ended coaxial probe can provide localized measurements with minimal sample preparation and is therefore suited for dielectric properties of heterogeneous biological materials [5][6][7][8]. Guan et al. (2004) measured the dielectric properties of mashed potatoes over 1–1800 MHz and 20–120 °C, analyzing the effects of moisture and salt content for optimizing microwave and RF pasteurization processes [9]. Zhu and Guo (2017) studied the dielectric behavior of potato starch over the 20–4500 MHz range, demonstrating how its properties vary with frequency, moisture levels, and temperature [10]. Mohamed et al. (2016) applied microwave techniques to non-destructively detect black heart cavities in potatoes, providing complex permittivity measurements from 0.5 to 20 GHz and confirming their simulation results through experimental validation [11]. Hamilton et al. (2023) conducted a comprehensive study comparing three dielectric measurement techniques—open-ended coaxial probe, broadband dielectric spectrometer, and a custom-designed stripline resonator—across a wide frequency range of 1 MHz to 20 GHz [12]. Instant mashed potato was employed as a standardized food model to assess the dielectric properties at varying moisture contents (20% to 75% by weight). El-Mohamed et al. (2017) conducted an in-depth investigation into how storage conditions affect the dielectric properties of 'Lady Rosetta' potato tubers [13]. Using an LCZ meter, they measured capacitance and conductance across frequencies ranging from 10 kHz to 1 MHz. These measurements allowed for the calculation of parameters such as complex

permittivity, conductivity, and the dissipation factor ($\tan \delta$). The study revealed that both complex permittivity and conductivity decreased with increased storage time, temperature, and applied load stress.

Although several studies have investigated the dielectric properties of potato materials, most of them have focused on processed forms such as slices, starch, or mashed samples. To date, there is a lack of research specifically dedicated to the non-invasive, non-destructive characterization of whole, intact potato tubers. This distinction is essential, as the potato tuber is a biologically active system. Invasive measurement techniques, such as needle probes or destructive sampling, can disrupt cellular integrity, trigger stress responses or pathogens attack, or alter water distribution within the tissue, thereby biasing the dielectric response. In contrast, a non-invasive approach preserves the native state of the tuber, required for accurate *in situ* monitoring of its internal properties. To the best of our knowledge, the present work is the first to address this challenge by proposing a fully non-destructive methodology for complex permittivity measurement on whole potato tubers, with potential implications for storage monitoring.

Section 2 describes the experimental setup, including the measurement system, calibration procedure, and the different configurations used for analyzing the potato tubers. Section 3 presents the main results, including demonstration of the correlation between dielectric properties and sugar content, the influence of measurement configuration, and the repeatability of the method. Section 4 analyzes the results and outlines next steps toward the development of a non-invasive, real-time monitoring system for agri-food applications.

2 Materials and Methods

2.1 Measurement Setup

The proposed measurement system relies on a dielectric probe kit (Keysight® SlimForm and HighTemp) [14], used in conjunction with a vector network analyzer (VNA P5008A, Keysight®). This setup is designed to characterize the dielectric properties of biological samples across a wide frequency range, from 200 MHz to 50 GHz. The SlimForm probe is optimized for flat or slightly curved surfaces, while the HighTemp variant is suitable for higher temperature conditions, enhancing measurement versatility and reliability. While the primary objective for practical and future industrial applications is to operate at the ISM frequency only (2.45 GHz), we intentionally considered the broadband capabilities of the system to investigate the frequency dependence of the complex permittivity and penetration depth in potato tubers. Limiting the study to a single frequency would significantly constrain our understanding of the dielectric mechanisms and the interaction of electromagnetic fields with the potato tubers. By spanning a broad frequency range, we are able to capture the dispersive behavior of water, ions, and other molecular constituents—critical factors in the dielectric response of living tissues.

The probes are connected to the VNA, which records the complex reflection coefficient (S_{11}) and enables the determination of the complex permittivity ($\epsilon = \epsilon' - j\epsilon''$) mainly through the Keysight® Materials Measurement Suite software [14] [15]. These dielectric parameters provide valuable information about the electromagnetic behavior of the material under test (MUT). Specifically, ϵ' reflects the material's capacity to store electric energy, while ϵ'' captures dielectric losses. In tubers, these parameters are influenced by internal variables such as moisture level, ionic concentration, and molecular composition. Because sugar content modulates these internal properties, the dielectric signature offers an indirect yet sensitive method to assess sugar levels. This non-destructive and broadband approach allows for real-time monitoring of internal changes within the tubers, which is essential for quality control and biochemical analysis.

The input RF power was set to -15 dBm with an intermediate frequency (IF) bandwidth of 100 Hz and 601 measurement points. Port 1 of the VNA was connected to the Slim form coaxial probe and Port 2 to the High temperature probe, covering their respective frequency ranges (500 MHz–50 GHz for Slim Form and 200 MHz–20 GHz for High Temperature). Both probes were connected via 60 cm-length coaxial cables. The ambient temperature during the measurement ranged from 22.3°C to 22.9°C.

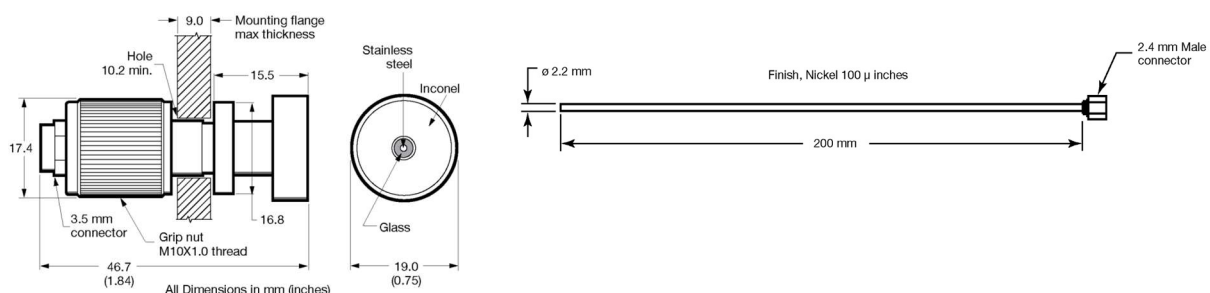


Figure 1. Drawings of both HighTemp (left) and SlimForm (right) probes (references: Keysight N1501A-101 and N1501A-102)

To ensure consistent contact between the probe and the sample, the potato tuber was placed in a glass beaker to maintain a stable position throughout the measurement. A simple vertical adjustment system allowed for manual raising and lowering of the tuber. Custom 3D-printed spacers of 1 mm and 10 mm thickness were used to control the distance and ensure a reproducible pressure between the tuber surface and the probe. Additionally, a temperature sensor was placed near the contact zone to monitor any thermal variations during data acquisition. These setup details are depicted in Figure 2, which provides a representation of the experimental configuration.



Figure 2. Measurement setup for dielectric characterization of potato tubers. The system includes: (1) Keysight P5008 Streamline Vector Network Analyzer (VNA), (2) control PC with Keysight Materials Measurement Suite, (3) Keysight SlimForm and HighTemp dielectric probes, (4) probe stops at 1 mm and 10 mm depths, (5) potato tubers from different varieties, and (6) temperature sensor for environmental monitoring. This setup enables broadband (200 MHz–50 GHz), non-destructive dielectric measurements using open-ended coaxial probe.

2.2 Reproducibility and Metrological considerations

The evaluation of measurement repeatability and reproducibility was carried out using the SlimForm probe on three different tuber varieties (Lady Claire, Désirée, Alix) of the same potato species (*Solanum tuberosum*). The protocol consisted of two distinct phases. In the first phase, the measurement setup was assembled and left untouched while three successive measurements were performed under identical conditions, this assessed the repeatability of the system. In the second phase, the probe was manually decoupled and repositioned on the tuber before each of three new measurements, allowing the evaluation of reproducibility. In both cases, care was taken to maintain consistent contact pressure using the same 3D-printed spacer. These procedures were repeated for each tuber variety. Based on the collected data, standard deviations were calculated to quantify variability. Only the results obtained with the SlimForm probe are presented in Figure 3, which summarizes the repeatability and reproducibility measurements for the three tested tuber varieties.

	Lady Claire		Désirée		Alix	
Magnitude (repeatability)	Mean (linear)	σ (%)	Mean (linear)	σ (%)	Mean (linear)	σ (%)
0.5GHZ	0.98	0.05%	0.97	0.45%	0.95	0.07%
2.45GHZ	0.95	0.11%	0.94	0.84%	0.91	0.12%
10GHZ	0.91	0.26%	0.90	1.79%	0.80	0.27%
50GHZ	0.66	0.26%	0.66	1.06%	0.63	0.04%
Phase (repeatability)	Mean (°)	σ (%)	Mean (°)	σ (%)	Mean (°)	σ (%)
0.5GHZ	-4.99	1.39%	-5.13	6.06%	-7.84	0.08%
2.45GHZ	-18.88	1.23%	-18.93	5.05%	-30.33	0.28%
10GHZ	-61.47	1.00%	-60.68	3.47%	-88.61	0.35%
50GHZ	-140.50	0.14%	-138.50	0.56%	-149.58	0.07%
Magnitude (reproducibility)	Mean (linear)	σ (%)	Mean (linear)	σ (%)	Mean (linear)	σ (%)
0.5GHZ	0.98	0.82%	0.98	0.21%	0.92	1.70%
2.45GHZ	0.95	1.46%	0.95	0.40%	0.87	2.09%
10GHZ	0.91	3.43%	0.91	0.81%	0.74	1.01%
50GHZ	0.67	4.40%	0.66	1.08%	0.62	0.41%
Phase (reproducibility)	Mean (°)	σ (%)	Mean (°)	σ (%)	Mean (°)	σ (%)
0.5GHZ	-4.93	19.34%	-4.97	5.09%	-10.08	14.13%
2.45GHZ	-18.73	17.84%	-18.61	4.86%	-38.97	13.04%
10GHZ	-61.04	14.90%	-60.50	4.21%	-102.37	8.87%
50GHZ	-139.02	3.53%	-138.87	1.00%	-151.75	3.01%

Table 1. Error analysis on the measured reflection coefficient S_{11} including repeatability and reproducibility.

The measurements demonstrated strong repeatability and reproducibility under varying test conditions. When the probe position was held fixed, repeated acquisitions yielded highly consistent results. Even with deliberate repositioning of the probe between measurements, the observed variations remained within acceptable limits, thereby confirming the robustness of the measurement procedure. This stability reinforces the reliability of the dielectric signatures obtained from the tubers.

2.3 Calibration Protocol

A full modified-SOL calibration was performed before each measurement campaign, following the standard procedure recommended by Keysight® for dielectric probe systems. Calibration was conducted separately for both the SlimForm and HighTemp probes using the Keysight® Materials Measurement Suite.

The calibration sequence included three standards: open (air), short (metallic shorting block), and a liquid reference. For the liquid standard, deionized water with a conductivity of less than 3.00 $\mu\text{S}/\text{cm}$ (RS PRO, reference 254-3687) was used. This specific product was chosen for its consistency and compatibility with high-frequency dielectric measurements, particularly where dielectric loss becomes more significant.

This protocol allowed for the correction of systematic measurement errors and ensured reproducibility of the complex permittivity values across all configurations and varieties tested.

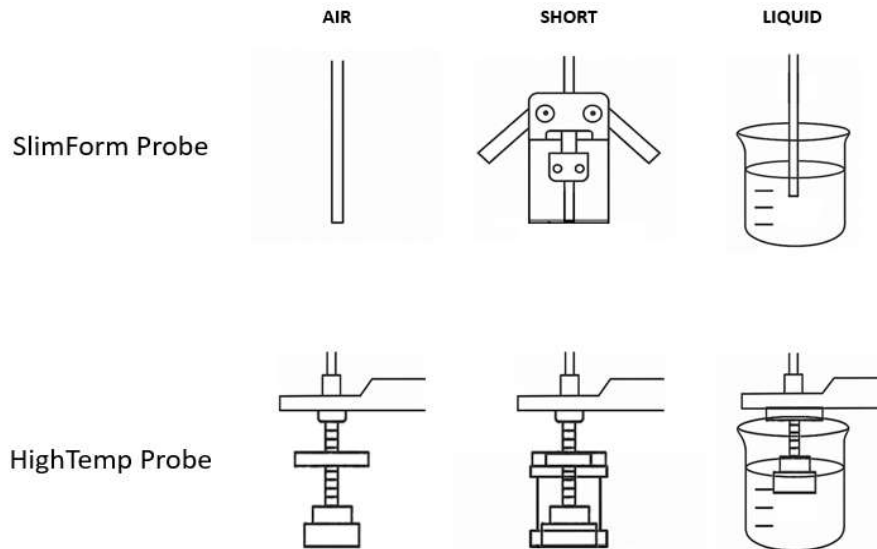


Figure 3. Calibration sequence for both the HighTemp and SlimForm probes.

2.4 Measurement Configuration

The measurement setup focused on three potato tuber varieties: Lady Claire, Désirée, and Alix. These varieties were specifically chosen because they are well-controlled within our cultivation process—we grow them ourselves and are thoroughly familiar with their behavior, especially in terms of sugar accumulation. This level of control allows us to confidently correlate the microwave measurements with their known physical and chemical characteristics.

To identify the most suitable method for obtaining reliable dielectric data, we tested three distinct measurement configurations: **Surface Measurement (Non-invasive)**: In this ideal non-destructive approach, the probes were simply placed in contact with the potato tuber skin. This configuration is particularly appealing because it does not require any sample preparation. However, it introduces complexity due to the multi-layered structure of the tuber, the skin and the underlying flesh, which can influence the dielectric response. **Peeled Surface Measurement**: To isolate the dielectric contribution of the flesh alone, the tubers were peeled prior to measurement. This removes the effect of the skin but introduces a new variable: the peeled surface tends to exude moisture, which can alter the contact conditions and influence the measurement. **Inserted Probe Measurement (Invasive)**: In the third configuration, the probes were inserted approximately 1 cm into the tuber to access internal dielectric properties, mimicking the conditions of an immersed probe. While this method offers deeper insight into the internal structure, it is clearly invasive and therefore not aligned with the principles of non-destructive testing.

By comparing these three approaches, we aim to balance measurement reliability with the practical constraints of non-destructive evaluation, and to better understand how surface conditions and probe placement affect the dielectric response of the potato tuber.

Both types of probes were used during the measurements: SlimForm and HighTemp probes. The SlimForm probe, due to its compact design, was mainly employed for surface measurements where minimal contact area is beneficial. While it is suitable for contact-based configurations, it is not particularly designed for deep insertion into the sample. The three previously described measurement conditions, surface contact on unpeeled tubers, contact on peeled surfaces, and insertion into the tuber flesh, were each tested using both types of probes. These configurations were applied systematically across all three potato varieties to evaluate the impact of the measurement technique on the quality of the dielectric data, particularly in terms of accuracy and repeatability.

The objective was to identify which combination of probe and measurement setup yields the most reliable data, while considering the trade-offs between invasiveness, practical feasibility, and consistency.

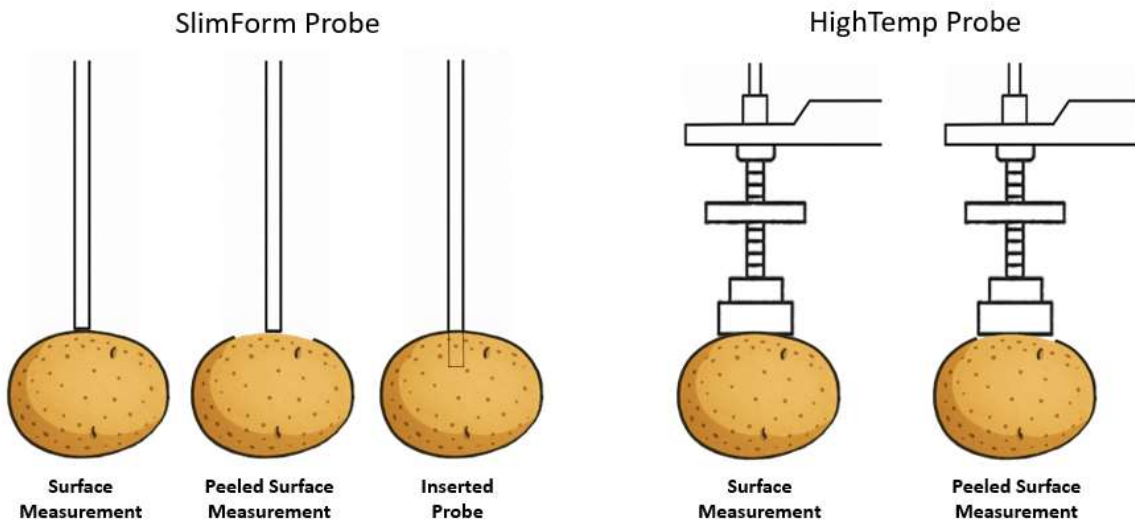


Figure 4. Measurement configurations for both SlimForm and HighTemp open-ended coaxial probes.

3 Results and discussion

3.1 Experimental results

Figure 6 illustrates the measured reflection coefficient response—both magnitude in dB and phase in degrees—of the three potato varieties (Lady Claire, Désirée, and Alix) in the frequency range from 0 to 50 GHz. In terms of magnitude, all samples show a general decline with increasing frequency, indicative of typical dielectric loss behavior. Lady Claire exhibits the highest reflection magnitude across the spectrum, followed by Désirée and then Alix, which shows the lowest values. This suggests that Lady Claire has the lowest dielectric losses, while Alix exhibits the highest. In the phase response graph, a similar trend is observed where all curves demonstrate a progressive phase shift with frequency, consistent with dispersive dielectric behavior. Again, Lady Claire and Désirée show less steep phase changes compared to Alix, whose phase drops more sharply, especially in the lower frequency range. These differences could be attributed to variations in internal moisture, sugar content, and tissue composition between the potato varieties, with Alix possibly having higher loss factors or different structural properties leading to a stronger attenuation and dispersion.

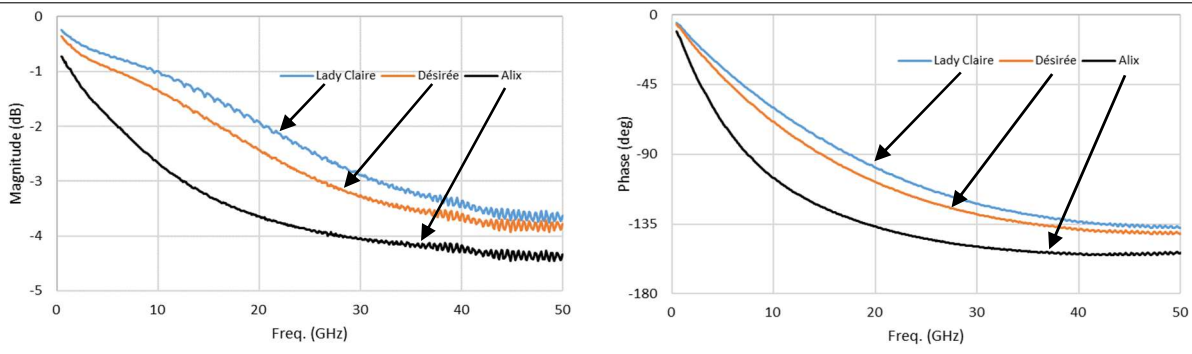


Figure 5. Measured reflection coefficient S_{11} (magnitude and phase) using the SlimForm probe.

From the measured reflection coefficient, dielectric spectra are extracted and presented in Figure 7.

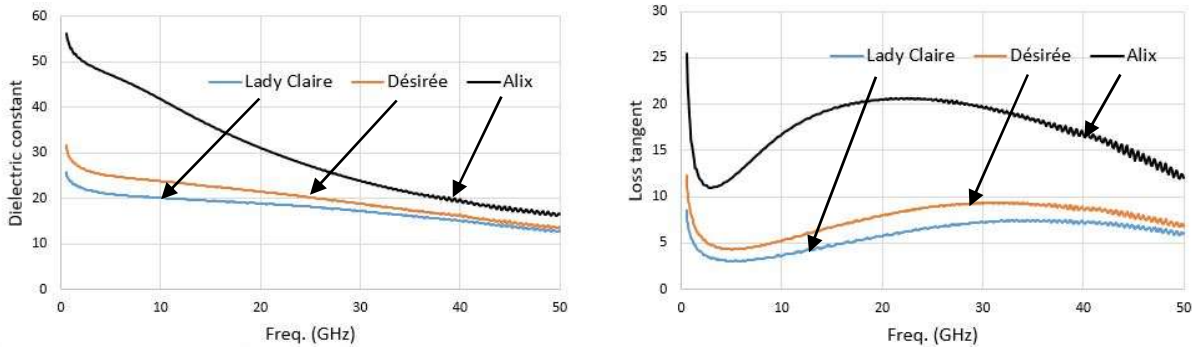


Figure 6. Extracted dielectric constant and Loss tangent from measured reflection coefficient using the SlimForm probe.

The dielectric constant plot shows that Alix exhibits significantly higher permittivity values across the entire frequency range, beginning above 50 and decreasing steadily toward approximately 25. In contrast, Lady Claire and Désirée display lower and relatively stable dielectric constants, with Désirée slightly higher than Lady Claire. This higher permittivity in Alix could be attributed to greater water content or distinct microstructural features enhancing dielectric storage capacity. The loss tangent, which quantifies the energy dissipation relative to energy storage, follows a distinct pattern among the varieties. Alix again stands out with relatively high loss tangent values, peaking above 25 at low frequencies and gradually declining yet remaining dominant throughout the spectrum. This indicates a much stronger dielectric loss mechanism, implying more significant energy absorption, possibly due to higher ionic conductivity. Conversely, Lady Claire and Désirée show lower loss tangent values, remaining below 10 over the full frequency range, with smooth curves suggesting stable, low-loss dielectric behavior. Overall, the analysis confirms that dielectric spectroscopy offers a robust method to differentiate potato varieties based on intrinsic electromagnetic properties.

Following microwave characterization, destructive analyses were performed to determine the exact sugar content in potato tubers. On the same day as the dielectric measurements, the corresponding tubers were collected and prepared for chemical analysis. Each sample was mechanically crushed to obtain a homogeneous pulp, ensuring optimal extraction of soluble sugars. The pulp was then centrifuged for 10 min at 4°C and at 16,000g and the collected supernatant was immediately boiled for 10 min to eliminate all enzymatic activities. After a new centrifugation step such as described above, the supernatant was collected for sugar quantification. Only the glucose content was measured by an enzymatic / spectrophotometric approach (adapted from Vandromme *et al* [16]) which gives a good image of total sugar concentration in the sample (glucose being the most abundant soluble sugars in such biological samples) The final results were expressed in micrograms of glucose per gram of tuber material ($\mu\text{g/g}$), providing a reference for correlation with the dielectric measurements.

Variety	Lady Claire	Désirée	Alix
Sugar concentration ($\mu\text{g/g}$)	86	200	8020

Table 2. Measured glucose concentration, expressed in μg per gram ($\mu\text{g/g}$).

The measured values of the reflection coefficient S_{11} (both in magnitude and phase), along with the extracted dielectric constant (ϵ') and dielectric loss factor (ϵ''), are given in Table 3 as functions of glucose content for selected frequencies, for Alix. The results demonstrate a clear relationship between increasing sugar concentration and the electromagnetic response. Specifically, the magnitude of S_{11} decreases with higher sugar content,

indicating increased signal attenuation due to elevated dielectric losses. Similarly, the phase of S11 becomes more negative. The dielectric constant (ϵ') increases steadily, particularly between 6.38 mg and 168.42 mg of glucose, suggesting that sugar contributes to the material's ability to store electric energy, likely through increased dipolar and ionic polarization. The dielectric loss factor (ϵ'') exhibits an even more pronounced rise, pointing to stronger energy dissipation mechanisms associated with higher glucose levels. These results demonstrate a strong correlation between sugar content and the dielectric properties of Alix, confirming the effectiveness of broadband microwave spectroscopy as a non-destructive method for assessing internal biochemical composition in potato tubers.

Frequency	Sugar concentration (mg)	Magnitude (dB)	Phase (deg)	ϵ'	ϵ''
0.5 GHz	2.33	-0.25	-5.00	25.64	8.49
	6.38	-0.36	-6.10	31.68	12.33
	168.42	-0.73	-10.52	56.19	25.49
1 GHz	2.33	-0.35	-9.31	23.59	5.43
	6.38	-0.49	-11.14	28.45	7.81
	168.42	-0.91	-20.04	52.50	15.07
10 GHz	2.33	-1.00	-60.46	20.09	3.64
	6.38	-1.35	-69.53	23.74	5.27
	168.42	-2.68	-105.62	41.69	16.82
50 GHz	2.33	-3.63	-137.43	12.79	5.94
	6.38	-3.78	-141.14	13.58	6.84
	168.42	-4.34	-153.72	16.63	12.00

Table 3. Comparative analysis of S11 parameters (magnitude and phase), dielectric properties (ϵ' , ϵ''), and glucose concentration

3.2 High Frequency Insights

Measurements were conducted up to 50 GHz, leveraging the wideband capability of the probe system for exploratory purposes. However, results showed that meaningful dielectric variations related to tuber composition, particularly water and sugar content, are primarily observable within the lower gigahertz frequencies. This aligns with the known dielectric behavior of water and polar compounds, whose frequency response dominates in the lower GHz range. Therefore, future applications may focus on limited frequency bands, simplifying instrumentation while retaining sensitivity to key biochemical variations.

3.3 Measurement configuration influence

The measurement configuration had a significant impact on the quality and consistency of the dielectric data. Among the three tested methods, probe insertion, peeled surface, and non-invasive surface contact, only the non-invasive approach yielded stable and reliable results. Invasive methods, such as inserting the probe or peeling the skin, appeared to trigger physiological responses in the tuber tissue. As a living organism, the tuber reacts to mechanical disturbance, which likely alters its internal composition and, consequently, its dielectric behavior. These findings highlight the importance of preserving sample integrity for accurate and reproducible measurements. The fact that only non-invasive methods yield reliable results is particularly advantageous, as the ultimate goal is to develop a non-destructive, practical monitoring technique.

4 Conclusion

This study demonstrates the promising potential of dielectric spectroscopy for non-invasive evaluation of sugar content in potato tubers. By employing broadband dielectric measurements from 200 MHz to 50 GHz on multiple potato varieties and under different configurations, we observed clear and consistent correlations between dielectric properties, particularly the imaginary permittivity (ϵ'') and loss factor ($\tan \delta$), and the tubers' sugar concentrations. These correlations were especially evident in the Alix variety, which exhibited higher sugar levels confirmed through enzymatic/spectrophotometric assay.

Among the tested measurement configurations, only non-invasive surface contact provided stable and exploitable results. Interestingly, this limitation aligns perfectly with the intended goal of developing a rapid, non-destructive monitoring technique. The physiological reactivity of the tubers to invasive procedures such as peeling or probe insertion further reinforces the importance of preserving sample integrity during analysis.

In addition, the strong repeatability and reproducibility of the measurements—even when the probe was repositioned—underscore the robustness of the approach. This reliability paves the way for the development of an empirical model capable of estimating sugar content directly from dielectric data. Future research will aim to refine these correlations by focusing on a single frequency, specifically around the ISM band at 2.45 GHz, in order to

optimize both simplicity and cost. The methodology will also be validated under real industrial conditions. Ultimately, integrating dielectric spectroscopy into processing lines could provide a powerful, real-time, and non-invasive tool for quality control in the agri-food industry.

Acknowledgement

This work was supported, in part by the French Renatech network, and in part by the CPER Hauts de France project IMITECH.

References

- [1] J. R. Sowokinos, "Biochemical and molecular control of cold-induced sweetening in potatoes," *American Journal of Potato Research*, vol. 78, p. 221-236, 2001.
- [2] T. Jakubowski, "The Influence of selected physical methods on the content of starch and simple sugars in stored potato tubers," *2019 Applications of Electromagnetics in Modern Engineering and Medicine (PTZE)*, Poland, 2019, pp. 63-66.
- [3] S. Trabelsi, A. Kraszewski and S. Nelson, "Simultaneous determination of density and water content of particulate materials by microwave sensors", *Electronic Lett.*, vol. 33, no. 10, pp. 874-976, May 1997.
- [4] K. Haddadi, M.M.Wang, O. Benzaim, D. Glay and T. Lasri, "Contactless microwave technique based on a spread-loss model for dielectric materials characterization", *IEEE Microw. Wireless Compon. Lett.*, vol. 19, no. 1, pp. 33-35, January 2009.
- [5] K. Haddadi, D. Glay, and T. Lasri, "Near-field scanning microscopy in liquid media based on microwave interferometry", *Proc. 9th Int. Conf. on Electromagnetic Wave Interaction with Water and Moist Substances, ISEMA 2011*, pp. 185-192, Kansas City, MO, USA, June 2011.
- [6] K. Haddadi, H. Bakli, and T. Lasri, "Microwave liquid sensing based on interferometry and microscopy techniques," *IEEE Microw. Wireless Compon. Lett.*, vol. 22, no. 10, pp. 542–544, Oct. 2012.
- [7] H. Bakli and K. Haddadi, "Microwave Interferometry Based On Open-ended Coaxial Technique for High Sensitivity Liquid Sensing," *Advanced Electromagnetics*, vol. 6, no. 3, pp. 88–93, Oct. 2017.
- [8] C. -H. Lee, K. Haddadi and P. J. Burke, "Combined Super-Resolution Fluorescence and Coaxial 3-D Scanning Microwave Microscopy: Proof-of-Concept In-Liquid Live-Cell Imaging: Toward a Biological Nano-Radar," *IEEE Microw. Wireless Compon. Lett.*, vol. 35, no. 1, pp. 131-134, Jan. 2025.
- [9] Y. Guan, J. Tang, B. Rasco, and S. Wang, "Dielectric Properties of Mashed Potatoes Relevant to Microwave and Radio-Frequency Pasteurization and Sterilization Processes," *Journal of Food Science*, vol. 69, no. 1, pp. FEP30–FEP37, 2004.
- [10] Z. Zhu and W. Guo, "Frequency, moisture content, and temperature dependent dielectric properties of potato starch related to drying with radio-frequency/microwave energy," *Scientific Reports*, vol. 7, p. 9311, 2017.
- [11] I. Mohamed, R. Dudley, A. Gregory, R. Mouthaan, Z. Tian, P. Andrews, and A. Mellonie, "Non-Destructive Testing for Black Heart Cavities in Potatoes with Microwave Radiation," *arXiv preprint*, arXiv:1610.05061, 2016.
- [12] J. K. Hamilton, C. P. Gallagher, C. R. Lawrence, and J. R. Bows, "Broadband dielectric characterization systems for food materials," *arXiv preprint*, arXiv:2303.12518, 2023.
- [13] S. N. Soliman and A. E. El-Sayed, "Dielectric Properties of Potato Tubers Related to Storage Conditions," *Misr Journal of Agricultural Engineering*, vol. 34, no. 4-2, pp. 2233–2250, 2017.
- [14] Keysight Technologies, "N1501A Dielectric Probe Kit 10 MHz to 50 GHz," Technical Overview, Publication No. 5992-0264EN, 2015. [Online]. Available: <https://www.keysight.com/us/en/assets/7018-04631/technical-overviews/5992-0264.pdf>
- [15] T. W. Athey, M. A. Stuchly and S. S. Stuchly, "Measurement of Radio Frequency Permittivity of Biological Tissues with an Open-Ended Coaxial Line: Part I," in *IEEE Transactions on Microwave Theory and Techniques*, vol. 30, no. 1, pp. 82-86, Jan. 1982.
- [16] C. Vandromme, C. Spriet, J. L. Putaux, D. Dauvillée, A. Courseaux, C. d'Hulst, and F. Wattebled, "Further insight into the involvement of PIII in starch granule initiation in Arabidopsis leaf chloroplasts," *New Phytologist*, vol. 239, no. 1, pp. 132–145, 2023.

Session ouverte

Expérimentation du temps négatif avec un circuit RC LP-NGD *Negative time experimentation with RC-network based low-pass NGD circuit*

B. Ravelo¹, N. B. Gurgel², S. Moussa^{3,4}, J. Rossignol⁵, Benoit Agnus⁶

¹NUIST, Nanjing 210044, Jiangsu, China, blaise.ravelo@yahoo.fr

²Applied EM & Microwave Lab., FUCG, Campina Grande 58429, Brazil, nathan.gurgel@ieee.org

³University of Antsirananana, 201 Antsirananana, Madagascar, moussainos@gmail.com

⁴LSE, LR11ES15, University of Tunis El Manar, ENIT, Tunis, Tunisia

⁵Université de Bourgogne, Dijon, France, jerome.rossignol@u-bourgogne.fr

⁶Scienteama, 4 Avenue de Cambridge, 14200 Hérouville Saint Clair, France, benoit.agnus@scienteama.fr

Mots-clés : Temps de Propagation de Groupe (TPG) négatif, avance temporelle, circuit RC, étude expérimentale.
Keywords: Negative group delay (NGD), Time-advance, Experimentation, RC-network.

Résumé

Cet article présente une étude expérimentale du temps négatif ($t < 0$) avec un circuit analogique RC. L'effet $t < 0$ est généré par la fonction électronique Temps de Propagation de Groupe (TPG) négatif ou NGD. Les principales caractéristiques de cette fonction inhabituelle, telles que l'avance temporelle et la fréquence de coupure du NGD en fonction des valeurs de résistance et de condensateur, sont présentées. Les résultats expérimentaux obtenus avec des signaux de forme d'onde arbitraire d'une durée de 23 ms confirment l'observation du $t < 0$ avec une avance temporelle d'environ -0,5 ms.

Abstract

This paper studies the negative time ($t < 0$) experimentation with RC-network electronic circuit. The $t < 0$ effect is generated from negative group delay (NGD) electronic function. The main characteristics of this uncommon function as time-advance and NGD cut-off frequency in function of resistor and capacitor elements are expressed. The experimental results with arbitrary waveform signals having 23 ms duration confirm the $t < 0$ observation with time-advance around -0.5 ms.

1 Introduction

Over the age, the history of science progresses naturally with emergency of successive new ideas upsetting the common and familiar ones. The experimental works constitute the decisive steps to bring the uncommon idea to the application area as a popular knowledge. Today, this historical process still happens when we have a close look about the sign of time status.

In 1980s, after theoretical intuitive postulate, the negative group delay (NGD) phenomenon was physically observed from negative group velocity media [1]. The existence and characterization of abnormal NGD function have attracted the attention of electronic engineering researchers since 1990s [2]. Thanks to the equivalence of transfer function (TF), NGD electronic topologies constituted by resistor, inductor, capacitor and operational amplifier were identified [2]. The particularity of NGD function is its possibility to propagate voltage signals with output detected in time-advance of its input [2-6]. Despite its counterintuitive behavior, it was emphasized that the NGD function does not contradict the causality [2]. However, so far, due to the plenty diversity of electronic topologies enabling to verify the possibility to demonstrate it, the meaning of NGD phenomenon remains an open question for non-specialist researchers.

For this reason, a fundamental basic NGD circuit theory inspired from the filter was initiated in the mid-2010s [3]. Even the topological structure can be exactly the same, the main difference between the NGD and filter circuit theory is the main function to be characterized. The filter circuits are essentially specified from the TF magnitude frequency response. However, the NGD circuits are elaborated from the group delay (GD) response. There may have confusion for non-specialists because the same electronic circuit topology can behave as both filter and NGD function.

It was pointed out from the developed fundamental theory that all NGD circuits can be innovatively identified as either low-pass (LP) or high-pass (HP) or bandpass (BP) or stopband (SB) or all-pass (AP) type topologies [4]. The present research work proposes a close look on the experimentation of LP type NGD function [4-6]. The LP-NGD topology under study is constituted by an RC-network [5-6]. We would like to popularize the possibility to analyze, characterize, study and experiment this LP type NGD topology. To do this, an experimental demonstration of negative time ($t < 0$) effect using LP-NGD circuit constitutes the main focus of the present work.

The paper is mainly organized in three main sections:

- Section 2 describes the theory of LP-NGD circuit constituted by RC-network,
- Section 3 examines the experimental work from the proof-of-concept and prototype dedicated to the $t < 0$ metrology,
- And Section 4 is the final conclusion.

2 Theory on the considered LP-NGD circuit composed of RC-network

This section addresses the theoretical analysis of the LP-NGD circuit constituted by an RC-network. The theory is established from the TF exploration. The main specifications of LP-NGD function are defined. Then, the design method of LP-NGD circuit is established in order to calculate the constituting component parameters in function of the desired to achieve $t < 0$ value.

2.1 Time-domain signature of LP-NGD function

The theory of electrical and electronic circuits exhibiting $t < 0$ behavior is elaborated under the same approach as the classical one. Based on the circuit and system theory, the linear time-invariant (LTI) TF approach represents the most pragmatic strategy to build an electronic engineering analytical investigation. We proceed under the same tradition for the present research work. Doing this, let represent the LP-NGD function as a two-port black box interacting with a time-dependent input signal $x(t)$ to generate the corresponding output $y(t)$ as illustrated in Fig. 1(a). The analytical expression of $t < 0$ concept studied in this work can be understood from the input and output signal transient relationship:

$$y(t) \approx x(t + t_a) \quad (1)$$

by taking $t_a < 0$ as time-advance parameter which represents a delay with negative sign.

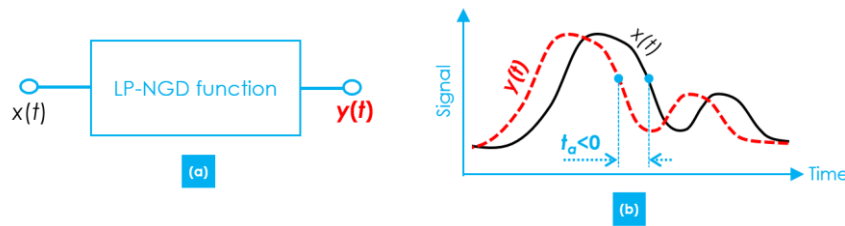


Figure 1: LP-NGD function (a) two-port black box and (b) time-domain signature diagram

To study this system in the frequency domain, the frequency variable is denoted by f . The LP-NGD TF $T(j2\pi f)$ can be expressed via the Fourier transform of input $X(j2\pi f)$ and output $Y(j2\pi f)$ which is traditionally expressed by the transmittance:

$$T(j2\pi f) = \frac{Y(j2\pi f)}{X(j2\pi f)} \quad (2)$$

The LP-NGD function basic definitions yielding from this TF are described in the next subsection.

2.2 Basic definitions for specifying the LP-NGD function

To materialize the LP-NGD function, we need a concrete electrical circuit in order to make us to be able to intelligibly experiment the $t < 0$ effect. Doing this, one considers the RC-network based LP-NGD topology attacked by input $x(t)$ and generating output $y(t)$ represented in Fig. 2. The LTI topology is constituted by $R_n // C_n$ and R -shunt passive network associated in upstream to an active cell with gain G . The LP-NGD analysis of this circuit consists in calculating the frequency responses following the circuit and system theory traditional approach.

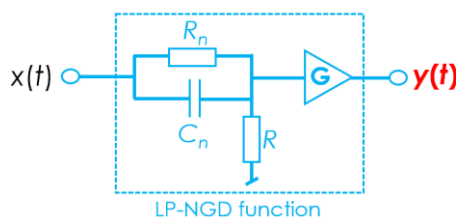


Figure 2: LP-NGD RC-network topology

Subsequently, the main parameters of the LP-NGD frequency domain study are the magnitude and phase classically expressed as:

$$T(f) = |T(2j\pi f)| = \sqrt{\text{real}[T(2j\pi f)]^2 + \text{imaginary}[T(2j\pi f)]^2} \quad (3)$$

$$\varphi(f) = \arg[T(2j\pi f)] = \arctan \left\{ \frac{\text{imaginary}[T(2j\pi f)]}{\text{real}[T(2j\pi f)]} \right\} \quad (4)$$

It yields from the latter one the GD parameter defined by:

$$GD(f) = \frac{1}{2\pi} \times \frac{-\partial \varphi(f)}{\partial f} \quad (5)$$

To reach the time-advance expressed in equation (1), as depicted in Fig. 3(a), we should have magnitude approximately equal to unity:

$$T(f \approx 0) \approx 1 \quad (6)$$

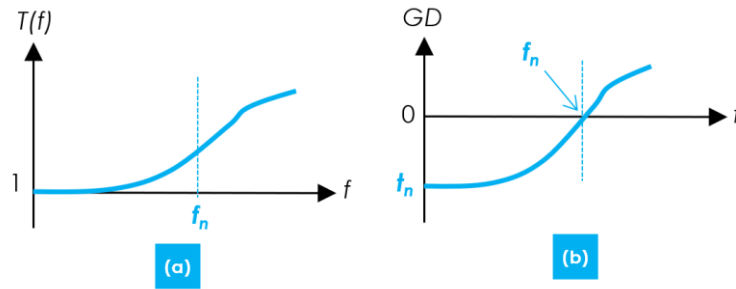


Figure 3: LP-NGD (a) magnitude and (b) GD frequency responses

It is more importantly to keep in mind that the LP-NGD function specifications are defined by:

- The GD value t_n at very low frequencies ($f \approx 0$) which must be negative:

$$t_n = GD(f \approx 0) < 0 \quad (7)$$

- And the NGD value f_n which is the root of equation:

$$GD(f = f_n) = 0 \quad (8)$$

Meanwhile, the LP-NGD function can be also analytically represented by the GD is spectrally negative:

$$\begin{cases} GD(f < f_n) < 0 \\ GD(f > f_n) > 0 \end{cases} \quad (9)$$

The exploitation of these two last equations permits to construct the LP-NGD theory of the topology introduced in Fig. 2.

2.3 LP-NGD analysis of the considered RC-network based topology

After the voltage TF exploration of the electrical circuit depicted in Fig. 2, one can mathematically demonstrate that the GD at very low frequency given in equation (7) is written as:

$$t_n = \frac{-R_n^2 C_n}{R + R_n} \quad (10)$$

We can remark that the GD t_n is always negative independently to the circuit resistor and capacitor values. Furthermore, the NGD cut-off frequency given in equation (8) becomes:

$$f_n = \frac{\sqrt{R + R_n}}{2\pi R_n C_n \sqrt{R}} \quad (11)$$

To operate with unity gain expressed in equation (6) at very low frequency, the LP-NGD active circuit must integrate an amplifier with static gain:

$$G = 1 + \frac{R_n}{R} \quad (12)$$

Of course, the gain must be more than unity $G > 1$ for an amplifier. These three last equations serve to establish the LP-NGD design equation elaborated in the next subsection.

2.4 Design equations of resistor and capacitor constituting the LP-NGD circuit

The concrete LP-NGD circuit diagram adopted in this work is represented in Fig. 4. It is terminated by a non-inverter amplifier with an operational amplifier associated to resistors R and R_n .

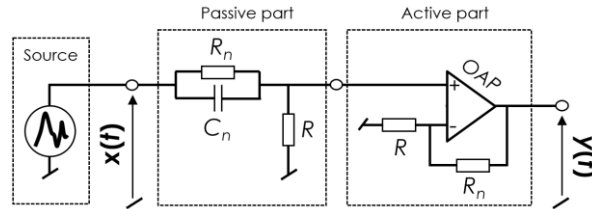


Figure 4: Adopted LP-NGD circuit to be designed and implemented

In function of the given gain $G > 1$ and time-advance $t_n = t_a < 0$, we can calculate the resistor and capacitor constituting the circuit proposed in Fig. 4 by inverting equations (9) and (10). To do this, we can, for example, fix resistance R_n as a given parameter. By inverting equation (10), we have the resistor design equation:

$$R = \frac{R_n}{G - 1} \quad (13)$$

Then, we have the capacitor design equation from equation (9):

$$C_n = \frac{-(R + R_n)t_a}{R_n^2} \quad (14)$$

This last term is always positive because we are dealing with $t_a < 0$. It is noteworthy that to experiment $t < 0$, the input signal spectrum bandwidth must belong to the base band spectrum $f < f_n$. This condition is also linked to the causality effect. It means that maximum bandwidth of input signal in function of the desired time-advance should be:

$$f_n = \frac{1 - G}{2\pi t_a \sqrt{G}} \quad (15)$$

The aim of the next section is to prove the feasibility of the established $t < 0$ circuit theory.

3 Negative time simulated and measurement results with LP-NGD prototype

This section focuses on the feasibility study of the LP-NGD function by experimentation of $t < 0$ effect with a circuit prototype.

3.1 Description of the demonstrator

The LP-NGD circuit proof-of-concept considered in this work is targeted to operate with t_a and amplifier gain G . After optimization and choice of nominal values, we utilized the components R , R_n and C_n having $\pm 5\%$ tolerances. Therefore, the LP-NGD cut-off frequency expressed in equation (14) is equal to f_n . All these parameters are indicated in Table 1.

Objective	Nature	Name	Value
Targeted specifications	Time-advance	t_a	-0.5 ms
	Amplifier gain	G	14 dB
LP-NGD circuit parameters	Resistor	R_n	2 k Ω
		R	500 Ω
	Capacitor	C_n	330 nF
NGD cut-off frequency	Frequency	f_n	569 Hz

Table 1: Specifications of the LP-NGD circuit proof-of-concept

The proof-of-concept of LP-NGD active prototype was designed in the SPICE environment of MULTISIM® as proposed in Fig. 5(a).

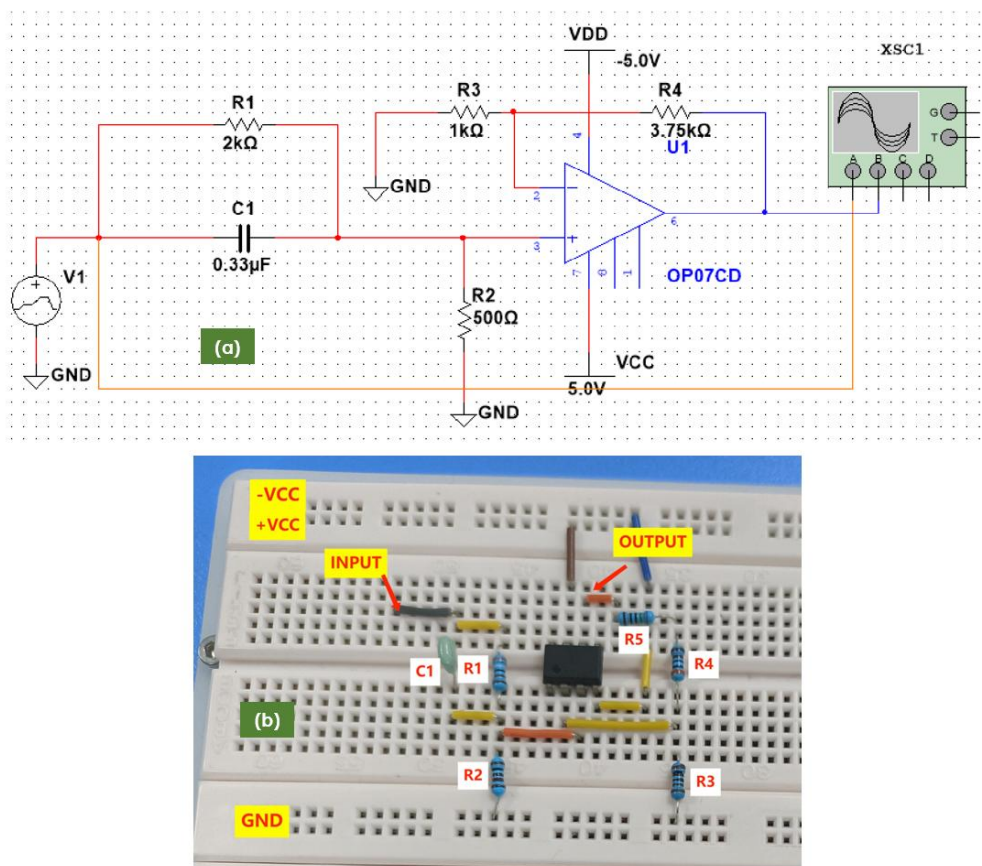


Figure 5: (a) MULTISIM® schematic and (b) tested prototype photo of LP-NGD circuit

In addition, the circuit prototype fed by DC power supply $V_{CC}=5$ VDC and $V_{DD}=-V_{CC}$ is implemented on a breadboard as seen in Fig. 5(b).

3.2 $t < 0$ experimental setup

The present $t < 0$ metrology was realized by simultaneous visualization of signals representing the input x and output y of LP-NGD circuit prototype. The performed experimentation was performed with the synoptic diagram illustrated in Fig. 6(a). As photographed in Fig. 6(b), the test is based on the input x provided from the arbitrary waveform signal generator with the visualization of the input and output signals by a digital oscilloscope. During the test, the LP-NGD active circuit prototype was fed by ± 5 V_{DC} power supply. The references of the test equipment are indicated in Table 2.

Instrument	Reference	Specifications
Digital oscilloscope	NDS102	<ul style="list-style-type: none"> - Precision: 12 bits - Bandwidth: 100-MHz - Sampling rate: 1 GSa/s
Signal generator	Siglent® SDG1062X	<ul style="list-style-type: none"> - Bandwidth: 60-MHz - Sampling rate: 150 MSa/s

Table 2: Test instrument specifications

The results of the carried-out experiment of LP-NGD prototype validating the counterintuitive effect $t < 0$ are discussed in the next subsection.

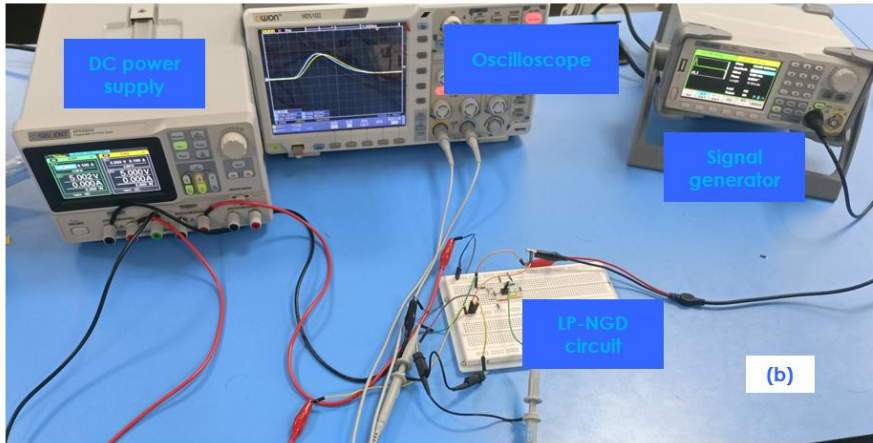
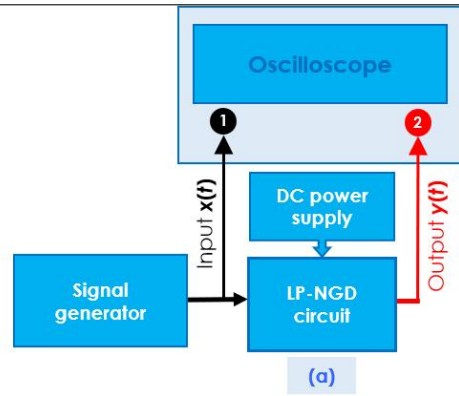


Figure 6: (a) Illustrative diagram and (b) photo of negative time testing with LP-NGD circuit

3.2 Discussion on the simulated and experimental results in the time-domain

The comparisons between time-domain results from the MULTISIM® simulation shown in Fig. 6(a) and measurement test photographed in Fig. 6(b) are plotted in Figs. 7.

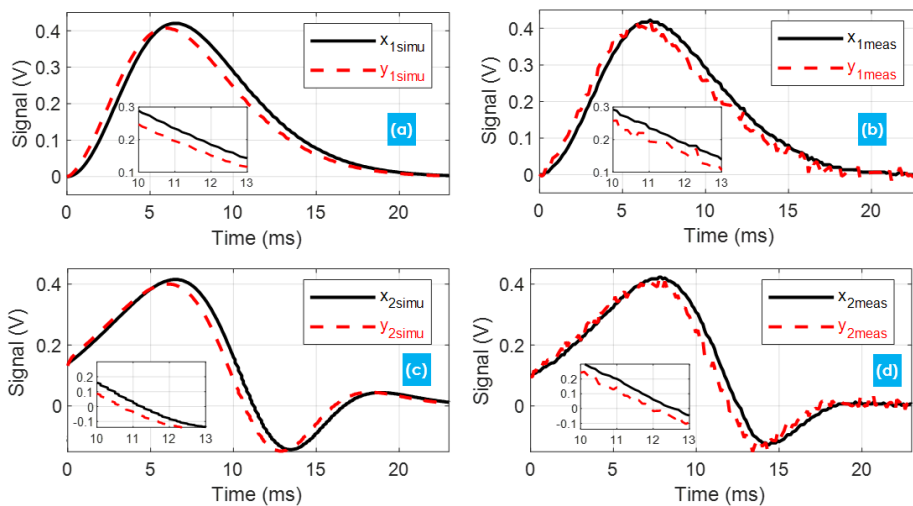


Figure 7: Responses of (a) simulated and (b) measured signal x_1 , and (c) simulated and (d) measured signal x_2

The experimentation was done by controlling the arbitrary wave form signal generator with CSV-format files containing the date of two-different input signals x_1 (bi-exponential waveform plotted in Fig. 7(a) and in Fig. 7(b)) and x_2 (arbitrary waveform plotted in Fig. 7(c) and in Fig. 7(d)). The time-domain experimental results were performed with input signals x plotted in black solid curves having 23 ms duration. The output signals y in apparent advance of x without violating the causality are plotted in red dashed curves. We can observe from Figs. 7 that the simulated and measured results are in good correlation. As expected, the output signals plotted in red dashed curves

present raising and falling edges in time-advance corresponding to ($t < 0$) effect. The transient outputs approximately expressed by:

$$\begin{cases} y_1(t) \approx x_1(t + t_{a1}) \\ y_2(t) \approx x_2(t + t_{a2}) \end{cases} \quad (16)$$

with $t_{a1}=t_{a2}\approx-0.43$ ms are observed.

4 Conclusion

The $t < 0$ effect is innovatively studied with NGD circuit. The fundamental LP-NGD circuit theory enabling to explore the counterintuitive $t < 0$ effect is developed. The basic specifications of the LP-NGD function are defined. Then, a concrete LP-NGD topology is studied from the TF examination. The mathematical demonstration showing why the circuit emanates the $t < 0$ effect is established. The design equations of LP-NGD circuit resistor and capacitor in function of the desired value of time-advance and the amplifier gain are formulated.

A study of LP-NGD circuit experimentation is presented by using an RC-network based topology. The NGD test technique is described. The simulation and measurement results confirm the LP-NGD effect. The $t < 0$ effect of about -0.5 ms is observed.

The time-advance property related to LP-NGD function can be exploited in term of prediction for very interesting potential applications especially in sensor [7-12], industrial, robotic, environmental, biologic and health medical areas where mostly using slow signals. The innovative idea can be understood with equation (1). By supposing, for example, we have LP-NGD circuit with any time-advance as $t_a = -1$ minute, the output $y(t) = x(t - 1 \text{ minute})$ represents the information about input with 1 minute in advance. Nowadays, according to recent research work results, the LP-NGD function application idea was validated with:

- LP-NGD analog circuit prototypes for:
 - Reconstruction of sensor signal distorted by unwanted perturbations [7],
 - Anticipating actuator with arbitrary mechanical actioning [8],
 - And temporally advanced detection of physiological medical signals [9],
- And also LP-NGD digital circuit prototypes for:
 - Luminosity sensing prediction [10],
 - CO₂ gas concentration prediction in real-time [11],
 - And real-time prediction of greenhouse temperature with results shown in Figs. 8 [12].

Acknowledgements: The present research work is supported by Natural National Science Foundation of China (NSFC) Grant No. 62350610268.

References

- [1] B. Ségard and B. Macke, "Observation of Negative Velocity Pulse Propagation," *Phys. Lett. A*, Vol. 109, pp. 213-216, 1985.
- [2] M. W. Mitchell and R. Y. Chiao, "Causality and Negative Group-delays in a Simple Bandpass Amplifier," *Am. J. Phys.*, Vol. 66, pp. 14-19, 1998.
- [3] B. Ravelo, "Similitude between the NGD function and filter gain behaviours," *Int. J. Circ. Theor. Appl.*, Vol. 42 No. 10, pp. 1016-1032, 2014.
- [4] B. Ravelo, "First-order low-pass negative group delay passive topology," *Electronics Letters*, Vol. 52 No. 2, pp. 124-126, 2016.
- [5] S. Junwen, C. Junyan, H. E. Silochi, R. Wieser, R. Sanchez Galan, N. M. Murad and B. Ravelo, "Positive-to-negative tunable delay circuit designed with NGD RC network," *Int. J. Circ. Theor. Appl.*, Vol. 52, No. 10, pp. 5010-5024, Oct. 2024.
- [6] J. Y. Cui, H. E. Silochi, R. Wieser, S. Junwen, H. Bilal, S. Ngoho and B. Ravelo, "Familiarity analysis and time-advance experimental study of LP-NGD RC-circuit intended to operate with Unity-normalized gain," *COMPEL-The int. j. for computation and math. in electrical and electronic eng.*, Vol. 43 No. 5, pp. 1007-1022, 2024.
- [7] B. Ravelo, W. Rahajandraibe, Y. Gan, F. Wan, N. M. Murad and A. Douyère, "Reconstruction Technique of Distorted Sensor Signals with Low-Pass NGD Function," *IEEE Access*, Vol. 8, No. 1, Dec. 2020, pp. 92182-92195.

-
- [8] B. Ravelo, F. Wan and J. Ge, "Anticipating Actuator Arbitrary Action with a Low-Pass Negative Group Delay Function," *IEEE Transactions on Industrial Electronics*, Vol. 68, No. 1, Jan. 2021, pp. 694-702.
- [9] C. Hymel, R. A. Stubbers and M. E. Brandt, "Temporally Advanced Signal Detection: A Review of the Technology and Potential Applications," *IEEE CAS Magazine*, vol. 11, no. 3, pp. 10-25, 3rd Quarter 2011.
- [10] B. Ravelo, M. Guerin, L. Rajaoarisoa and W. Rahajandraibe, "Luminosity Sensing Application of Negative Group Delay Predictor," *IEEE Transactions on Industrial Electronics*, vol. 71, no. 8, pp. 9875-9885, Aug. 2024.
- [11] B. Ravelo, M. Guerin, and W. Rahajandraibe, "Negative Group Delay Predictor Application for CO₂ Gas Concentration Real-Time Forecasting," *IEEE Sensors Journal*, Vol. 24, No. 3, 2024, pp. 3874-3887.
- [12] B. Ravelo, M. Guerin, W. Rahajandraibe and L. Rajaoarisoa, "Low-Pass NGD Digital Circuit Application for Real-Time Greenhouse Temperature Prediction," *IEEE Transactions on Circuits and Systems II: Express Briefs*, Vol. 70, No. 9, Sept. 2023, pp. 3709-3713.

Analyse dispersive des guides d'ondes pour les antennes à ondes de fuite
Dispersive Analysis of Waveguides for Leaky-Wave Antennas

Yuhuan Tong^{1,2}, Davide Comite³, Beatrice Ambrogi³, Guido Valerio^{1,2}

¹Sorbonne Université, CNRS, Laboratoire de Génie Electrique et Electronique de Paris (GeePs), Paris, France

²Université Paris-Saclay, CentraleSupélec, CNRS, GeePs, Gif-sur-Yvette, France yuhuan.tong@sorbonne-universite.fr, guido.valerio@sorbonne-universite.fr

³Sapienza University, via Eudossiana 18, 00184, Rome, Italy, davide.comite@uniroma1.it, beatrice.ambrogi@uniroma1.it

Mots clés: Symétrie de glissement, antennes à ondes de fuite, antennes tout métal, analyse dispersive
Keywords: Glide symmetry, leaky wave antennas, all metal antennas, dispersive analyses

Résumé

Cet article présente une étude du comportement dispersif de guides d'ondes à plaques parallèles présentant une symétrie de glissement, perturbés par l'ouverture de fentes sur l'une des plaques, ce qui permet le rayonnement d'un mode à onde de fuite. Les caractéristiques de rayonnement de ce mode peuvent être prédites en calculant la partie réelle (constante de phase) et la partie imaginaire (constante d'atténuation) du nombre d'onde complexe associé à l'onde de fuite. Une méthode des moments périodique est utilisée pour effectuer ce calcul, et nous nous concentrons ici sur une étude paramétrique de l'atténuation dans la bande interdite ouverte. Nous effectuons une comparaison entre des guides d'ondes avec et sans symétrie de glissement, mettant en évidence des niveaux d'atténuation et des largeurs de bande interdite différents.

Abstract

This paper presents an investigation of dispersive behaviour of glide-symmetric parallel-plate waveguides perturbed with the opening of slots on one plate of the waveguide, allowing for radiation of a leaky-wave mode, whose radiation features can be predicted by computing the real part (phase constant) and imaginary part (attenuation constant) of the leaky-wave complex wavenumber. A periodic method-of-moment is employed to perform this calculation, and we focus here on a parametric study of the attenuation in the open stopband. We perform a comparison between glide- and non-glide symmetric waveguides, finding different levels of attenuation and stopband bandwidth.

1 Introduction

Current and next-generation wireless communications are pushing to a wider use of millimeter waves in order to grant connections with wider bandwidth and therefore higher data rates. At these frequencies all-metal structures can reduce losses and enable compact designs. Metallic glide-symmetric (GS) metasurfaces, i.e. metasurfaces invariant under a translation and a mirror reflection, have already proved to lead to non-dispersive designs and higher tolerance manufacturing. This paper studies the effect of introducing slots on the top plate of an all metal glide-symmetric (GS) parallel-plate waveguide (PPW) to explore the possible conversion of stopband modes into radiating leaky-wave modes. A periodic Method-of-Moment (MoM) is employed to rigorously analyse the dispersion and attenuation characteristics, comparing GS and non-GS structures, and offering new insights for designing low-attenuation leaky-wave antennas.

2 Approach for modal analysis

For the modal analysis of periodic open waveguides, a numerical code based on an efficient periodic MoM formulation, which rigorously accounts for both the periodic structure and the open radiation conditions by simulating a single unit cell.[1], is introduced to study the dispersive behaviour of all-metal 1-D periodic waveguide. The problem is formulated by an Electric-Field Integral Equation (EFIE) including a periodic kernel rigorously enforcing Floquet boundary conditions on the boundaries $x=0, p$ of the unit cell in Fig. 1(b). In the case of a TM^x polarization, the EFIE is

$$\hat{\mathbf{n}} \times \int_C \left(1 + \frac{1}{k^2} \nabla \nabla \right) \mathbf{J}(\mathbf{r}') G_p(\mathbf{r}, \mathbf{r}'; k_x, \omega) d\mathbf{r}' = \mathbf{0} \quad (1)$$

where $\mathbf{J}(\mathbf{r}')$ is the modal current flowing on the metallic line C and $\hat{\mathbf{n}}$ is the normal vector to C . G_p is the periodic Green's function of the bidimensional space with periodicity along the x direction. It depends on \mathbf{r} and \mathbf{r}' , the

source and the observation points on \mathcal{C} respectively, on the Floquet wavenumber $k_x = \beta - j\alpha$ and on the angular frequency ω . In a modal analysis, sources are absent and the right-hand side of (1) is null: we compute $k_x(\omega)$ such that $\mathbf{J} \neq 0$ exists.

The EFIE (1) can be transformed into matrix form

$$[\mathbf{Z}][\mathbf{J}] = \mathbf{0} \quad (2)$$

where the entries Z_{mn} of the system matrix are

$$Z_{mn} = \int_{\mathcal{C}} \mathbf{\Lambda}_m(\mathbf{r}) \cdot \int_{\mathcal{C}} \mathbf{\Lambda}_n(\mathbf{r}') G_p(\mathbf{r}, \mathbf{r}'; k_x, \omega) d\mathbf{r}' d\mathbf{r} + \frac{1}{k^2} \int_{\mathcal{C}} \nabla \cdot \mathbf{\Lambda}_m(\mathbf{r}) \int_{\mathcal{C}} \nabla' \cdot \mathbf{\Lambda}_n(\mathbf{r}') G_p(\mathbf{r}, \mathbf{r}'; k_x, \omega) d\mathbf{r}' d\mathbf{r} \quad (3)$$

The propagation wavenumber $k_x(\omega)$ corresponds to complex zeros of the determinant of the system matrix, which are found in the complex plane by means of an iterative method based on type II Padé approximation [2]

Figs 1(a) and (b) show the structure under analysis. Fig. 1(c) presents the dispersive behaviour (phase β and attenuation α constants of the fundamental Floquet mode) of an open GS structure with a slot on the upper metallic plate. The results demonstrate good agreement with those obtained using the multi-modal transmission matrix method (MMTMM) [3], an approximate method for the extraction of wavenumbers of Floquet modes from the simulation of a truncated cascade of cells. With this MoM, two key geometrical operations are investigated described in the following subsections.

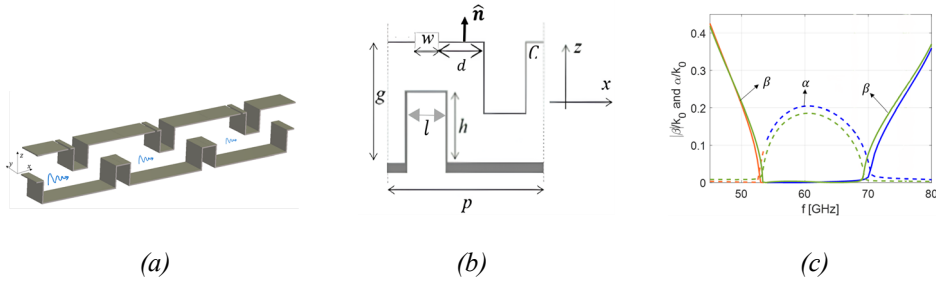


Figure 1: Geometry of the GS structure under analysis. (a) 3D view. (b) Later view. (c) Dispersive behaviour of the structure in (a) MMTMM (green lines), MoM (orange and blue lines)

3 Analysis of symmetric configurations and radiation slots

In this section, we investigate the influence of various structural parameters on the dispersive behaviour of the open waveguide. The introduction of slots breaks the original symmetry, thereby disrupting the glide symmetry effect [4]. To assess the impact of this disruption, we first compare the dispersive behaviours of the LWAs based on glide- and conventional nonglide-symmetric structure to investigate the influence of the background waveguide. Following this, we further analyse how introducing a second slot and modifying the corrugation shape in the structure of Fig. 1(a) can optimize the dispersive performance.

3.1 Study of mirroring and translation

The effects of the two operations of GS structure-mirroring and translation-are examined. Three configurations are compared: a slotted GS structure and two non-GS structures, where only one plate is corrugated with a slot—

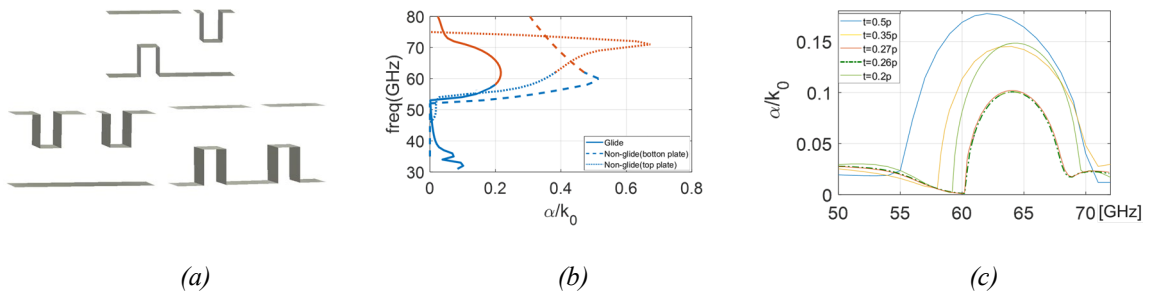


Figure 2 (a) Unit cell of the slotted GS and non-GS structure (b) Normalized attenuation constant of the structures in (a). (c) Normalized attenuation constant of quasi-glide symmetric structures with different translation, t is the distance between two adjacent corrugations.

either on the corrugated or on the flat plate, as shown in Fig. 2(a). Results in Fig. 2(b) show that the mirroring operation significantly reduces the attenuation constant and the frequency bandwidth of the stopband at $\beta = 0$. Moreover, by varying the distance t between upper and lower corrugations while keeping the period constant, an optimal value ($t = 0.26p$) is identified at which attenuation is minimized, as depicted in Fig. 2(c). These insights can be useful as a starting point to design leaky-wave antennas with open-stopband suppression.

3.2 Study with the radiation slots

We further investigate the influence of introducing a second slot and modifying the corrugation shape. A two-slot configuration, where the slots are placed asymmetrically[5], is found to lower the attenuation as the slot spacing increases, as shown in Fig. 3(b). Additionally, replacing a rectangular corrugation with a trapezoidal one, as shown in Fig. 3(c), and fine-tuning its dimensions further reduces the maximum normalized attenuation constant to 0.0234, thereby dividing by almost a factor 10 the attenuation in the original GS structure of Fig. 2(a).

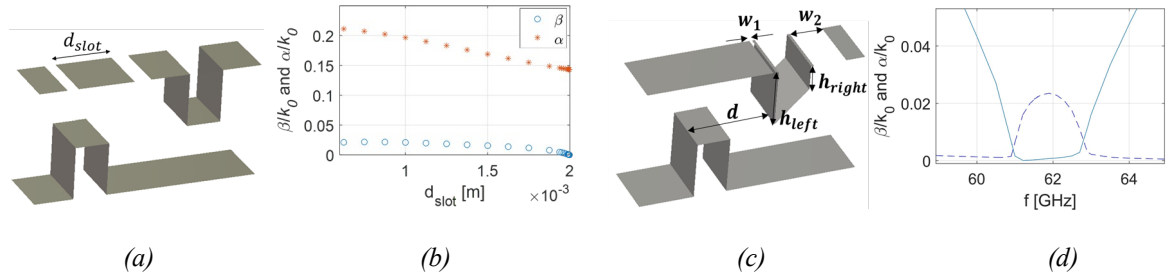


Figure 3 (a) GS unit cell with two slots (b) Wavenumber at 60 GHz with different distance between slots (c) Unit cell with a trapezoidal corrugation on the top plate. (d) Dispersive behaviour with optimized geometrical parameters.

4 Conclusion

This study analysed the stopband of periodic double-corrugated all-metal waveguides, examining the impact of slot and corrugation geometry on attenuation constants. An *ad-hoc* periodic MoM approach led to rigorous dispersion analyses. Results show that a simple optimization of the slot and corrugation position and shape can significantly reduce the attenuation in the open stopband, thus selecting structures candidates for directive broadside radiation. In the full paper a complete design leading to an open stopband suppression will be discussed.

References

- [1] M. Petek, J. Rivero, J. A. T. Vázquez, G. Valerio, O. Quevedo-Teruel, and F. Vipiana, ‘Method of Moments for the Dispersion Modeling of Glide-Symmetric Periodic Structures’, *IEEE Trans. Antennas Propagat.*, vol. 72, no. 1, pp. 756–766, Jan. 2024, doi: 10.1109/TAP.2023.3325207.
- [2] V. Galdi and I. M. Pinto, ‘A simple algorithm for accurate location of leaky-wave poles for grounded inhomogeneous dielectric slabs’, *Microw. Opt. Technol. Lett.*, vol. 24, no. 2, pp. 135–140, Jan. 2000, doi: 10.1002/(SICI)1098-2760(20000120)24:2<135::AID-MOP17>3.0.CO;2-P.
- [3] F. Mesa, G. Valerio, R. Rodríguez-Berral, and O. Quevedo-Teruel, ‘Simulation-Assisted Efficient Computation of the Dispersion Diagram of Periodic Structures: A comprehensive overview with applications to filters, leaky-wave antennas and metasurfaces’, *IEEE Antennas Propag. Mag.*, vol. 63, no. 5, pp. 33–45, Oct. 2021, doi: 10.1109/MAP.2020.3003210.
- [4] M. Bagheriasl, O. Quevedo-Teruel, and G. Valerio, ‘Bloch Analysis of Artificial Lines and Surfaces Exhibiting Glide Symmetry’, *IEEE Trans. Microwave Theory Techn.*, vol. 67, no. 7, pp. 2618–2628, Jul. 2019, doi: 10.1109/TMTT.2019.2916821.
- [5] J. Liu, W. Zhou, and Y. Long, ‘A Simple Technique for Open-Stopband Suppression in Periodic Leaky-Wave Antennas Using Two Nonidentical Elements Per Unit Cell’, *IEEE Trans. Antennas Propagat.*, vol. 66, no. 6, pp. 2741–2751, Jun. 2018, doi: 10.1109/TAP.2018.2819701.

Mushroom multi-vias pour des structures empilées à bande interdite avec symétrie de réflexion glissé

Stacked Multi-Via Mushroom-Type EBG Structures with Glide Symmetry

Ashray Ugle^{1,2}, Massimiliano Casaletti^{1,2}, Marta Arias Campo³, Simona Bruni³, Guido Valerio^{1,2}

¹ Sorbonne Université, Laboratoire de Génie Électrique et Électronique de Paris (GeePs), 75005, Paris, France, ashray.ugle@sorbonne-universite.fr, massimiliano.casaletti@sorbonne-universite.fr, guido.valerio@sorbonne-universite.fr

² Université Paris-Saclay, CentraleSupélec, CNRS, GeePs, 91192, Gif-sur-Yvette, France

³ Department of Antennas & EM Modelling, IMST GmbH, 47475, Kamp-Lintfort, Germany, simona.bruni@imst.de, marta.arias@imst.de

Mots-clés / Keywords: Analyse de dispersion / Dispersion analysis, Matériaux à bande interdite électromagnétique / Electromagnetic bandgap materials, Symétrie de réflexion glissé / Glide symmetry, Analyse multimodale / Multimodal analysis.

Résumé/Abstract

Cette étude examine la dispersion de structures à bande interdite électromagnétique (EBG) de type mushroom empilées avec multi-vias, intégrant une symétrie de glissement, dans la plage de fréquences de 50 à 90 GHz. Il est observé que la cellule élémentaire innovante à symétrie de réflexion glissée peut fonctionner comme une structure EBG indépendamment du nombre de couches empilées. En utilisant la méthode matricielle de transfert multi-modale (MMTMM), le nombre d'onde complexe de la structure périodique est obtenu par post-traitement des paramètres S généralisés issus d'un solveur commercial. Les résultats mettent en évidence que les structures EBG de type mushroom empilées avec multi-vias et symétrie de réflexion glissée offrent des avantages significatifs pour la conception de composants de guides d'ondes à fente, en utilisant une technologie de circuits imprimés (PCB) multicouches économique.

The presented study investigates the dispersion behaviour of stacked multi-via mushroom-type electromagnetic bandgap (EBG) structures with glide symmetry in the 50-90 GHz frequency range. It is observed that the novel glide-symmetric unit cell is able to function as an EBG independent of the number of layers when stacked. Using the multi-mode transfer matrix method (MMTMM), the complex wavenumber of the unit cells is obtained by post-processing the generalised S-Parameters from a commercial solver. The findings highlight that the stacked multi-via mushroom-type EBG structures with glide symmetry offer significant advantages in the design of gap-waveguide components using cost-effective multi-layer printed circuit board (PCB) technology.

1 Introduction

The growing advancement in millimeter-wave (mm-Wave) automotive radar technology [1], [2] has increased the demand for low-loss and cost-effective antenna and waveguide solutions. While traditional metallic waveguide technology offers minimal losses, they are expensive to manufacture. PCB based solutions are cost-efficient but suffer from high material losses in this frequency range. Gap waveguide technology [3], realised with PCB based EBG structures combines the advantages of both technologies. Mushroom-type EBGs [4] have been proven to be effective in PCB configurations [5]-[8], but suffer a reduction in stopband bandwidth when stacked [9], [10], as the number of layers increase. Also, the studies in [4]-[10] have been conducted primarily at lower frequencies. A periodic structure is said to be glide-symmetric, if it is invariant after a translation by half the period followed by a reflection. Recently, periodic structures with glide symmetry have been shown to produce wide stopbands [11] and they were used in [12] to improve the stopband bandwidth of mushroom-type EBGs. To address the challenges of stacking in the 50-90 GHz range, a glide-symmetric EBG cell has been investigated to maintain its stopband performance in stacked configurations, making it ideal for multi-layer PCB based gap-waveguides.

2 Modelling Methodology

The conventional mushroom-type EBG is modified with multiple vias, and glide-symmetry is introduced to be enclosed in a parallel plate waveguide (PPW) environment as shown in Figure 1a. The dispersion characteristics of the proposed multi-via glide-symmetric mushroom-type EBG are analysed using MMTMM [13], [14]. To compute the complex wavenumber of a 2-D periodic structure using MMTMM, the unit cell is simulated in CST using frequency domain solver [16] with N waveguide modes on each of the four faces, to account for the

interactions from the adjacent cells. The multi-mode transfer matrix $[\mathbf{T}]$ of size $4N \times 4N$ can be obtained from the generalised scattering parameters from CST, and can be used to solve a non-standard eigenvalue problem in the form of

$$[\mathbf{T}] \begin{bmatrix} \mathbf{V}_x \\ \mathbf{V}_y \\ \mathbf{I}_x \\ \mathbf{I}_y \end{bmatrix} = \begin{bmatrix} \lambda_x \mathbf{V}_x \\ \lambda_y \mathbf{V}_y \\ \lambda_x \mathbf{I}_x \\ \lambda_y \mathbf{I}_y \end{bmatrix}; [\mathbf{T}] = \begin{bmatrix} [\mathbf{A}] & [\mathbf{B}] \\ [\mathbf{C}] & [\mathbf{D}] \end{bmatrix}, \quad (1)$$

where $\lambda_i = e^{-jk_i p_i}$; $i = x, y$, such that, k_i is the complex wavenumber and p_i is the periodicity along the i direction. The multi-mode transfer matrix $[\mathbf{T}]$ consists of four submatrices $[\mathbf{A}]$, $[\mathbf{B}]$, $[\mathbf{C}]$, $[\mathbf{D}]$ of sizes $N \times N$, respectively. The complex wavenumber $k_i = \beta_i - j\alpha_i$; $i = x, y$ contains the phase constant β_i and attenuation constant α_i along the i direction. The eigenvalue problem in (1) is non-standard, and can be solved using root-finding algorithms or by following a linearisation procedure as in [15], the latter of which is employed in this work. After employing the linearisation procedure, the eigenvalue problem in (1) can be modified as

$$[\tilde{\mathbf{T}}] \begin{bmatrix} \mathbf{V}_x \\ \mathbf{I}_x \\ \mathbf{V}_y \\ \mathbf{I}_y \end{bmatrix} = \begin{bmatrix} \lambda_x \mathbf{V}_x \\ \lambda_x \mathbf{I}_x \\ \lambda_y \mathbf{V}_y \\ \lambda_y \mathbf{I}_y \end{bmatrix}; [\tilde{\mathbf{T}}] = \begin{bmatrix} [\tilde{\mathbf{T}}_{xx}] & [\tilde{\mathbf{T}}_{xy}] \\ [\tilde{\mathbf{T}}_{yx}] & [\tilde{\mathbf{T}}_{yy}] \end{bmatrix}, \quad (2)$$

where $[\mathbf{T}]$ is permuted as $[\tilde{\mathbf{T}}] = [\mathbf{P}][\mathbf{T}][\mathbf{P}]$ with a suitable permutation matrix $[\mathbf{P}]$. This procedure results in two standard eigenvalue problems

$$\{[\tilde{\mathbf{T}}_{xx}] + [\tilde{\mathbf{T}}_{xy}][\mathbf{Q}_x][\tilde{\mathbf{T}}_{yx}]\} \begin{bmatrix} \mathbf{V}_x \\ \mathbf{I}_x \end{bmatrix} = \lambda_x \begin{bmatrix} \mathbf{V}_x \\ \mathbf{I}_x \end{bmatrix}, \quad (3)$$

$$\{[\tilde{\mathbf{T}}_{yy}] + [\tilde{\mathbf{T}}_{yx}][\mathbf{Q}_y][\tilde{\mathbf{T}}_{xy}]\} \begin{bmatrix} \mathbf{V}_y \\ \mathbf{I}_y \end{bmatrix} = \lambda_y \begin{bmatrix} \mathbf{V}_y \\ \mathbf{I}_y \end{bmatrix}, \quad (4)$$

such that

$$[\mathbf{Q}_x] = (\lambda_y [\mathbf{1}] - [\tilde{\mathbf{T}}_{xx}])^{-1} \quad (5)$$

$$[\mathbf{Q}_y] = (\lambda_x [\mathbf{1}] - [\tilde{\mathbf{T}}_{yy}])^{-1} \quad (6)$$

where $[\mathbf{1}]$ is an identity matrix of size $N \times N$.

The complex wavenumber for the glide-symmetric mushroom-type EBG structure is then computed in the irreducible Brillouin zone. By fixing λ_y and λ_x in (5) and (6), respectively, The eigenvalue problems in (3) and (4) can be solved to obtain k_x for the $\bar{\Gamma}\bar{X}$ segment and k_y for the $\bar{X}\bar{M}$ segment. For the $\bar{M}\bar{\Gamma}$ segment, the eigenvalue problem in (1) is already linear, and can be solved directly since $k_x = k_y$.

3 Results and Discussion

The dispersion diagram for the unit cell in Figure 1a in the irreducible Brillouin zone computed using MMTMM with $N = 5$ modes for the glide-symmetric multi-via mushroom-type EBG in Figure 1a is compared with CST eigenmode solver (ES) in Figure 1b. The MMTMM computation shows good agreement with the CST ES results with a stopband observed from 43 to 93 GHz. The normalised attenuation constants obtained using MMTMM in the $\bar{\Gamma}\bar{X}$ and $\bar{M}\bar{\Gamma}$ directions, is shown in Figure 1c. The minimum of the two constants is highlighted in red, depicting the minimum attenuation in the stopband.

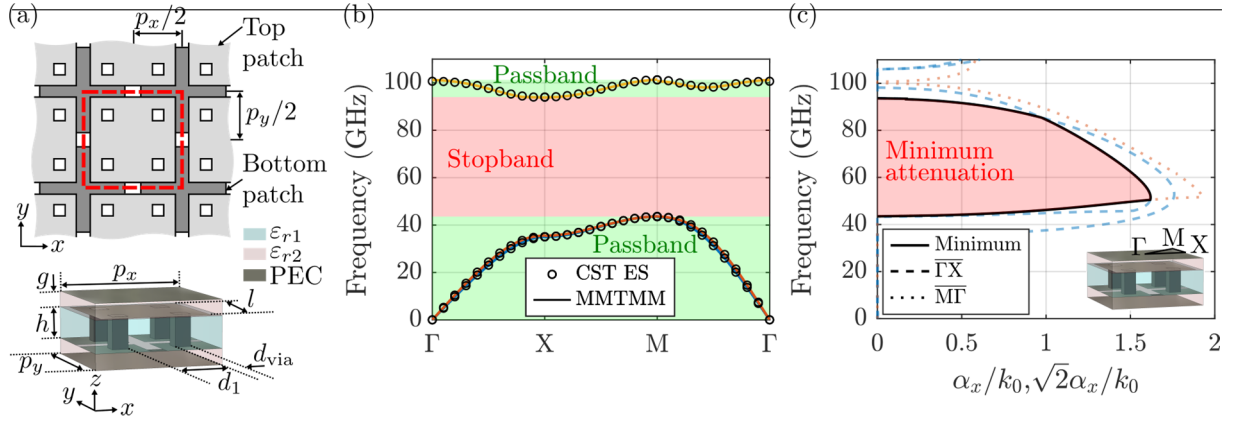


Figure 1: (a) Multi-via mushroom-type EBG with glide symmetry inside a PPW environment with dimensions $p_x = 0.8$ mm, $p_y = 0.8$ mm, $g = 0.04$ mm, $h = 0.2$ mm, $l = 0.7$ mm, $d_{via} = 0.1$ mm, $d_1 = 0.3$ mm and material properties $\epsilon_{r1}, \epsilon_{r2} = 4.4$. (b) Normalised phased constant in the irreducible Brillouin zone, with the stopband and passband regions shaded in red and green, respectively. (c) Normalised attenuation constants in the $\overline{\Gamma X}$ and $\overline{M\Gamma}$ direction, showing the minimum of the two constants in red.

The easiest way to stack the EBG structure in Figure 1a is to simply translate the unit cell vertically. No stopband is observed when stacked by translation. However, when the unit cell in Figure 1a is stacked by performing a mirror operation, as shown in Figure 2a, the stopband is retained. The dispersion diagram in the irreducible Brillouin zone for the stacked structure in Figure 2b is computed using MMTMM ($N = 5$) and is compared with CST ES in Figure 2b. Once again, the MMTMM calculation coincides well with the CST ES results. The normalised attenuation constants calculated with MMTMM in the $\overline{\Gamma X}$ and $\overline{M\Gamma}$ directions with the minimum of the two, highlighted in red, is shown in Figure 2c. It is observed that both the stopband width and minimum attenuation of the stacked structure is preserved, making it well-suited for multi-stacked gap waveguide components realised using PCB technology.

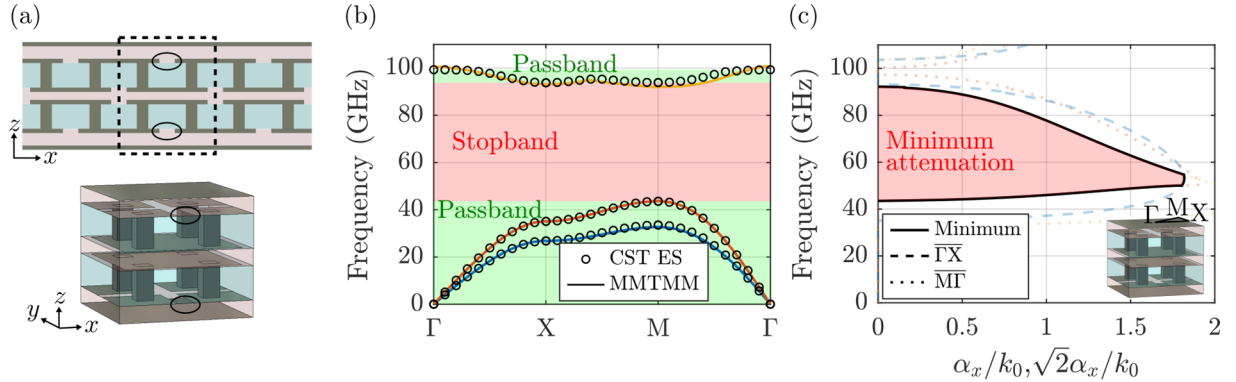


Figure 2: (a) Stacking of the EBG structure inside a PPW environment in Figure 1a using mirroring. (b) Normalised phased constant in the irreducible Brillouin zone, with the stopband and passband regions shaded in red and green, respectively. (c) Normalised attenuation constants in the $\overline{\Gamma X}$ and $\overline{M\Gamma}$ direction, showing the minimum of the two constants in red.

4 Conclusion

This study presents a novel stacked multi-via mushroom-type EBG with glide symmetry whose stopband is unaffected when stacked in a mirrored configuration. The results demonstrate its suitability for multi-layer PCB-based gap waveguide components for low-loss and low-cost implementations in mm-Wave automotive radar.

Acknowledgement

This publication is based upon work supported by the Horizon Europe Research and Innovation Program and UKRI under the GENIUS Project, Marie Skłodowska-Curie Grant under Agreement 101072560.

References

- [1] C. Waldschmidt, J. Hasch, and W. Menzel, “Automotive radar — from first efforts to future systems,” *IEEE Journal of Microwaves*, vol. 1, no. 1, pp. 135–148, 2021.
- [2] J. Hasch, E. Topak, R. Schnabel, T. Zwick, R. Weigel, and C. Waldschmidt, “Millimeter-wave technology for automotive radar sensors in the 77 ghz frequency band,” *IEEE Transactions on Microwave Theory and Techniques*, vol. 60, no. 3, pp. 845–860, 2012.
- [3] E. Rajo-Iglesias, M. Ferrando-Rocher, and A. U. Zaman, “Gap waveguide technology for millimeter-wave antenna systems,” *IEEE Communications Magazine*, vol. 56, no. 7, pp. 14–20, 2018.
- [4] D. Sievenpiper, L. Zhang, R. Broas, N. Alexopolous, and E. Yablonovitch, “High-impedance electromagnetic surfaces with a forbidden frequency band,” *IEEE Transactions on Microwave Theory and Techniques*, vol. 47, no. 11, pp. 2059–2074, 1999.
- [5] S. Rogers, “Electromagnetic-bandgap layers for broad-band suppression of tem modes in power planes,” *IEEE Transactions on Microwave Theory and Techniques*, vol. 53, no. 8, pp. 2495–2505, 2005.
- [6] E. Pucci, E. Rajo-Iglesias, and P.-S. Kildal, “New microstrip gap waveguide on mushroom-type ebg for packaging of microwave components,” *IEEE Microwave and Wireless Components Letters*, vol. 22, no. 3, pp. 129–131, 2012.
- [7] C.-D. Wang, Y.-M. Yu, F. de Paulis, A. C. Scogna, A. Orlandi, Y.-P. Chiou, and T.-L. Wu, “Bandwidth enhancement based on optimized via location for multiple vias ebg power/ground planes,” *IEEE Transactions on Components, Packaging and Manufacturing Technology*, vol. 2, no. 2, pp. 332–341, 2012.
- [8] N. Bayat-Makou and A. A. Kishk, “Contactless air-filled substrate integrated waveguide,” *IEEE Transactions on Microwave Theory and Techniques*, vol. 66, no. 6, pp. 2928–2935, 2018.
- [9] M. A. M. Hassan and A. A. Kishk, “Bandwidth study of the stacked mushroom ebg unit cells,” *IEEE Transactions on Antennas and Propagation*, vol. 65, no. 8, pp. 4357–4362, 2017.
- [10] X.-F. Zhao, J.-Y. Deng, J.-Y. Yin, D. Sun, L.-X. Guo, X.-H. Ma, and Y. Hao, “Novel suspended-line gap waveguide packaged with stacked-mushroom ebg structures,” *IEEE Transactions on Microwave Theory and Techniques*, vol. 69, no. 5, pp. 2447–2457, 2021.
- [11] O. Quevedo-Teruel, Q. Chen, F. Mesa, N. J. G. Fonseca, and G. Valerio, “On the benefits of glide symmetries for microwave devices,” *IEEE Journal of Microwaves*, vol. 1, no. 1, pp. 457–469, 2021.
- [12] B. A. Mouris, A. Fernández-Prieto, R. Thobaben, J. Martel, F. Mesa, and O. Quevedo-Teruel, “On the increment of the bandwidth of mushroom-type ebg structures with glide symmetry,” *IEEE Transactions on Microwave Theory and Techniques*, vol. 68, no. 4, pp. 1365–1375, 2020.
- [13] F. Mesa, G. Valerio, R. Rodríguez-Berral, and O. Quevedo-Teruel, “Simulation-assisted efficient computation of the dispersion diagram of periodic structures: A comprehensive overview with applications to filters, leaky-wave antennas and metasurfaces,” *IEEE Antennas and Propagation Magazine*, vol. 63, no. 5, pp. 33–45, 2021.
- [14] M. Bagheriasl, O. Quevedo-Teruel, and G. Valerio, “Bloch analysis of artificial lines and surfaces exhibiting glide symmetry,” *IEEE Transactions on Microwave Theory and Techniques*, vol. 67, no. 7, pp. 2618–2628, 2019.
- [15] F. Giusti, Q. Chen, F. Mesa, M. Albani, and O. Quevedo-Teruel, “Efficient bloch analysis of general periodic structures with a linearized multimodal transfer-matrix approach,” *IEEE Transactions on Antennas and Propagation*, vol. 70, no. 7, pp. 5555–5562, 2022.
- [16] “CST Studio Suite 3D Electromagnetic Analysis Software Package.” <https://www.3ds.com/products/simulia/cst-studio-suite>.

Liste des auteurs

- Agnus B., 96–103
Allal Djamel, 33–40, 47–54
Ambrogi Beatrice, 104–106
Arias Campo Marta, 107–110
Arnaud Saint-Jalmes, 2–6
- Ba Doudou, 25–32
Baccar Sahbi, 76–81
Bruni Simona, 107–110
Burokur Shah Nawaz, 71–75
Bêche Bruno, 2–6
- Casaletti Massimiliano, 107–110
Combette Philippe, 15–21
Comite Davide, 104–106
Cormerais Hervé, 2–6
- D'hulst Christophe, 87–94
De Doncker Philippe, 82–85
Delille Nolane, 7–14
- El Korso Mohammed Nabil, 71–75
- Gastebois Jordan, 2–6
Gauffre Fabienne, 2–6
George Océane, 87–94
Gurgel Nathan, 96–103
- Haddad Madjid, 76–81
Haddadi Kamel, 33–40, 47–54, 87–94
Hamrouni Nawres, 76–81
Hervé Lhermite, 2–6
- Khalifeh Rania, 76–81
- Lallechere Sebastien, 7–14
Lenoir Clément, 47–54, 87–94
Liu Jiang, 60–69
- Meftah Nawel, 71–75
Melki Mathis, 82–85
Monsef Rabah Florian, 55–58
Morán-Meza José A., 23, 24
Moussa Sonia, 96–103
- Naït-Abdesselam Farid, 65–69
- Paboeuf Gilles, 2–6
Pistre Séverin, 15–21
- Ratni Badreddine, 71–75
Ravelo Blaise, 7–14, 96–103
Risacher Christophe, 41–46
Rossignol J., 96–103
Rossignol Jerome, 7–14
- Sarrazin Julien, 82–85
Sebbache Mohamed, 47–54, 87–94
Seck Daouda, 33–40, 47–54
Sun Qunfei, 65–69
Szymczyk Anthony, 2–6
- Tong Yuhuan, 104–106
Troesch Nicolas, 15–21
- Ugle Ashray, 107–110
- Valerio Guido, 104–110
Vena Arnaud, 15–21
Vié Véronique, 2–6
- Wang Shanshan, 60–69
Wuart Joe, 60–69
- Zhang Yarui, 60–69

AVEC LE SOUTIEN DE



INSTITUT DE FRANCE
Académie des sciences



EXPOSANTS

ROHDE & SCHWARZ



**COMITÉ NATIONAL FRANÇAIS DE RADIOÉLECTRICITÉ SCIENTIFIQUE
UNION RADIO SCIENTIFIQUE INTERNATIONALE**

Siège social : Académie des Sciences, 23 quai de Conti, Paris 6ème
Site Internet : <http://www.ursi-france.org>

Adresse postale : Alain Sibille, Secrétaire général d'URSI-France,
Telecom Paris, 19 place Marguerite Perey, F-91120 Palaiseau
Téléphone : + 33 1 75 31 93 13
Courriel : contact@ursi-france.org